University of Nottingham
UK | CHINA | MALAYSIA

Reducing measurement time for X-ray computed tomographic surface metrology

Lars Körner

Thesis submitted to the University of Nottingham
for the Degree of Doctor of Philosophy

January 2020

Abstract

This thesis addresses the measurement time in X-ray computed tomography (XCT). XCT is a non-destructive volumetric imaging technique that acquires radiographic projection data to reconstruct the measured object. XCT has recently started to be used as a tool for the measurement of surface topography, especially in the field of additive manufacturing. But long acquisition times in XCT are a major shortcoming and impede its industrial integration. The aim of this work is to identify and evaluate strategies, methods and approaches which reduce the required number of radiographs in XCT for surface topography measurement.

A review is conducted of both the medical and industrial literature on approaches and methods to reduce the measurement time in XCT. From the review of the state-of-the-art research, two methods were identified for further in-depth investigation. The thesis builds on a two-pillar approach for the evaluation of the reconstruction quality. The quality of the reconstructions are analysed in terms of image quality (e.g. noise and resolution) and the measured surface topographies are quantified.

A method of compensating for the negative imaging artefacts arising from a simple reduction of the number of projections is evaluated and the parameter space of the method is mapped out. This method is called sinogram interpolation and stems from the medical literature. It is shown that the acquisition time of an XCT measurement can be reduced by 80%, while the losses to resolution, noise and the surface topography described numerically.

A method that uses variable projection spacing under continuous motion of the sample is proposed and evaluated. It is demonstrated that the proposed projection spacing can lead to a reduction in the total number of projections, which is dependent on the object’s shape.

Abstract

The variable projection spacing method is a promising approach to reduce the acquisition and reconstruction times without major losses to the reconstructions.

The thesis evaluates two approaches (variable projection spacing and sinogram interpolation) of tackling the measurement time burden of XCT. This thesis contributes to the broader research field by adding a further stepping stone to the cumulative body of work to advance the industrial competitiveness of XCT.

Acknowledgements

I would like to thank my supervisors Richard Leach and Simon Lawes for their support throughout the PhD. Further, I would like to thank Chris Fox, David Bate, Nicola Senin and Rong Su for the fruitful discussions and their continuous help.

I am also indebted to my friends and colleagues Daniel B., Ian B., Patrick B., Jorge F., Joe H., Lewis N., Luke O., Michael K., Osiris S., Luke T., and all the others I forgot to list, for all the moments of laughter and the moral support while sharing coffees and beers together over the years.

I would like to express my gratitude to my father Bernd and my mother Iris. Without you I would have never been able to stand through the stresses of the last four years nor would I be the person who I am today. And I would also like to apologise to my siblings Inga and Jan for introducing myself as an Akademiker to the family. And finally, I would like to thank my dearest Emily for the encouragement and for supporting me to stay on the bright side during all the years.

This research was carried out as part of the Centre for Doctoral Training in Additive Manufacturing and 3D Printing, which is kindly funded by the Engineering and Physical Sciences Research Council and generously supported by Nikon Metrology Ltd.

Declaration of authorship

I declare that the presented work is of my own doing. Where work of others is quoted, proper accreditation to the source has been given in the text. The work presented was undertaken during my time as a PhD candidate at the University of Nottingham. Part of this work has been published in multi-authored papers and conference proceedings. Areas utilising material from multi-authored papers have been highlighted. The work was undertaken under the supervision, guidance and assistance of Richard K. Leach, Simon Lawes and Nicola Senin. Part of the methods used in this thesis is based on methods and software developed by Nicola Senin and has been indicated as such.

Lars Körner 14.01.2019

Table of contents

List of figures

List of tables

Abbreviations

AM	Additive manufacturing
CAD	Computer-aided design
CI	Confidence interval
CMM	Coordinate measuring machine
CNR	Contrast-to-noise ratio
DART	Discrete algebraic reconstruction technique
DT	Discrete tomography
FBP	Filtered back projection
FDK	Feldkamp-Davis-Kress
FoV	Field of view
HART	High aspect ratio tomography
IR	Iterative reconstruction
keV	kilo-electronvolts
LINAC	Linear particle accelerator
MPE	Maximum permissible error
ODD	Object detector distance
PBF	Powder bed fusion
ROI	Region of interest
SART	Simultaneous algebraic reconstruction technique
SI	International system of units
SIRT	Simultaneous iterative reconstruction technique
XCT	X-ray computed tomography
E	Photon energy
$F(u,v)$	Spatial frequency domain of a tomogram in 2D
$f(x,y)$	Spatial domain of tomogram in 2D
Θ	Cumulative rotation angle
θ	Step angle
μ	Linear attenuation coefficient

1 Introduction

1.1 Motivation

X-ray computed tomography (XCT) is a non-destructive, volumetric imaging technique and is most commonly known for its diagnostic use in medicine. Nonetheless, the technology is used in the non-destructive engineering sector and is currently evaluated as a metrological tool for both dimensional and surface metrology [1–3].

The volumetric nature of XCT has led to an interest in applying XCT on additively manufactured (AM) parts, in particular to laser and electron beam powder bed fusion (PBF) parts [4]. Part of this research interest stems from the challenges of AM's design freedom and material composition. The often optimised and complex designs of AM parts and highly irregular surfaces pose challenges to tactile and optical measuring devices, not just for form metrology but also for surface metrology [5]. Thus the volumetric nature of XCT has led to applications such as the study of porosity, dimensional conformity and the surface roughness [4,6,7]. Especially the ability of XCT to measure internal voids, surfaces and geometries is repeatedly quoted as a vital advantage of XCT in the measurement of AM. Some of the most recent research avenues of XCT measurements include the surface topography analysis of AM parts [2,6,8–12].

While XCT has strong advantages in dealing with complex geometries, issues remain in establishing XCT as an accepted and widely used tool in both dimensional and surface metrology [1,6]. Shortcomings such as geometrical calibration [13] are the focus of recent research, along with assessing methods for estimation the measurement uncertainty of XCT [14–18]. A 2015 report by Frost and Sullivan on the Strategic Analysis of Computed Tomography Technology in the Dimensional Metrology Market [19] reported that a significant reduction in the measurement time is needed for the widespread commercialisation of XCT [19,20]. This need for the reduction in measurement time has even influenced the aims of a large project of the European Association of National

Metrology Institutes (EURAMET), which kicked off in 2018 [21]. Alongside uncertainty and traceability investigations, the EURAMET project aims at the reduction of measurement times of XCT scans from hours to minutes.

Large measurement times in XCT are due to a complex interaction of system limits and user variables, and cannot easily be attributed to a single factor. Modern XCT systems with flat-panel detectors often need thousands of projections for a full, volumetric reconstruction [3,22]. The number of radiographs shifts into the focus as the exposure of each individual radiograph is considered; the exposure of each radiograph can surpass several seconds. The founding mathematical and physical constraints dictating the number of radiographs of analytical reconstruction techniques often clash with the economic and time requirements of a modern manufacturing environment. Thus, investigations into methods to reduce the number of radiographs are of current interest to the research and industrial community. This yields the questions, what methods exist to reduce the acquisition times and what characterises their effects on surface topography measurements?

The aim of this thesis is to identify and evaluate strategies, methods and approaches which reduce the required number of radiographs in X-ray computed tomography for the surface metrological evaluation.

The realisation of the aim is constructed around the following objectives. Review existing technologies in both medical and industrial use of XCT. Find means to assess and compare the performance of the different technologies. Identify suitable methods and evaluate their performance in reference to surface topography measurements. The work presented is structured into 7 chapters.

1.2 Structure of the thesis

The first chapter has given some insight into the background and the aim and motivations of the thesis.

The second chapter is included as it reflects on the basics of X-ray physics and some of the concepts associated with computed tomography, which are a prerequisite for the later chapters. It contains a short introduction to the XCT measurement chain. This is written with the intent to help with the basics needed to understand the world of XCT as an imaging and metrology system.

The third chapter is a detailed literature review which aims to include medical and industrial research on how other researchers have used the XCT system set up to acquire radiographic projections. This includes the use of projections in the reconstruction and why they have acquired them. The driving factor behind the literature review is to aim for methods approaches and thoughts on how to improve XCT or how to increase the speed of XCT.

The fourth chapter describes the methods used in the characterisation and evaluation of the methods explored in the later chapters. Each section explains the methods used and a short rationale on why the investigated quantity is of interest. The characterisation is split into three separate categories, noise, resolution and topography comparison, followed by a short introduction to the XCT system and simulation tool used in the investigations of the later chapters.

The fifth chapter arose from medical literature publications reviewed in the second chapter. It explores the method of sinogram interpolation, defined later, as a tool to overcome some of the issues associated with a reduced number of projections when applied to surface topography measurements of additively manufactured parts.

The sixth chapter is inspired by another technique found in the literature review: adaptive projection spacing for circular acquisition trajectories of high aspect ratio parts. The medical literature concludes that variant projection spacing can be beneficial. This chapter

is a simulation study on the effects of variant projection spacing on surface topography measurements with XCT.

The seventh chapter reflects on and discusses the whole of the presented work within this thesis. The penultimate subchapter concludes on the entirety of the thesis, followed by the final subchapter that highlights some future areas of research and experimental investigation.

2 Fundamentals of XCT in the context of metrology

Chapter 2 first introduces a simplified measurement chain of XCT for metrology applications in order to set the scene for the rest of this chapter and the rest of the thesis. The field of surface metrology of additively manufactured parts is highlighted as an area of application. Section 2.2 looks at the principles behind tomography and how cross-sectional images are obtained. Section 2.3 reflects on the image formation process and how X-ray physics dictates it.

2.1 XCT for metrology

Metrology is the science and application of measurement [23]. A measurement is the process of "*experimentally obtaining one or more quantity values that can reasonably be attributed to a quantity*" [23]. No measurement can determine a 'true' value of a measurand but for any measurement – no matter how accurate and precise – a degree of doubt remains, which is known as measurement uncertainty [23]. Uncertainty is a quantitative measure which characterises the dispersion of possible values associated to the measurement [23]. Traceability is a fundamental concept in metrology, and relates to the idea of a measurement to be linked back to the fundamental definition of the seven base units of the international system of units (SI); Figure 2-1 depictures the traceability chain in a modern-day industrial setting [3]. The seven base units are: length (measured in metres), time (measured in seconds), amount of substance (measured in mole), electric current (measured in ampere), absolute thermodynamic temperature (measured in kelvin), luminous intensity (measured in candela) and mass (measured in kilogram). Each SI base unit is uniquely defined, and most recently the 26th General Conference on Weights and Measures (anno 2018) ratified a major revision of the definitions of the SI base units, which came into effect on May 20th 2019 [24].

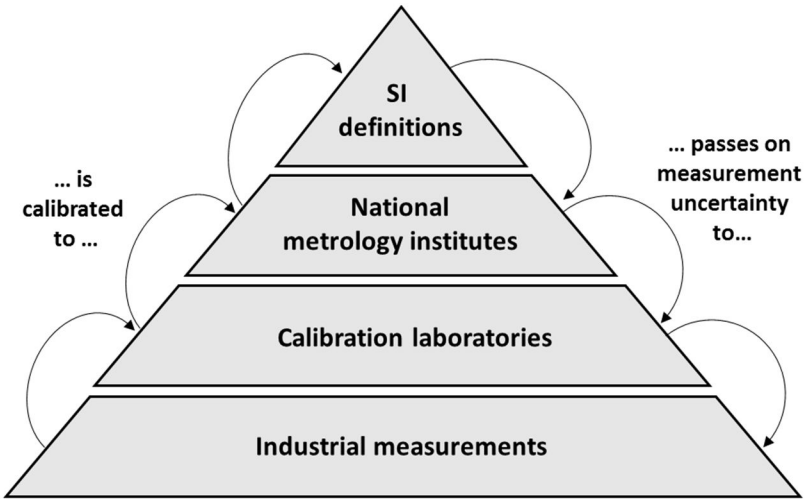

Figure 2-1 The traceability pyramid, based on [3].

The SI base unit of the metre is defined by "*taking the fixed numerical value of the speed of light in vacuum, c, to be 299 792 458 when expressed in the unit $\mathrm{m\,s^{-1}}$, where the second is defined in terms of the caesium frequency $\Delta\nu$*"; the definition can be realised through an optical interferometer with a stabilised laser source [24]. For measurement technologies that do not align with the definition of the metre, such as rulers, callipers or XCT, traceability needs to be established by following the traceability pyramid. Here a part, such as a gauge block, is measured at a national metrology institute. This gauge block is then used at a calibration laboratory to calibrate other gauge blocks, which are subsequently used in factories and laboratories to calibrate metrology tools, such as rulers, callipers.

Surface metrology

Dimensional metrology is the branch of metrology that focuses on measuring and quantifying objects and their physical shape, geometry and size [25]. Surface metrology concentrates on measuring the surface topography, often within, but not limited to, an industrial and manufacturing setting. The surface topography can be defined as the "*overall surface structure of a part*" [26]. Surface form and surface texture both constitute the surface topography. Surface form can be defined as "*the underlying shape of a part"* [26] and surface texture as the "*features that remain once the form has been removed*" [26]. The term surface profile measurements is used when a line is measured

across a surface and as such can be represented as a height function in the form of $z(x)$ [26]. On the hand other, the term areal surface texture measurement is used when an area is measured in the form of $z(x, y)$.

Among the first surface metrology instruments to be used in surface metrology was the stylus, and is still frequently used today [27–29]. But also optical instruments such as focus variation microscopes, coherence scanning interferometers, confocal microscopes can be frequently found as means to measure areal surface texture today [26,29]. Lately, also XCT has been added to the instruments to quantitatively measure surface topography [2].

A fundamental concept in the world of surface metrology is the concept of spatial frequencies. Building on the concept of spatial frequencies, a backbone of the areal

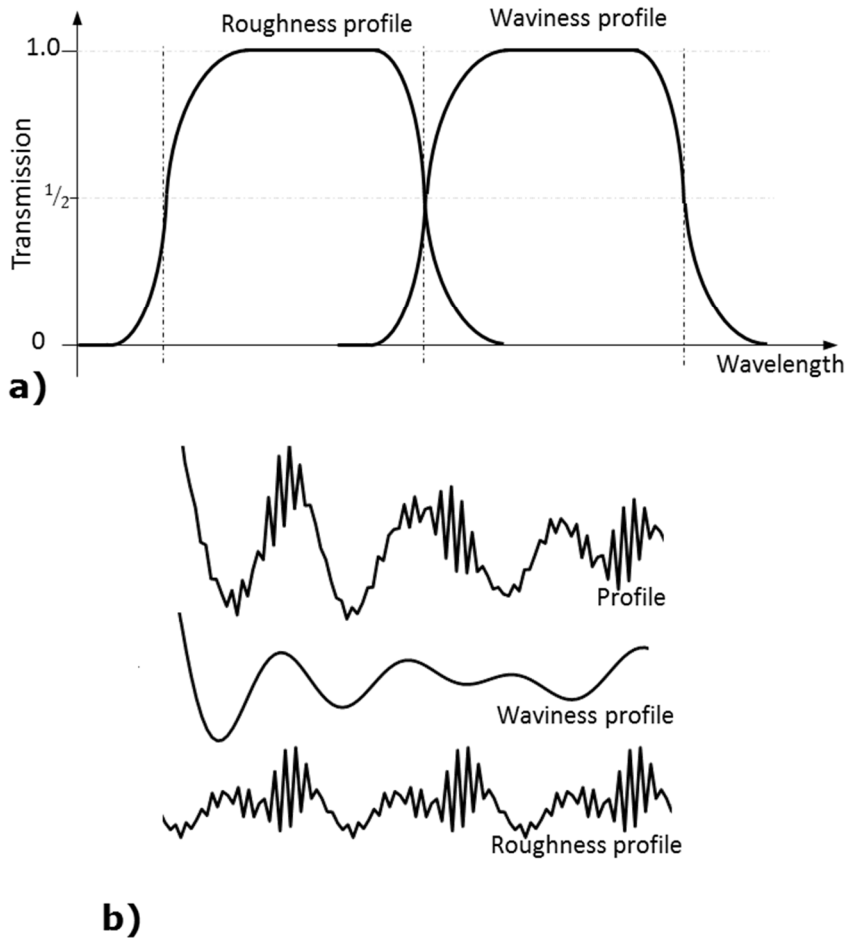

Figure 2-2 a) roughness and waviness filters in the frequency domain, and b) the effects of filtering operations on a surface profile. The primary profile is shown and its constituting waviness and roughness profiles after the primary profile has been filtered

topography analysis is to break (i.e. filter) a surface function into its constituting spatial frequency components. As such, the use of filtering operations can separate long scale components and short scale components known as form, waviness and roughness from the measured data [27]. Therefore, the primary measured profile can be separated into waviness profile, spatial frequencies of larger wavelengths, and the roughness profile, the shorter wavelengths, using filters such as the ones shown in Figure 2-2 a). Figure 2-2 b) shows the effects of this separation event and highlights the waviness and roughness profiles of the primary profile.

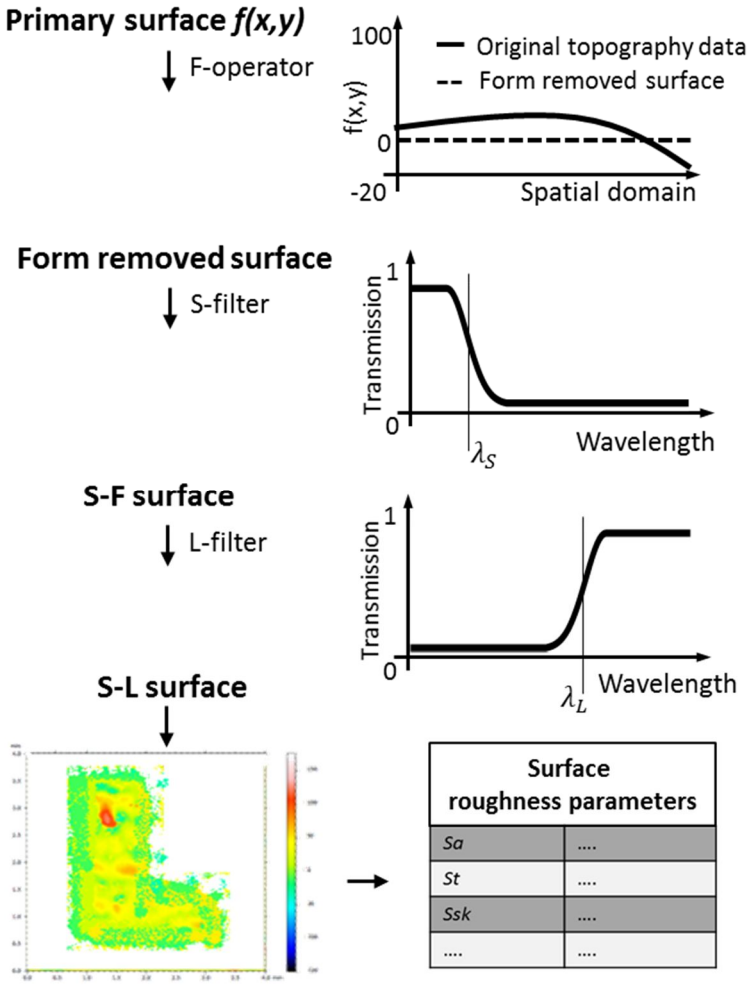

Figure 2-3 Common filtering steps of surface metrology. The topography evaluation shows a basic approach to obtain a surface roughness surface from the primary surface. Also shown are (1D) L- and S filter operations and likely schematics of their low and high pass nature.

In areal surface metrology, the use of filtering operations can similarly be applied. Following the depictured simplified chain in, the first operation of a topography evaluation aims to remove the form from the primary surface. This operator is coined the F-operator, and different methods exist to perform this operation, but a default approach is to subtract a total least squares fit of the nominal form [29]. The scale limited S-F surface is obtained after the form removed surface is filtered using an S-filter [27,29]. The S-filter is a low pass filter with a cut off frequency of λ_S. The S-filter removes the highest spatial frequency components of the surface (shortest wavelengths) to suppress possible noise and undesirable high frequencies. Waviness characteristics of a surface can be calculated from the S-F surface.

The scale limited S-L surface is obtained by filtering the S-F surface using an L-filter [27]. The L-filter is a high pass filter with a cut off frequency of λ_L, which only allows high spatial frequencies components to pass, and thus contains the spatial long scale components like waviness are removed [29].

Parameters are often used to characterise a surface into a single number to obtain figure of merits. Several areal surface texture parameters exist. The areal surface texture parameters are calculated from the S-L surface. Some commonly quoted areal surface roughness parameters are Sa (the arithmetic mean height), St (the root mean square height) and Sz (the maximum height of the surface) [29].

2.1.1 The measurement chain for XCT

X-ray computed tomography is a non-destructive, volumetric imaging technique capable of providing cross-sectional images of the imaged object. Dimensional metrological applications of XCT are relatively modern and only date back to the 1990s [1], surface metrology applications are even younger dating only to the 2010s [30]. Nowadays more and more manufacturers are bringing 'XCT systems for metrology' to the market. Interestingly it is not just companies of the non-destructive testing (NDT) or medical market bringing new dedicated metrology systems to the market, but also metrology firms such as Werth GmbH, Wenzel GmbH, and most recently GOM GmbH are adding XCT systems to their product range of metrology tools [31–33].

XCT relies on the penetrative nature of X-ray radiation. The beam of X-rays diverges, and the diverging nature of the X-ray beam generates a geometrical magnification, see Figure

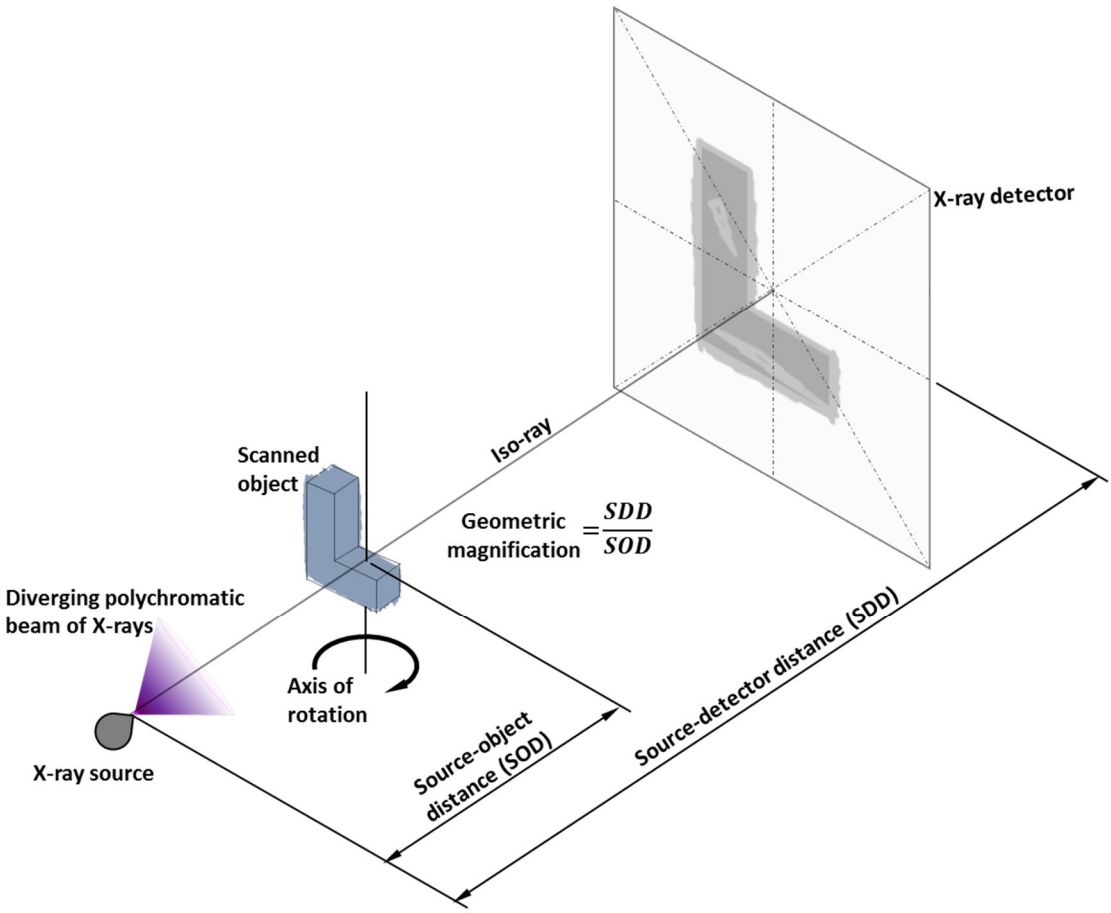

Figure 2-4 An idealised geometry of a cone-beam XCT system.

2-4. If the X-ray detecting sensor is a line-detector, the XCT is a fan beam system. If the X-ray detector is a 2D areal detector, the XCT is a cone-beam system; an example of a cone-beam setup is shown in Figure 2-4. If for each detecting element, the beam is collimated to a parallel beam, a system is called a parallel XCT system (and thus without magnification). The work in this thesis addresses only cone beam systems.

Figure 2-5 shows a simplified measurement chain for the metrological application of XCT. Fundamentally, the process chain starts with the acquisition of radiographs/projections of

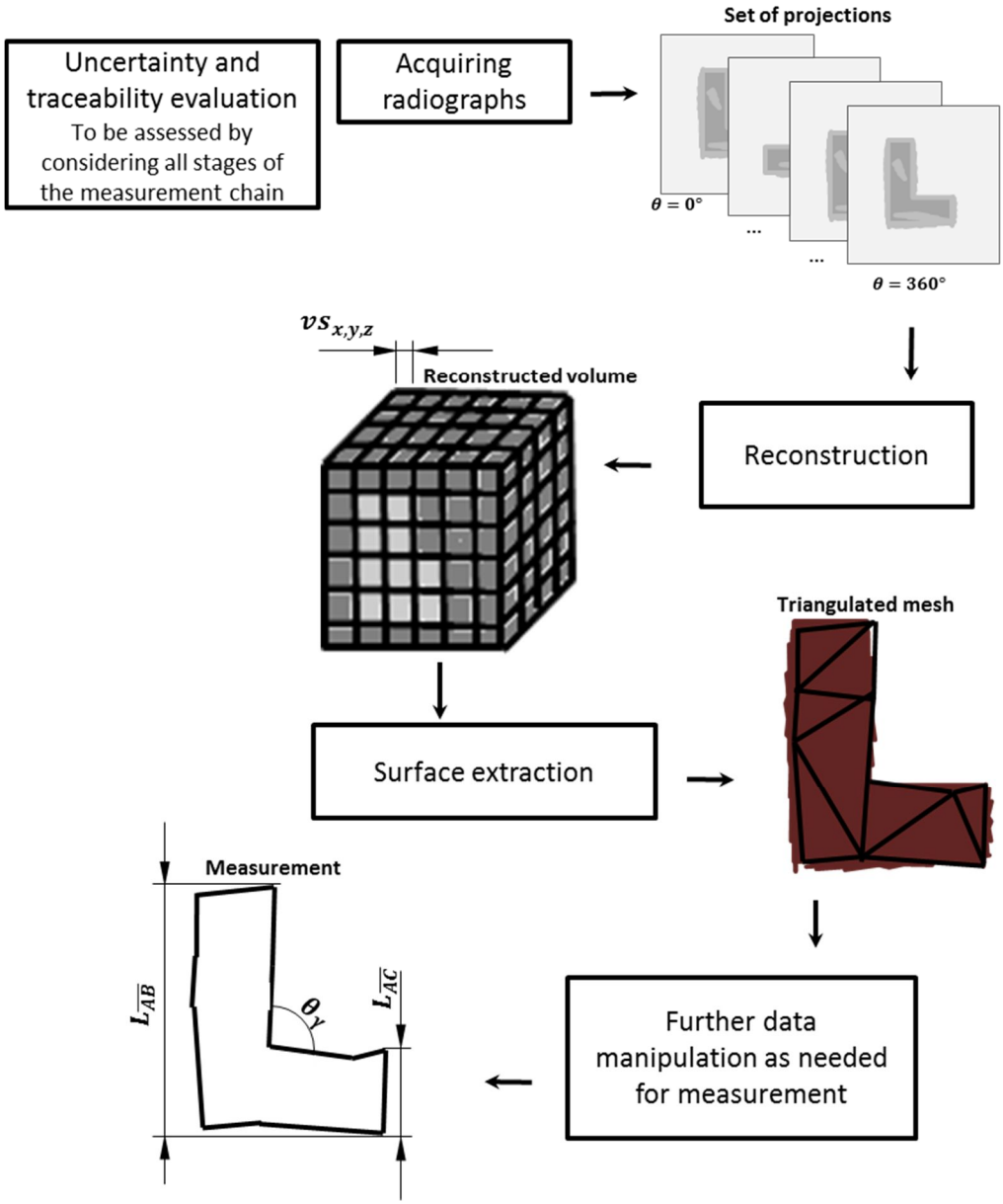

Figure 2-5 A simplified measurement chain of an XCT measurement.

the prepared object. In a radiograph, the intensity of the penetrative X-ray radiation is recorded by the detector, such that areas with more deposited energy are brighter, and areas with fewer recorded photons are represented as a darker shade of grey. These projections are taken at various different angles around the object, often, but not exclusively, around a single axis of rotation, also see Figure 2-4. Once enough projections are acquired, a discrete (3D) volume can be reconstructed. This discrete 3D volume describes the cross-sectional information of the object, to be more exact, it describes the attenuation behaviour of the scanned volume. The principles behind the two stages of obtaining radiographs and reconstruction are discussed more detail in sections 2.2 and 2.3.

The measurement time of an XCT scan consists of the preparation time, where the XCT system is set up and the sample is prepared; the acquisition time, when the projections are acquired; and the postprocessing time, where the projections are reconstructed and analysed.

Surface determination

For taking XCT data further for metrological evaluation, the current dominant paradigm in the research and industrial community is the idea of a surface determination [1]. The aim of the surface extraction is to create a finite surface model of the scanned object from the discrete reconstruction volume. The output of the surface determination is a surface triangulated mesh (often in the file format of 'stereolithography' (STL)) or occasionally a point cloud [1]. Figure 2-6 a) shows an exemplary slice of a reconstructed volume.

Figure 2-6 c) shows a detail image of the slice of Figure 2-6 a), along with the determined surface in white, whereas b) shows a rendering of the entire objects triangulated mesh. Figure 2-6 d) shows a histogram distribution of the reconstructed volume with the grey

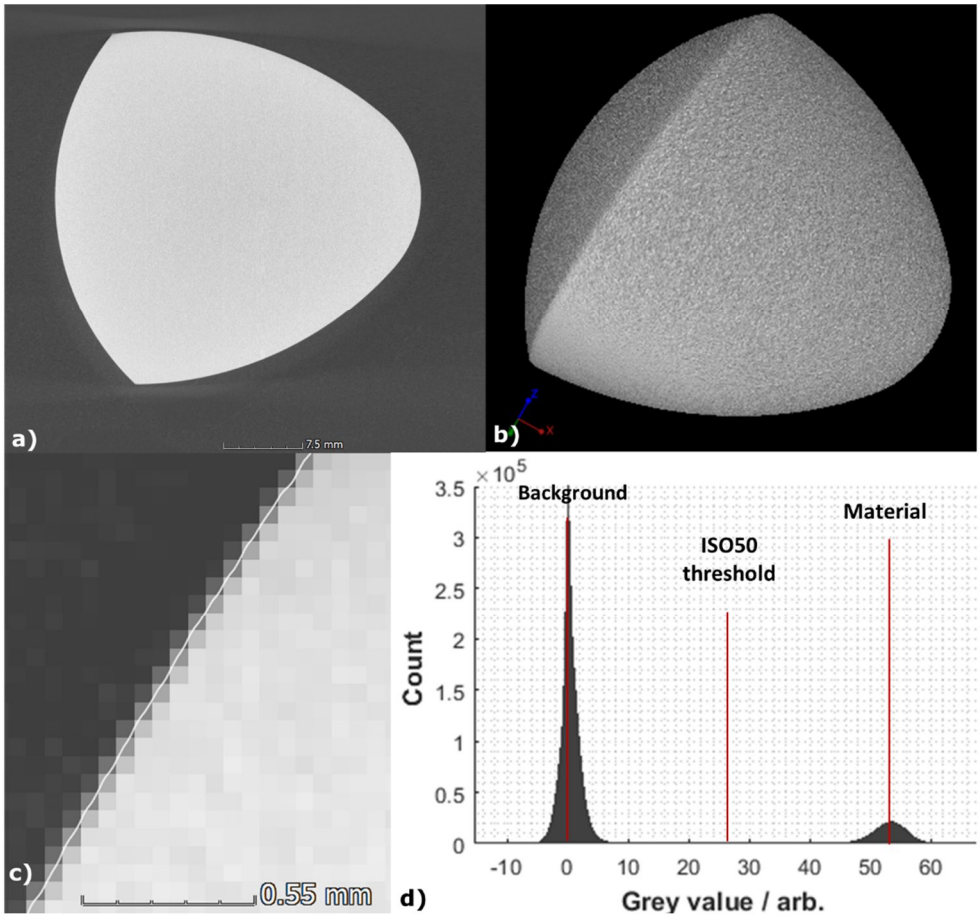

Figure 2-6 a) A single slice of a reconstructed volume, and c) a detail of the slice with the determined surface highlighted as a white line; b) is a rendering of the obtained triangulated surface mesh d) shows an exemplary histogram with the mean material and mean background and ISO50 threshold values identified.

levels highlighted, which correspond to the mean background and mean material grey values.

As the triangulated mesh is the basis of any dimensional measurement, it is of importance to the accuracy and precision of the measurement [1,34–36]. Within the metrological XCT community threshold-based surface determination methods are most dominant, often followed by a refinement processes [1] (a frequent threshold determination method is known as the ISO50 method, where the threshold value is the mid-grey value between the mean material and the mean background grey value, see Figure 2-6 d)).

Depending on the task at hand and the defined measurand, the obtained triangulated mesh can undergo further processing stages. Common processing includes tasks such as fitting to geometric primitives or fitting the data against computer-aided design (CAD) models for dimensional metrology, and further steps are required for surface metrology.

Measurement Uncertainty

A final consideration of the measurement process is the estimation of the measurement uncertainty. Estimating uncertainty is not associated with a single stage of the measurement chain, but needs to reflect on the entirety of the measurement, starting from uncertainty arising from the definition of the measurand (and any ambiguity of it) to the last stages of data processing and reporting. Estimating uncertainty in XCT is an ongoing discussion in the research community [3,37]. A rough classification system of uncertainty estimation methods is: model-based approaches, simulation-based approach, comparator method, and combinations of such [1,3,38,39].

Modelling approaches are analytical methods to estimate the measurement uncertainty. Here the relationship of influencing factors and variables are known and well understood (empirically or analytically derived), and the uncertainty estimate can be derived from those relationships [3,18,40,41]. The most prominent guideline to modelling uncertainty estimates is known as the GUM method [3,37]. In the GUM method, all potential sources

of uncertainty are identified, for example uncertainty due to repeatability, temperature, calibration and vibration. For each identified source of uncertainty, a likely distribution is associated with it, e.g. a quantitative description of how the variable might vary. Further, each variable requires a mathematical model on how the variable affects the measurement, and then the overall measurement uncertainty can be found from the contributing sources of uncertainty. In the context of XCT however, the complexity of the XCT measurement chain, such as the tomographic process and the X-ray imaging process, limit the applicability and validity of modelling approaches [3,37].

Simulation approaches aim at simulating a measurement by numerically evaluating the imaging process and all other steps of the entire measurement chain. The simulation is repeated multiple times often following a statistical approach called the Monte Carlo method [17]. For each influencing factor which are included in the simulation, a distribution is associated with it. This distribution describes the range the variable reasonably could vary during a measurement. Based on this distribution, the simulated variables are varied for each simulation. Software tools using such numerical simulations are sometimes referred to as 'virtual machines' [42]. From the repeated simulations, the uncertainty estimate can be derived [3,17,37,43]. The advantage here is that the exact relationship between variables is not needed, though the computational expense can be high.

The comparator method is an empirical approach to estimate the uncertainty and requires a calibrated test piece [37,39,44–46] and guidance of this method is outlined in ISO 14253-2:2011 [46]. The calibrated workpiece should be very similar to the measured object. Measurements of both the calibrated workpiece and of the object of interest are needed. The comparator method depends on repeated measurements of the calibrated workpiece. From the deviation of the repeated measurements and the calibrated values of the calibrated test piece, an uncertainty estimate can be derived [47]. This empirical uncertainty estimate can then be extrapolated to a measurement of the object of interest. Any significant divergences between measured objects and the reference object will

directly limit the transferability and thus the validity of the uncertainty statement. While requiring multiple repeat measurements [39,45,46], the comparator method generally is considered the method which currently provides the most reliable uncertainty estimates [3].

Current efforts of standardisation committees around the world have led to the VDI/VDE 2360 framework and unpublished, under-debate concepts for the ISO 10630-11 standard (ISO 10630-11 is an extension to the ISO 10630 series, itself is a framework for verification tests for coordinate measuring machines (CMMs)). Specific test procedures for acceptance and verification tests have been defined under the VDI/VDE 2630-2.1 framework to allow reproducible and thus comparable measurement setups [44]. Similar verification procedures to are being proposed in the currently-in-draft ISO 10360-11 [48]. Both the VDI and the ISO propose concepts and methods to establish maximum permissible errors (MPE) of defined verification tests of calibrated parts (in other words, an MPE is the largest error the measurement system will produce when measuring a defined part under conditions defined in the VDI/VDE 2630 2.1 and ISO10360-11). The MPE is not a global statement for a system, and thus the MPE must be stated in conjunction with the characteristic it refers to [49] and is limited to the measuring instrument [49]. The characteristics for which the MPE is frequently quoted are length measurement errors, probing size errors, and probing form error. A stated MPE should be quoted in conjunction with the characteristic measured, e.g. MPE_{PF} for probing form errors and $MPE_{PS}$for probing size errors. In XCT systems, the resolution is linked to the probing form error, as it is in other optical systems [50]. An MPE is not a task-specific uncertainty estimate, it simply states the maximum error of a particular measurement against a calibration value.

As the measurement principle in XCT does not correlate to the definition of the metre, the traceability needs to be established in XCT. The common methods for this is the use of calibrated parts to be placed into the measured volume [1,2,51], as well as relying and controlling on a geometrical calibration of the cone beam geometry and the flat panel detector [13,52–54]. The XCT system used in this work relies on periodic calibration of the XCT geometry using calibrated objects to establish a connection to the definition of

unit metre. However, this link in the traceability chain needs to be taken with caution, as in XCT the measurement results can get confounded by the material and the geometry of the object of interest [16,55–57].

Extending the measurement chain for surface metrology

For surface topography measurements further data manipulations are needed. Sections of the triangulated mesh are exported into 2D heightmap data. 2D heightmap data is a conventional and importable data format for surface topography processing software, and can be represented in the file format of *.sdf* [58,59]. Triangulated mesh data most often have an irregular spread of the data points describing the mesh, whereas the 2D heightmap is a discrete matrix with regular x- and y-increments. Thus, a process of raster scanning (and such as interpolation) of the mesh data is needed to convert the mesh data to 2D heightmap data. Here for each 2D heightmap grid point an intersection of the mesh

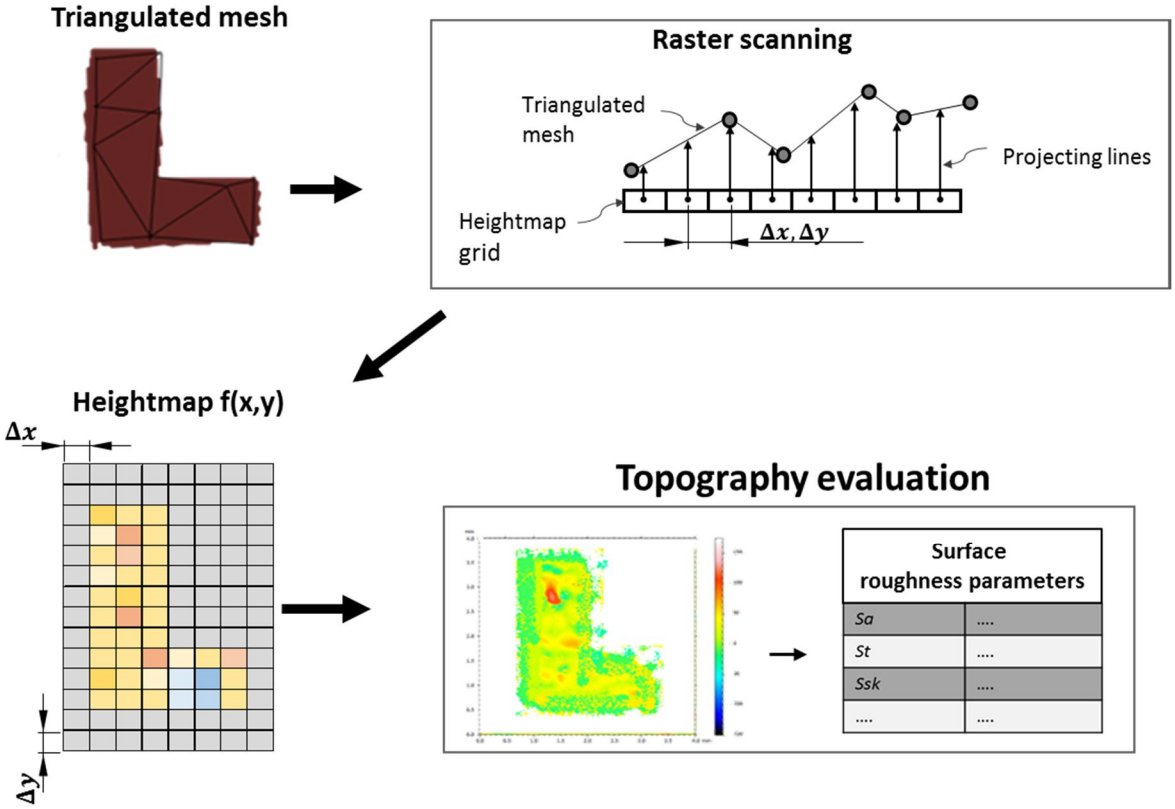

Figure 2-7 Outlines the additional data processing route to perform topography evaluations on heightmap data.

and a projection line is used to determine the z value of each heightmap data grid point. The 2D heightmap data can then be imported and analysed in surface topography processing software, refer to Figure 2-7 for a figurative depiction. Raster scanning the XCT data is needed since the current definitions of areal surface topography requires a function in the form of *f(x,y)*. (Current work is aiming to the bridge gap between fully 3D data of XCT and *f(x,y)* data paradigm of surface metrology by redefining surface texture parameters and filters and to create software tools to allow for compatibility with fully 3D data [60].)

Once the data is reduced to the form of *f(x,y)*, fundamental concepts of surface topography measurements, such as form removal and other filtering operations, can be applied to the heightmap data, and areal surface texture parameters can be extracted, using the concepts shown in Figure 2-3.

2.1.2 XCT to measure AM surfaces

AM is a group of manufacturing processes which are characterised by joining materials to form 3D objects [61]. The joining process happens normally in a layer by layer fashion [61]. One AM process which has gained a large amount of research and commercial interest is powder bed fusion (PBF), both in the form of laser powder bed fusion (LPBF) and electron beam powder bed fusion (EPBF). In PBF a 3D object is formed by consecutively melting layers of metal powder using a laser or an electron beam.

A large degree of research interest has formed recently on the evaluation of surface roughness using XCT of both laser and electron beam PBF parts [2,6–8,10,30,62]. A 2016 review by Townsend et al. [6] focused on surface topography evaluation of LPBF metallic parts. Both Townsend [6] and Thompson [8] identified that the measurement of surface topography is challenging using optical and tactile methods, yet of importance when investigating AM parts and AM processes. The importance of measuring the surface of AM parts has led to multiple research studies focusing on describing and characterising the

surface texture of AM parts, see the references of [6] for metal AM alone. Part of the interest aims at exploring the manufacturing process, whereas some researchers aim to characterise the surface for functionality [6]. A rough surface finish of L-and E-PBF parts have been attributed to limited fatigue life behaviour [6]. While the design freedom of AM parts is of interest to the biomedical industry, such as manufacturing customised implants, the existence of rough and unfavourable surface topographies, as well as fused powdered particles on the surfaces of PBF parts, possess challenges to the function and acceptance of implants, and makes the inspection of PBF parts an important research area [63].

One of the earliest publications on measuring PBF surfaces using XCT is by Pyka et al. [30]. This initial study investigated how XCT can capture surface texture of AM lattice struts. However, further research has been undertaken since [2,7,8,10,62]: One such research effort is the ability of XCT for measuring metal surface topographies, which was investigated in a visual and non-numeric comparison of XCT to a stylus measurement by Du Plessis et al. in 2018 [7]. However, more rigorous work has been presented to demonstrate the ability of XCT to measure AM surfaces. Zanini et al. [10] showed that for high-resolution scans, XCT shows a high level of accuracy for metal AM surface topographies, as compared to a CMM with an imaging probing sensor. In a quantitative comparison, Thompson et al [62] were able to show a good agreement of a confocal scanning interferometer and XCT, while the agreement was dependent on system settings. Similarly, Thompson et al. [8] compared XCT measurements of metal AM surfaces to a focus variation optical system and concluded that XCT is capable of measuring data for surface texture analysis. Townsend et al. [2] was able to show in a quantitative comparison of XCT and a focus variation system that there is good agreement between the optical measuring instrument and XCT.

One reason in particular contributes to the growing interest of using XCT to visualise but also to measure surface topographies. The volumetric nature of XCT is a trumping attribute over traditional optical and tactile techniques. The volumetric nature of XCT allows to measure inaccessible areas of complex geometries, such as within undercuts, inside

internal ducts and pipes. This volumetric nature of XCT is not just of interest to inspection of conventional manufactured parts and assemblies, but is especially of interest for the AM community, since the layered based manufacturing process can allow for complex geometries with internal and otherwise inaccessible features.

Concluding, Townsend et al. [2], Zanini et al. [10], Thompson et al.[62] and Pyka et al. [30] all demonstrated and proved the ability of XCT to measure metal AM surface topography using high resolution and low noise acquisitions. The volumetric nature of XCT inspection is a unique trumping feature of over other inspection techniques and as such shifted XCT into the focus of and interest to the industry and academic communities. However, no research effort so far has aimed to explore approaches to reduce the measurement time of XCT measurements of AM surfaces.

2.2 Tomography

The development of computed tomography is generally traced back to the late 1960s and early 1970s. Godfrey N. Hounsfield and Allan M. Cormack were jointly awarded the Nobel Prize in Physiology and Medicine in 1979 for their founding work on XCT [64]. Tomographic approaches without the use of computational systems can even be traced to the 1940s, and mathematical principles to the late teens of the 20th century [64]. The earliest scientific publication about concepts of tomography was most likely the founding mathematical work by Johann Radon (1887-1956) on the determination of functions through their integrals along certain manifolds. Radon's work has been so influential in the domain of tomography that line integrals and thus the logarithmic normalised X-ray projection data are still commonly referred to as Radon data and the space associated with it as Radon space. The concept of tomography is not limited to X-ray or ultrasound. Other applications of tomography stem from other physical principles such as electrical impedance, neutrons, coherent visible light and even seismic waves [65]. The word *Tomography* stems from the Greek word *tomos*, derived from the Greek word for slice and *Graphy* meaning writing. One definition for tomographic reconstruction can be "*A method for imaging a single slice*

of [a] three dimensional object" [66]. The word tomogram refers to such a cross sectional slice.

So, how is the reconstruction process performed? Three main categories of reconstruction approaches have been proposed: Algebraic, analytical, and statistical reconstruction approaches [67–69].

In algebraic reconstruction approaches, the discretisation of the reconstruction problems is the starting point. The 2D algebraic reconstruction process considers the tomogram to be a vector $\boldsymbol{f}$ of size N by N, thus having N^2 unknown elements [67–69]. Considering a simple imaging model $\boldsymbol{M}$, the imaging model can be described in vector mathematics as $\boldsymbol{p} = \boldsymbol{M} \cdot \boldsymbol{f}$ where $\boldsymbol{p}$ describes the measured data and $\boldsymbol{M}$ describes how the elements of $\boldsymbol{f}$ contribute to $\boldsymbol{p}$ [67] (basically $\boldsymbol{M}$ is a matrix describing the imaging process). The objective in algebraic reconstruction is to solve the imaging model for the tomogram $\boldsymbol{f}$ [67]. However, the direct inversion is often not feasible due to computational limits, input data limits, and inaccuracies in the measured data and in the imaging model [67,68]. Thus proposed algebraic solutions rely on iterative techniques for solving this inversion [64,67,69].

In analytical approaches, the object is described by and treated as a continuous function, $f(x,y)$ for a 2D tomogram [67]. The measured projection data and the image formation process are also treated as continuous data and as a continuous process. Using the central slice theorem (see section 2.2.1), an inversion formula is derived. The discretisation of the reconstruction process is only considered when integrating it into the computer program, details of the discretisation of the continuous quantities are described in the following section, '*2.2.1The central slice theorem and* its discretisation'. They are the most prominent approaches today, in medical and industrial applications [67,68].

Statistical reconstruction methods rely on estimating the imaging process using statistical methods; the most prominent approach is the maximum likelihood method [67]. In a maximum likelihood estimation, the pixel values of the tomogram, the parameters are estimated given a set of observations, the measured projection data, according to a

statistical model of the measurement process [67]. Statistical reconstruction methods are, like algebraic techniques, solved iteratively [67,68].

2.2.1 The central slice theorem and its discretisation

Analytical propositions on tomographic reconstruction are based on the *central slice theorem* or *Fourier slice theorem* [64,66,67]. This theorem states the following: when one assumes that a 2D object can be described as a continuous function $f(x,y)$, and its 2D spatial frequency domain as $F(u,v)$; and assuming that the objects measured projection data $Rf\ (\theta)$ is also continuous, the radon data at this angle is equal to a single radial line through the centre of the 2D frequency representation of that object, see Figure 2-8 a).

The radial nature of the central slice theorem is of importance for the discretisation. The two main directions in the discretisation are the radial and the azimuthal direction, compare to Figure 2-8 b). While the azimuthal direction is linked to the number of projections taken, the radial direction sampling is linked to the detector pixel spacing, a [64,70].

Considering that a single 2D tomogram of an object can be denoted as $f(x,y)$, the 2D frequency description of this object can be named as $F(u,v)$. For 2D XCT, the spatial frequencies sampling points of $F(u,v)$, assuming a reconstruction grid equal to the size of the projected detector size, are going to be separated by v_r – in the *radial* direction. If the spacing between the detector element is a and the number of detecting elements in the detector is M, v_r can be determined by [22]:

$$v_r = \frac{1}{Ma}. \qquad \text{eq. (1)}$$

However, the angular spacing of the spatial frequency points can similarly be determined by [22]:

$$v_{azm} = \frac{2\pi}{N}, \qquad \text{eq. (2)}$$

for a full $360°$ rotation and if the projection data was sampled at equal angular increments, with N unique views. Precise guidance on how many projections are needed for real, noisy recorded X-ray data is more extensive [22,71–75] and is discussed in section 3.2.

2.2.2 Filtered back projection

Direct Fourier space implementations of the reconstruction process are uncommon, and back projection algorithms are most dominating [64,76]. The filtered back projection process is the most dominant (analytical) reconstruction process [69]. The back projection 'smears back' the acquired projection data back over the tomogram at the angle it was acquired, see Figure 2-9. (Even for algebraic reconstruction, the imaging matrix $\boldsymbol{M}$ is rarely directly calculated or inverted.)

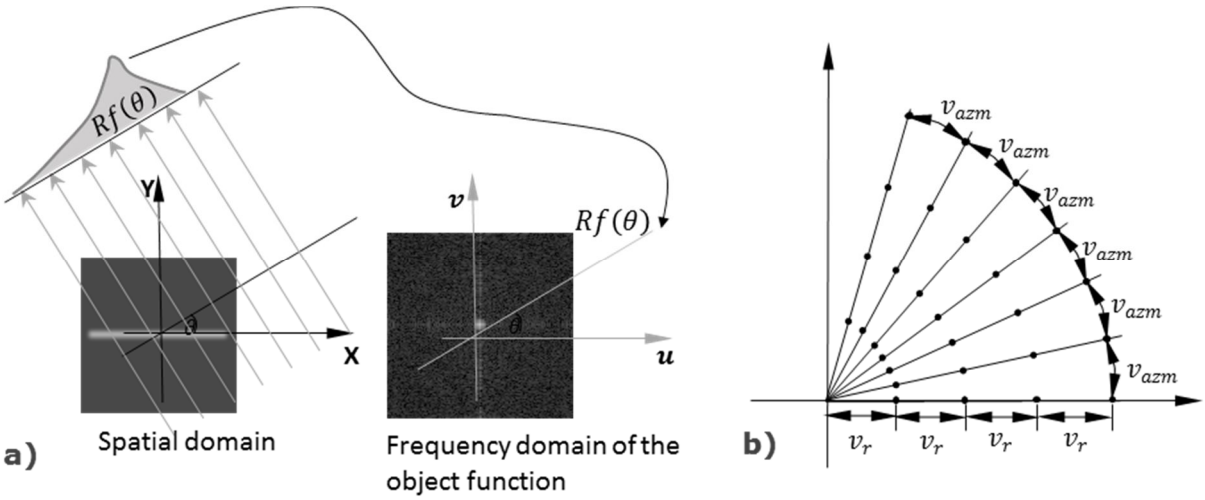

Figure 2-8 Showing the radon transform $Rf(\theta)$ of the object function $f(x,y)$, the radon transform at angle θ equals to the slice at angle θ through the k-space of the object function. b) shows a sector of the k-space of the object function and highlights the radial nature of the sampling points of the k-space.

Inspecting Figure 2-8 b), one quickly realises that, dictated by the central slice theorem, the reconstructed Fourier space should be naturally in a polar coordinate system. Further, one will also realise that, again dictated by the radial-angular nature of the central slice theorem, the sampling is not Cartesian equispaced, but that the polar nature creates diverging lines of the sampling points [76,77]. Since the central area of the Fourier space represents the lower spatial frequencies of the object function, the high spatial frequencies – away from the centre – are sampled at coarser intervals.

The radial nature of the Fourier slice theorem thus causes an overestimation of the central, low spatial frequency part of the spatial frequency domain. This overestimation of the low spatial frequencies manifests itself as a blurring of the reconstructed tomogram [76,77]. Figure 2-10 compares an unfiltered and filtered reconstruction, and showcases the resultant blurring effect.

To not overestimate the lower spatial frequencies in the reconstruction, the projection data is filtered using high pass filters to attenuate the low spatial frequency components. For

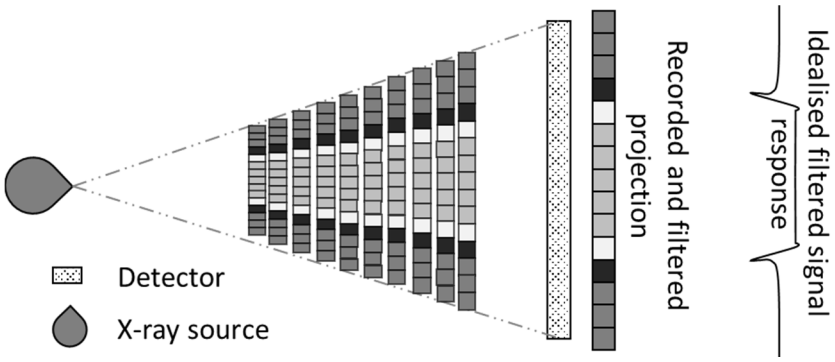

Figure 2-9 Schematic of the back projection process for a 2D tomogram. The pixel grid of the tomogram itself is not shown.

this reason, filtering is applied during the reconstruction, hence the name filtered back projection. The choice of filter type and its cut-off frequency affects the sensitivity of the analytical reconstruction process in terms of resolution and image noise [64,78,79]. As this filter is needed to suppress the low frequency components of the radiographs, it will amplify the higher frequency components. As such by varying the filter cut off frequency as well as the filter type, any softer filter will negatively affect the resolution in the reconstructed image, however will be more forgiving on noise present in the radiographic

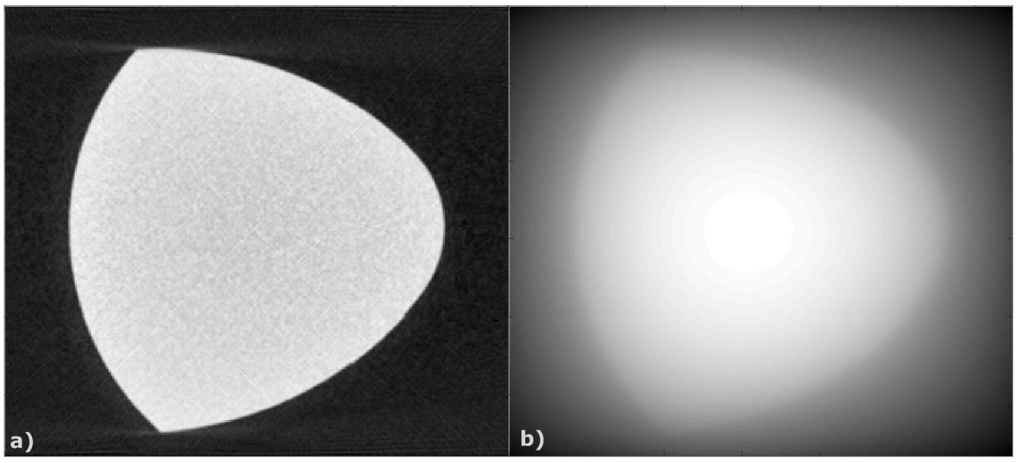

Figure 2-10 a) shows a filtered reconstruction of an object using a ramp filter, while b) shows an unfiltered reconstruction. The blurring effect dominates the reconstructed image.

data [80], whereas the absence of a filter will yield unusable reconstructions, compare back to Figure 2-10.

2.2.3 Extending a 2D solution to a cone beam problem: Feldkamp-Davis-Kress

The theoretical introduction so far concerned only 2D XCT, where the source trajectory is on the same plane as the single-row detector. 3D reconstruction methods have been around for several decades now, but one needs to be aware that the majority of reconstruction methods are *not* exact. Reconstruction volumes of flat panel detectors, with a circular source trajectory, are only exact for the central plane along the iso-ray. The iso-ray is the imaginary line connecting the source with the centre of the detector. The introduction of the Feldkamp-Davis-Kress (FDK) 'the industry workhorse' reconstruction algorithm [81] was a "*heuristic*" guess of extrapolating the 2D case to 3D [81], and it is not an exact solution. The limitations of the FDK and other 3D-FBP are raised in multiple publications [64,76,82–85]. The FDK reconstruction requires filtering and 3D back projection of the back projection data [81]. The back projected filtered data also needs to

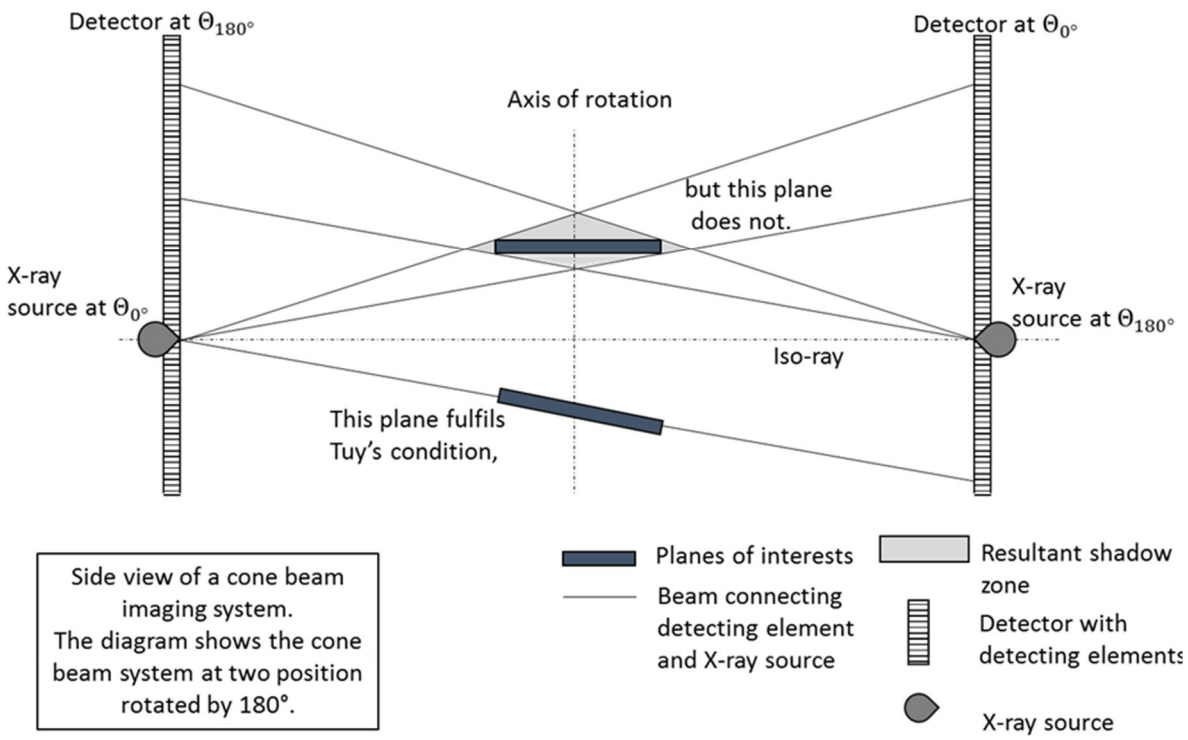

Figure 2-11 Spatial description of the Tuy's condition, the rhombus created by the back projection lines for the unsupported plane indicates the expected spatial spread of this plane, as the other plane is directly cut, no artefact is created.

be correctly adjusted by applying a weighting function [81]. This weighting function is crucial for the quality of the reconstructed data [81]. Hence, the 3D reconstruction is made feasible by the weighting function used in the reconstruction, as this mimics the path length differences of the different rows of the detector. The weighting function is needed because the cone beam geometry is not equal to the assumptions of the 2D Radon transform which would be needed for an exact analytical solution. But this leads to the well-known cone beam artefacts. These artefacts are a reconstruction blurriness, which is caused by the system geometry (the cone beam angle), and essentially caused by the lack of information in the recorded data, as can be seen in Figure 2-11.

The cone beam angle is a function of distance away from the iso-ray, and the source detector distance –and hence the effect is accelerated at the edges of the field of view (FoV), see Figure 2-11.

Thus the reduction of the 3D cone beam case into a stack of 2D tomograms is only equivalent to the 2D Radon transform, as long as the source trajectory is in the plane of the 2D tomogram [84]. Further, Tuy concluded that for time and engineering constraints a series of 2D tomograms are not always feasible– which holds true today as multi-row and flat-panel detectors (i.e. cone beam systems) are still utilised by many researchers. In his 1983 publication, Tuy proposed an analytical inversion formula of the 3D cone beam setup, which proves that an exact reconstruction is possible, as long as a set of conditions are met. These Tuy or Tuy-Smith sufficiency conditions have been pictured as a torus in multiple theses and publications. This common torus visual representation describes the volume covered by the flat panel detector which can be analytically reconstructed from its line integral – for a circular source trajectory. Tuy's three-part sufficiency condition can be applied for *all* source trajectories. While in 1983 Tuy introduced an inversion formula, Natterer pointed out that this formula might not be feasibly turned into a reconstruction algorithm, as it would require an implementation in the frequency domain [71].

2.2.4 Trajectories

Other trajectories than the circular one are feasible. Early solutions were proposed by Tuy, but Tuy refers to several publications with source trajectories which allow for exact reconstruction, most of which are double orbit solutions [84]. However, Grangeat [86] introduced an inversion formula, applicable for cone beam geometries, which was used by

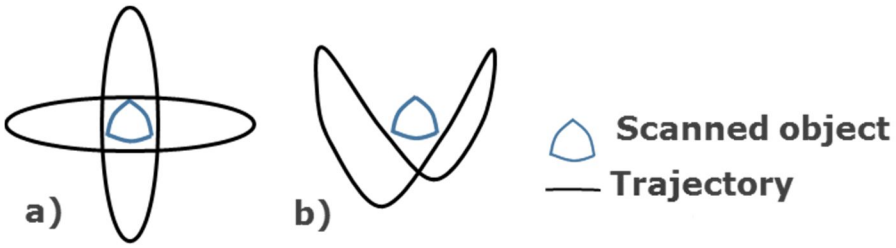

Figure 2-12 a) Double orbit source trajectory, and b) a saddle orbit, based on [84].

Clack and Defrise [87] to develop a reconstruction technique which allows for a large variety of source trajectories. In practice not many source trajectories are commercialised other than circular and helical XCT systems.

The helical source trajectory allows for exact reconstruction of the volume, as it meets the Tuy sufficiency condition for the entire object. While reconstruction is possible, an exact reconstruction algorithm for helical source trajectories, using back projection was only proposed in 2002 by Katsevich [88]. The importance of this proposed algorithm lies in being an exact solution.

A frequently used space to describe the collected projections for circular acquisition trajectories is the sinogram. The sinogram denotes the space which is created if all acquired projections are stacked behind one another in a two-dimensional array (for 2D tomography), refer forward to Figure 2-18 for an example of a 2D sinogram.

2.2.5 Image quality: Image noise and resolution

At the first most instance, XCT is an imaging technology. Thus the image noise and resolution are important concepts in XCT to be considered. A classical concept (stemming from the optical literature) of spatial resolution is the separation of two diffracted light points on a detecting plane. In wave optics, point sources will, under theoretical conditions, diffract into a bell-shaped intensity profile known as an Airy disc [89], see Figure 2-13 a). When two diffracted light sources are projected onto a plane, the question arises: How far do the diffracted points have to be separated in order to resolve the two projected points apart, see Figure 2-13 b) to d). Lord Rayleigh was among the first physicists to propose a limit on the separation criteria, but other limits have been proposed [89,90].

Another approach on ‘understanding the theory of microscopic vision’ was founded by Abbe [89,91]. Abbe proposed that the imaging system can be modelled as a filter which degrades the recorded image [89]. As such, the image is captured by the imaging system of finite performance and a blurred response is created. Using the foundations of spatial

frequency analysis, the performance of the system can be analysed as a function of spatial frequency. The function which describes the performance of the optical system is known as an optical transfer function, and for (height) measuring instruments the name instrument transfer function is used [89].

The spatial resolution of an image describes the ability to resolve fine details within the image [92]. Different notions of spatial resolution exist in the metrological world of XCT stemming both from the industrial-metrology background and the medical history [3,50,92–94].

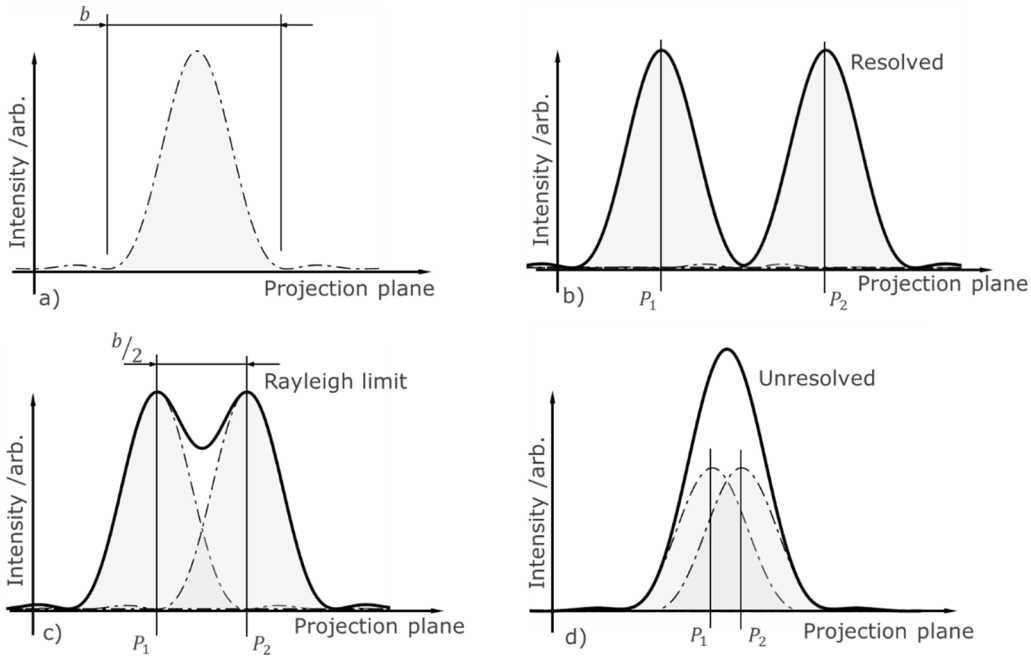

Figure 2-13 a) Shows a diffracted pattern of a point source (Airy disc) and highlights the width b of where the first minimum of the Airy disc occurs. b) to d) shows two diffraction patterns of two point sources P_1 and P_2 (dashed lines) projected onto a detecting plane and their accumulative signal (solid black line). b) shows a good separation of the two point sources and thus allowing the two points to be resolved. c) shows the resolution limit as proposed by Rayleigh, and d) shows a separation of the two point sources where the two points can no longer be resolved.

Spatial resolution in the image domain

The modulation transfer function is the real, modulus part of the optical transfer function [92]. The modulation transfer function describes how a system modulates (attenuates) the contrast as a function of the different spatial frequencies [92]. The modulation transfer function is a function, and thus any kind of figure of merit, like the Rayleigh limit, requires to quote the function at some specified value of the ordinate. Common values are 5% and 10% modulation [92].

The modulation transfer function can be derived from several spatial events such as imaging points, lines and edges. From the obtained images, edge spread functions, line spread function and point spread functions [92] can be derived, **see** Figure 2-14. The line spread function, edge spread function and point spread function are related mathematically [92]. From each of those three functions, the modulation transfer function can be derived.

The imaging system of computed tomography is digital. And as a digital system, the sampling interval is limited and finite and equal to the voxel size. The Nyquist limit describes the highest frequency that can be measured in finitely sampled data and is $f_N = \frac{1}{2 \times sampling\ interval}$ [92]. In order to obtain a 'continuous' modulation transfer function, the Nyquist limit needs to be overcome. One approach is to oversample a slightly slanted edge, see section 0 .

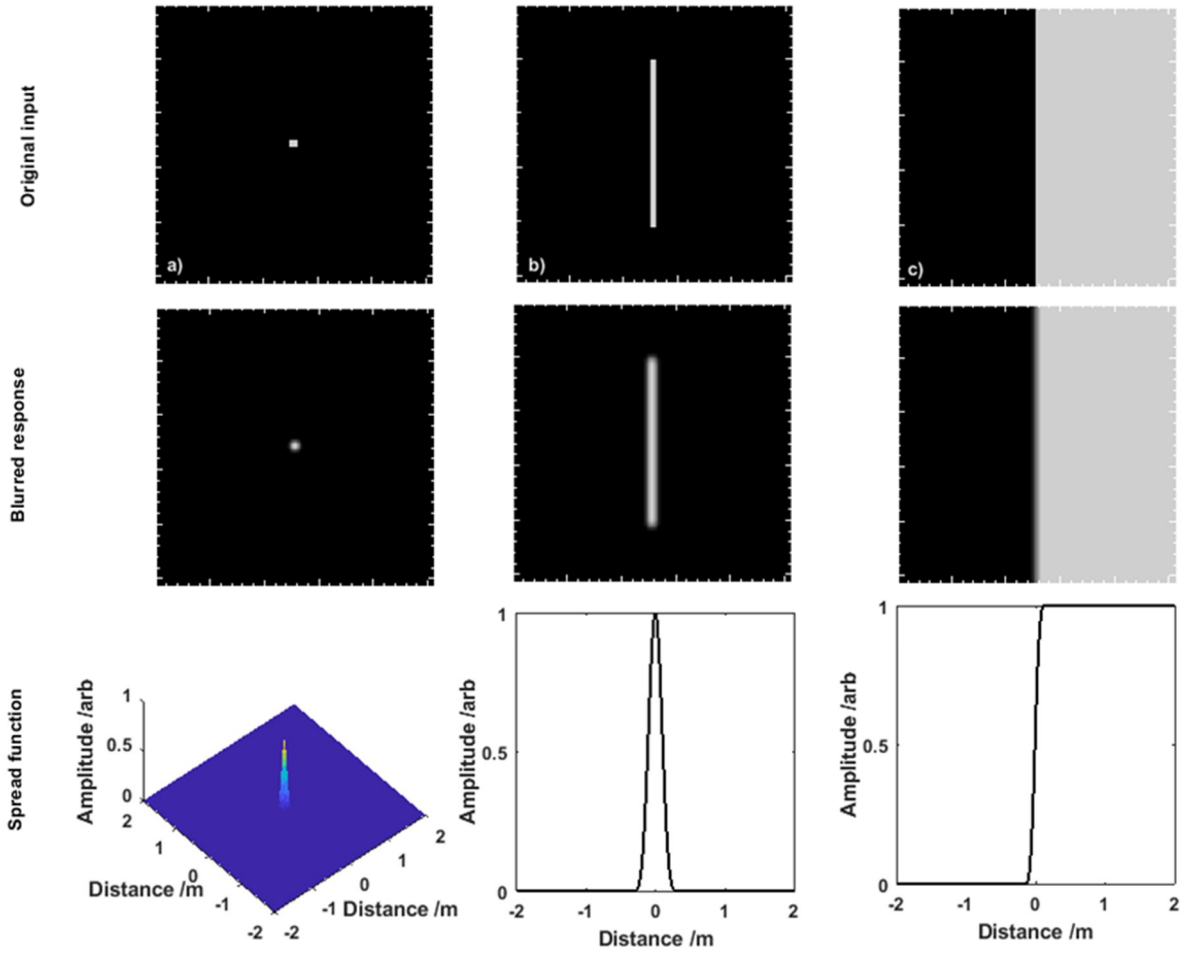

Figure 2-14 The first row of columns a) to c) shows three spatial inputs, a point, a line and an edge. The second row shows a modelled system response, and the final shows the point spread function the line spread function and for the edge spread function.
Based on the work of [92].

Other concepts have been developed to directly measure the resolution using artefacts such as a Siemens star or line pairs [95]. These are physical artefacts with fine details, and the resolution can be quantitatively judged on which details are still visible. This approach is still dominant in the medical field to assess the resolution [92]. In the industrial setting, ISO 15708-2 [96] describes a measurement procedure for determining the spatial resolution from line pair standards.

Spatial resolution beyond the image domain

The short introduction to spatial resolution so far only addressed the optical transfer function. This means the discussion was limited to XCT as an *imaging* system. When XCT is addressed as a measurement instrument, the instrument transfer function needs to be found [89]. Thus the resolution measurement needs to be performed at the end of the measurement chain, which means it needs to include the key stage of surface determination [97].

The VDI/VDE 2630 1.3 [97] defines the *"structural (also called spatial) resolution [...] [as] the size of the smallest structure that can still be measured dimensionally."* The spatial resolution in the image domain affects the structural resolution of the measurement but does not necessarily equate directly to it [80,97,98]. Figure 2-15 is included to

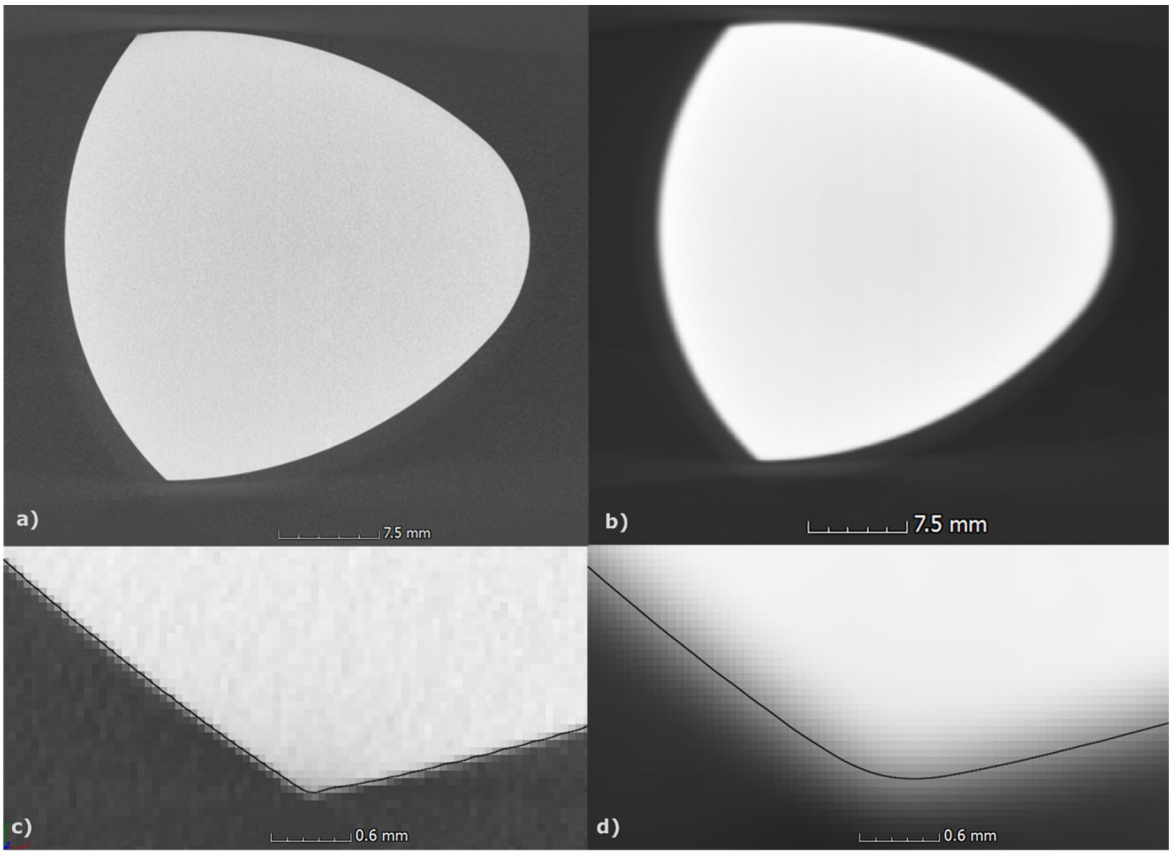

Figure 2-15 a) and b) Shows two reconstructions of the same part. The acquisition of b) was performed at a lower resolution than a). b) and d) show a detail of a) and b) respectively. The detail images highlight illustratively and pictorially the effect of lowering resolution on the determined surface of an edge (black line): the perceived radius of the edge increases.

illustratively demonstrate the effect of worsening resolution in the image on the determined surface. Working on the point cloud/ triangulated surface level, different methods of determining the structural resolution have been proposed [35,93,94,99]. The proposed methods [35,93,94,99] depend on dedicated artefacts, and as such are difficult to be incorporated into a measurement. The edge spread function method is simple to integrate into an experimental setup since it does not require dedicated measurement artefacts; only a straight edge with negligible surface roughness is needed. Thus the edge spread function is the utilised method in the following studies.

Image noise

Image noise is the undesirable variation of the grey value around a mean value [92]. Image noise affects the determined surface and thus contributes to the measurement error [36,80,100–102], see Figure 2-16 for an exemplary comparison between a noisy and

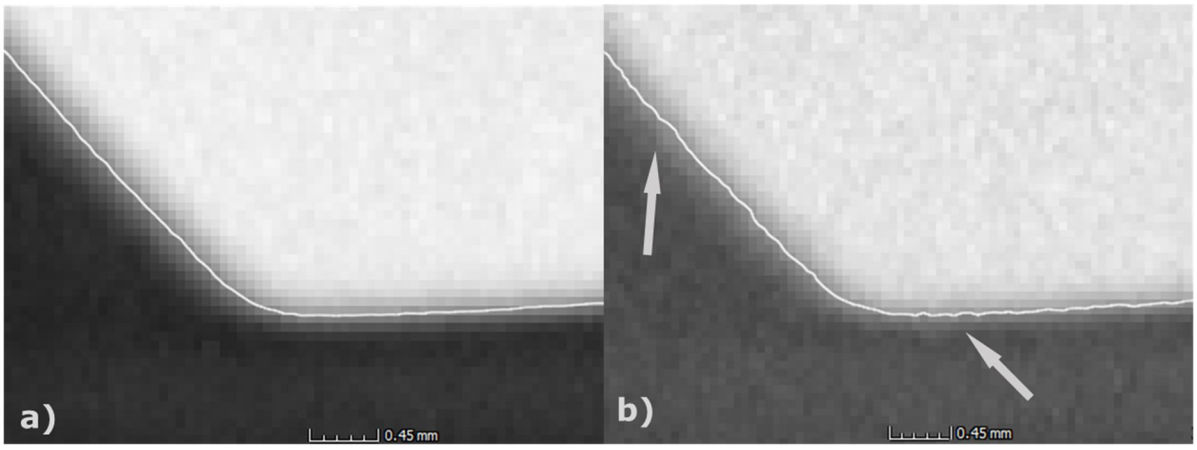

Figure 2-16 Shows two details of the images shown in Figure 4-6 a) and b). Acquisition of a) was done using a high number of frame averaging to reduce noise, whereas the acquisition of b) was aimed to have higher levels of noise. The arrows indicate some of the areas of the determined surface which are affected by the noise in the volume.

less noisy acquisition. The image noise is used frequently in the medical literature to discuss quality of XCT reconstructions [64,66,67,74,92,103–105].

Despite the long duration of the literature discussion on image noise metrics for XCT discussion, no final conclusion can easily be drawn [92]. Two of the earliest measures, dating back to as early as the 1940s [106,107], for the image quality includes the signal

to noise and contrast to noise ratios (SNR and CNR respectively). Both the SNR and CNR pitfall by requiring user-defined regions of evaluations. One volume-histogram based measure has recently been shown to be more sensitive to the existence of artefacts and noise, the Shannon entropy [108]. The work of Schienlein et al. [108], showed a strong sensitivity of the Shannon entropy to image artefacts and noise and were able to show a better agreement between the occurrence of image artefacts than by using signal-to-noise ratio.

2.3 X-ray production, interaction and detection

X-rays describes electromagnetic waves with a wavelength in the region of nanometres [109]; which is equivalent to a frequency of the peta- and exahertz region, and an energy of approximately of up to a few to hundred kilo-electronvolts (keV). Throughout this document, electromagnetic waves will be described by their energy. The energy of a photon can be found by

$$E = h\,v, \qquad \text{eq. (3)}$$

where E is the energy in Joule, h is Max Planck's constant which equals to approximately $h = 6.63 \times 10^{-34}\ \mathrm{J \cdot s}$, and v is the frequency of the electromagnetic wave in Hertz. One keV is equal to approximately $1.60 \times 10^{-16}\,J$. If an X-ray beam consists only of a narrow band of photon energies it is monochromatic. When multiple and different X-ray energies contribute to the X-ray spectrum, one refers to it as polychromatic.

A MatLab library was created from which the graphs in this chapter are derived. The aim of the library is to allow for polychromatic modelling of the X-ray photon/matter interactions as well as the X-ray detecting process. The library is extensive accounting for over 100 elements, and compound materials and mixtures can be created. It supports detector models and allows for tungsten spectra in the range of 20 keV to 640 keV.

2.3.1 X-ray production

Traditional lab-based X-rays sources accelerate electrons and X-rays are produced once the electrons hit a target. Lab-based electron acceleration can be done through the use of linear particle accelerators (LINACs), or - more commonly in the laboratory setting - the acceleration is performed via an electrical potential difference.

The sudden deceleration of the electron upon hitting the target yields to Bremsstrahlung. Bremsstrahlung is a continuous polychromatic spectrum of X-rays, which decreases with increasing photon energy. The acceleration voltage determines the maximum photon energy of the Bremsstrahlung spectrum.

Large peaks dominate experimental spectra, see Figure 2-17, and are referred to as the characteristic radiation of the (target) material, and are not caused by the Bremsstrahlung, but by the stream of accelerated electrons interacting with the target atoms [110]. Figure 2-17 shows a spectrum of a tungsten target under excitation of an electron beam of 225 kV. The focal spot can be defined as the X-ray producing area of the target [61]. The focal spot has several properties associated to it: size, shape, location, and drift behaviour.

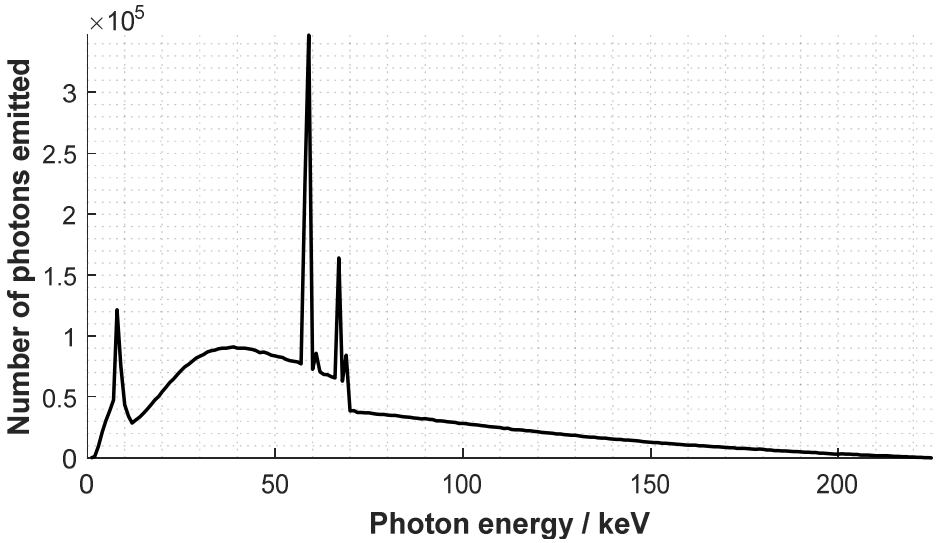

Figure 2-17 Spectral profile of an X-ray with a tungsten target and an acceleration voltage of 225 kV. The continuous Bremsstrahlung can be seen and the characteristic peaks of tungsten. The data for plotting is based on [111].

A key quoted property of the focal spot is the size, as the increased focal spot size is a known limiting factor of the magnification achievable, as the pixel size limit decreases in importance at high magnifications. One approach to model the effect of the spot size on the resolution is described in [95]. Here the expected amount of loss of resolution is termed geometrical blurring, b, and can be expressed as:

$$b = \frac{1}{M}\sqrt{p^2 + (s(M-1))^2}\,, \qquad \text{eq. (4)}$$

where M is the geometrical magnification, p the pixel size and s the spot size. X-ray tubes are often characterised in terms of their spot size, such as micro focus and nano focus tubes.

The terminology associated with the emitted number of X-rays/intensity is flux, and several factors can affect the flux, such as filament and target lifetime [112–114], see Figure 2-18 for an example of flux variation during a XCT scan. The maximisation of the flux by increasing the power of the X-ray tube is limited by the geometrical unsharpness and the thermal behaviour of the target [15,115].

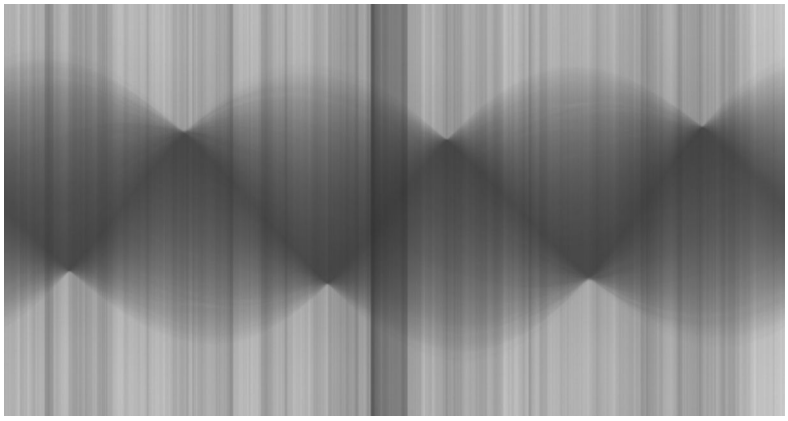

Figure 2-18 Flux variations; displayed is an experimental two-dimensional sinogram of a 2D XCT scan with 2514 projections of an aluminium cuboid.

2.3.2 Photon/matter interaction

The peak-energy of medical XCT devices ranges from 20 keV to 140 keV, whereas industrial XCTs are in the range 50 keV to 450 keV, but can reach into the gamma-ray regime up to 8.5 MeV [116]. However, the author is unaware of any XCT applications exceeding beyond a few hundred keV, which focus and include detailed discussions of uncertainty.

The photon interactions with atoms in the energy range up to 450 keV are dominated by four main interaction modes: photoelectric absorption, coherent scatter, incoherent scatter and pair production. The photon matter interactions are energy-dependent [117]. Pair production will not be discussed in detail here, as pair production only becomes significant, depending on the element, in the energy range of a few MeV [117]. Figure 2-19 shows the linear attenuation coefficients of the different photon interactions of elemental aluminium in the range of 0 keV to 640 keV. The figure reports the constituting parts of the total attenuation coefficients of aluminium.

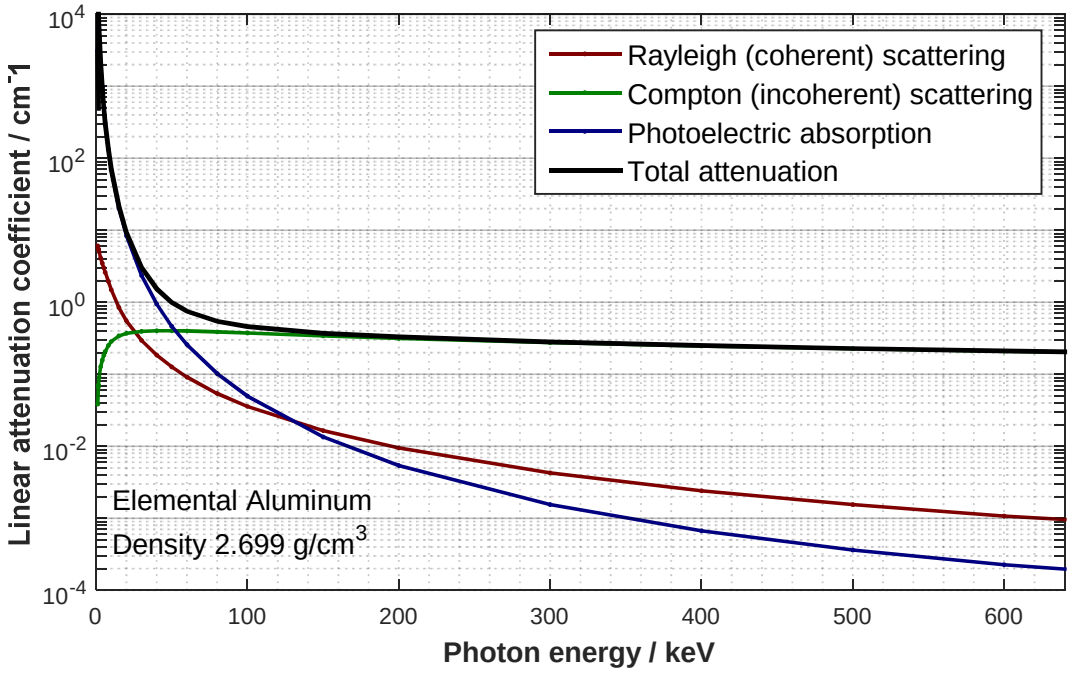

Figure 2-19 The linear attenuation coefficient of different X-ray interactions of Aluminium for an energy of up to 640 keV. Data for plotting is derived from NIST.gov [118].

The Lambert-Beer [119] law describes quantitatively the change of intensity of a parallel beam of photons travelling through a material with a linear attenuation coefficient $\mu(E)$:

$$I(E,x) = I_0(E)\, e^{-\mu(E)\, x}, \qquad \text{eq. (5)}$$

where $I_0(E)$ denotes the initial intensity spectrum of the parallel beam, and $I(E,x)$ the intensity after having travelled the mass length x through the material. As the attenuation coefficient is energy-dependent, the function needs to be evaluated for all photon energies E of the incident spectrum.

Two attenuation coefficients are frequently reported in the literature, the linear attenuation coefficient and the mass attenuation coefficient [109,117]. The mass attenuation coefficient is normalised to the density of the material, whereas the linear attenuation coefficient is the product of the mass attenuation coefficient and the density. The differentiation between linear and mass attenuation allows easier integration of the materials varying density in the numerical lookup tables [109,118]. For example, liquid water and water vapour have the same mass attenuation coefficient, but the linear attenuation coefficients vary due to their respective densities.

When a polychromatic X-ray spectrum travels through a material, the spectrum changes. The change of the spectrum while travelling through the material is termed beamhardening, as the spectrum 'hardens': i.e. loses the lower keV contributions and its mean value shifts into the higher keV domain.

The infographic in Figure 2-20 pictures the change of the spectrum as the material travels through aluminium. The incident spectrum is based on a tungsten spectrum with a self-filtration of 5 µm of tungsten followed by a filter of 500 µm of beryllium.

This can easily be observed by the shift of the yellow lines in the infographic of Figure 2-20. The yellow lines correspond to the first, second and third quartile of the spectral composition. The blue-yellow surface plot shows the X-ray spectrum as it travels across 90 mm of aluminium. The detector response is estimated by the mass attenuation of 800 µm CsI combined with a photon yield of 54,000 photons/MeV. The purple line shows the total number of photons as a function of distance, while the green line is the estimated

detector signal response. The varying grey background shows the expected effective attenuation coefficient of aluminium as the spectrum hardens, while the uniform black background shows the expected attenuation coefficient for air.

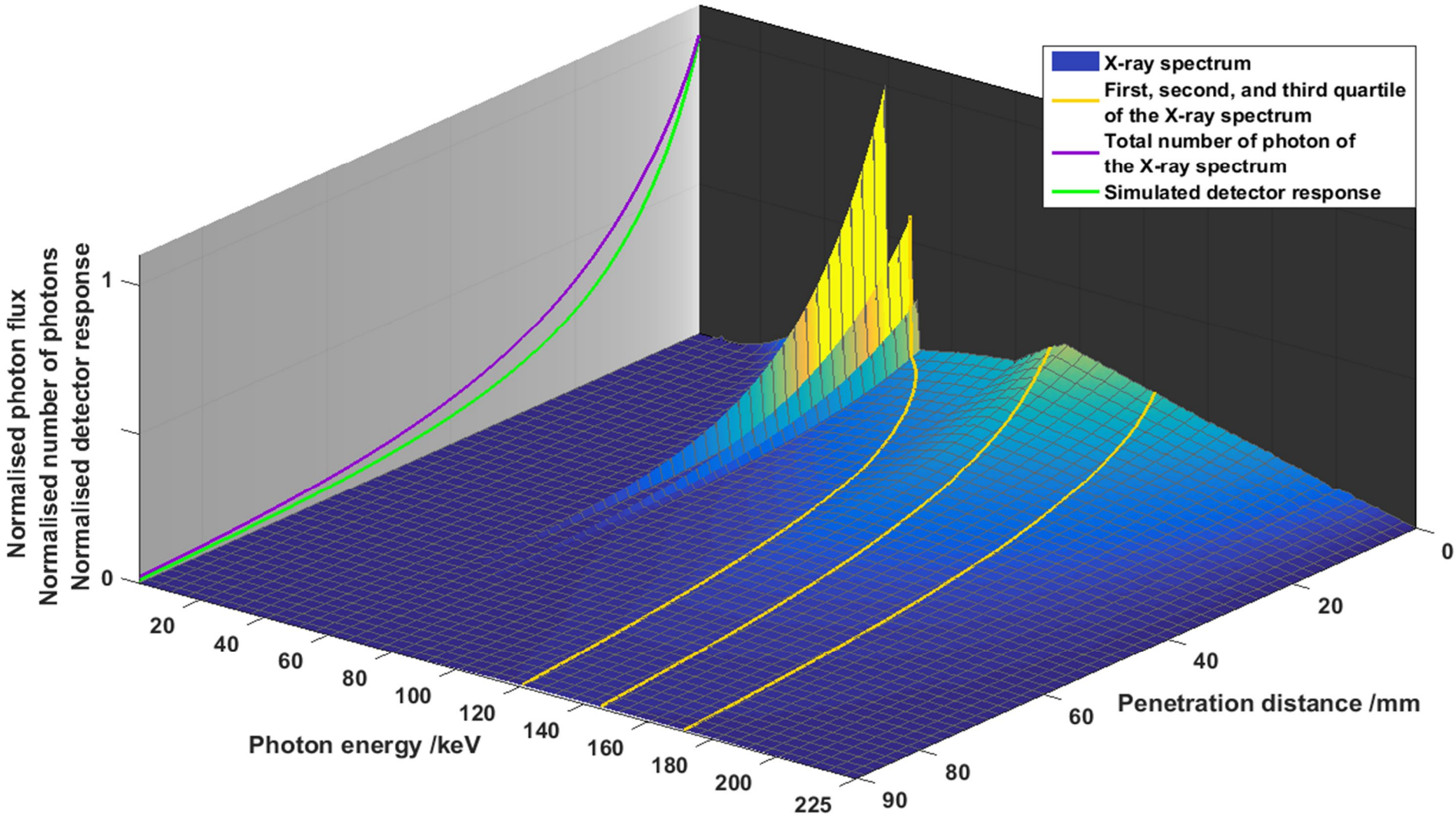

Figure 2-20 Infographic showing key properties of the penetration of aluminium by a spectrum created with a tungsten target and an acceleration voltage of 225 kV

Bookmark not defined.

Photoelectric absorption is the most desirable attenuation mode for conventional XCT. During photoelectric absorption, the incident photon is completely absorbed by the atom of interaction. The energy is then transferred to an electron, which subsequently is ejected from its orbit and travels on at an angle. Through the loss of the electron, the atom is thus ionized [109]. Figure 2-21 shows a schematic representation of the photoelectric absorption and Rayleigh and Compton Scattering.

Scattering attenuation describes the reduction of the intensity of the incident X-ray beam through deflected photons. Rayleigh scattering is the result of the X-ray interacting with the atom as a whole [110]. Rayleigh scattering is a form of elastic scattering (no energy is lost in the interaction). In Rayleigh scattering the incident and emitted photon radiation are of the same energy, i.e. $hv_o = hv'$, where v_o denotes the frequency of the incident wavelength and v' frequency of the scattered photon, and h is Planck's constant.

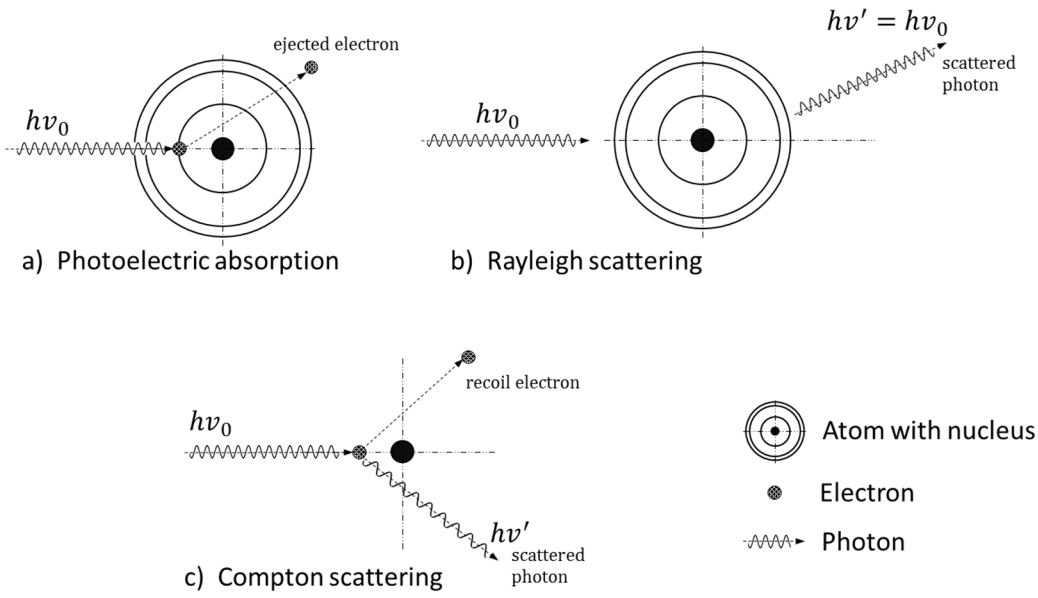

Figure 2-21 Photon/matter interaction schematics, based on figures of [109,120]

The angular distribution of coherent Rayleigh scattering can be estimated for elements and mixtures of elements and is dictated by the atomic number of the element [66,109]. The probability of Rayleigh scattering increases with larger atomic number numbers, and decreases with higher photon energy [121], also compare back to Figure 2-19. As a rough approximation, in medical XCT only around 5% of all scatter events are due to Rayleigh

scattering [121]. Interestingly, as Rayleigh scattering is elastic and therefore cannot deposit energy in the material, there is no radiation harm to biological tissue [122].

Compton scattering is a form of incoherent scattering (the energy and phase of the photon are not preserved) [70,110]. Compton scattering is due to the interaction of the incident photon and an electron of the interacting atom [121]. Compton scattering events result in both a photon and a recoil electron, which travel on at different angles. Unlike the photoelectric effect or Rayleigh scattering, Compton scattering is not directly dependent on the atomic number but is dictated by the electron density [123,124] (it is an interaction between photons and electrons). Compton is the most dominant scattering-type in the medical and industrial XCT.

2.3.3 X-ray detection

An XCT system's detector is key in determining the performance of the system and is the starting point of XCT as a digital system. For XCT, the detector is defined as a component of the system which records the deposited X-ray radiation [125]. In modern industrial transmission XCT systems, flat panel detector designs are dominant. The objective of the digital detector array (DDA) (terminology for X-ray detector as in VDI/VDE2630) is to convert the X-ray signal into a digital signal. The X-ray signal can have multiple attributes: energy levels, intensity, phase and even the direction of travel could be considered an attribute. Thus different detector types exist to measure these different attributes. The XCT system used within this thesis is an attenuation tomography system. Hence the detector only records the intensity of the X-rays falling onto the detector.

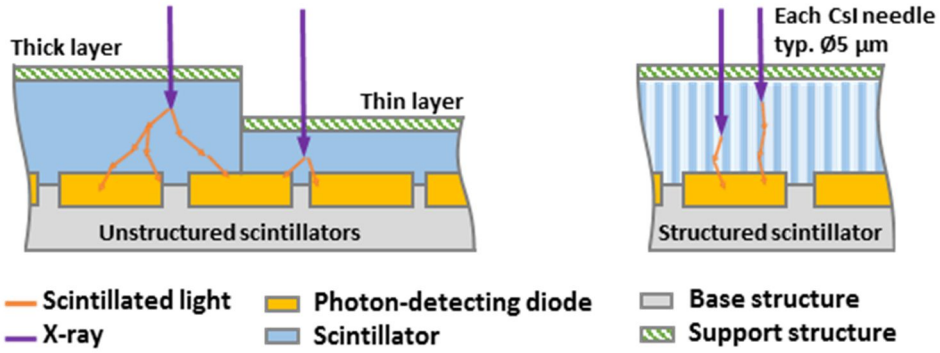

Figure 2-22 Schematic showing the interaction area of a scintillator with the incident radiation, based on [126].

Many of the current detectors are scintillator based, including the detector of the XCT system used in this study. The electromagnetic signal received on the scintillator is converted into a lower energy (near- or visible light) signal which can interact with the analogue-to-digital converter inside the DDA. An important aspect of the DDA is the sensitivity or efficiency, i.e. the responsiveness of digital counting events. While the sensitivity of the X-ray detector relies on the spectrum, the scintillator material and the scintillator thickness, an undesirable effect can occur with thicker, more sensitive scintillators: loss of spatial resolution of the detector. A common engineering approach to overcome the limit is the use of structured scintillators such as caesiumiodide (CsI) grown into needle structures, see Figure 2-22. This tunnelling effect is beneficial for the spatial resolution [126]. With the emerging of XCT for metrology applications, the characterising of the flat panel detectors started to gain more attention again. An extensive amount of geometrical characterisation (flatness, distortions etc.) of the detector has been raised in the dimensional XCT literature [13,53,127–130].

The spectral detection sensitivity of the scintillating material can be estimated from the scintillator's attenuation characteristic and the thickness of the scintillating layer [110,131]. Figure 2-23 shows the normalised spectral sensitivity of CsI with a scintillator thickness of 0.8 mm and without filtration.

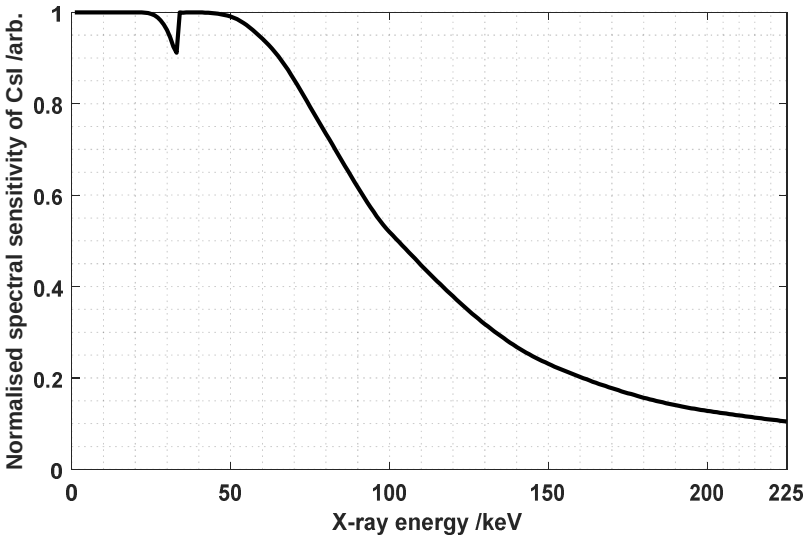

Figure 2-23 The spectral sensitivity of 800 μm CsI with no inherent filtration.

Photon yield describes the scintillation efficiency of a scintillator and is quoted in (scintillated) photons per deposited radiation energy [132]. For CsI structures with thallium inclusions a photon yield of 54 photons/keV is quoted [132].

When the spectral sensitivity of the scintillating material, the photon yield and the source spectrum (as well as any filtering) are known, the overall XCT systems spectral sensitivity can be calculated [131]. The systems spectral sensitivity can then be used to assess the effective linear and mass attenuation coefficients for any material [131]. Figure 2-24 reports the total mass attenuation coefficients for elements Z=1 to Z=100. The computation of the spectral sensitivity is based on the data of Figure 2-17 and Figure 2-23 and photon yield of 54 photons/keV.

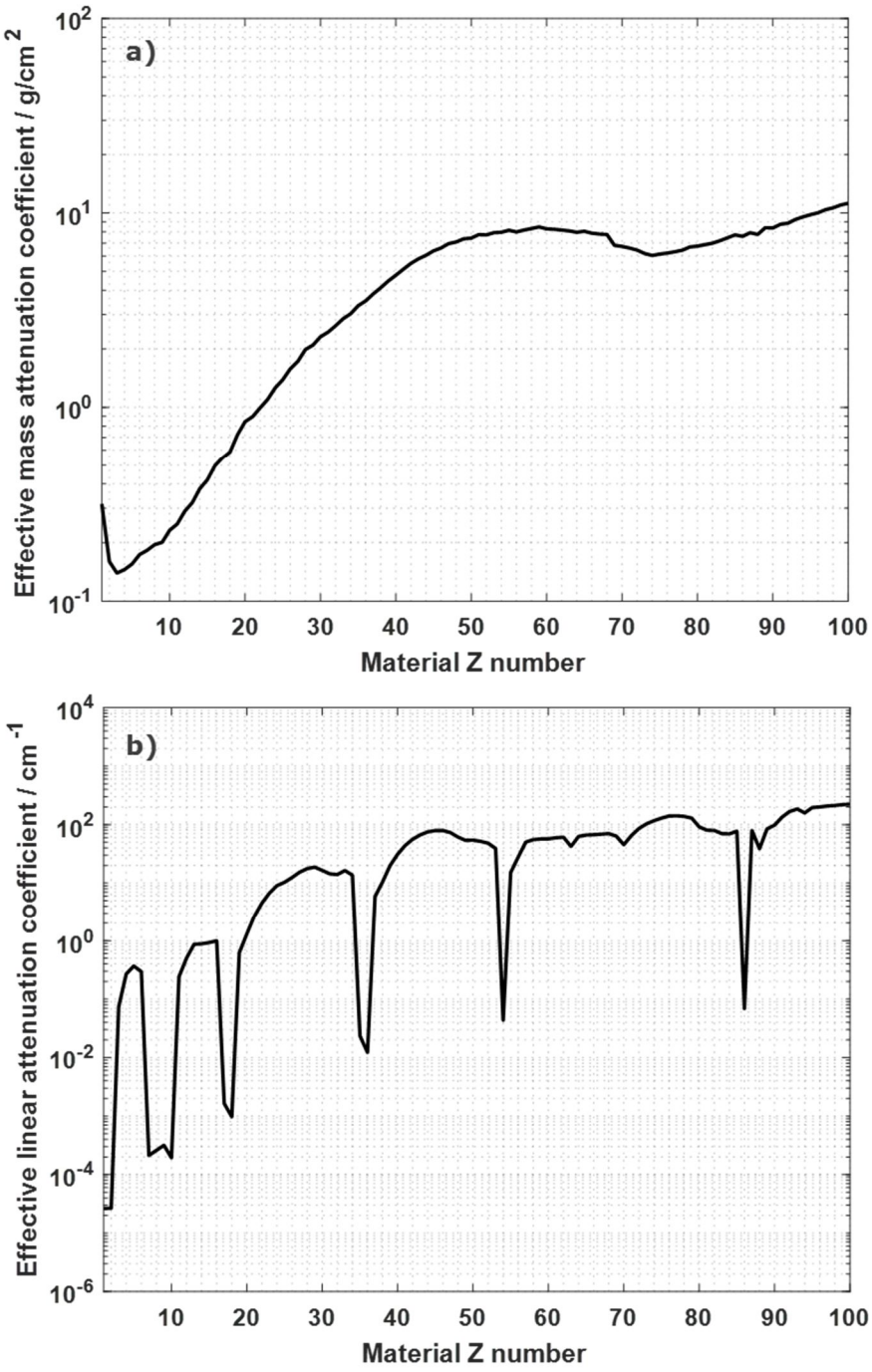

Figure 2-24 The effective mass absolute attenuation coefficient (a) and the effective linear absolute attenuation coefficient (b) for elements Z=1 to Z=100, evaluated for a tungsten source spectrum (with an acceleration voltage of 225 kV) and a CsI scintillating detector.

2.4 Chapter summary

The interaction between X-rays and matter is a well-studied area of physics. X-ray physics limits and dictates the available data in the recorded radiographs and the process can be modelled and simulated. Tomography is the process to gain cross-sectional information of an object form its Radon data. In its analytical form, it has been studied in mathematics for over a century, and the underlying concepts have been introduced in this chapter. A short introduction to XCT in the setting of metrology has been presented. Multiple publications have demonstrated and showcased the ability of XCT to measure AM surface topographies. To the author's knowledge, no research effort so far has focused on reducing the measurement time of XCT surface topography measurements.

In this chapter, the basics of the image formation process in XCT was introduced. With this prerequisites, the next chapter is going to introduce a detailed review of projection acquisition that builds on the fundamental theories introduced in this chapter.

3 Projection acquisition in XCT: A review

This chapter is a literature review on different approaches to use projection data in transmission XCT. The review aims to ask how existing research has led to improved scanning strategies, but also why projections are taken and where they should be taken. The driving factor behind the literature review is to aim for methods approaches and thoughts on how to improve the reconstruction quality or increase the speed of XCT.

3.1 Aim and limits of the review

While XCT is currently developing into a recognised metrological tool for industrial use [1], large measurement times – and hence low throughput rates – are major drawbacks of current XCT systems. Within medical XCT, the need to increase the scan speed is often required for cardiac scans. As temporal resolution in imaging a moving heart is critical, medical XCT systems have been optimised to be run at half scan – i.e. limiting the trajectory to a half-circle [133,134]. The demand to increase the speed in the industrial setting has led to a diverse set of approaches, such as algebraic reconstruction techniques and total variation reconstructions; however, not many techniques have yet been applied for metrological use. This might be because the metrological applications of XCT is a relatively young discipline; but other thresholds to adopting new and different setups, reconstruction techniques and settings is the in-depth level of the effects, in particular: how is the noise in the reconstructed volume going to affect the uncertainty of the measurement, the effects on the resolution, and are the effects generalizable to scans of different objects at different settings.

The number of projections has been discussed frequently in medical literature, as more views – at constant X-ray power – increases the patient dose, while it is often quoted that an increased number of projections increases the imaging quality and thus improves diagnostics. Within the industrial XCT literature, a large number of views does not get limited by dose consideration, though the higher number of views increases measurement

time. While on an economic scale the number of projections is aimed to be reduced, imaging quality generally increases with the number of views [1]. Further, the user has a wide range of tools to choose from such as angular spacing, source trajectory, pixel binning, field of view extension, just to name a few. This range of choices becomes obvious when one is trying to compare scan settings across the literature. This literature review aims to ask how existing research has led to improved scanning strategies, and also why and where and when one should take projections.

The scope of this literature review is limited to X-ray transmission computed tomography.. This work's main focus is cone beam XCT, which utilised multi-row DDAs. While other imaging techniques, using X-ray transmission recordings, are capable of creating depth information of an object, e.g. tomosynthesis or other laminography techniques, only XCT is considered. Furthermore, the scope of this document does not include the acceleration voltage of the electron beam and hence the photon energy or any other imaging settings. The complexity of the material interaction and the photon energy, combined with the detector response and filtration is worthy of its own literature review and exceeds the scope of this review. Optimising acquisition parameters has been focus in other studies [101,102]. Further, while the author acknowledges the diversity of the reconstruction solutions, the documents will mostly reflect on analytical reconstruction solutions and only briefly reflect on the two other classes of algebraic and statistical reconstruction [67]. The work will also briefly reflect on discrete tomography – where the greyscale value cannot be continuous but is limited to a set of grey scales [135]– but also on industrial reconstruction considerations which allow for a priori information. The author acknowledges the existence of many software packages that incorporate some of the later reviewed techniques. A special focus on the ASTRA toolbox [136] (University of Antwerpen), the TIGRE toolbox [137] (University of Bath) as well as the Core imaging library [138] of the CCPI group at University of Manchester. The toolboxes include implementation of some of the reviewed methods, as well as analysis tools, FDK implementations and visualisation tools [138].

3.2 Number of projections

When the number of projections is reduced, changes to the reconstructed volume start to appear, such as image noise distortions and streaking artefacts [64,139]. Practical guidelines on how many projections are needed were already discussed in the 1970s. While early studies were limited to parallel scan setups only [22] and were heuristic approaches which relate the minimum number of projections to the number of pixels in the detector, later approaches extended to fan and cone beam [22]. Natterer [71], under the assumption of equispaced view sampling over a half-circle in a parallel beam 2D setup, showed that for a bandlimited function limited at a largest spatial frequency component b the minimum number of views is given by $\frac{2}{\pi}b^2$; however only for parallel scanning geometry.

In 1980, Joseph and Schulz [22] published a detailed analysis of view sampling in fan beam setups. While initial work relates the number of projections to the number pixels of the detector, Jospeh and Schulz [22] argued that more robust relationships need to relate the number of views, N, to the largest spatial frequency component of the reconstructed volume. Assuming that the largest spatial frequency component in the reconstructed volume is v_M, Joseph and Schulz [22] proposed that the minimum number of projections, N_{min} for a reconstruction radius of R can be stated as:

$$N_{min} = 2R\pi v_M. \qquad \text{eq. (6)}$$

eq. (6) is for an angular range of 180°, and the reconstruction radius, R, is the field of view: the product of the number of detector elements, M and the projected detector size, a. eq. (6) is derived from eq. (2) and the Nyquist limit. This is for a coverage of 180°, and the authors stated their results are in line with a longer and rigorous analysis by Snyder and Cox [73]. A rule of thumb stated by Buzug [72] for a perfect imaging system that $N_{min} = M$.

A rule of thumb according to Zhao et al. [74] argues that the number of views should be chosen such that the angular increment (the arc between projections at the edge of the reconstructed volume) is less than a side length of a the voxel, b_{vox} [74]:

$$N_{min} = \frac{2\pi}{atan\left(\frac{b_{vox}}{R}\right)}. \qquad \text{eq. (7)}$$

The idea of having the movement of the outermost part of the reconstruction radius to be less than one voxel is of relevance when considering continuous motion during the acquisition (see section 3.7).

In a conference talk on optimising the number of projections Buratti et al. [75] approximate the effects of the number of projections on the reconstruction with different radial filters. A projection showing the features of interest was filtered with various reconstruction mimicking filters. While reducing the number of projections, once the contrast-to-noise ratio (CNR) drops significantly, the metrological minimum number of projections can be defined. This limit needs to be experimentally evaluated for each measurement.

3.3 Scan coverage

As now the concept of the equispaced number of projections and their angular spacing has been introduced, one should further discuss another property of the projections, their location aka. the circular coverage. While in the text above the 2D XCT system the circular coverage is generally sufficient by 180° plus full-fan angle, the cone beam setup is still is often used with full 360°.

For 2D reconstruction, the general minimum coverage for analytical solutions is given by 180° + fan angle [64,67,140]. However in 3D, most scans are carried out with a full 360° scan, as appropriate handling of the data redundancies is needed for maximising the reconstruction from half-scan data [64], a schematic of such a trajectory is shown in Figure 3-2 a). In a scan of just 180° + fan angle, some voxels will be covered by more back-projected rays than others. To handle the data correctly in short scans, i.e. less than 360°, Parker et al. [64,141] introduced an often adapted data weighing approach, the so-called Parker weighing function. For cone beam systems, a Grangeat based analytical reconstruction was proposed by Lee et al. [134], which is an analytical reconstruction

method which compensates for the missing projection data. As a detailed discussion on implantation and comparison of Lee et al.*'s* method [69,104,133,134] is not within the extent of this document. A method based on the Parker method was presented in 2017 to work on 'super-short scans' where the scan coverage is only a few degrees [142]. While the method performed better than normal FDK, imaging artefacts remained in the volume.

Interlacing scan strategies describe scanning methods for full circular coverage. In interlacing methods, the detector or source is shifted such that the back projection rays of the view n_x and the opposing view $n_{x+180°}$ are not overlapping, but the detector offset reduces the sampling distance, see Figure 3-1. While flying focal spot techniques and quarter detector offsets are established in medical XCT [64,67], only two recent (anno 2017, 2019) conference contributions tried to evaluate it into terms of industrial use [143,144]. Desbat et al. [145] though showed that interlacing scan strategies can be extrapolated for 3D systems, and showed in a detailed derivation that showed that interlacing scan strategies could be extrapolated to helical scan setups.

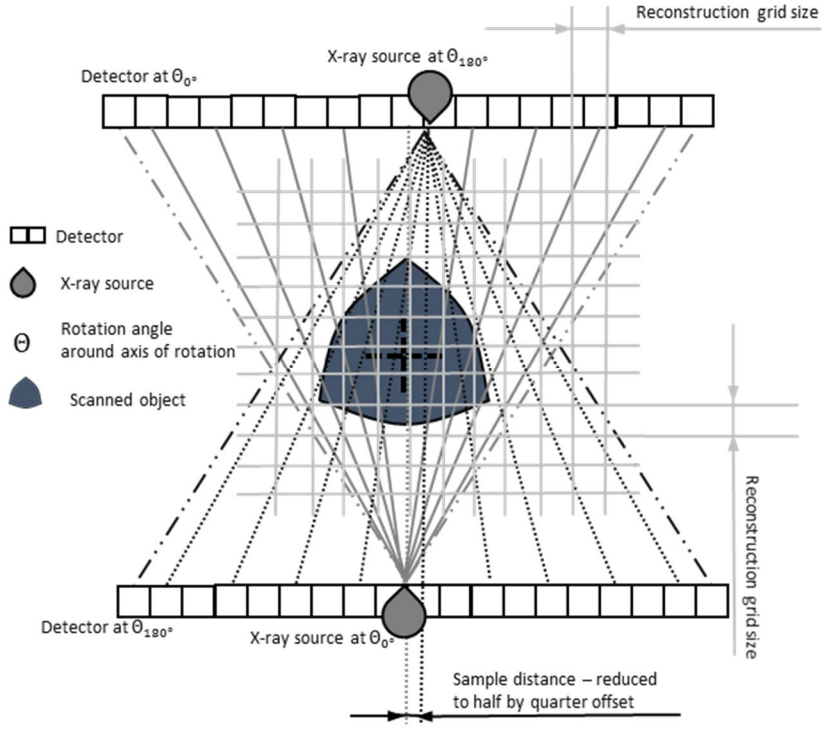

Figure 3-1 showing two opposing views of a $360°$ scan, and a reconstruction the same through the Iso-ray plane, it shows that the a quarter source offset, which causes a reduction of the sampling distance.

Zhao et al. [74] found that the noise in the reconstructed volume is worse using 40 projections than 39. The 39 projections also showed less view streak artefacts, which was reasoned through the interlacing effect; Zhao et al. [74] further concluded, that redundant views should be avoided, hence the views should not be separated by exactly 180°. Hence following the central slice theorem, this finding can be argued that with 40 projections redundant sampling points in the Fourier space are measured, whereas if 39 projections are acquired, the measured radiographs sample the Fourier space at a finer interval. Similar to the circular trajectories, better sampling trajectories can be used with helical scan techniques to increase the pitch angle without losing resolution: Carl Zeiss X-ray Microscopy, Inc., filed a patent to apply an irregular sampling grid to helical scanning [146]; similar to Desbat et al. [145].

While the analytical solutions are dictated by the central slice theorem, any non-equispaced variation of the location of the projections can only be derived from the k-space density function of the reconstructed volume and the fundamental sampling limit, i.e. Nyquist limit. The non-equispaced variations of the projections have been discussed in the medical literature at least since 1995 [147]. Algebraic and discrete reconstruction techniques received the most literature attention for projection selection algorithm, which this document will summarise in a later section 3.6. For analytical reconstructions, Placidi et al. [147] proposed an angular selection algorithm which is not in need of any a priori information but works from four initial projections. In this early work, the number of projections is estimated based on an "entropy measure" of each projection, from which the proposed algorithm estimates the next angular position.

A further concept which can be used to judge the dynamic spacing of the projection for analytical solutions is the "spectral richness" of the tomogram. If the k-space of the tomogram is known, this information can be used to place sampling points in k-space, the projections at optimised positions. A common cause for a known skewed k-space is a large aspect ratio of the part. The literature and industrial implementations show that for high aspect ratio parts the acquisition can change from uniform spaced angular projections to

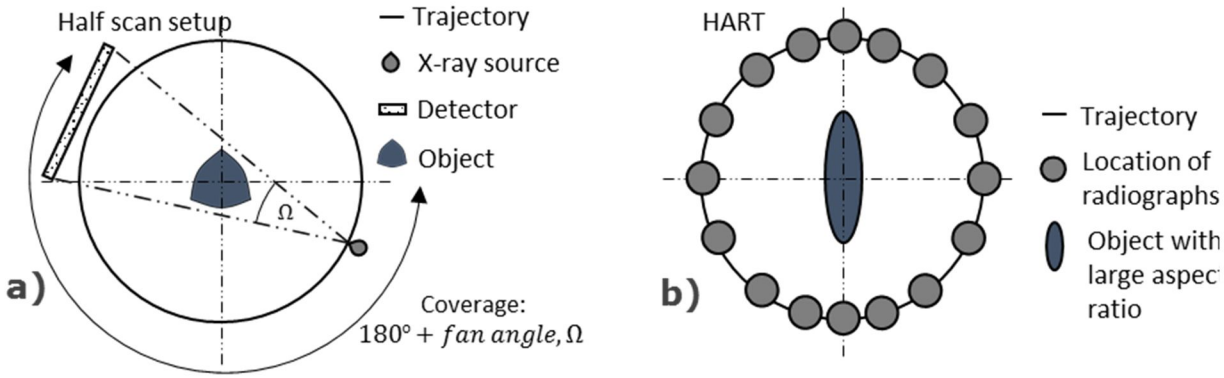

Figure 3-2 a) Half scan setup and b) the principle of projection spacing in HART.

a non-uniform spacing [148–151]. Such methods have been coined high aspect ratio tomography (HART) and an exemplary projection spacing is shown in Figure 3-2 b).

3.4 Out of view issues

Field of view (FoV) is the area which is seen by the detector. This review so far has only considered cases where the object is *fully within the reconstruction radius*, and the object never cuts the detector borders (thus is always in the FoV). When the FoV is larger than the object, the reconstruction radius can be reduced and therefore the number of projections. But within FDK and other analytical reconstruction solutions, as well as statistical techniques [152], it is well established that truncation artefacts occur when the part of the object moves in and out of the FoV during the scan [64,152,153] – i.e. the FoV is smaller than the object, see Figure 3-3.

In essence, truncation artefacts are caused as the reconstruction radius is limited to the coverage of the detector, and hence the additional attenuation of the material outside the reconstruction radius gets accounted for on top of the grey value of the reconstructed data, thus causing a cupping like truncation artefact. Taking the truncation of projections even further are region of interest (ROI) scans. ROI is also known as volume of interest scan, limited field of view scans, interior/local reconstruction or as extended field of view

reconstruction [76,154]. ROI scans where only a section of the object is imaged hence the FoV is much smaller than the object.

Several correction techniques exist for ROI scans [64,152,153,155,156]. The compensation techniques try to estimate – or from a priori knowledge assume – the shape, aka the object function, outside of the reconstruction radius to avoid the overlaying of the grey values. While simple approaches extend the projections, more sophisticated approaches have been proposed. Different approaches to cope with truncation and ROI have been reviewed by [156], including a sensor-fusion approach with photogrammetry and XCT.

While some truncation reconstruction approaches can be extended to ROI problems, other truncation algorithms do not allow for all projection data to be truncated [156]. In the commercial setting, the author was only able to find Werth Messtechnik, Gießen, Germany who advertises ROI scans. Here the object function outside the reconstruction radius is determined from a prior scan, where the object is fully within the FoV – but at a lower resolution. In an academic setting Mass et al [154] performed a comparison study on

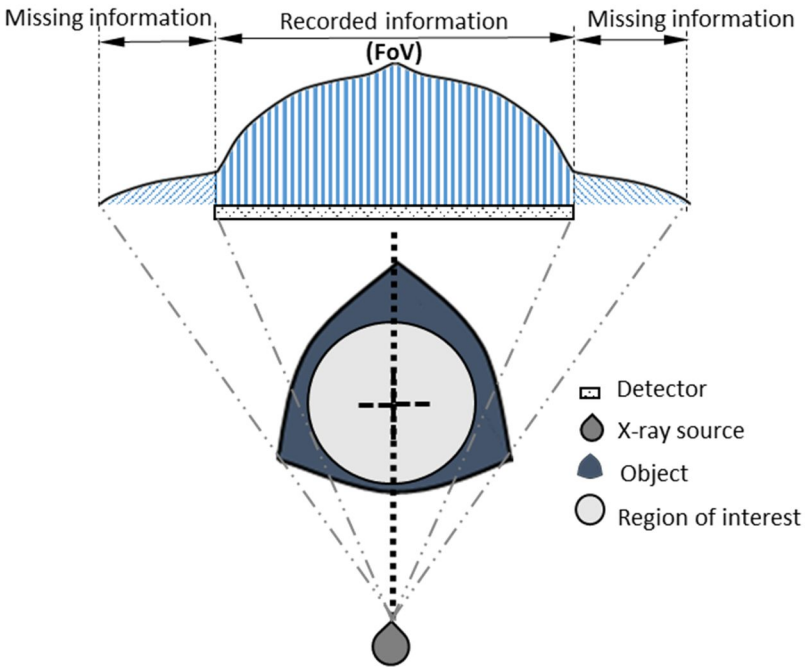

Figure 3-3 a) A view of the central beam for a ROI scan and b) an example of a truncation artefact.

different methods to deal account for truncated ROI data. Based on visual inspection, Maaß et al. [154] identified extending the projection to be the gold standard for ROI. However, extending the projection data increases the computational cost of the reconstruction dramatically. Maaß et al. [154] identified a data weighting approach to be a sufficient solution, in terms of resolution, noise levels and computational cost. With a data weighting approach, the object shape information, from a low-resolution scan, is translated into the weighting function of the reconstruction algorithm. In [157], Maaß et al. describe the implementation of the weighting function, which was developed for off-centre detector position scans, see in a later section 3.9.

According to [158], to fully reconstruct the ROI the number of projections needs to be increased to account for the larger object: i.e. the number of projections needs to be increased as if the reconstruction radius is as large as the object.

With cone beam XCT, large cone-beam angles also cause issues at the extreme ends of the FoV along the rotation axis, see Figure 3-4 b) for an example image. This geometry determined axial truncation causes these border regions to leave the FoV during a full rotation [83]; see Figure 3-4 a) for a schematic of this effect. Grimmer et al. [83] proposed a correction approach, which allows the reconstruction area to extend to the end regions of the detector. The approach of [83] uses a weighting function to account for the missing data, but the noise levels were shown to increase in the end regions.

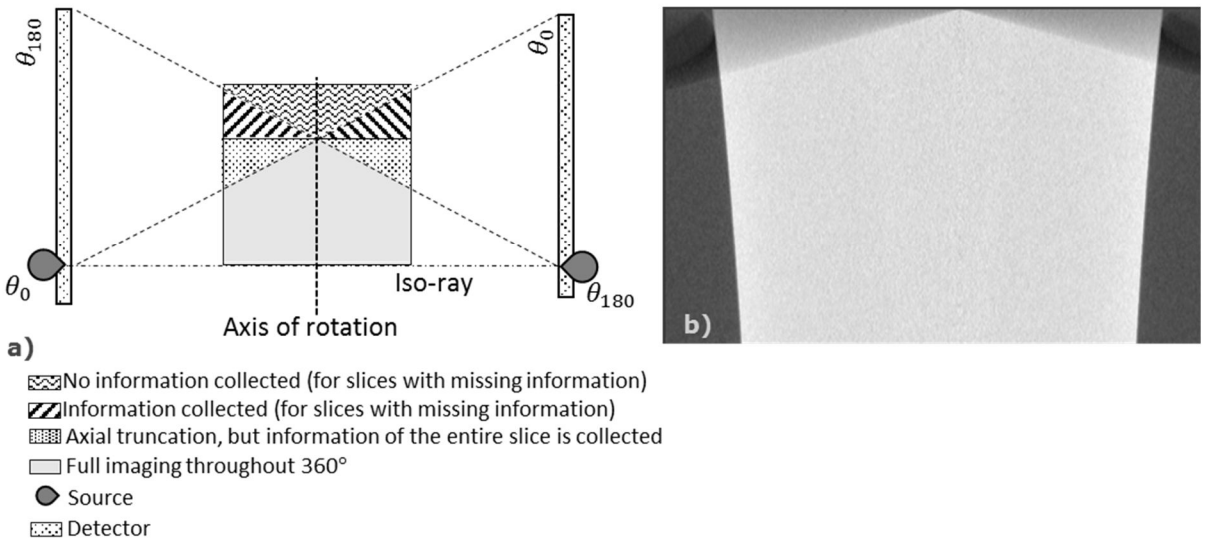

Figure 3-4 a) Schematic of axial truncation, b) an example of axial truncation artefact

3.5 Virtual projections

Virtual projections are projections which are not recorded experimentally but are artificially synthesised. Medical literature also refers to the creation of radiographs from digital data as digitally reconstructed radiographs. Early medical publications showed that streaking artefacts can be reduced by virtual projections [78,139,159,160]. The virtual creation of extra projections to reduce streaking has been addressed via two approaches traditionally: interpolation and forward projection [159]. In interpolation approaches, the streak artefacts are reduced in the reconstructed volume, by creating interpolated views from the real, neighbouring views. The virtual creation of extra projections have been proven to be of satisfactory quality for medical diagnostic applications [149], but their application is not yet explored for metrological applications of XCT. While they might decrease the streak artefacts, one should be aware of the additional complexity regarding the higher frequency components of interpolated views [139]. The use of interpolated views does lead to an additional reduction in resolution [139].

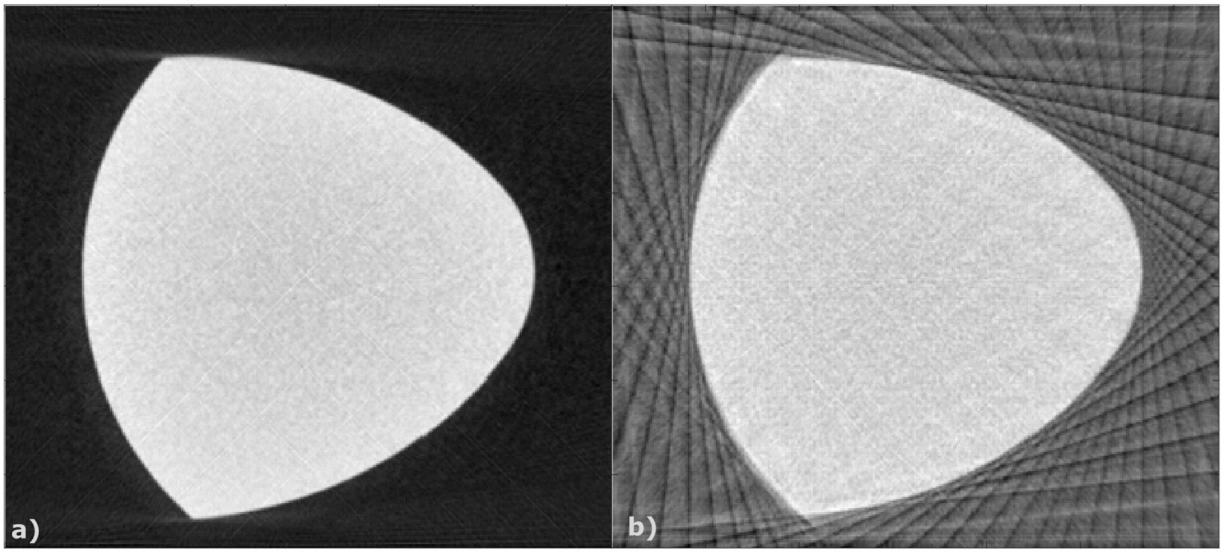

Figure 3-5 a) a reconstructed image with sufficient views, whereas b) shows streaking due to an insufficient number of projections.

3.6 Non-analytic reconstruction approaches

Iterative reconstruction (IR) and sparse data reconstruction are prominent in the medical literature and deserve a review of its own. Good introduction material on the general taxonomy, function, and notable developments can be found in [68,69]. For the algebraic and statistical approaches, the problem of how many – and which – views to take is more elaborate. Work has indicated that in IR, whether algebraic or statistical, the location of the projections affects the obtained reconstruction [135,150,161]. The most dominant solving approaches in IR are algebraic reconstruction technique (ART), simultaneous algebraic reconstruction technique (SART) and simultaneous iterative reconstruction technique (SIRT) [64,68,69]. In essence all of the three reconstruction techniques use forward project to reconstruct the volume. The forward projection mimics the imaging system of the XCT and creates a projection image from the reconstructed volume. The error between the forward projection and the recorded projection data is calculated. This error in the projection data is then back-projected. This process is repeated until a convergence limit is met. How well the reconstruction converges to a solution is of

importance in IR techniques, see Figure 3-6 for an example of different solutions with different degrees of convergence. To assess solution convergence in IRs error based measures have been proposed to decide if the number and positions of the projections are sufficient [149]. Other approaches to choose the projection can also include algorithmic measure such as the spectral richness of each projection [150]. In the medical field, Stayman [162] and also Dabravolski et al. [163] and Varga et al. [164] proposed projection selection techniques and task-based trajectories for IR for discrete tomography (DT). In DT the reconstructed grey values are constrained to a finite set of grey values (similar to thresholding of an image). In an industrial XCT paper, Fischer et al. [161] proposed an algorithm which optimises the location of the projections used in a statistical reconstruction algorithm, a penalised likelihood reconstruction. While the author concluded that this optimisation work is unlikely to be superior to traditional circular orbits for full scans, the author aimed their optimisation work on ROIs.

In the work of Fischer et al. [161], the projections from various locations are simulated from a double orbit scan. Each pose is simulated through a model function, and the poses where the ROI is most detectable are chosen – between six and eighteen projections, depending on the test object. The authors identified that the current implementation of this scan strategy planner takes several hours of computation. However, while the result indicated that the features were reconstructed enhanced compared to equispaced projections and half-scan data, a detailed discussion of measurement error, and resolution and stability of the algorithm are still needed.

Discrete algebraic reconstruction technique (DART) is a DT and IR, where the reconstructed grey values are bounded to a subset defined through prior knowledge of the scanned object [165,166]. Basically, the reconstructed volume is segmented and thus the complexity of the reconstruction problem reduced. Not much research has focused on discrete tomography for metrology use, but DT has been explored for agricultural XCT [167]. Alves Pereira et al. [167] applied DT through DART to an inline XCT system

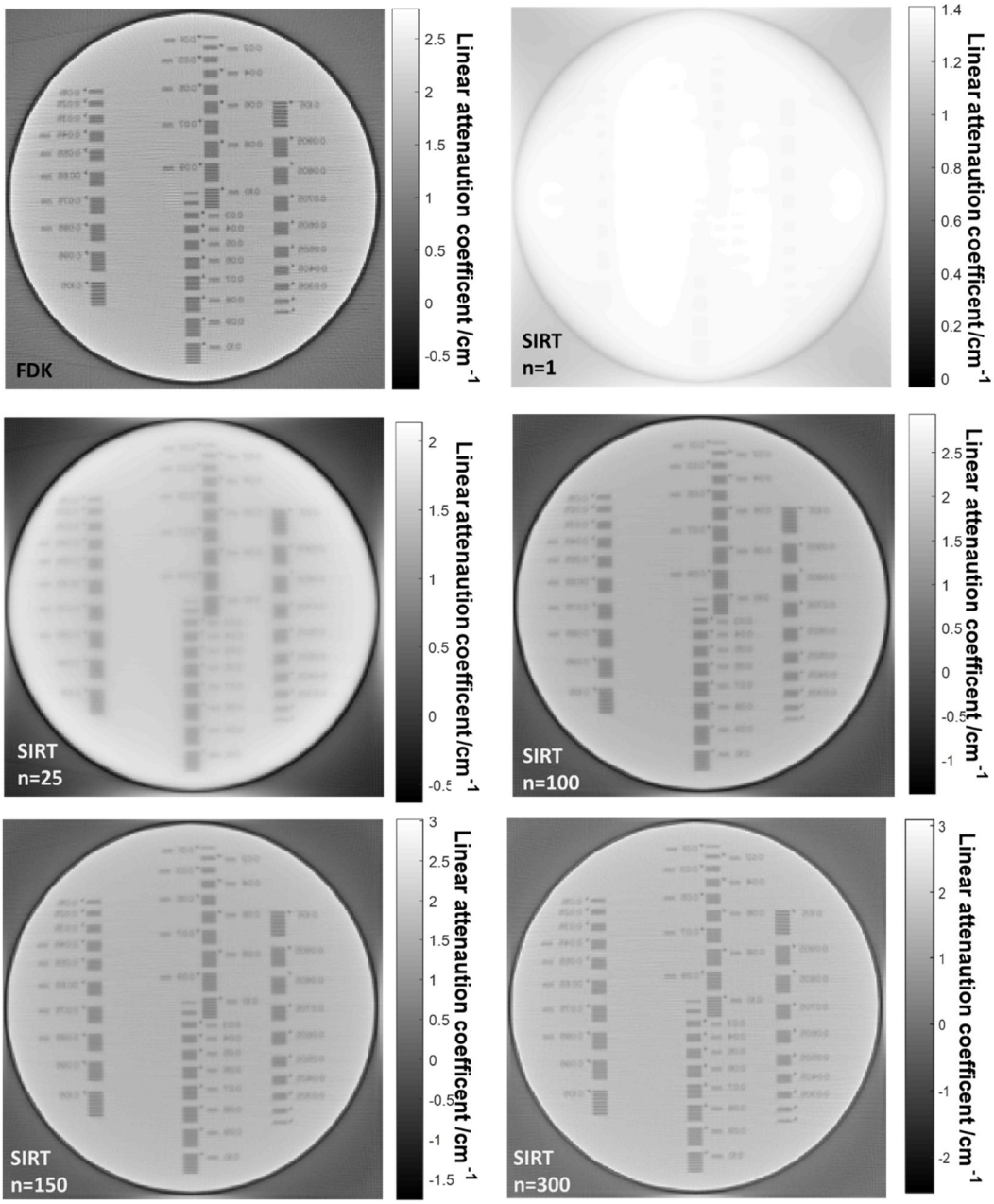

Figure 3-6 Reconstructions using polychromatic simulated data. The top left reconstruction is the central slice of a FDK reconstruction whereas the others are SIRT reconstructions at different number of iterations (n).

and were able to show that limiting the grey values via prior information improved reconstruction as compared to back projection techniques and simultaneous IRs. Further, the work of [167] also combined geometric a priori to reduce the number iterations of the DART. Here, the reconstruction domain (aka. volume), was limited to the geometry as measured with an optical sensor; the authors referred to this as the expected object domain (EOD). While the resultant tomograms were analysed, a detailed discussion of resolution and image quality remains open. The author would like to highlight one paper, which incorporates inhomogeneous sensor fusion as a constraint of an IR solution in industrial XCT [168]. Working on a highly scattered scan of a turbine blade, the authors of [168] used outer surface data obtained from an optical scan system to bound the reconstruction volume; and secondly applied a superiorisation approach with an edge map obtained from ultrasound data of the internal and external surfaces. In the first approach, the EOD is derived from the 3D surface scan: first binary shape mask is obtained from the 3D scan, a fuzzy surface mask is obtained by smooth filtering the binary shape mask, and the reconstruction was carried out by a regularised SART. The second proposed approach, the superiorisation approach, worked on ultra sound data. The third approach combined both the ultrasound data and the optical scanner data to define the EOD. The authors' [168] results showed an improved recognition of the internal walls using all sensor fusions, while only using the EOD, the internal features showed oscillations in the grey values of the material and internal edges are not well preserved.

3.7 Scan mode

The scan mode in the context of this document will be used as a descriptor for how the projections are taken: either stationary or whether the object is moving continuously during the exposure. This is not to be confused with step-and-shoot or axial scan mode, from the medical literature, which describes a scan geometry which is formed by circular trajectories and stepwise axial motion (which is similar but not equal to helical scanning) [64]. For the continuous scan mode, one basic assumption is made in this reflection: a constant speed of the object during the projection of each frame, hence any higher derivatives of the angular displacements are considered to be zero. Generally speaking, step-and-shoot yields slower acquisition times when using the same settings [169], due to the accelerations and decelerations in the associated control of the rotation stage and the interfacing of the detector.

The continuous motion leads to a blurring effect of the acquired projection. For a continuous motion from angle θ_n to θ_{n+1}, the attenuated projection value $I(r)$ of an X-ray beam $L_{r,\alpha}$ can be found by extending the Lambert-Beer law to [169,170]:

$$I(r) = \frac{I_0}{\Delta}\int_{\alpha=\theta_n}^{\alpha=\theta_{n+1}} \exp\left(-\int_{L_{r,\alpha}} \mu(x,y)\, ds\right) d\alpha, \qquad \text{eq. (8)}$$

assuming a constant speed of the continuous motion and a fan beam system. I_0 is the unattenuated intensity of the X-ray beam. Δ is the angular span of the continuous motion projection and can be found by $\Delta = \theta_{n+1} - \theta_n$. α is the rotation angle of the system and $\mu(x,y)$ describes the object.

Some published reconstructions, such as [169,170], integrate the recorded projection over the entire angular span of the projection in the frequency domain. However, some general conclusion can be drawn. Cant et al. [170] used an iterative reconstruction, which used a linear model for the continuous forward projection, and showed, that the reconstruction of the central region of the tomogram is improved. However, in metrological applications the angular span is generally smaller, e.g. [50], than the ones investigated by Cant et al. [170]. Gondrom-Linke [171] argued that using continuous rotation, it is advisable to

change the angular coverage to 180° + fan angle, rather than covering a full circle – at constant number of projections to avoid large angular blurring. An XCT manufacturer [172] recommends the number of projections for continuous motion acquisition to be limited such that no part of the object rotates more than one pixel projected onto the detector, this yields for an object fully in FoV to a relationship of $N_{blurring<1\,pixel} = \pi\, M$, where M is half the number of pixels of the detector (radius away from the projected centre of rotation) [172].

3.8 View averaging

The noise level in the projection data does translate into the reconstructed volume. Using a simple image model, Barret and Swindell [66] showed that the standard deviation of the CT value of a reconstructed disk in a parallel beam setup is given as:

$$\sigma_{vol} = \frac{k\,\sigma_P}{s\sqrt{N_P}}, \qquad \text{eq. (9)}$$

given that σ_P is the standard deviation of the grey value in the projections, s is the z-size of the voxel, and N_P is the number of projections, and k is a constant depending on the filter used in the back projection.

Based on eq. (9), any reduction of the noise in the projection will translate to a less noisy reconstructed volume. View averaging is common practice [50,173–175] and is expected to reduce random, photonic noise. View averaging is a form of coherent averaging of the acquired signal, however, for continuous rotation the additional exposures need to be accounted for in the rotation speed calculation. As the view averaging is done in the projection domain, it cannot remove ring artefacts due to bad pixels (see [64,176]), nor can it remove artefacts arising from the objects orientation (such as cone beam artefacts, refer back to section 2.2.3).

Volume averaging is similar to view averaging but in the reconstructed volume domain. While volume averaging can work simply as coherent averaging when the part is not moved in-between scans, more promising advantages exist when the object orientation is

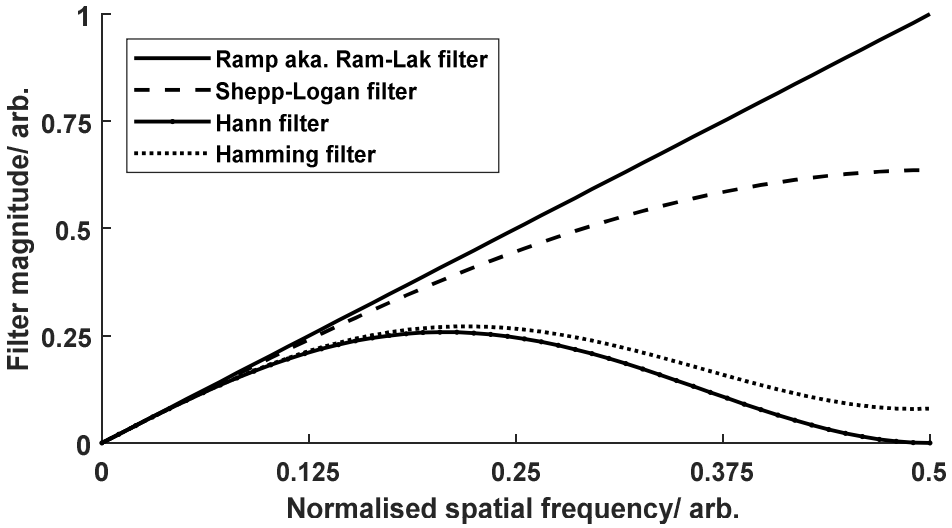

Figure 3-7 Different reconstruction kernels in the frequency domain. The x-axis is limited to the Nyquist frequency, based on [64,178,179].

changed, which has been named Dual Viewing. Dual Viewing has been introduced into the industrial XCT community by the Heinzl et al. [177]. When changing the object's location or orientation, the volumes can no longer simply be averaged, but data fusion concepts need to be utilised. Heinzl et al. [177] measurement chain utilises an initial coarse registration of the data sets, followed by an automated fine registration process, which minimises the median quadratic grey value difference. Once registered, a statistical segmentation engine is applied to both data sets. The statistical segmentation process attributes a probability vector to each voxel (using Bayes theorem). Each element of the vector describes the probability of the voxel to each segmentation class. The statistical segmentation process is followed by a data fusion process. Hence, the advantage of this process is that artefacts can be reduced, once those are reflected in the probability vector. However, it would be interesting to explore how this process compares, in terms of time and reconstruction results, to a double orbit or helical trajectory. Though, the main hindrance of this dual viewing approach is the increase in the scan time, under the assumption that both scans are performed at the same settings.

It is known that different reconstruction kernels will affect the image noise and the resolution [50,64,92,140]. Figure 3-7 shows the frequency response of different

reconstruction. Considering again the initial work shown by Barrett and Swindell [66], the filter kernel is an influencing factor in the equation estimating the pixel noise level of a uniform disc, eq. (9). Further, the cut off frequency of the reconstruction kernel, and hence the severity of the response will determine the resolution, and the response to noise. While this has been discussed frequently in medical literature, Bartscher et al. [50], carried a study to evaluate the effects of 24 different projection based filtering and reconstruction kernel combinations on metrological parameters. Among the evaluated measures were the signal to noise ratio, the edge response and form and length errors as compared to other CMMs. While Bartscher et al.'s [50] data showed that the more filtering reduces the form errors, they concluded this is not a general conclusion as this the smoothing causes a reduction of the resolution and hence the absolute length error can increase. This effect was shown both for smoother reconstruction kernels and projection level filtering. However, the quantitative generalisation of such findings is still limited. The lack of an agreed, meaningful and easily obtainable measure to describe the resolution in the projection and volume data hinders the theoretical generalisation.

3.9 Other approaches

As a high spatial resolution is desirable, raster tomography approaches have been combined with the traditional circular trajectory. Raster tomography or shift and stitch scan approaches are applied for large scan objects, where the object covers more than FoVs of the detector, at the desired magnification [85]. Here a relative motion of the system allows extending the effective FoV [85]. Thus a larger object can be imaged at higher magnifications without requiring larger detectors and without requiring ROI reconstruction techniques. Werth Messtechnik GmbH [31] advertises the use of the raster tomography. In a 2019 conference submission Sun et al. [144] explored a method to enhance the detector resolution. The proposed method is based on shifting the detector multiple times with a small increment at a fraction of a pixel size, and uses the multiple radiographs to calculate a higher resolution image using an interpolation method.

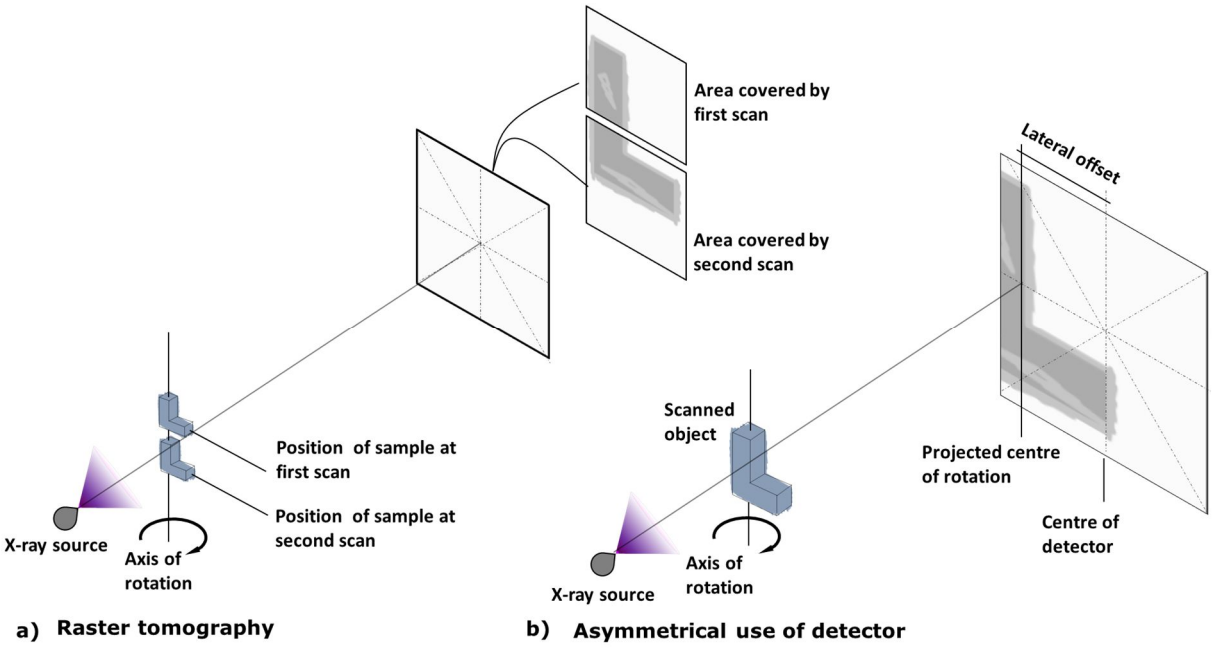

Figure 3-8 A schematic of a possible raster tomography setup and b) an asymmetrical use of the detector.

A further approach to increase the resolution of an existing detector is to utilise it asymmetrically. Hence the centre of the detector is shifted away from the centre of rotation in a lateral direction, and it will remain there during the entire scan [180]. While the asymmetrical configuration allows for a larger lateral FoV, an important issue arises: the data redundancy. In a normal set up, the projected rays are sampled multiple times throughout a full scan, but with asymmetrical scanning the extremely beneficial data redundancy is reduced and thus most likely will lead to an increase in noise.

3.10 Temporal aspects

So far the projection sampling has not considered the temporal dependencies of the system stability. One of the major temporal dependencies is the focal spot. Reisinger et al. [181] evaluated three methods for focal spot drift compensation. This included the comparison of spreading the same number and same spaced projections over either a 360° rotation or across several rotations ($n \times 360°$), this is not to be confused with helical scans, as there is a no linear axial movement [181]. The advantage of creating a multi-rotation sinogram is that the centre of rotation, and thus the geometry of the XCT system,

can be evaluated multiple times, which in turn was shown to improve reconstruction results, but also allows to reduce the post-processing time as the reconstruction can start during the acquisition [181].

3.11 Chapter summary

This chapter has reviewed the state of the art approaches of capturing projections in XCT. Analytical reconstruction approaches are well understood, however, analytical reconstruction does not allow for much optimisation of the acquisition of the projections unless the part's spatial frequency spectrum is well known. For analytical reconstructions, only HART allows for potential scope for optimisation of the acquisition, while HART is used in industrial advertisement material, there is a lack in the literature on HART. Several techniques exist that can overcome some of the geometric limitations of the conventional back projection techniques, such as region of interest scan, asymmetric use of the detector to extend the field of view, and raster scanning. However, the industrial adoptions are limited to only a small number of commercial vendors. Similarly, there is a lack of detailed scientific publications that detail and showcase the possible effects of those methods in terms of noise and resolution and a discussion in the metrological context is even further limited. Algebraic techniques are computationally expensive but have reported sophisticated tools for optimisation the acquisition of projections within the non-destructive testing context. Interestingly, the use of sinogram interpolation seems to have shown some diagnostic benefits in the early medical literature and has not yet been explored for industrial cases nor for cone beam systems with large area detectors. As such, there is a gap in the literature to what extent the computationally inexpensive method of sinogram interpolation can be applied to large areal detector cone beam system. While HART shows promise for reducing the measurement time of high aspect ratio parts, similarly, there is a lack of publications detailing the effects of HART on industrial and metrological applications.

4 Methodology: assessing reconstruction quality

Since in the later chapters methods are explored which alter the quality of the reconstructed volume, this chapter describes the methods used later to judge the distortions introduced. How does one assess, describe, quantify and compare the quality of different reconstructions and measurements obtained by XCT? (The question is easy, the answer can be convoluted.) The first section describes a state of the art method to directly assess and compare topographies from XCT data. The next section then highlights the use of image quality metrics as a method of deepening the understanding and judging reconstruction qualities in the world of metrological XCT. This section then introduces the methods used in this thesis for judging and quantifying image degradation. The final section will broadly highlight the XCT system and simulation software used within this work, which is then followed by the conclusion of this chapter. Parts of this chapter was published in [182,183].

The novelty of the proposed method is the three pillar approach to evaluate reconstructing quality. The reconstructed surface topographies are not just compared in terms of disagreement, but the raw reconstructed volume data is analysed in terms of noise and resolution too. This novel three pillar approach allows for a larger to understand effects of image degradation caused by manipulating the reconstruction process of XCT.

4.1 Topography comparison

The aim of the later chapters is to explore signal acquisition and processing methods which reduce the acquisition times of the XCT set up. Thus it is expected that the fidelity and nature of the obtained topographies will differ. The ability of XCT to image metal AM surface topographies was demonstrated multiple times in literature [2,10,26,30,184], highlighted in section 2.1. However, when altering the signal acquisition and processing methods, the error introduced to the topographies needs to be established and quantified.

The current state of guidance and accepted and convincing methods on assessing measurement uncertainty in XCT is sparse, as briefly highlighted earlier. Thus to assess the effects of different reconstructions and filtering methods on the surface topography, an empirical statistical method building on repeat measurements has been chosen to be the main focus of the comparative assessment of the surface topographies. Part of the method for topography comparison outlined below utilises and is built upon from Senin's (University of Nottingham, the University of Perugia) unpublished *xLib* library [58], and was used previously in literature [8,26,62,182,184].

4.1.1 Extraction of surface topographies from reconstructed XCT data

Reconstructed volume data are imported into VGStudio Max 3.0 [185], where the surface determination was performed. The 'advanced' surface determination setting of VGStudio was used, which is split into two steps. The first step is to obtain a starting contour, based on a threshold value. For efforts of comparability and consistency, the threshold value was set by using the automatic with the interval setting, where VG computes the ISO50 value, from user input which identified the mean material and background value. The second step of adapting the surface determination method was set to operate at the default search distance of four voxels. In addition, the software was instructed to 'remove particles and all voids' setting (i.e. removal of small, topologically disconnected portions of the surface appearing as floating particles and voids). Using VGStudio's default export settings, the surface data was exported into a STL mesh.

Measurements of the same area are aligned in three-dimensional space. Working on the triangulated mesh data, the iterative closest point (ICP) was used in this work, using the implementation of Senin's (University of Nottingham and the University of Perugia) unpublished *xLib* library [58], and demonstrated multiple times in [8,26,62,182,184]. ICP is a registration method which aligns two point clouds [186]. The ICP is a global, rigid alignment operation working in six degrees freedom. The transformation assumes that one point cloud remains rigid in the six degrees of freedom, while the other one is rotated.

It is an iterative process, which starts by matching data points of both point clouds to closest one of the other point cloud. From the matching, a transformation operator is derived [58,186], which is applied to the non-fixed point cloud. This process is repeated until the mean square root difference of the matched data points converges.

After finishing alignment, the triangulated mesh data are raster-scanned into heightmap formats, i.e. a 2D array of defined *x*-*y* pitch, which contains the height value of the surface at each array element, compare back to Figure 2-7. In the raster scanning process for each element of the 2D heightmap, a 'ray' (along the *z*-direction) is cast through the mesh. The intersection of the ray and surface mesh is recorded as the z-value for the heightmap element. The raster scan is performed using Senin's *xlib* [58]. The pitch of the raster scanning is set as half the voxel size (5 µm for chapter 5 and 10 µm in chapter 6). The height value is calculated using floating-point precision by interpolation from the triangulated mesh points. The data sets are then exported in the *.sdf* format. *.sdf* stands for surface data file [187,188]. The file format is an ASCII, human readable file format [187]. The file format describes *x*-*y* gridded data points, which are separated by constant x- and y values. The file header contains the magnitude of the *x*- and *y*- pitch [188], as well as the total number of data points recorded in the file. For each element of the *x*-*y* gridded data points a single height value is recorded file [187,188].

4.1.2 Statistical surface models

If multiple surface heightmaps of the same surface have been obtained under repeat conditions and are aligned, statistical surface models can be obtained [26,62]. For obtaining statistical surface models, Senin's (University of Nottingham, the University of Perugia) unpublished *xLib* library [58] is used. Statistical surface models describe the dispersion of the topography data. A statistical surface model contains for each point in a discrete *x*-*y* space a *mean value* and a *confidence interval* (CI). Both the mean and the confidence interval are calculated by treating all points on the surface as *independent*

variables, thus the calculation of the mean and confidence interval is done separately for each point of the *x*-*y* heightmap. The mean value is the arithmetic mean of all repeats. The confidence interval is a measure of the dispersion of the repeats of the *z* height of each *x,y* point. It is calculated from the student t-distribution. The student t-test is a statistical hypothesis test. It can be used for analyses where neither the population mean and population standard deviation are known and the sample size is small [189]. Thus, the degrees of freedom, v, for the t-distribution in this work was taken as $v = n - 1$, where n is the sample size. The sample mean $\bar{x}$ and the sample standard deviation s from the degrees of freedom (v). The confidence interval is the range around the mean, such that

$$CI_{lower} = \bar{x} - \delta, \qquad where\ \delta = \frac{t\ s}{\sqrt{n}} \qquad \text{eq. (10)}$$

and,

$$CI_{upper} = \bar{x} + \delta. \qquad \text{eq. (11)}$$

The t-value t can be obtained from the t-table or t-distribution with a degree of freedom of v. Within this work, the CI is always quoted at 95% (by convention [25]) any work in the later chapter uses three repeats, which yields a t-value of 4.303. An example of a

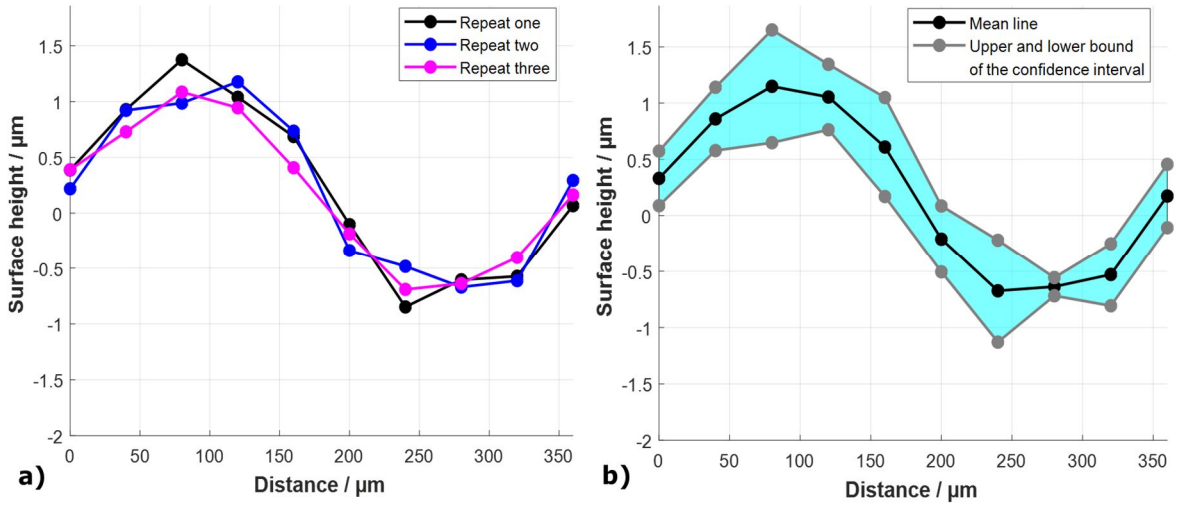

Figure 4-1 a) shows three repeats measurements of a surface line with ten measurement points, b) shows the corresponding the confidence intervals for the ten heightmap points

statistical surface model for a line profile is shown in Figure 4-1 b), while Figure 4-1 a) shows the repeated line profiles used for the computation.

The magnitude of the confidence interval reflects the local repeatability. A figure of merit for an areal surface texture can be obtained by calculating the width of all data points of the statistical surface model. This *mean CI width* will be used in the later chapters to assess the precision of a surface model.

The statistical surface model only considers uncertainty attributed to the *z*-axis and currently excludes the localisation error of the *x*-*y* directions. Part of the *x*-*y* error is compensated by the lateral alignment procedure, which is implemented to construct the statistical model, but this cannot take into account all error components.

4.1.3 Comparing two statistical surface models: The discrepancy ratio

To compare two statistical surface models of the same surface, the amount of disagreement between the statistical topography models of each measurement can be reported with the *discrepancy ratio*. The discrepancy ratio is the fraction of surface points where the confidence intervals of the local means do not overlap [8], such that,

$$discrepancy\ ratio = \frac{n_{CI}}{n}. \qquad \text{eq. (12)}$$

n_{CI} denotes the number of elements of the two statistical surface models which do not overlap and n is the total number of elements of the statistical surface models. With no overlapping escribes areas where the two CIs do not intersect in the *z*-domain, compare to the first two points in the graph of Figure 4-2. Data points where the CIs do overlap indicate that the null hypothesis cannot be rejected. For heightmap data points where the CIs do not overlap, the provided observations indicate the two measurements of the same surface are discrepant. The discrepancy ratio is used as a figure of merit in the later chapters to assess agreement between different surface models.

4.1.4 Comparison by surface roughness parameters

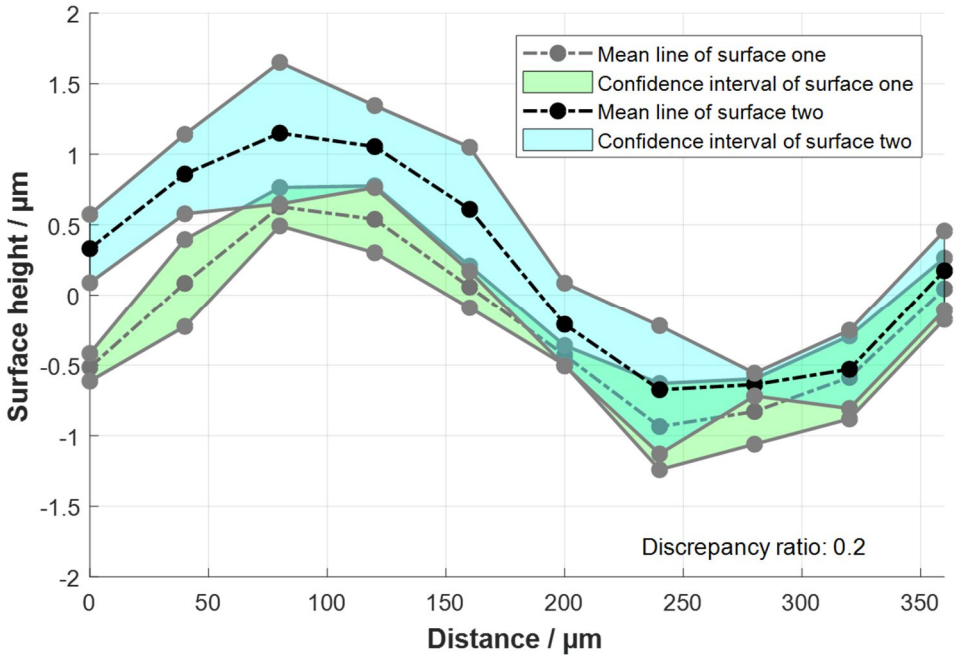

Figure 4-2 shows two statistical surface models. Only for first two of the ten data points the hypothesis of difference cannot be confirmed.

Areal field surface texture parameters are frequently used in the industrial surface topography analysis [29]. For the computation of ISO 25178-2 areal field surface texture parameters [190], the heightmap data was transferred into the surface metrology software MountainsMap© [59]. The computation of the parameters was performed in MountainsMap©. Unless otherwise stated, the parameters are calculated on an extracted area of (4 × 4) mm and are levelled by a least-squares mean plane subtraction. The S-filter was set with a nesting index at 12 µm; and the L-filter of nesting index at 800 µm. Both the S-filter and the L-filter were chosen to be in line with the guidance of ISO 25178-2 [190].

Two areal surface texture parameters were chosen for the comparative process within the thesis, the Sa parameter and the Sz. The Sa is the arithmetic mean height of the surface [29,59]. The Sa parameter can be expressed as

$$Sa = \frac{1}{A} \iint_{A} |f(x,y)| \, dx \, dy \qquad \text{eq. (13)}$$

for a continuous function of a surface$f(x,y)$, where A is the sampling area [29,190].

The Sz is the maximum height of the surface [29,59,190]. The Sz parameter can be expressed as

$$Sz = Sp - Sv, \qquad \text{eq. (14)}$$

where Sp is the maximum surface peak height of the surface within the area of evaluation and Sv is the height of the lowest surface pit [29]. The Sz is sensitive to peaks and pits of the surface, and isolated peaks of the surface can affect it. Figure 4-3 b) shows illustrative explanation of eq. (13) and indicating the positive direction and that the height function $f(x,y)$ is zeroed at its mean value $\bar{z}$. Figure 4-3 a) shows an illustrative derivation of the Sz parameter.

Since the Sa is based on the arithmetic mean of the surface, its sensitivity to the outliers is limited. The Sa was chosen to due this unresponsiveness, thus change in the Sa parameter can be used as indictor that the different reconstruction approaches are effecting the measured topography. Opposing the insensitivity and robustness of the Sa parameter, the second parameter Sz was chosen due to the high sensitivity to single outliers present in the surface texture. Thus it can be used to assess the introduction of

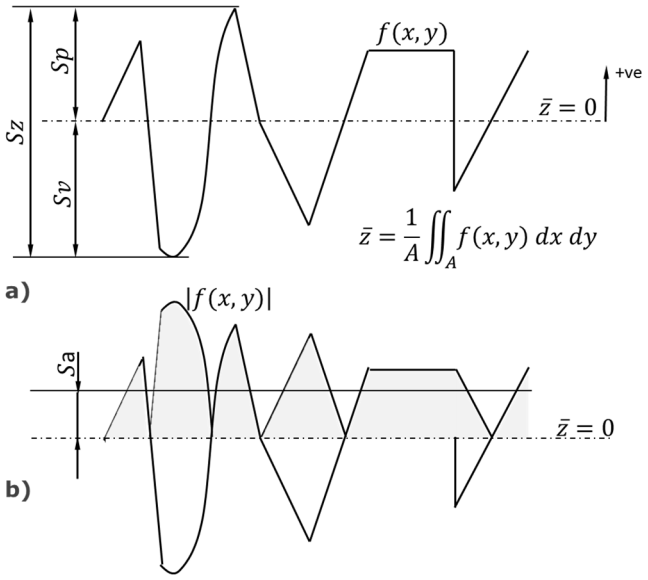

Figure 4-3 a) shows a diagrammatic representation of Sz and b) shows a diagrammatic representation of the Sa parameter. The grey underlined function is the absolute of $f(x,y)$. For easier visualisations, $f(x,y)$ is displayed in 1D.

noisy and sharp outliers of the topography easily. In combination, the analysis benefits of having both an insensitive and a sensitive parameter.

4.2 Assessment of XCT scans based on image quality

An XCT system is an optical imaging system [64,103]. In an imaging system the image quality of the reconstructed image can be described in terms of resolution, the local ability to resolve small features, and noise, the random variation of the voxel values around a mean value [92]rep. The image-based assessment of reconstructions is widely used in the medical literature [64,66,67,92,103].

4.2.1 Spatial resolution

The *10%-90%* resolution value of the edge spread function

The chosen method for quantifying the resolution is the edge spread function, and the figure of merit from the edge spread function is the 10%-90% resolution value [191]. This method is limited to straight edges of an object, a recommended value of inclination is at approximately 5° [191]. The edge spread function is found via an averaged super-sampled approach similar to [191]. To obtain the averaged super-sampled edge spread function, first, the image of a slanted edge is needed. Each row across the slanted edge, compare to Figure 4-4 a), is basically an edge spread function sampled at a sampling interval of the voxel size. To find an averaged super-sampled edge spread function, the angle of inclination is needed. To obtain the angle of inclination of the slanted edge, the image is segmented using an algorithmic method of finding the threshold value. The threshold approach implemented in this work is the Otsu method [192]. The Otsu method determines a single and unique threshold value from histogram data without the need of user input [192] and can be used on data which consists of two material classes [103]. Using the histogram data, the Otsu method aims to minimise the intra class variance [103,192]. The intra class variance is calculated for all possible thresholds and the

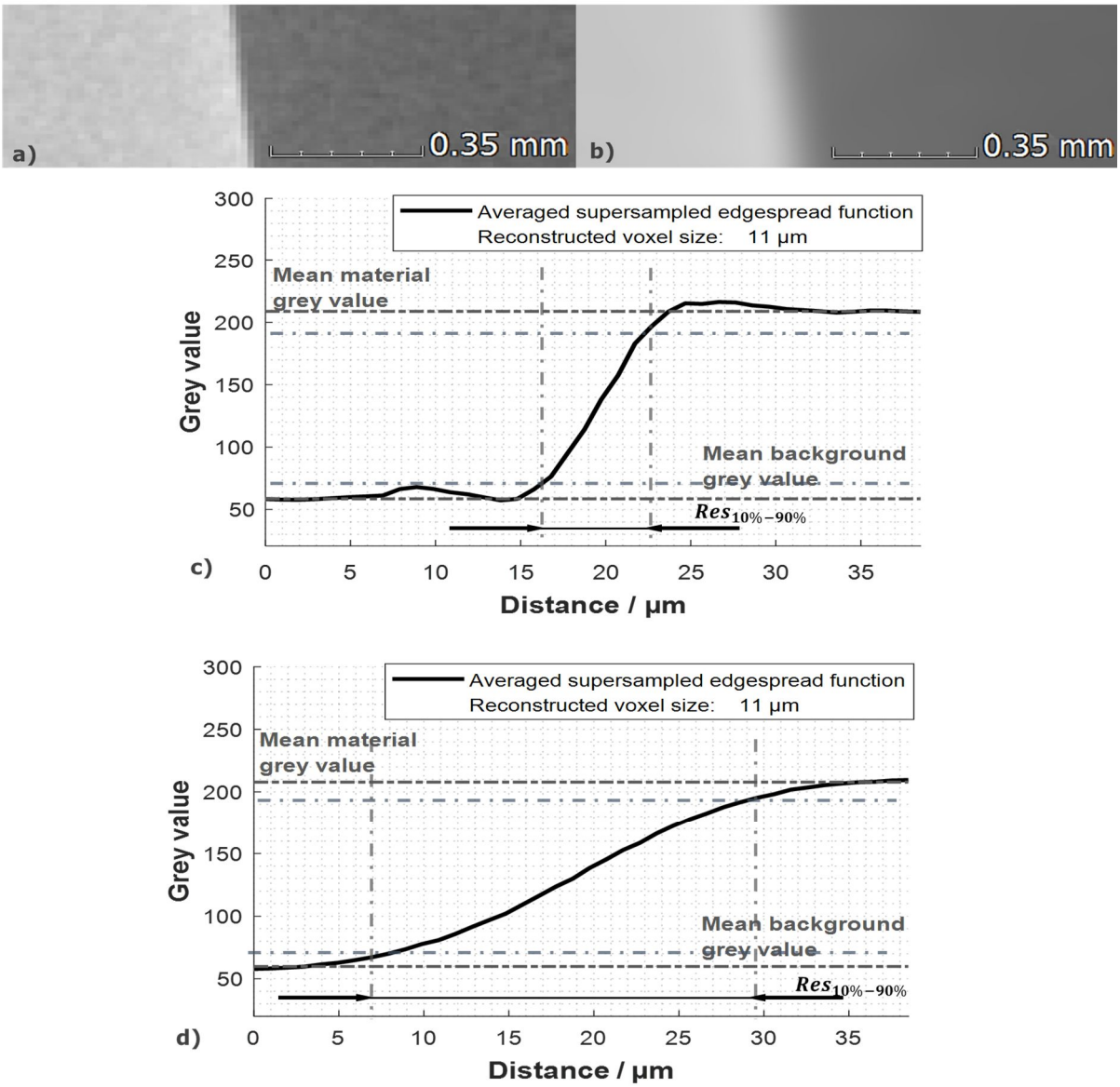

Figure 4-4 a) Shows a detail of a slanted edge and b) shows corresponding details but at a lower resolution. c) and d) show the super-sampled edge spread functions of a) and b) respectively. The dashed lines schematically indicated how the 10%-90% resolution value was obtained programmatically. The 10%-90% resolution values of a) and b) are 6 µm and 23 µm respectively.

threshold is chosen that minimises the intra class variance. The intra class variance can be found by calculated the weighted sum of two identified classes [192]. A line is fitted to the identified edge in the segmented image and the function of the line is expressed in terms of the image coordinate system. This is of importance for the super-sampling and averaging stage.

A single row vector (ESF_SS) is initialised, which contains four times more entries than the initial rows across the edge [191]. The ESF_SS row vector will later contain the averaged super-sampled edge spread function. Now ten rows across the edge are chosen. For each row across the edge, the respective offset distances are calculated using the angle of inclination determined earlier. The elements of the original row across the edge are inserted into the averaged super-sampled edge spread function. The location of the insertion is determined from the offset distances. Comparing the offset value to the pixel width of the averaged super-sampled edge spread function, the closest match of the pixel width is identified. The first entry of the original row across the edge data is inserted into this pixel of the averaged super-sampled edge spread function, the second-pixel value of the original data into the fifth of the averaged super-sampled edge spread function, and so on [191]. The overall process is outlined in Figure 4-5.

An example of two averaged super-sampled edge spread function is shown in Figure 4-4 c) and d). The examples show one sharp edge spread function, and a low resolution, the change of the 10%-90% resolution value is indicated.

Currently there are no guidelines published how to evaluate the edge spread function for industrial XCT. Therefore, the implementation of the edge spread function is based on a ISO standard to evaluate digital still photography images [191]. However, the digital, discrete and pixelated nature of the reconstructed image allows to translate the proposed methods to the reconstructed images in XCT. This method is however limited to the small region of evolution and does not account for the 3D nature of XCT.

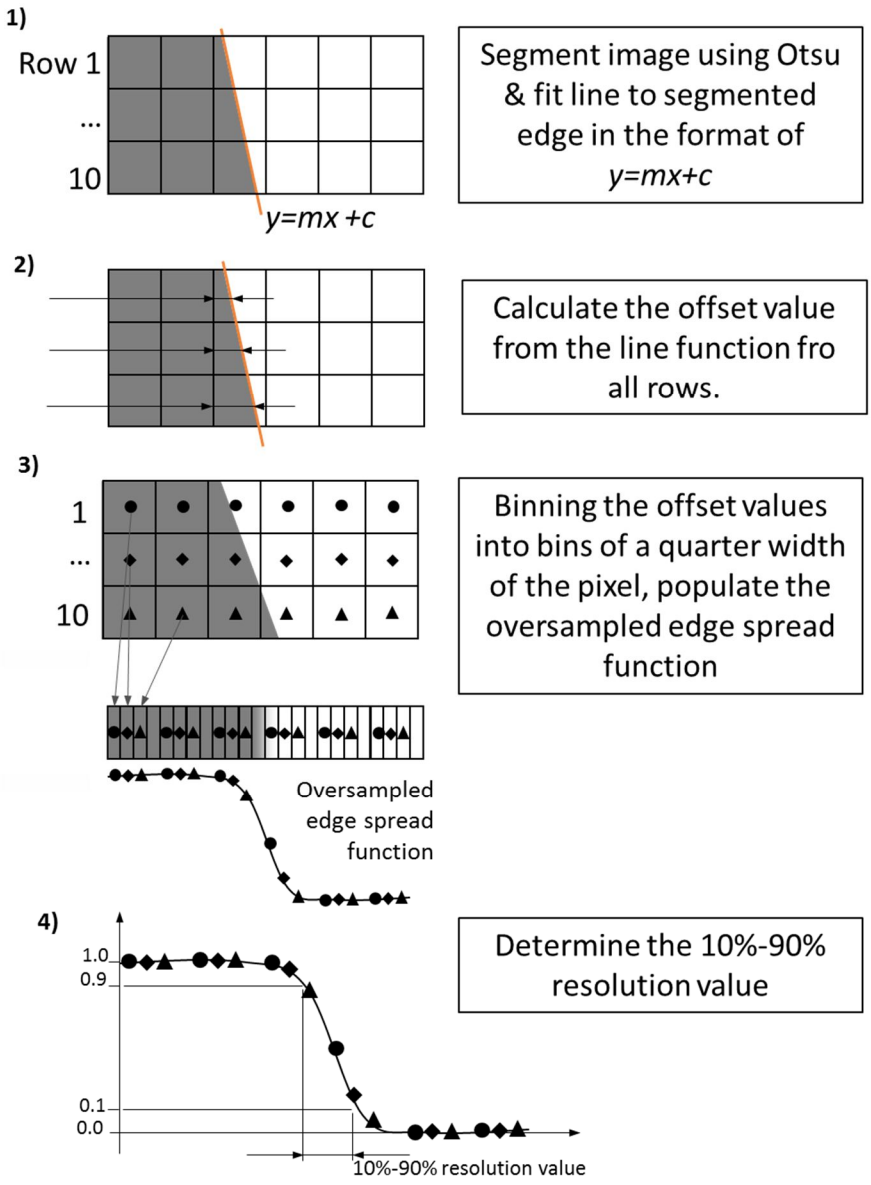

Figure 4-5 Figurative follow diagram of determining the 10%-90% resolution value. Based on work of [191].

4.2.1 Noise

The Shannon entropy

Within this work, the Shannon entropy is used to quantify the image noise. The Shannon entropy, applied to the reconstructed volume, is used to quantify a comparative measure of noise in the reconstructed volume data. The Shannon entropy is a histogram based, i.e.

unlike signal-to-noise ratios it works not directly on the reconstructed volume data but its histogram space. The Shannon entropy is defined as [108]:

$$H \coloneqq -\sum_{i=1}^{N} p_i \, log_2 \, p_i \qquad \text{eq. (15)}$$

where p_i is the probability of a voxel value to fall within the i^{th} histogram bin and N is the total number of histogram bins. The Shannon entropy is calculated on the normalised histogram [108].

The Shannon entropy approaches one for a histogram with uniform distributions and computes zero for a histogram of an image with just a single grey value. Regarding bimodal histograms as seen in XCT reconstructions, the Shannon entropy corresponds to lower values for better image qualities and increases for images which show very broad, noisy, distributions of the image content [108]. In this work, histograms with 2^{16} data bins were exported from VG Studio 3.0. Figure 4-6 highlights a case of two different acquisitions of the same part (Figure 4-6 a) and b)), one with higher levels of noise (Figure 4-6 b)), and shows the effects on the histogram distribution (Figure 4-6 c) and d)). The corresponding Shannon entropies are reported in the caption. In a configuration where a part of uniform material properties is imaged, a lower value of Shannon entropy is usually indicative of a bimodal distribution with better separation of the two modes (i.e. the part and the surroundings can be better separated, which is important for surface determination), whereas higher values of Shannon entropy indicate a less clear separation of the modes, hence lower discriminability of part and surroundings). Thus lower Shannon entropy is expected with better image quality, as discussed in [108]. The Shannon entropy is defined on a 0 to 1 scale, with 1 corresponding to a uniform distribution (no separability) and 0 corresponding to a histogram distribution of a single Dirac delta function.

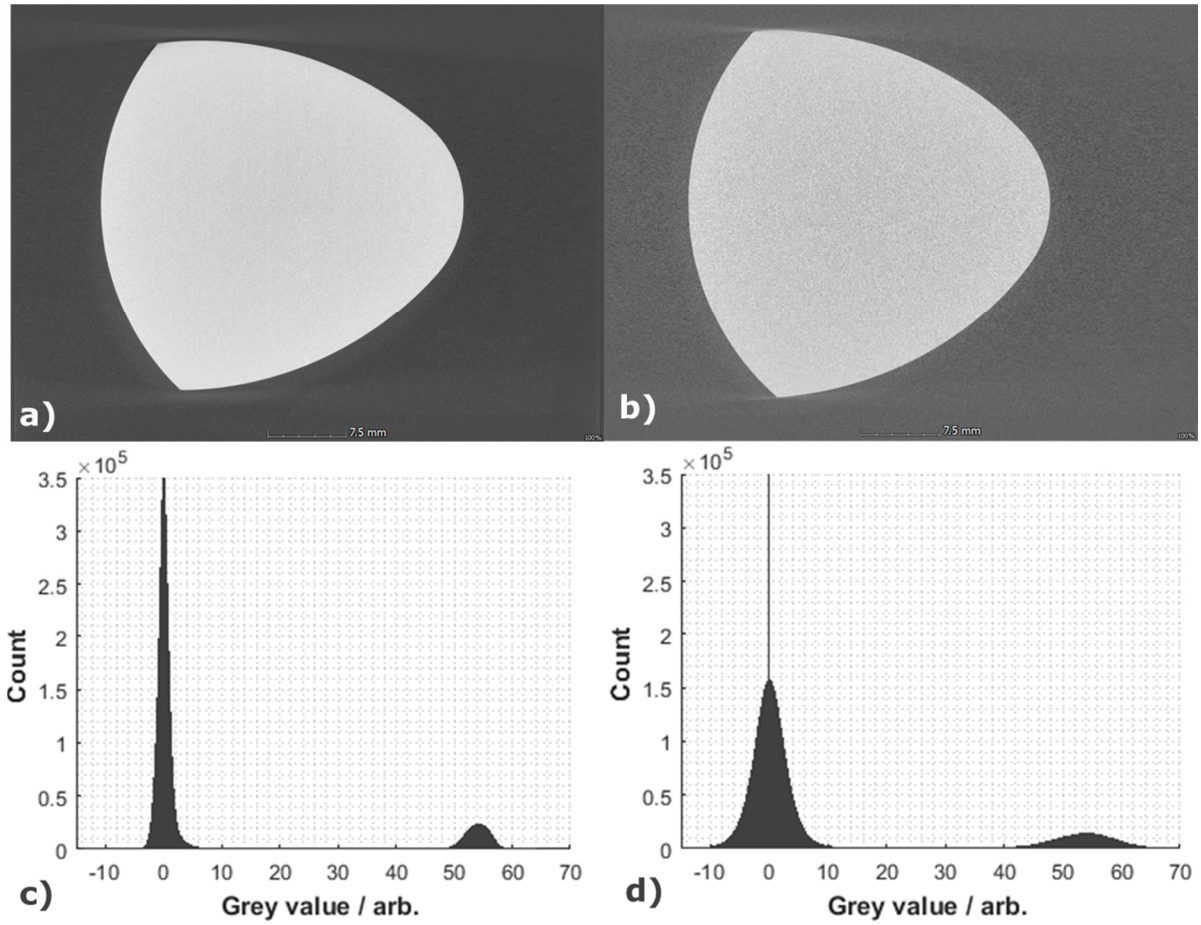

Figure 4-6 a) and b) Show slices of the same part but of different XCT acquisitions. a) was acquired to reduce image noise, and b) was a short scan to facilitate a noisy image quality. c) and d) show the histogram of the reconstructed volumes of a) and b) in that order and have a Shannon entropy of 0.66 and 0.70 respectively. Figure 2-16 shows details of image a) and b).

4.3 XCT system and simulation software

4.3.1 The Nikon MCT225 system

For experimental work, a Nikon MCT225 has been used in this thesis. It has a 2000 by 2000 pixel caesium iodide flat-panel scintillating detector, with a nominal uniform pixel size of 200 µm. The manufacturer states the maximum permissible error in accordance with the VDI/VDE 2630-1.3 for this system as: $MPE_{SD} = 9 + \frac{L}{50}$ µm (for the sphere distance characteristic, where L is in millimetres) [193]. The MPE_{SD} statement is a performance verification value, and is found by measuring calibrated sphere standards [97]. As such the MPE_{SD} value is not comparable to the later measurements performed in the subsequent chapter and is only quoted for full disclosure of the utilised tools. As introduced in section 2.1.1, model based and analytical uncertainty models are difficult to obtain in XCT [3,18,37,40,41].

The system is located in a temperature-controlled room, with the temperature set as (20 ± 1) °C. The radiation chamber of the XCT has additional, independent temperature control which is stated at (20 ± 1) °C. The X-ray gun temperature is monitored by thermocouples at several locations. A representative image of the system and its interior is reported in Figure 4-7 a) and b).

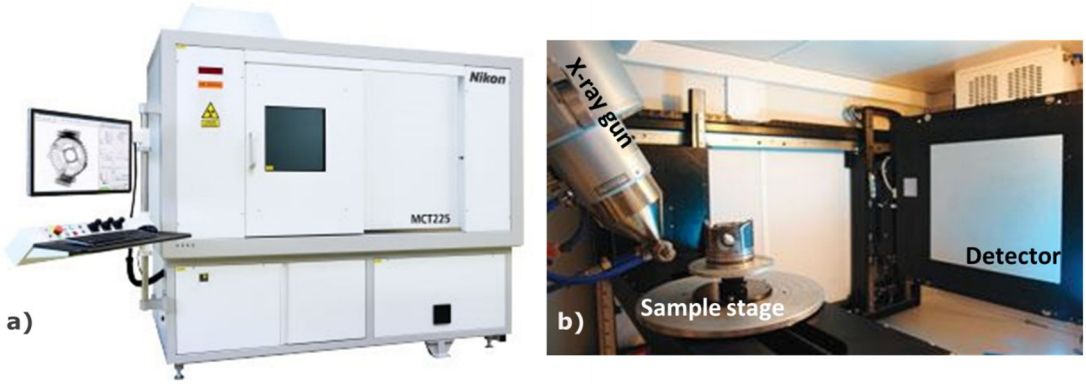

Figure 4-7 a) A Nikon MCT225 system as used for experimental work undertaken in this thesis, and b) a representative picture of the inside. Both pictures are taken from [193].

The XCT system has a maximum acceleration voltage of 225 kV is rated at a maximum power of 225 W. The microfocus X-ray gun is fitted with a cooled tungsten reflection target and with an inherent filtering of 0.5 mm Beryllium.

The Nikon MCT225 does not require a (first-order) scaling operation for each scan, such as work presented in [2,18,54,194–196]. The geometrical calibration is performed during the manufacturer's installation and is periodically adjusted using a calibrated artefact during the maintenance process of changing the filament.

4.3.2 X-ray image simulator

For simulation work, the *artist* simulation software has been used [197]. It is a raytracing simulator developed by the Bundesanstalt für Materialforschung und –prüfung, Germany. *artist* is an analytical simulation software, and within the context of this work has only been used to simulate photoelectric absorption. It allows the simulation of different materials and the object is described from a triangulated mesh surface and uses a numerical approach to simulate a Tungsten spectrum [197]. A rotational axis can be specified to simulate sets of radiographs for tomographic reconstruction. Unless otherwise stated the tungsten spectrum was simulated with a resolution of one keV. Artist allows for ray-tracing simulations. In ray tracing, the path length of the object is calculated for all pixels of the detector, by connecting a vector line (e.g. a ray) from the detector element to the source. As such the amount of material the x-ray penetrates can be calculated. Then the Lambert Beer law (see section 2.3) is applied to the path lengths to calculate analytically the attenuated beam intensities for all pixels, hence forming an X-ray image of the object.

4.4 Genesis of chapter five and six

To determine the research direction, the review of chapter 3 was conducted. Some initial work was carried out in the support of choosing research direction and scouting the performance of the reviewed methods in chapter 3 and other techniques. The preamble

work was based on a qualitative inspection only, where the reconstruction quality was assessed visually only, no quantitative surface texture was performed. One technique that was explored was the use of deconvolution to compensate for the large focal spots of X-ray source. For this purpose, an X-ray simulation was developed to create large focal spots, and different deconvolution techniques and blind deconvolution techniques were tested on the projection data and the reconstructed volume data. However, the severity of image and aliasing artefacts render this research effort useless. Similarly, the region of interest scans and different compensation techniques were investigated using experimental data, following the literature described in section 3.4. While the image quality of the reconstructed volumes was improving, the work is not addressed in the scope of this thesis, as compensating for the out view artefacts is not directly within the constraints of the research question. Multiple SIRT and ART reconstructions (using the implementation of the ASTRA toolbox [136]) of simulated noisy and noiseless data were performed. However, the significant increase in reconstruction times and the occasional occurrence non-linear alias-like imaging artefacts shifted the focus of this work away from further investigations into the SIRT. Similar issues arose, as predicted by the literature [104,134]

From the reviewed techniques in chapter 3, one of the two most promising initial scouting work were high aspect ratio tomography, as a simulation-based pilot test showed little to no adverse image quality when reconstructing noisy simulated data from a reduced number of projections. While conventional HART showed promise for reducing the acquisition without increasing the reconstruction time, chapter 6 investigates HART under continuous motion. Hence, chapter 6 furthers the idea of HART by analysing the feasibility of continuous motion while using HART. To demonstrate the feasibility of continuous motion HART and to avoid damage to the warranty and the geometrical calibration and to remove possible influences of the black box motion control system, the study in chapter 6 is limited to a noisy simulation study. HART is in line with the research directive of reducing the measurement time by having the ability to reduce the number of projections, and as such the reduces the acquisition time.

As opposed to IRT, sinogram interpolation showed little additional processing time during the pilot studies, when reducing the number of projections. However, the occurrence of streak artefacts and the noise was successfully suppressed with limited loss of resolution, given the qualitative inspection of the pilot study. Since the author was unable to find any studies that investigated sinogram interpolation on large areal detectors in modern industrial cone beam systems, a gap in the literature was identified. Hence, the sinogram interpolation method was chosen as a candidate for further, quantitative and in-depth investigation. Since sinogram interpolation is not an analytical method, but a heuristic method from the medical literature, the need to map out the performance of sinogram interpolation for different degrees of reduction in the number of projections.

4.4.1 Test samples

For the two chapters five and six, two different test samples are used. An LPBF test part was chosen for the experimental study in chapter five. This cubic part was chosen to be in line and replicate the parts used in previous experimental literature investigations into the characterisation of LBPF surface texture, such as [2,10,198]. This allows for the investigated case study to be direct of interest to the AM community, particular for the surface texture characterisation of LBPF. Especially since the investigated method of chapter five aims at increasing throughput, using a part of the same geometry and dimension shifts the presented work directly into the interest to the AM community. Thus the work is of interest to potential future work on mapping manufacturing variables in PBF. If one was to aim to compare the effects of different building parameters on the surface texture, any design of experiment could require large sets of measurements as the number of LBPF building parameters and variables can be large [6,62]. As such providing a case study to showcase a method and the effects of it on measuring LBPF surfaces at the reduced time was chosen a study. The sample part is shown in Figure 4-8 a). The sample was manufactured on a laser powder bed fusion system (a Realizer SLM 50). The raw material used is a sieved powder with grain size below 32 µm. The surface for investigation

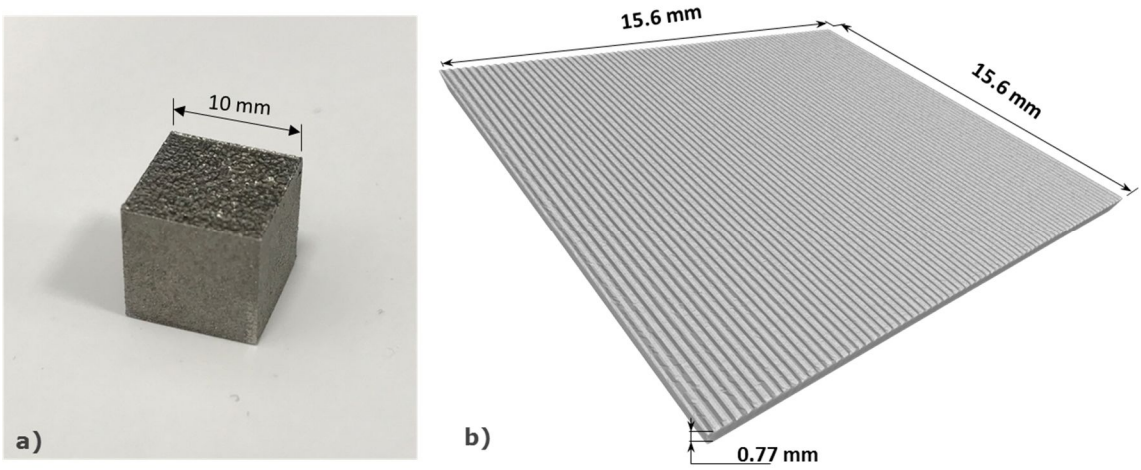

Figure 4-8 The test parts used in the later chapters. a) is used in chapter 5 and is an LBPF part and b) is used in chapter 6 and is a sinusoidal wave on a rectangle.

is the top one, facing upwards in the build direction. The opposing side of the surface for investigation was polished, to allow resolution assessments to be performed on this side.

For chapter six a different test part geometry was decided on, which is shown in Figure 4-8. Since chapter six is a simulation study to assess if HART can be operated in continuous motion, a high aspect ratio part was chosen with a superimposed sinusoidal wave. The part was chosen due to its simplicity and its close relation to surface texture test specimens such as those by Rubert & Co Ltd. [199]. The sinusoidal profile was given a wavelength of 0.21 mm and an amplitude of 0.03 mm. The design was loosely based on a specimen of Rubert & Co Ltd. While this sinusoidal wave is not topological not inspired by PBF surfaces, the main thriving force was to come up with a surface with features small compared to the voxel size and thus sensitive to changes arising from reconstruction artefacts, loss of resolution and noise. The superimposed surface on the part was chosen such that the amplitude is small in relation to the voxel size (the amplitude is 30 µm whereas the voxel size approx. 20 µm). As such, the small scale of the surface is expected to amplify any possible effects of loss of resolution and noise on the extract topography and making quality degrading and undesirable effects easy to spot in the parameters and the extracted statistical surface models.

4.5 Chapter summary

The proposed methodology explores three separate quantitative aspects: the resolution and the noise of the reconstructed volume and as well as a statistical approach of comparing obtained surface topography data. While the statistical topography comparison method alone is capable of quantifying changes to the measurand of interest, the additional investigation of noise but also resolution allows for further insight into the underlying causes of the changes to the surface topography. This novel multiple pillar approach to the analysis of reconstructed volumes allows furthering the analysis of the reconstruction techniques to understand the deterioration caused inside the volume data and how this translates into adverse effects of the measurement.

Two methods are identified from pilot work and the reports of the literature to be of interest for further and detailed investigation in the later chapters, HART under continues motion, and sinogram interpolation. Both methods were reported to reduce measurement time in literature in chapter 3. Chapter 6 will address a feasibility study of running HART in continuous motion, and as such is limited to simulation work. Chapter 5 will map out experimentally the performance of sinogram interpolation using case studies.

5 Sinogram interpolation

This chapter explores the effects of sinogram interpolation to increase the throughput of X-ray measurement for the inspection of surface topography and investigates how such interpolation affects the reconstructed topographies, the resolution and noise levels.

This work is split into two sections. The first one maps out the effects of sinogram interpolation, while the second one compares sinogram interpolation against other methods to reduce the acquisition times. The results are analysed and compared in terms of noise, resolution, agreement of the reconstruction results and values of surface texture (i.e. roughness) parameters. The first section is derived from a publication accepted in 2019 [183] and the second is based on a conference proceedings submission [182].

5.1 Introduction

Sinogram is the term given to the dataset obtained by stacking a row of each acquired radiograph behind each other, building a 2D space where the second axis is the rotation angle, compare back to section 2.2. Repeating this for all detector rows, a three-dimensional space is built. The resulting three-dimensional space is sometimes referred to as Radon or sinogram space. Sinogram interpolation techniques use the existing radiographs to estimate radiographs at intermediate rotation angles. Being an interpolation method, the original data points are not affected and additional ones are created. Clearly, the theoretical advantage of sinogram interpolation is that one could obtain full volumetric reconstructions from a reduced set of radiographs (hence, shorter measurement times), just by computing the missing projections by interpolation. Methods proposed for sinogram interpolation include linear interpolation [139] and Fourier approaches, such as sinc interpolation [149,182]. The interpolation methods exclusively use the greyscale information in the available radiograph data. In early work from the medical community, it has been observed that, whilst reconstruction artefacts and noise

can be reduced by sinogram interpolation, interpolation can yield to a reduction of resolution in the reconstructed volume [139].

5.2 Experimental investigation: Mapping out the parameter space of sinogram interpolation

The work presented here explores the effects of sinogram interpolation to increase the throughput of XCT measurement for the inspection of surface topography, and investigates how such interpolation affects the reconstructed topographies. More specifically, the goal is to assess how sinogram interpolation affects the resolution and noise levels associated with volumetric reconstruction and ultimately propagates through to the topography of the extracted surfaces.

In this work, continuous motion XCT is used to achieve shortened measurement times. Starting from a complete set of radiographs taken as reference, the use of increasingly smaller subsets of projections is investigated, combined with the application of sinogram interpolation to reconstruct the missing data. Each resulting volume is then used to extract surface topography. The topography datasets are compared in terms of repeatability error and values of surface texture parameters. This section follows the initial ex-ante work published in [182].

5.2.1 The interpolation method

The Whittaker–Shannon interpolation method, also known as sinc interpolation [159], was used in this work. The sinc interpolation was chosen as it is successfully applied in the medical literature [159]. Sinogram interpolation has been successfully been utilised to suppress metal artefacts [200], but also for removing sparse projection artefacts as shown in [139,159,201,202]. Sinc interpolation is based on inserting additional zero components into the discrete Fourier space of the sinogram. The number of zeros needed can be derived from the relationship between Fourier space points and spatial points. Because of memory limitations of the available computer hardware for this work, the volume was split into two sub-volumes of equal size, which were processed separately. Each sinogram slice

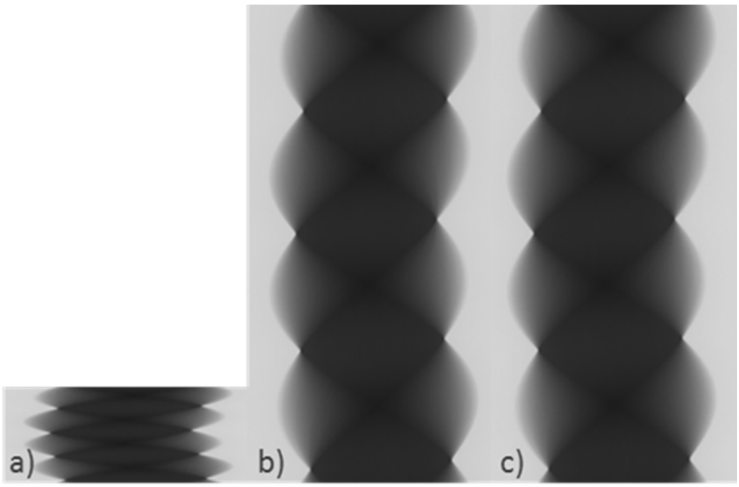

Figure 5-1 Three 2D central slices of three different sinograms are shown. The sinograms are a) has 628 projections, b) 3142 projections and c) has 3142 projections interpolated from 628. While all three sinogram slices represent 360° rotation, for visualisation the pixel in the direction of rotation, the vertical axis, are not stretched and the pixel representations is kept square.

of each sub-volume was then interpolated independently. Figure 5-1 shows an example of a 2D sinogram. Figure 5-1 a) shows sinogram with 628 projections whereas b) shows one with 3142 projections. The sinogram shown in Figure 5-1 c) has 3142 projections interpolated from 628.

5.2.2 Experimental campaign

For the setup of the XCT system, the number of projections needed was calculated as 3142, given the number of detector pixels and assuming that the sample fully covers the field of view (FoV) [172]. Five test conditions were considered, each consisting in measuring the sample with a decreasing total number of projections corresponding to 80%, 60%, 40% and 20% of the theoretical reference number. For each test condition, three measurements were performed with identical setup (repeatability conditions). Then, each sinogram was upsampled using the sinogram interpolation by different amounts in order to match all the previous downsampling levels up to no downsampling, i.e. the reference number 3142. So, for example, the test conditions realised with 40% of the reference theoretical number of projections (1257 projections) were upsampled at 1885 (60%), 2514 (80%) and 3142 (100%) projections. The full set of experiments and the

naming conventions used are summarised in Table 1. The acquisition time of 628 projections was around 42 min, around 84 min for 1257 projections, around 126 min for 1885 projections, around 168 min for 2514 projections and 3142 projections required around 209 min.

5.2.3 XCT setup and data processing parameters

The XCT system used in this study is a Nikon MCT225. The test sample is a Ti-6Al-4V additively manufactured cube with nominal side length of 10 mm. The test object is chosen over other possible test objects for the following reasons. The range of non-linear, material and geometry dependent influence factors in XCT is large [55], hence the validity of extrapolation statements between different setups within XCT is limited. For this case study, an AM surface was chosen, due to the range of scales of features and the complexity of the surface texture [6].

Figure 5 2 a) shows an obtained projection and d) shows an image of the sample. The sample was mounted on a bespoke polymer fixture. The fixture was designed to tilt the sample by 5° with respect to the central slice, see Figure 5-2 b) and c). The part was scanned at a magnification of approximately 18.7×, which yields a projected pixel size of

Table 1 Experiments, indicating conditions and naming convention.

Original experimental data					
100% of projections required: 3142	80% of projections required: 2514	60% of projections required: 1885	40% of projections required: 1257	20% of projections required: 628	**Number of projections used in reconstruction**
ORG3142	ORG2514 UP3142	ORG1885 UP3142	ORG1257 UP3142	ORG628 UP3142	3142
	ORG2514	ORG1885 UP2514	ORG1257 UP2514	ORG628 UP2514	2514
		ORG1885	ORG1257 UP1885	ORG628 UP1885	1885
			ORG1257	ORG628 UP1257	1257
				ORG628	628

approximately 10.69 µm. The voxel size is of similar magnitude of other surface texture investigations of metal PBF surfaces, such as [2,10,198]. The sample was not moved from its fixture between the scans. The gun of the MCT225 was set up with an acceleration voltage of 190 kV and a current of 53 µA. The focal spot of this X-ray gun was not quantified, but the expected spot size relied on the empirical type data of the manufacturer, but guidance on quantifying the spot size can be found [203–207]. According to the manufacturer's specification, the used settings lead to an apparent focal spot size smaller than the projected pixel size. The spectrum produced by the cooled tungsten target was filtered sequentially by 0.5 mm copper, then by 0.5 mm aluminium to harden the X-ray spectrum. This filter combination showed good performance in reducing the beamhardening artefacts in the reconstructed in prior scouting XCT acquisitions. By using less copper, but in combination with aluminium, this dual filter hardens the spectrum while limiting the effects on the exposure time. The detector exposure time was set to 2000 ms, and two exposures were taken and averaged to obtain a radiograph. Before performing each scan, a two-point white level correction was performed. The white level correction contained 128 radiographs in the fully exposed condition and the same number of radiographs were taken for the dark reading. All the collected radiographs were corrected for variations in the X-ray flux by Nikon's flux normalisation tool. The XCT was set to measure with the part in continuous rotation. Each reconstruction was performed in Nikon's CT PRO software. No beam hardening correction was applied to any of the data sets. The same reconstruction settings were applied to all the data sets. No additional filtering was applied during, before or after the reconstruction other than the reconstruction filter. The reconstruction filter was a basic Ramp-filter (also known as the Ram-Lak filter) and was the same for all experimental conditions. The reconstruction filter is needed to avoid blurring during the reconstruction. For the sake of comparability and consistency of treating all experimental conditions, all reconstructions performed in this section of the thesis uses exactly the same reconstruction parameters. The angular position of each radiograph was derived by assuming equal spread around

360°. The manufacture's tool to calculate a sub-voxel location of the centre of rotation was used.

The Shannon entropy, applied to the reconstructed volume, was used to quantify the amount of noise associated with each experimental set-up. The resolution on the volume data was quantified using the 10% to 90% value. The resolution value was computed on the polished edge of the test part which is highlighted in Figure 5-2 c).

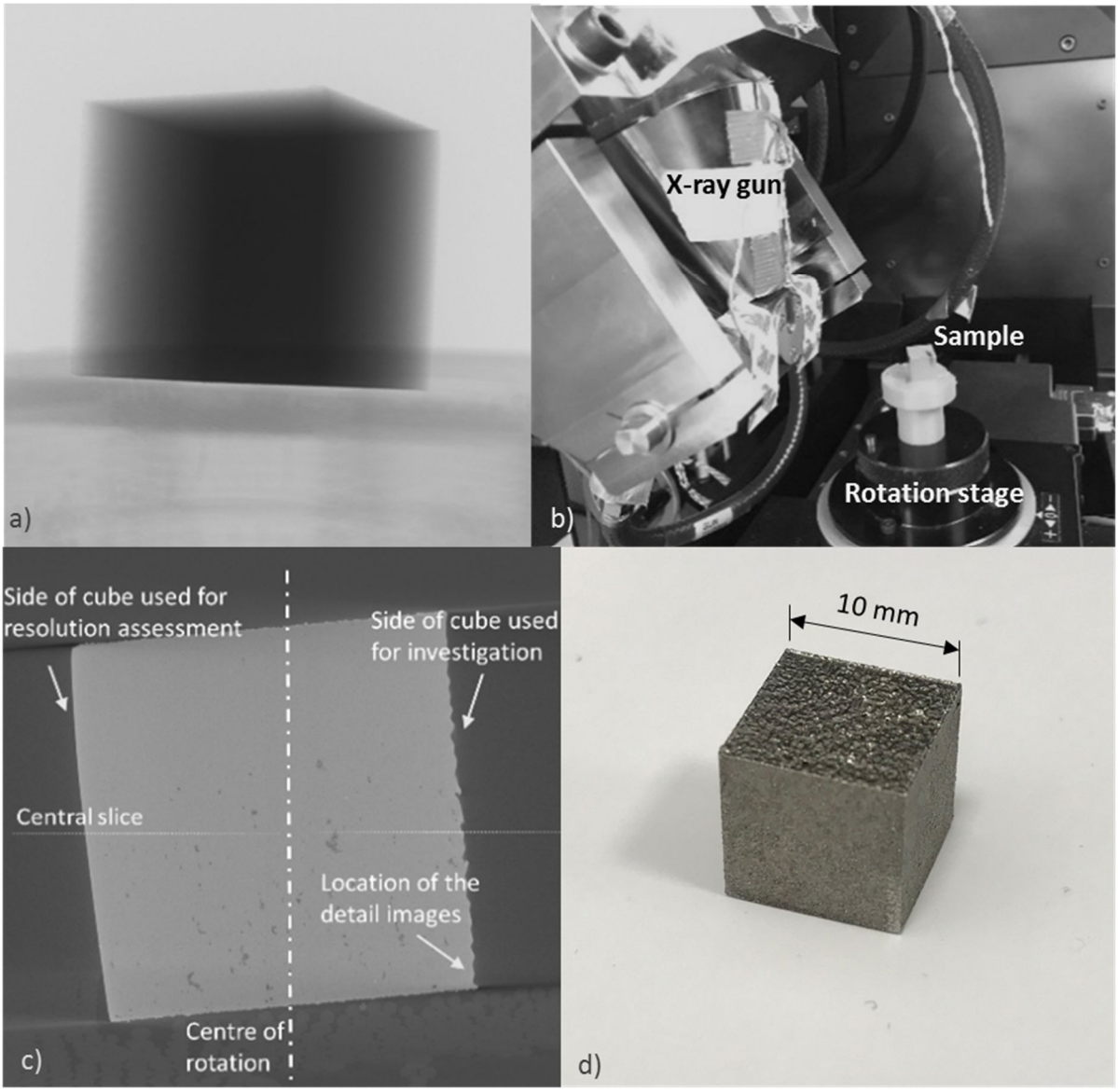

Figure 5-2 one of the radiographs acquired, b) a view of the sample in the XCT system, c) a reconstructed slice and d) an image of the sample.

The reconstructed volume datasets were imported into VGStudio Max 3.0, where the surface determination was performed using the advanced surface determination method. Following the methods described in section 4.1 the surface topographies of all data sets were exported as STLs.

Following section 4.1, the STL datasets were aligned to a common reference, which was selected as the surface region extracted from ORG3142, the dataset obtained by using the reference number of projection and no sinogram interpolation. The aligned datasets were raster scanned into 2.5D heightmaps with a point spacing of 5 µm, as it matches closely to half of the reconstructed voxel size.

The obtained heightmaps of the repeat measurements were used to compute the statistical surface models, as highlighted in section 4.1.

The obtained heightmaps were then transferred into the surface metrology software MountainsMap [59] for the computation of ISO 25178-2 areal field surface texture parameters [190]. Parameters were calculated on an extracted area of (4 × 4) mm; levelled by least squares mean plane subtraction; S-filter of nesting index at 12 µm; L-filter of nesting index at 800 µm. Both the S-filter and the L-filter were chosen to be in line with the guidance of ISO 25178-2 [190] .

5.2.4 Results

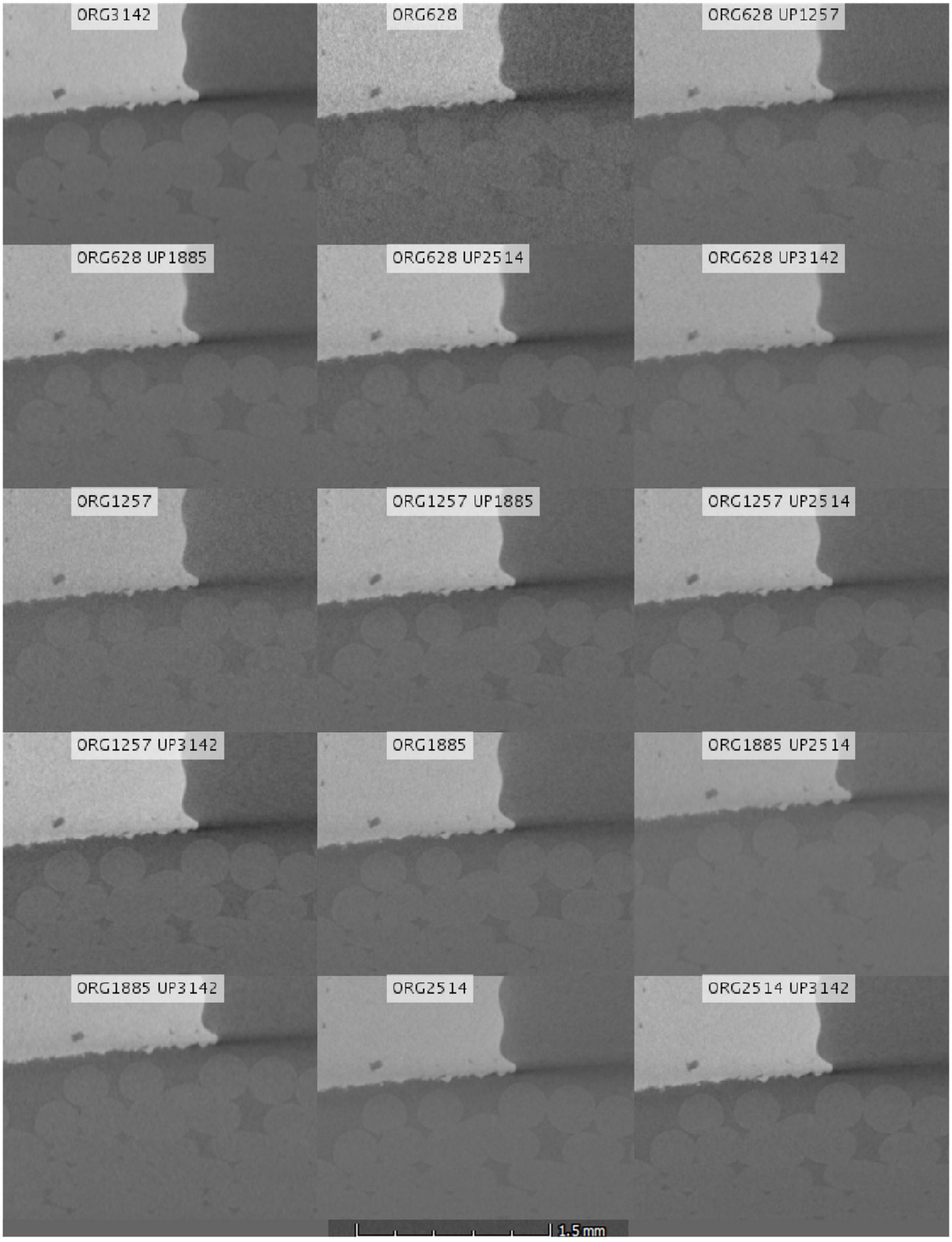

Figure 5-3 A collection of details of various reconstructed data sets. The location of detail is highlighted in Figure 5-2 c). The variation in noise between the different experimental conditions can be observed. All images had approximately the same grey scale distributions, by manual manipulation of the transfer function of VG Studio.

The results section is split into four subsections each discussing one of the following themes: noise, resolution, areal texture parameters, and comparison via statistical topography models. The interpolation of ORG628 UP3142 needed around 12 min using non-complied code on an Intel Xeon E5 processor.

For a qualitative inspection, a sample slice of the reconstructed volume is shown in Figure 5-3. Here several pores can be seen in the LPBF sample, with the most prominent in the lower-left corner of the sample. The low contrast of the sample holder material can be seen in all images in the bottom half of the image. However the recognisability and the visual inspection of the sample holder material is limited for faster acquisition such as ORG628 and ORG1257, however upsampling restores the responsibility to some degree.

Statistical topography models

Figure 5-4 and Figure 5-5 show the statistical topography models obtained for the different experimental conditions. A qualitative inspection of the presented statistical topography models also allows for observation: the amount of measurement noise and undesirable high spatial frequency components are reduced when increasing the number of projections from which the interpolation starts. This can be understood by observing the spikes in the green surfaces, which are the upper bounds of the local confidence intervals computed on triplicate data points. Each spike corresponds to a local confidence interval larger than the neighbouring ones, indicating a larger spread of the data points at the same location. One such spike that is shown in all experimental conditions is highlighted in Figure 5-6.

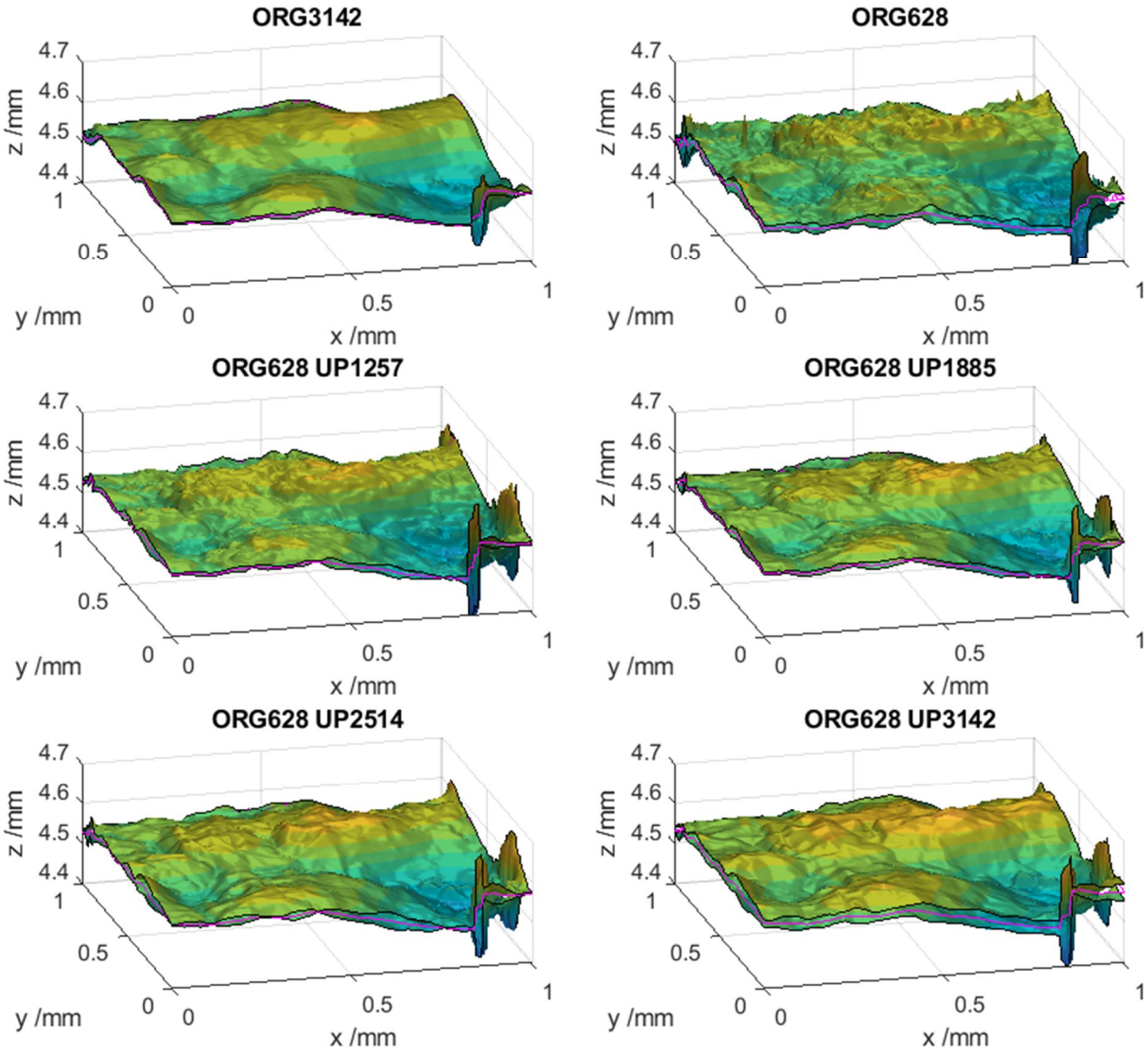

Figure 5-4 Statistical topography models from the repeated measurements (triplicates) for each experimental condition. Six experimental conditions are reported. For each: the top, colour surface is the upper limit of the local confidence interval of the mean and the lower surface the lower bound. The upper bound is highlighted by a black line at the sides of the region considered. The magenta surface, also visible at the sides, is the mean topography.

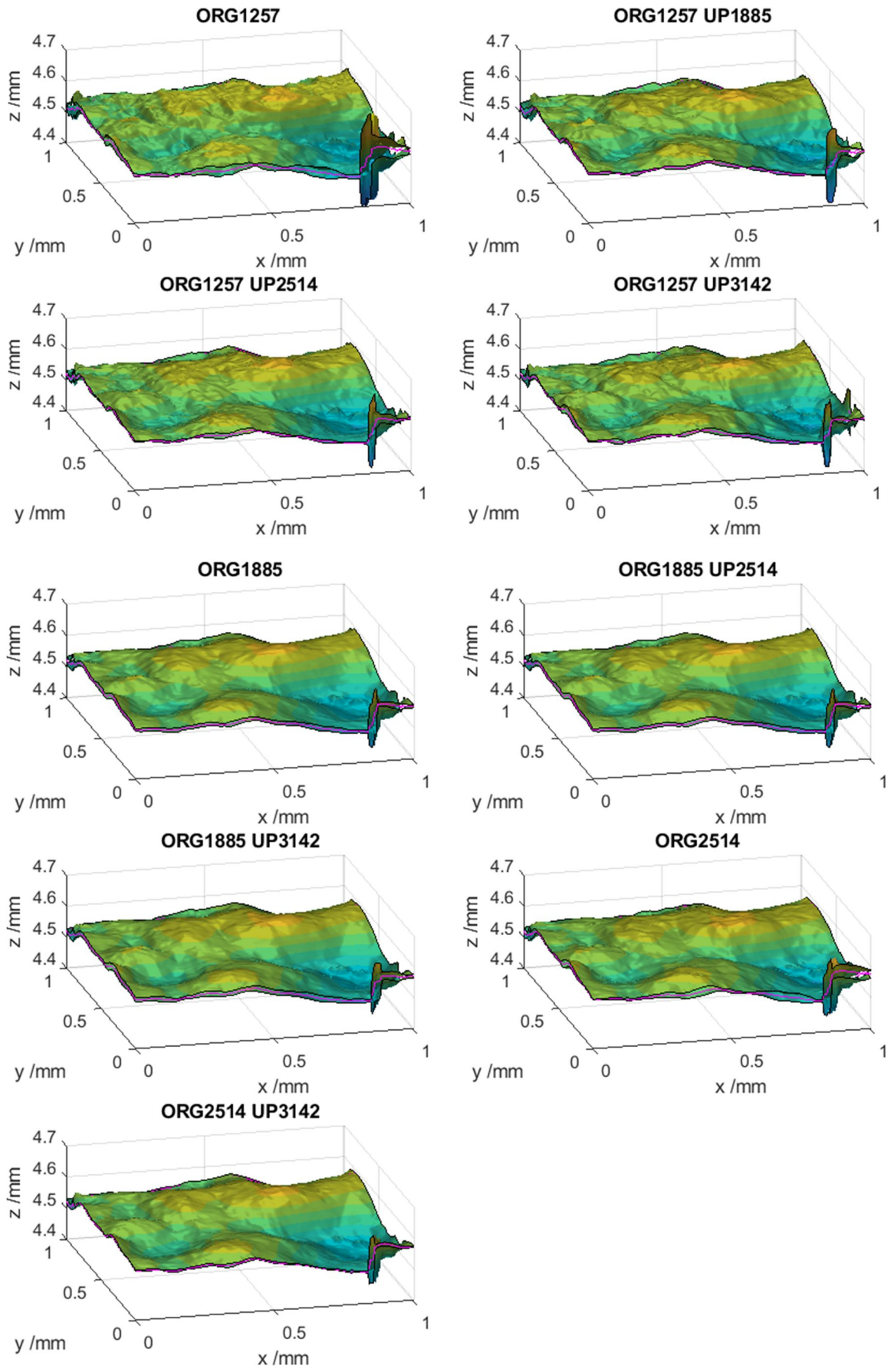

Figure 5-5 The remaining statistical topography models of experimental conditions which were not reported in Figure 5-4.

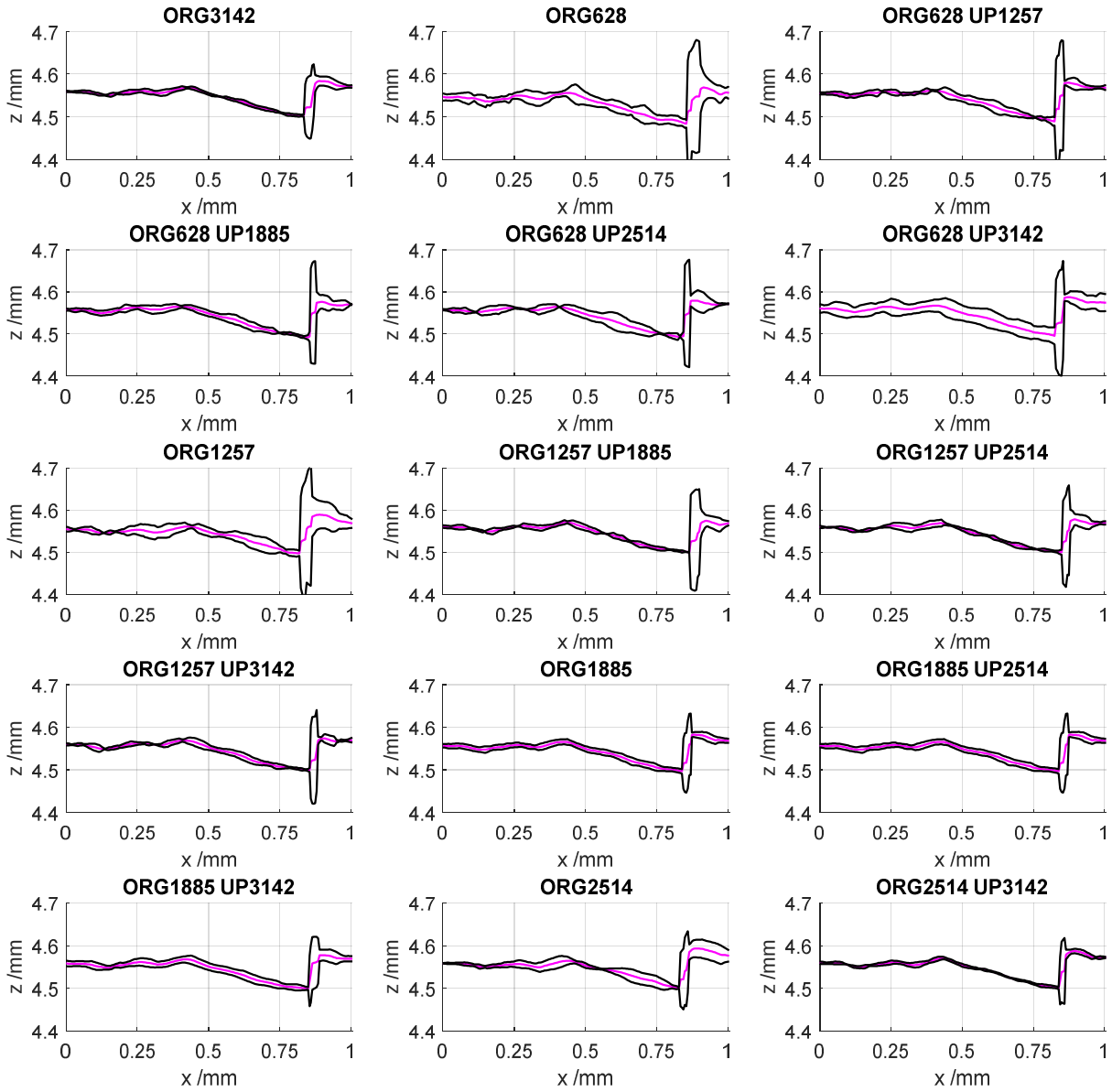

Figure 5-6 Details highlighting a feature of large CI width at roughly $x = 0.85$ mm. This area of large CI width is found across all experimental conditions. The black lines represent the CI, and the magenta line the mean line. The presented data is located at $y = 0$ mm in the plots shown in Figure 5-4 and Figure 5-5.

Noise in the reconstructed volume

The histograms of the voxel intensities of two scans are shown in Figure 5-7. Qualitatively inspecting the two histograms of Figure 5-7, the contrast, i.e. the separation in the greyscale between the reference value of material and background, of both distributions coincide well as expected. Comparing the two histograms, the histogram of only 628 projections shows a wider and flatter shape of the material and background peaks, which is generally attributed to noisier datasets.

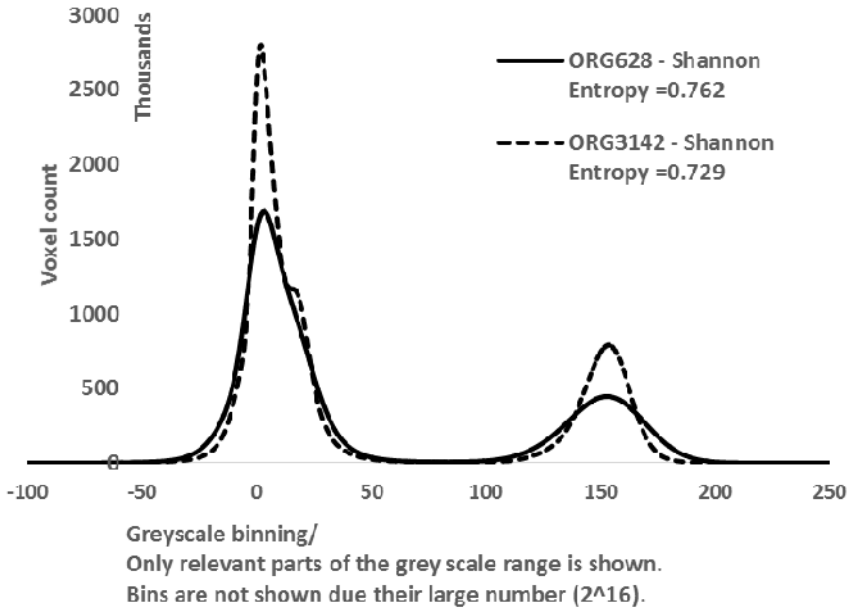

Figure 5-7 Histograms of the reconstructed volume data of two exemplary experimental conditions.

The Shannon entropy was computed and is shown in Figure 5-8. The data sets of the third repeat of ORG1885 and its interpolated variants show outlier behaviour, hence they were excluded from further processing. Due to operational reasons, the system had to be shut down before the last set of repeats could be acquired. The sample was not moved and an additional warmup scan of over two hours was added before commencing the remaining scans. The first scan after the second warmup was the final repeat of ORG1885, thus it is considered an outlier.

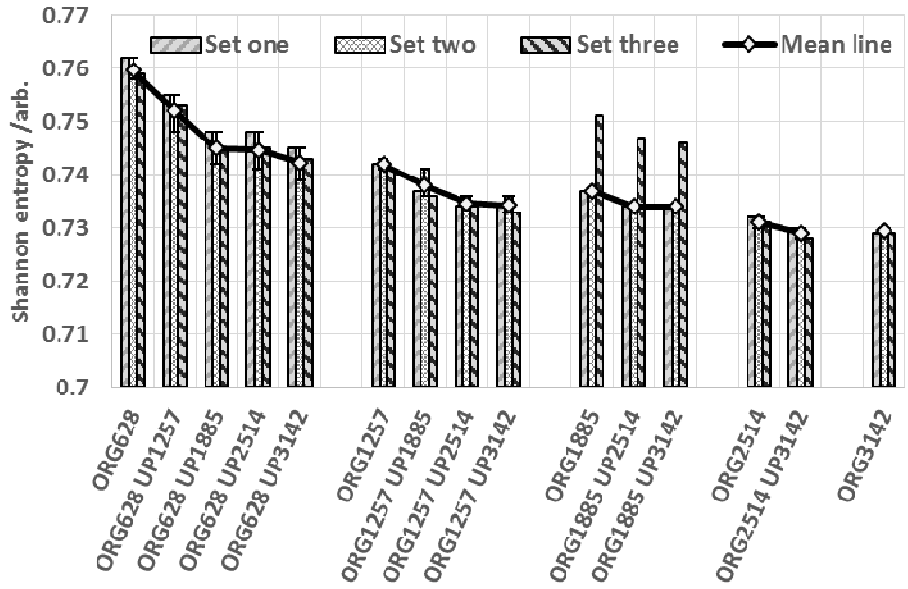

Figure 5-8 Shannon entropy values for the experimental conditions (mean and range from three repeats). The experiments are ordered by the total number of projections used in the reconstruction.

The repeatability between Shannon entropy values for the different repeats of each experimental condition was high, with a maximum difference limited to less than 1% of the Shannon entropy value. Despite reducing the Shannon entropy, sinogram interpolation does not reach the same low level of noise achievable by acquiring the actual number of projections without interpolation. Also, while the error bars provide some indication of the spread of the entropy results, clearly a higher number of repeats would be beneficial for improving confidence.

Figure 5-8 shows a strong trend of decreasing noise with increasing amounts of interpolation, as measured by the Shannon entropy. The noise in the ORG datasets is expected to change dramatically as the number of photons recorded is different. In fact, if one were to think of the number of photons per voxel, a common helpful quantity when comparing scans, the ORG628 will obviously only equate to 20% of the energy recorded by the detector, which is a significant reduction. For example, the large degree of noise in ORG628 was significantly reduced by interpolation, even by upsampling to only 1257 projections. In all cases, the upsampling of each originally undersampled set of projections led to reduced noise. When comparing all the experimental conditions, the ORG3142 and the ORG2514 UP3142 sets were the ones which showed the best results. Excluding the

outlier represented by the third ORG1885 set, the low repeatability error of the Shannon entropy results also supported the significance of the results. As can be seen in Figure 5-8, ORG1257 UP3142 achieved similar noise behaviour to the upsampled versions of ORG1885 series. However, the best noise behaviour is achieved when acquiring a full set of projections, closely followed by ORG2514 UP3142.

Resolution in the reconstructed volume

The values shown in Figure 5-9 are the mean values of the resolution, obtained as described in chapter 4 on the location highlighted in Figure 5-2, for the three repeats of each experimental condition and ten edge spread computations per repeat. This yields thirty edge spread measurements per experimental condition, and the error bars are the maximum range of the thirty repeats.

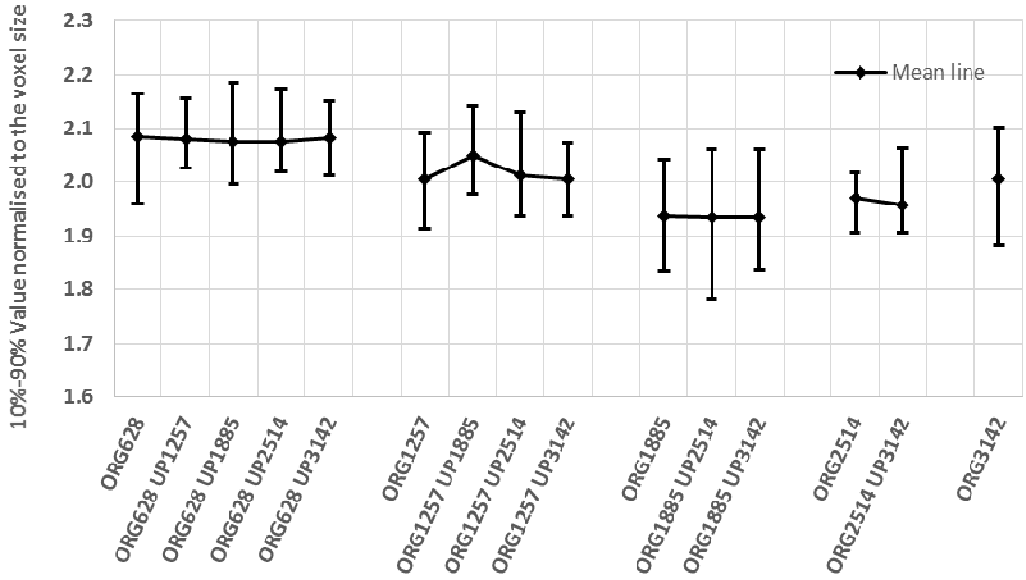

Figure 5-9 Mean values of the resolution estimate via edge spread determination. The error bars show the spread from thirty repeats, which are ten edge spread computations per each reconstructed data set.

The range of the obtained resolution values is large, across all experimental condition. All upsampled versions of ORG1885 showed lower resolution values than ORG3142, but within the margins of the error bars. Also the range of the error bars of all experimental conditions is large, even of the ORG3142 condition. As such the conclusion of the results on resolution

are directly limited. The magnitude of nearly all error bars, including the ORG3142, is approximately 0.2 of the voxel size. Therefore the experimental conclusions below one fifth of the voxel size cannot be drawn. The ORG1885 was also the test sample which showed outlier behaviour in the Shannon entropy. While it is expected that a large angle during the continuous motion will worsen the resolution, no trends are particularly prominent in the collected data.

The measurement procedure adopted to estimate the resolution of the different scans is based on the assessment of edge spread. The author is aware that this method does not represent the entire measurement chain, but is limited to the analysis of a single slice of the reconstructed volume. However, at least it can be noted that pixel intensities are the usual input to the surface determination stage. The conclusions that can be drawn from these results are difficult to summarise, due to the large error bars which yield no experimental condition showing any significant difference in resolution. The error bars were chosen conservatively as the maximum spread, rather than the standard deviation. The experimental campaign should be expanded with further experimentation on how the edge spread method of measuring resolution is affected or even confounded by noisy data such as exploring alternative methods [80,93,94,208,209]. Despite the issue of not having detected significant variations of resolution, one can at least conclude that resolution does not degrade to an extent that can be adequately captured with the adopted edge spread method. However, the author believes that the extent of resolution degradation should be worse, at least based on the findings of the medical literature [139,159]. The discrepancy could be due to the different nature of the sinogram space of a multi-material object, such as when scanning a human body, compared to the single-material object presented in this work, but more detailed experimental and analytical work on how the interpolation propagates into the reconstructed volume is needed. In summary, not much confidence is given to the resolution measures obtained within this study. In the wider scope of comparing measurement setups of XCT, a reliable and sensitive method of expressing the achieved resolution is needed. Initially, it was the author’s intention to use the obtained heightmap data to calculate the spatial frequency content of the measured topographies,

in particular focusing on the high-frequency content as a means to obtain a quantitative assessment of the capability of capturing small-scale topographic detail. However, the presence of noise rendered this approach impractical. While not within the scope of this work, it is anticipated that similar problems will occur when using frequency-based resolution test-artefacts, such as in [93]. Furthermore, given the angular motion, it could be expected that the resolution will vary depending on the radius around the centre of rotation. The design of the fixture for the part assured that the investigated surface topography and the flat side used for investigation into the resolution are approximately at the same radial distance from the axis of revolution (see Figure 5-2), which was placed close to the edge of the reconstruction volume. As such it can be argued that the observed resolution changes will be, from the geometrically assumption, largest observable.

Discrepancy and repeatability error of the extracted surface topography

In addition to the already discussed visual inspection of the results shown in Figure 5-4 and Figure 5-5, statistical topography models allowed for quantitative comparison between experimental conditions. Figure 5-10 shows both the discrepancy ratio and the mean confidence interval height of each experimental condition. The results of the discrepancy ratio are zero for any experimental condition after ORG1885 in Figure 5-10 and zero for ORG3142 by design.

Figure 5-10 shows the discrepancy ratio of each experimental condition with respect to the ORG3142 condition (taken as reference) and the mean width of the confidence interval calculated for each experimental condition aligned to ORG3142. The resultant mean confidence interval width is of the order of tens of micrometres. One interesting feature has been identified for ORG628 UP2514 and ORG628 UP3142.

Here, the discrepancy ratio to ORG3142 is reduced, while the mean width is increased. This can be explained as the discrepancy ratio will reduce if the confidence interval is large – as there is more chance for overlap. The cause of the increase of the confidence interval can possibly be attributed to a loss of resolution. Both ORG628 UP2514 and ORG628 UP3142 have the largest upsampling ratios, which is four and five respectively. This might indicate that too much upsampling has occurred and might affect the quality of the obtained surface topography data.

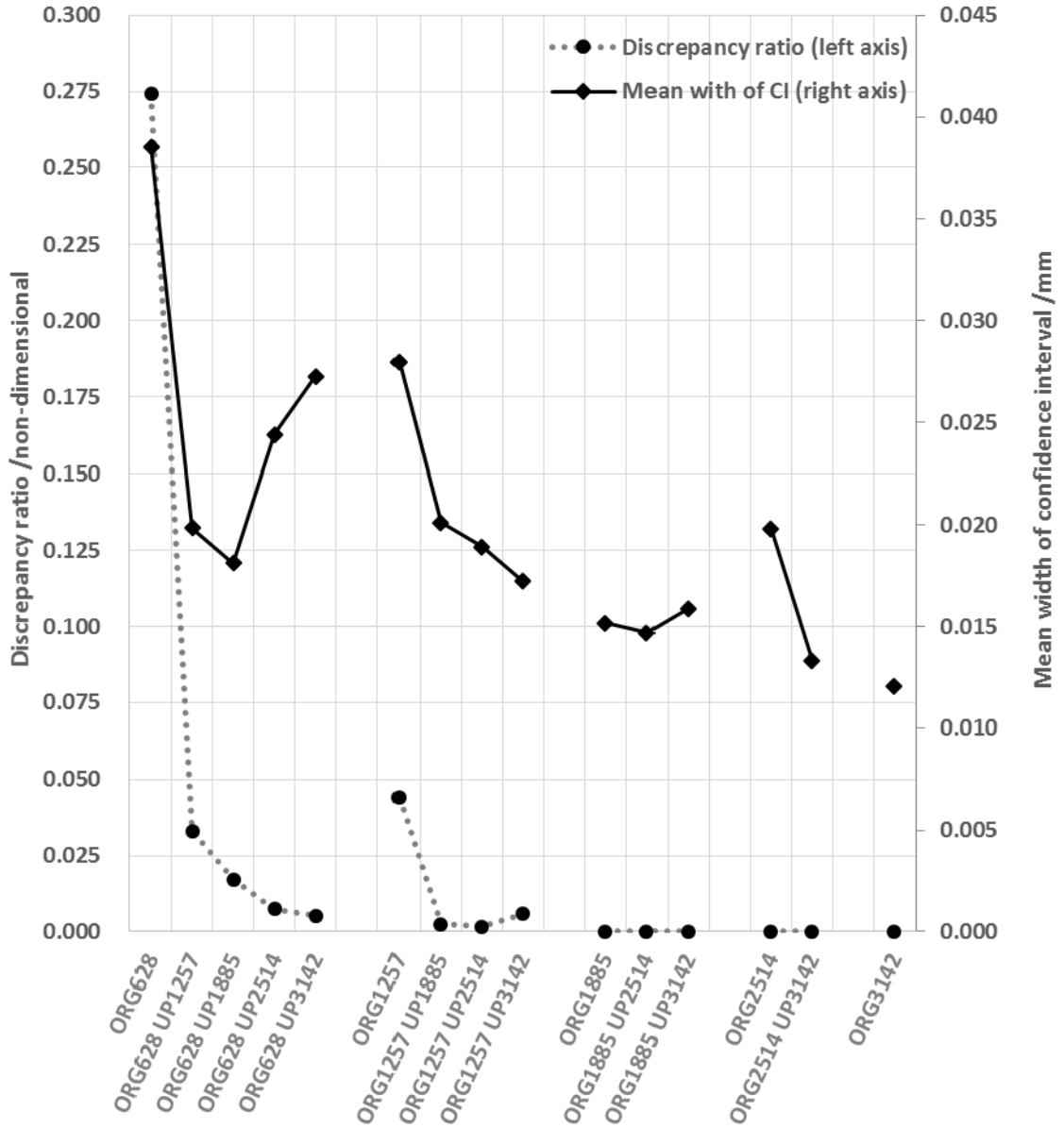

Figure 5-10 Discrepancy ratio between each experimental condition and ORG3142. The second axis to the right of the panel shows the mean width of the confidence intervals.

Following Figure 5-10, the discrepancy ratio drops to zero, for all cases which are based on 1885 real projections or more – while maintaining mean confidence interval widths of around ten to twenty micrometres. This finding may indicate that a reduced number of projections is feasible. The discrepancy ratio of ORG628 is as expected largest, but subsequent sinogram interpolation reduced this ratio, this might be due to the increasing mean CI width. However, the effects of interpolation are not dramatic for the cases which are based on more than 1885 projections. While ORG1257 has large mean confidence interval width, and a large discrepancy ratio, a substantial improvement can be seen when increasing the number of projections used in reconstruction to 1885. However, the case of ORG1257 UP3142 shows an increase in the discrepancy ratio compared to ORG1257 UP2514. Most experimental test conditions do not reach the same confidence interval mean width levels as ORG3142. Overall, the interpolation in ORG1257 seems to be promising, however, it would be interesting to explore the loss of resolution in more detail, and compare the interpolation against other filtering methods on the volume data. This point is investigated in the next section 5.3.

Areal texture parameter comparison

The results for the areal surface texture parameters Sa and Sz [210,211] are shown in Figure 5-11 a) and b) respectively. The mean values of the parameters over three replicates are reported, together with error bars representing the min-max range. Notice that Sa was chosen as an indicator of the average spread of surface height values about a mean reference; being an average value, it is less sensitive and changes in the observed Sa might indicate significant changes to the measured topography. On the contrary, Sz was chosen as an indicator of the min-max range of height values, so it should be considered more sensitive to extreme values. Once a reconstruction uses more than 628 projections (interpolated or real), all computed Sa values are within 0.6 µm, and once more than 1257 projections are used in the reconstruction this range drops to 0.3 µm. These findings can be interpreted, that the changes of the surface topographies from

undersampling and sinogram interpolation only minimally effect the Sa, and thus – within the limitations of the averaging Sa parameter itself – the changes in obtained topographies are only small. When analysing the Sz results, the average values of the Sz are of similar magnitude for all experimental conditions. Given the sensitive nature of the Sz to outliers, it is interesting to see that the range of Sz of ORG628 is smallest. However this small range of ORG28 is most reasonably driven by ORG628 repeatedly having the most noise induced outliers. The mean values of all Sz are roughly within 20 µm of each other, and the ranges of most experimental conditions is around twice the voxel size.

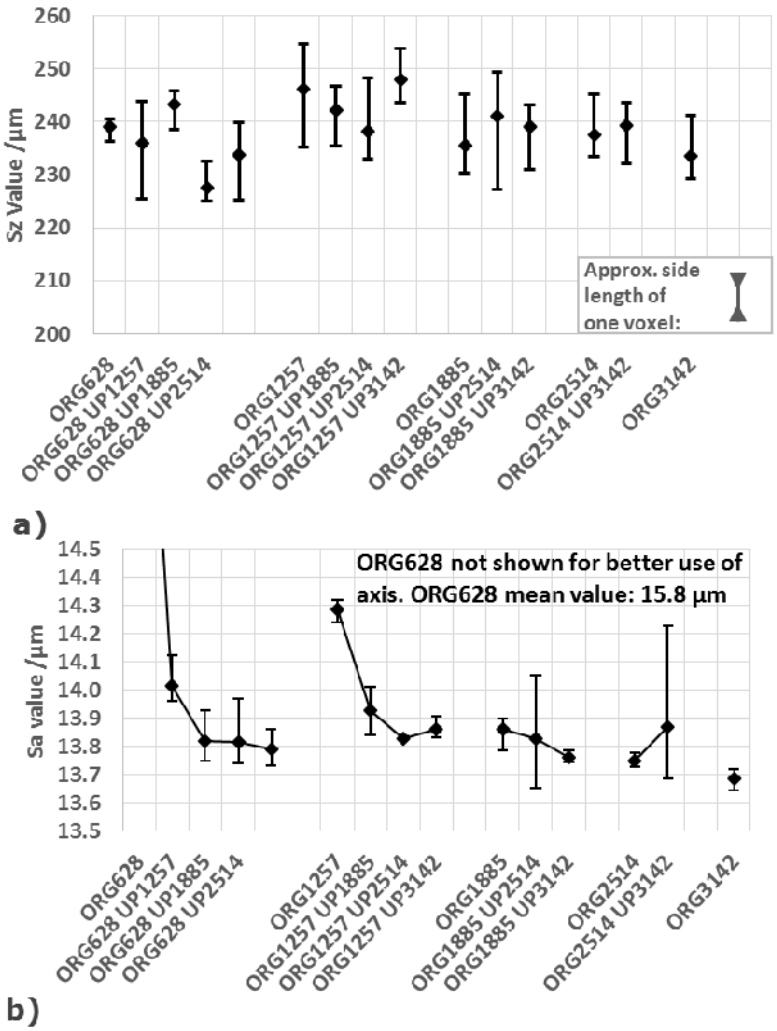

Figure 5-11 a) mean Sa value and its min-max range over three replicates; b) mean Sz value and its min-max range over three replicates. For a) and b) the error bars show the maximum range of the data.

5.2.5 Discussion

XCT measurements can be relatively slow and a method to decrease acquisition time has been explored in this section. The method is based on using a reduced number of projections in combination with sinogram interpolation. The presented work is a case study to showcase the effects of sinogram interpolation at various degrees of undersampling and thus only one test sample was investigated. While the test sample was chosen as a typical application. The sample is of similar size and shape compared to the other work undertaken of studying metal PBF surface in XCT [2,10,62]. Since this work did not focus establishing traceability in XCT and all analyses were done in relation to a reference setup ORG3142, the need for a traceable test sample was not given for this work. Sinogram is a heuristic method with no direct analytical foundations, and sinogram interpolation manipulates the directly the sinogram data which in return depends on the geometry and material. Hence, there is only limited scope to obtain a justified and realistic quantitative generalised statement on the performance of sinogram interpolation. Only three repeats were performed per experimental set-up, and the data obtained from one repeat is visibly worse than the other two. This means that within the context of drawing a conclusion of the presented data, the statistical validity and confidence is limited. This is a common issue in XCT metrology where, somewhat ironically, repeated measurement is rarely used due to lengthy measurement times. In fact, due the large number of experimental conditions, the realistic filament life time of the XCT system used directly limits the chance of more repeats without changing the filament in between. As a result, the experimental campaign included three repeats, without moving the sample. But no investigation was undertaken into the reproducibility of these experimental findings. Due to operational reasons, the system shut down before the last set of repeats was acquired. While the sample was not moved and an additional warmup scan of over two hours was added before commencing the remaining scans. The first scan after the second warmup was the final repeat of ORG1885, thus it is considered an outlier. Due to the difficulty of operating an XCT system continuously over so many hours more repeats are not realistic. A possible future research question could be asses if similar outliers would be observed in acquired

data during a reproducibility study. Thus the assessing reproducibility of XCT in general, would be another potential future research question.

So, which experimental condition could be recommended to increase the throughput rate for the investigated scenario? All data derived from ORG628 should be immediately excluded as they showed on average a much worse performance in terms of noise, and even more importantly they showed a significant difference from the reference measurement in terms of the discrepancy ratio.

Both ORG1885 UP2514 and ORG1257 UP2514 do not perform worse than their respective counterparts which used 3142 in the reconstruction, in terms of noise. ORG2514 and its upsampled partner only decreased the measurement time by approximately 20%, while slightly outperforming the ORG1257 UP 2514 and ORG1885 UP 2514 in terms of Shannon entropy. The most important findings though are shown in graphs on the numerical topography comparison in Figure 5-10. The topography comparison showed that the ORG1885 UP2514 achieved similar results to the ORG3142 in terms of the mean width of the confidence interval and has a zero discrepancy ratio. However, ORG1257 UP2514 does have a larger mean width of the confidence interval and does have good levels of discrepancy ratio, but reduced the measurement time by 60%. While the overall recommendation depends on how much of the fidelity and speed is needed, both the ORG1885 UP2514 and ORG1257 UP2154 cases are promising candidates.

This section mapped out the performance of sinogram interpolation to reduce the number of acquired projections in an XCT measurement of a PBF surfaces. The different experimental conditions were compared and characterised in terms of noise, resolution and a direct comparison of the obtained surface topographies. Sinogram interpolation was applied to data sets which were undersampled by 20%, 40%, 60% and 80% of the analytically required number of projections. The XCT system was set up to rotate continuously during acquisition to keep the time associated with each radiograph low. An additively manufactured test cube was used as a test sample. The method for assessing

resolution showed limits when capturing the resolution changes between the various configuration setups. The noise was found to worsen with increased undersampling (decreased number of projections) but it could be reduced by sinogram interpolation. The topography comparison showed that sinogram interpolated versions of the cases which used 40% and 60% of the required radiographs, had a strong potential of delivering the information needed, while also reducing the acquisition time significantly. However, the limitations of these findings should be considered carefully as the extrapolation is limited due to the feature size as a function of voxel size, the use of only a single material case and the statistical limitations of having only three repeats. Overall, the findings here show that there is a potential for decreasing the acquisition time of topography measurement – as long as the user is aware of the additional limitations added by reducing the number of projections and introducing interpolation.

5.3 Comparative work: Sinogram interpolation in comparison to the performance of median filtering and binning methods

The objective of this section is to investigate and compare detector pixel binning and median filtering against sinogram interpolation and to examine the effects of continuous and stationary acquisition motion for limited projection scans. Binning is known to allow for increased acquisition speeds, due to increased apparent pixel size and median filtering is a non-linear filtering operation which is frequently used to suppress noise in industrial XCT scans [80]. The quality of the volumetric reconstruction is assessed through measures of noise and resolution. The quality of the surface topography extracted from the volumetric reconstruction is in turn assessed via the computation of statistical topography models designed to quantify local dispersion of height values in repeated measurements, and the discrepancy between reconstructions obtained with different methods.

5.3.1 Experimental campaign

As part of this investigation, the number of projections was reduced from the ideal reference of 3142, in steps of 0.2, to 2514, 1885, 1257 and 628 projections. One

experimental condition was acquired using a 2 × 2 binning of the detector pixels. In binning the detector pixels are summed together to increase the apparent size. For some experimental conditions, the reconstructed volume data was filtered using a median filter. A median filter is a non-linear filtering operation, where, in the spatial domain, a kernel of size three by three by three voxels is run across the volume. For each voxel the kernel centres on, the central value of the kernel is replaced by the median value of all voxels covered by the kernel. A naming convention was introduced such that ORG628 describes a scan that used 628 real projections in the reconstruction, ORG628 UP3142, used 3142 projections which are interpolated from 628 real projections, which were acquired using continuous motion mode. ORG628 STAT describes a reconstruction, which was acquired under stationary acquisition. ORG628 FILT used 628 real continuously acquired projections, but the reconstructed volume was filtered using the median filter, see Table 2 for the full breakdown of the naming convention. Each experimental condition was repeated three times.

Table 2 Overview of experimental conditions highlighting the naming convention

Original experimental data							
3142 projections (continuous only)	Binned acquisition (continuous only)	1257 projections		628 projections			
		continuous	stationary	continuous	stationary		
ORG3142	Binned data	ORG1257	ORG1257 STAT	ORG628	ORG628 STAT	No data manipulation	
		ORG1257 UP1885	ORG1257 UP1885 STAT	ORG628 UP1885	ORG628 UP1885 STAT	Sinogram interpolation to: 1885	
		ORG1257 UP3142	ORG1257 UP3142 STAT	ORG628 UP3142	ORG628 UP3142 STAT	3142	
		ORG1257 FILT		ORG628 FILT		Median filtering	

5.3.2 XCT setup and data processing parameters

As in the previous section, the Whittaker–Shannon interpolation formula was used for the sinogram interpolation. The data was collected under the same conditions as the previous section, and in the same experimental session as the previous section. The binned data was acquired with continuous motion at the same magnification. The exposure time was adjusted to 0.5 s, the gun current was set to 78 µA and 1571 projections were acquired. The median filter was set up with a kernel size of 3, which was performed as a post-reconstruction filter in Nikon's CT PRO software. The remaining parameters and settings are as stated in 5.2.3.

5.3.3 Results

Figure 5-12 & Figure 5-13 shows the sample used in this investigation, as well as detail images from slices of the reconstructed volume data for different experimental conditions. The stationary acquisition, ORG628 STAT took 44 minutes, ORG628 required 42 minutes of exposure, ORG1257 84 minutes, ORG1257 STAT 89 minutes, and ORG3142 209 minutes. The binned data acquisitions were fastest and only required 13 minutes. Qualitative inspection of the volumes highlighted some aliasing artefacts, of which a detail is shown in Figure 5-14. On a visual inspection only, different noise behaviour and smearing of the edges is observable of the different experimental conditions. The recognisability of the polymer fixture the sample rests on is impaired for the stationary acquisitions. This recognisability of this feature is limited on the binned acquisition in Figure 5-13 too due to lower resolution.

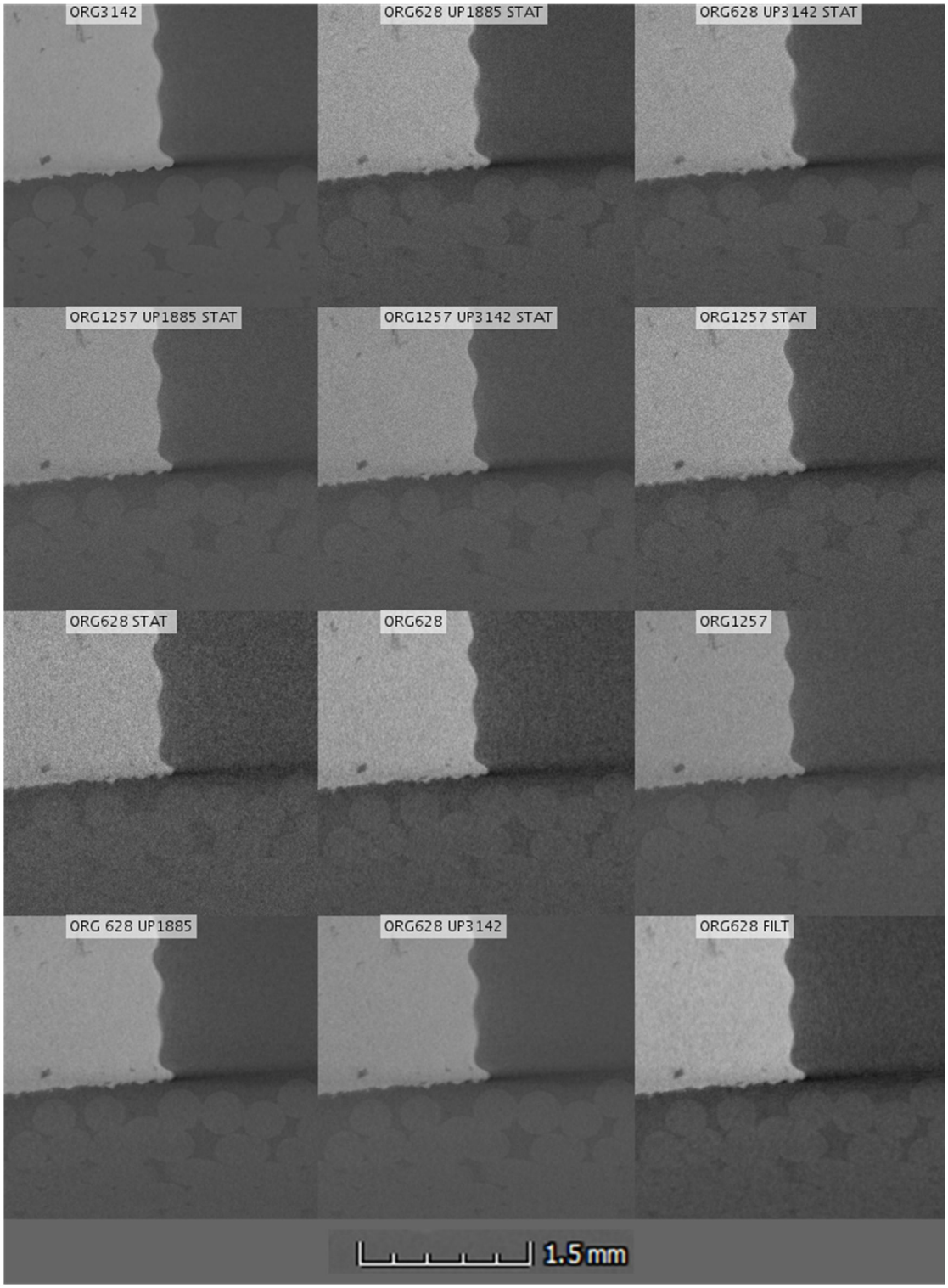

Figure 5-12 A collection of details of various reconstructed data sets.

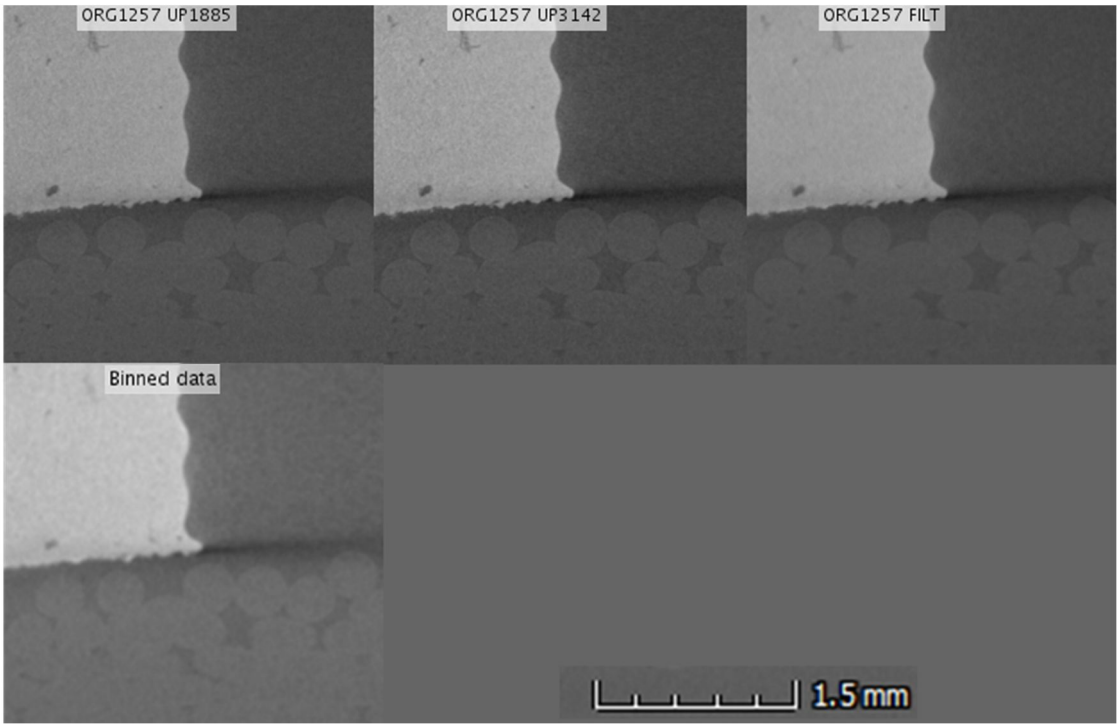

Figure 5-13 Remaining details of various reconstructed data sets.

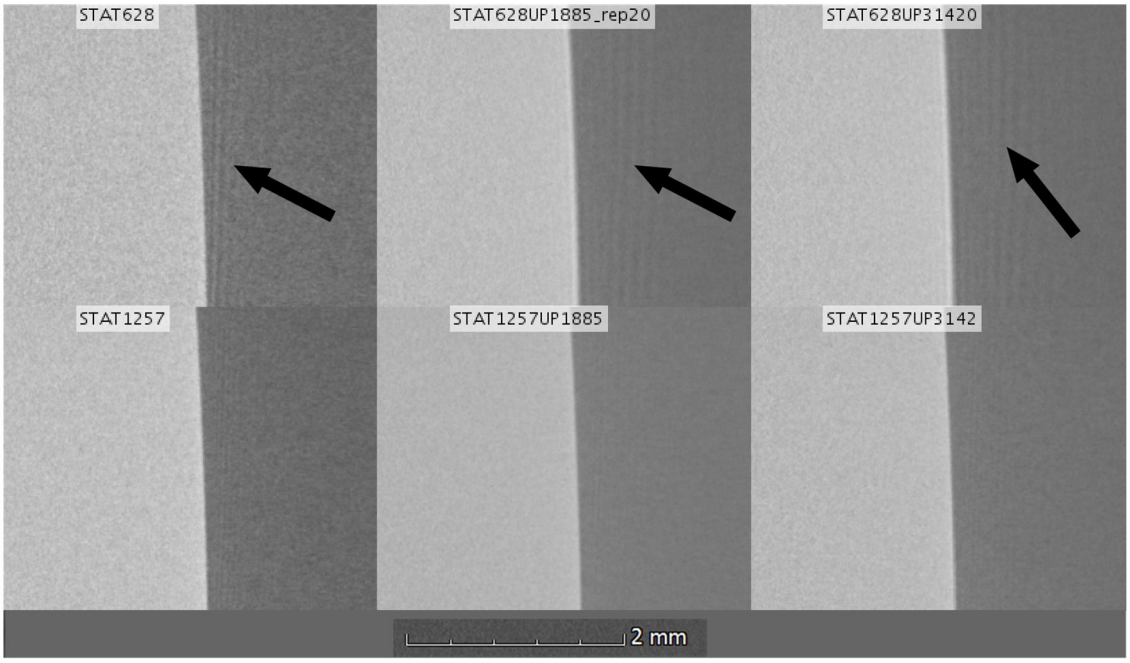

Figure 5-14 Detail images highlighting aliasing artefacts.

Statistical topography models

Details covering an area of (1 × 1) mm of the calculated CIs are reported in Figure 5-15 & Figure 5-16, which correspond to the same physical area of the sample as shown in the previous section. The statistical surface topography models of the stationary acquisitions are erratic and are of poor nature. The binned acquisition and the filtering operations show wide CIs. A detail graph of a profile line across the topographies is shown in Figure 5-17, it the highlights the erratic and inconsistent nature of the performance of the stationary acquisitions.

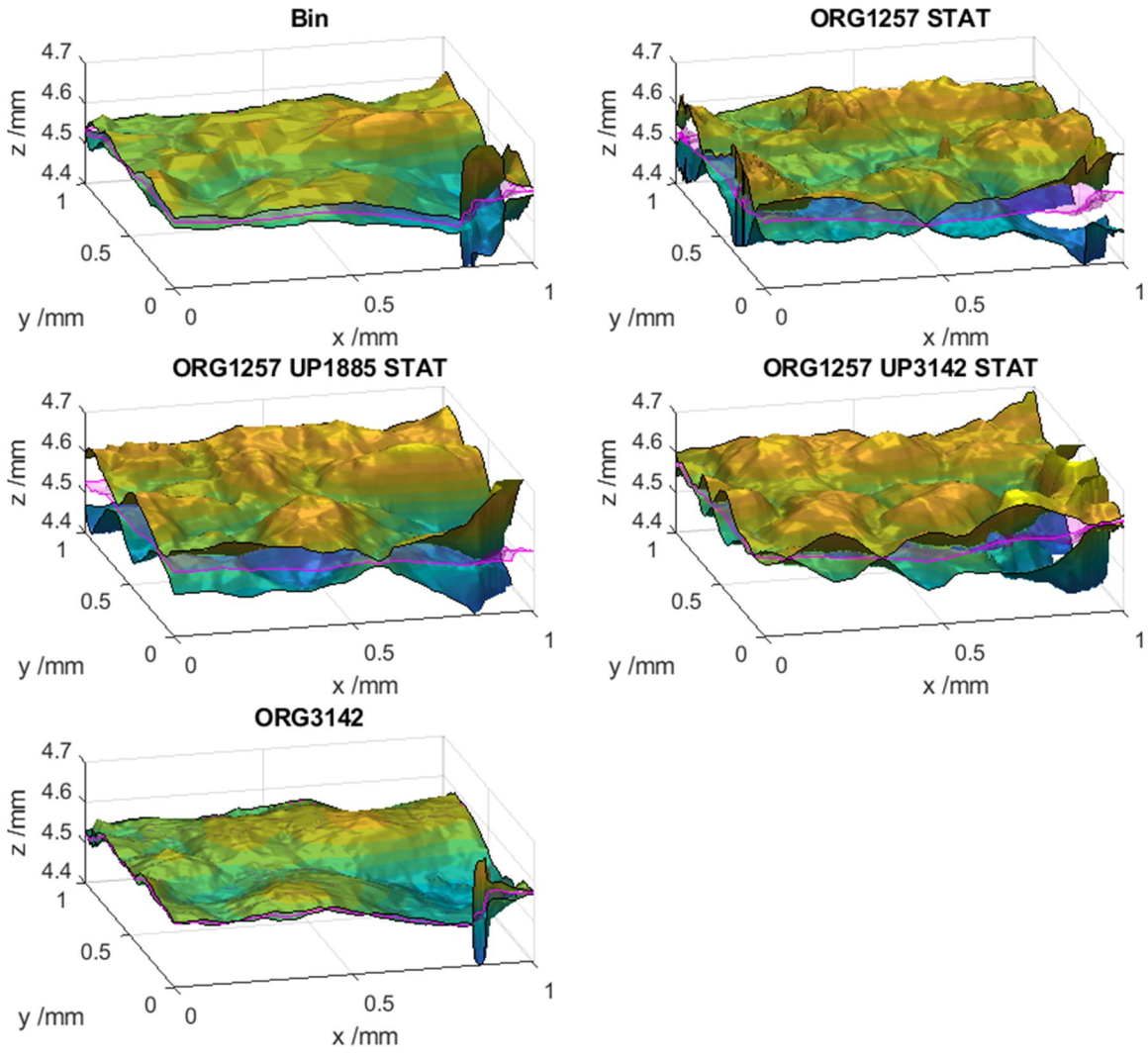

Figure 5-15 Statistical topography models from the repeated measurements (triplicates) for each experimental condition. The details correspond to the same physical region as shown in Figure 5-4 and Figure 5-5.

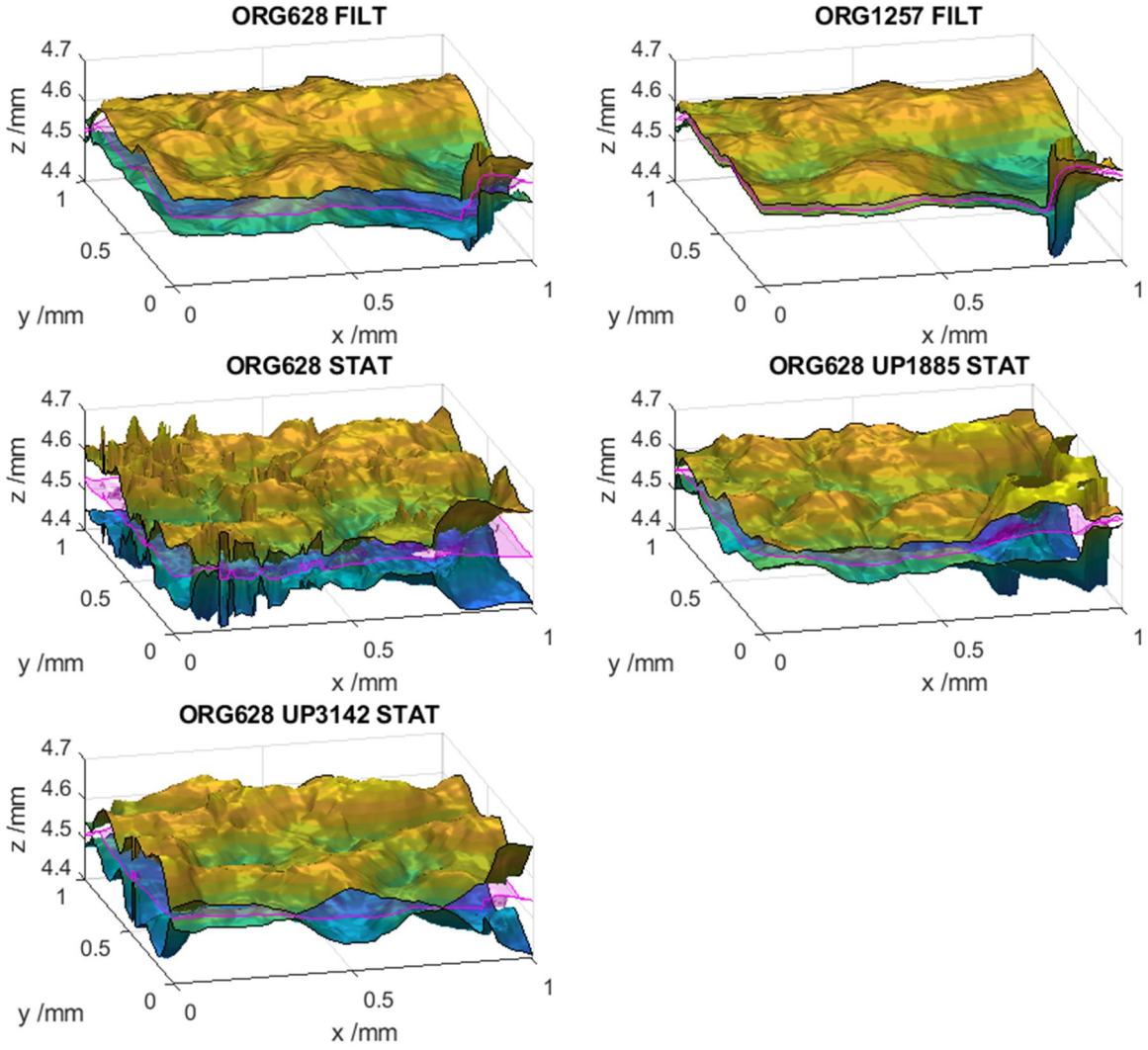

Figure 5-16 Statistical topography models from the repeated measurements (triplicates) for each experimental condition. The details correspond to the physical same region as shown in Figure 5-4, Figure 5-5 and Figure 5-15.

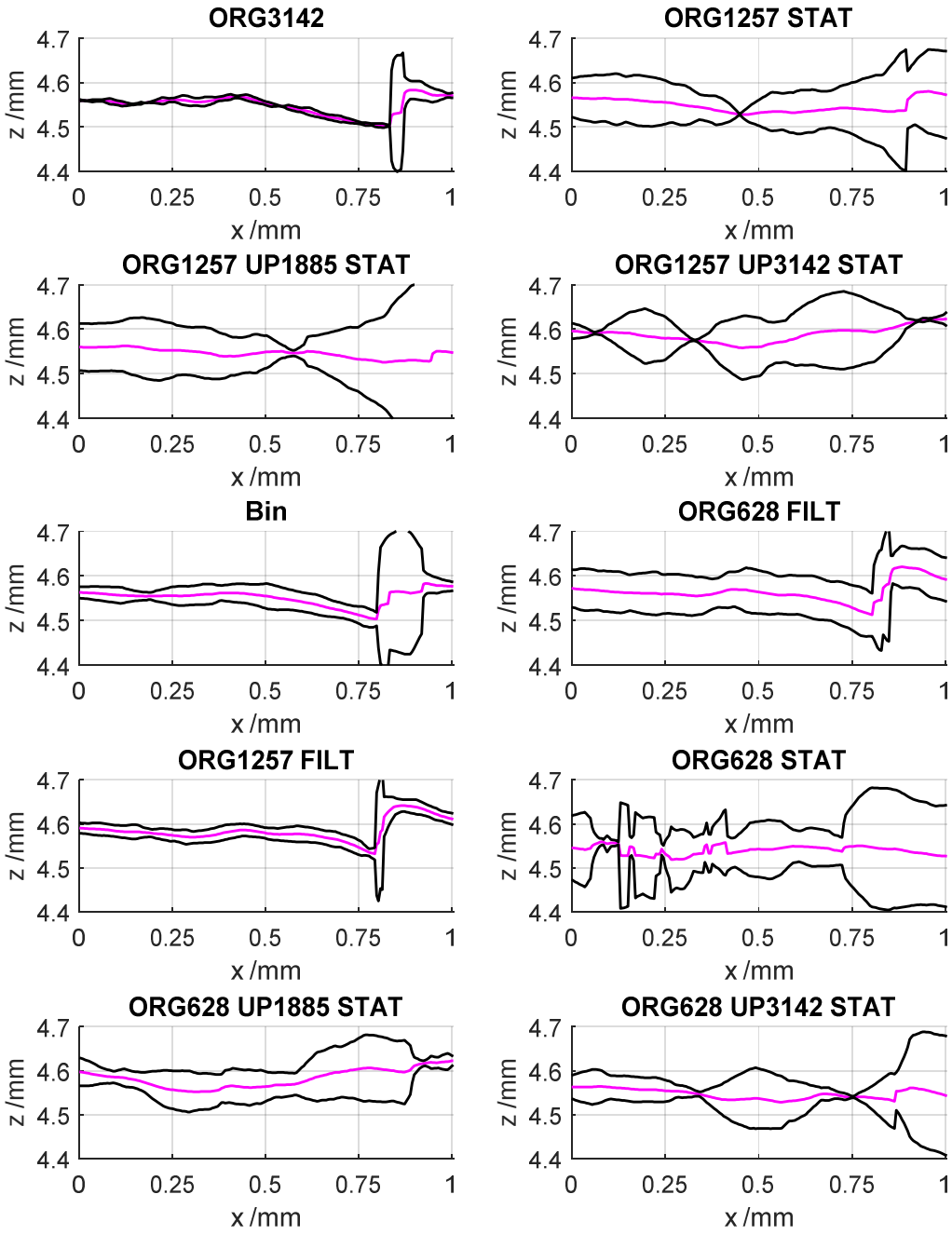

Figure 5-17 Details highlighting a feature of large CI width at roughly x=0.85 mm. The stationary acquisitions compare worse than the filtered continuous motion acquisitions. The black lines represent the CI, and the magenta line the mean line. The presented data is located at y=0 mm in the plots shown in Figure 5-15 and Figure 5-16.

Noise in the reconstructed volume

The Shannon entropies were computed for the exported histograms and reported in Figure 5-18. The mean of three repeats is reported for all experimental conditions. The first nine conditions reported in Figure 5-18 (counting from the left) pertain to acquisitions performed with continuous motion. The following six are in the stationary mode, whilst the last two (at the right side of the horizontal axis) pertain to acquisitions performed using pixel binning at the detector, whilst using all 3142 projections.

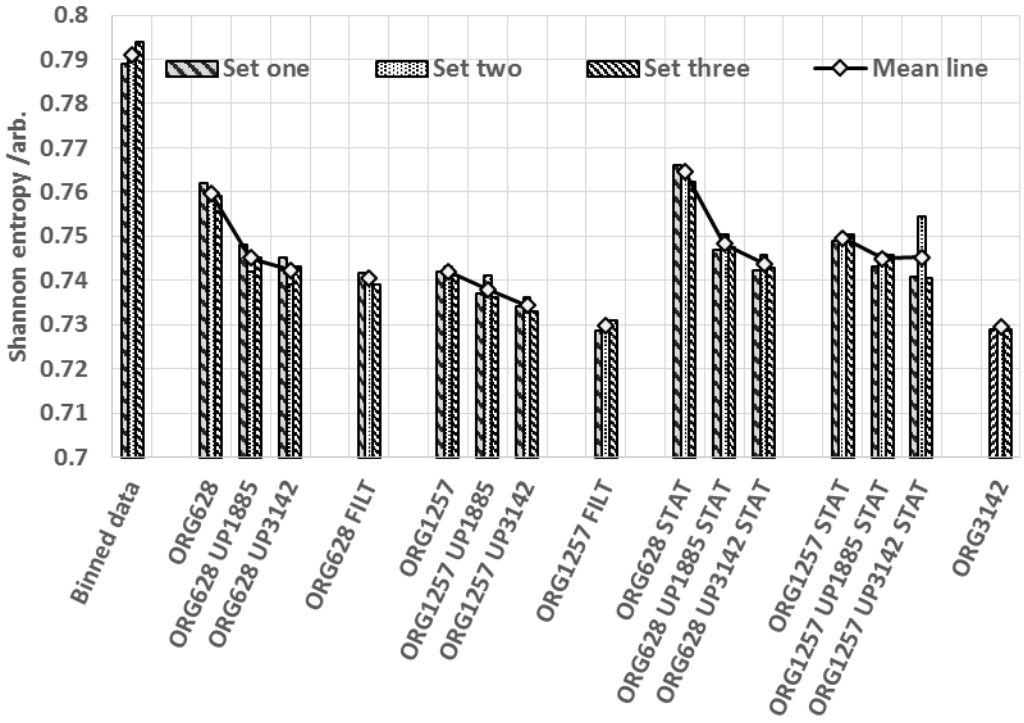

Figure 5-18 Shannon entropies of the investigated experimental cases.

The noise of the datasets using fewer radiographs is expected to change as the number of recorded photons is different, but undersampling the sinogram space can introduce streaks and artefacts. Overall, the expectation is that the noise in the volumetric reconstruction is reduced both by sinogram interpolation and median filtering. Median filtering showed a larger decrease in noise than sinogram interpolation. Concerning noise in the volumetric reconstruction as measured by Shannon entropy, unexpectedly, the largest value was obtained for the binned detector case. This is probably not because the volume is actually

noisier, but because of limitations intrinsic to how Shannon entropy is computed: the indicator is obtained from the frequency distribution of voxel values (histogram), and there are far fewer voxels in the binned case (one eighth of the unbinned cases), which is likely to affect the final calculated value.

Resolution in the reconstructed volume

Figure 5-19 shows the mean values obtained from the oversampled edge spread function evaluated over the three repeats of each experimental condition. As all data sets were acquired at the same magnification, the 10% to 90% value of the oversampled edge spread function was normalised to the nominal reconstructed voxel size, except for the case of the detector binning, where the edge spread function was normalised to half of the voxel to be comparable to the other data sets. The data is with limited significance if one considered the range bars. The stationary acquisition data sets perform worse than their continuous counterparts, and binning shows the worst mean 10%-90% resolution value.

Assessing the resolution by means of the edge spread function does not allow to evaluate resolution along the entire measurement chain and does not directly address the problem of assessing the resolution of the extracted surface. However, only a small number of methods has been presented in the literature about assessing resolution after the surface determination stage [208,212,213] and resolution in the volumetric dataset already provides some indication of what resolution will be in the final surface. When assessing the resolution in the volumetric dataset using the edge spread function, the reconstruction using detector binning showed the worst resolution out of all test cases, followed by the cases based on 628 projections (the least number of projections) as expected. Reconstructions based on at least 1885 projections resulted in similar resolution levels to the ORG3142 reference setup. These resolution results were only minimally affected by sinogram interpolation or median filtering, which is not in line with expectations or with results in the literature [139].

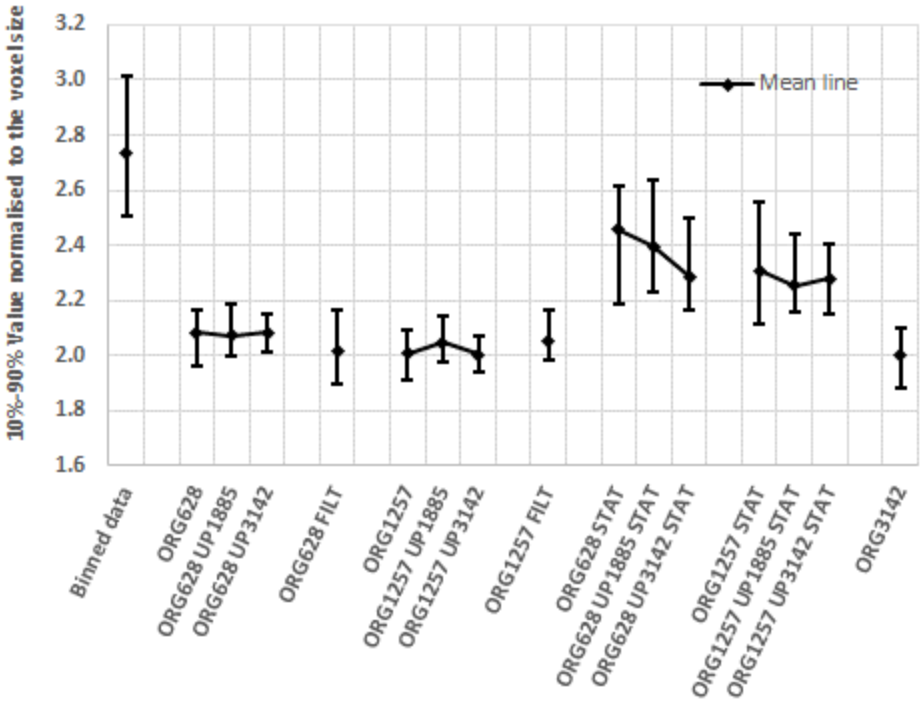

Figure 5-19 10%-90% value of the oversampled edge spread function for the different experimental conditions. Reported are the mean values of the resolution estimate. The error bars show the spread from thirty repeats, which are ten edge spread computations per each reconstructed data set.

Discrepancy and repeatability error of the extracted surface topography

The calculated discrepancy ratios and mean width of the CIs are reported in Figure 5-20, the figure shows both the mean width of the calculated CI, and the discrepancy ratio of each experimental condition compared to the reference configuration ORG3142. As illustrated previously, precision in repeatability conditions, represented by the mean width of the CIs obtained from the statistical topography models, and discrepancy ratio between setups, represented by the number of regions where the mean topographies of the statistical topography models are significantly different (i.e. the CIs do not intersect) were analysed for all the investigated experimental conditions and compared to the ORG3142 reference case. When comparing median filtering as a tool for suppressing undersampling noise against sinogram interpolation, only the case using 2514 projections and median filtering showed comparable values in precision and discrepancy ratio. For all other cases,

the mean width of the CI was largest (i.e. lower precision) for the cases involving median filtering. This indicates that for large undersampling, sinogram interpolation may be a better method for extracting surface topography data from highly undersampled XCT data. However, when looking at the effects of sinogram interpolation, the upsampled case of both ORG628 and ORG628 STAT showed an increase of mean CI width (decrease of

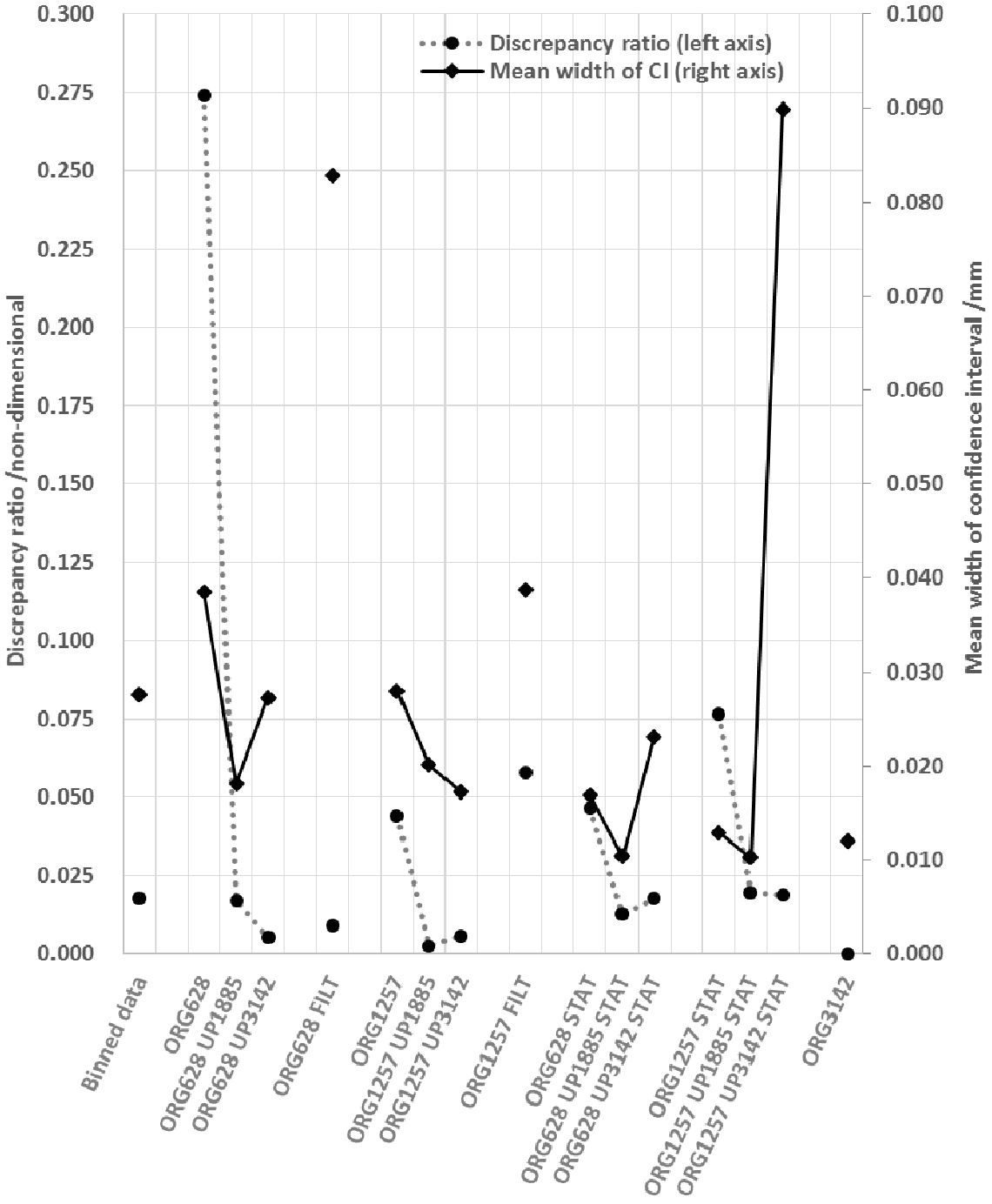

Figure 5-20 Discrepancy ratios and mean width of the CIs for the different experimental conditions.

precision) when upsampled to 3142 projections. This suggests that a larger degree of manipulation of projection data deteriorates the extracted topography data through decreasing its precision. In other words, with a larger degree of interpolation, more artificial projections are created from fewer real projections, and as such the projection data used in the reconstruction is more manipulated and negatively effects the precision of the extracted topography data.

Areal texture parameter comparison

Figure 5-21 reports both the calculated mean Sa values and the mean Sz values. The range of three repeats are represented by the error bars. The binned case showed the lowest Sa value, and differs to the Sa of ORG3142 with around the same magnitude as ORG628. For the continuous acquisitions, the Sa texture parameter is not affected greatly once more than 628 projections are used for the reconstruction, and even for the filtered reconstruction of 628 projections the Sa remains in 1 µm bracket compared to ORG3142. However, the Sa is more erratic and compares much worse in the stationary acquisitions, even for the sinogram interpolated reconstructions. This indicates that the obtained topographies are to a large degree aliased by the artefacts as observed in Figure 5-14. This indicates that the stationary acquisition approach is not fit for propose to acquire surface topography data, which is further supported by the Sz results. The stationary upsampled stationary acquisition ORG1257 UP3142 STAT shows a range of approx. 0.1 mm for the Sz values, which just simply indicates the uselessness of the obtained surface topography data.

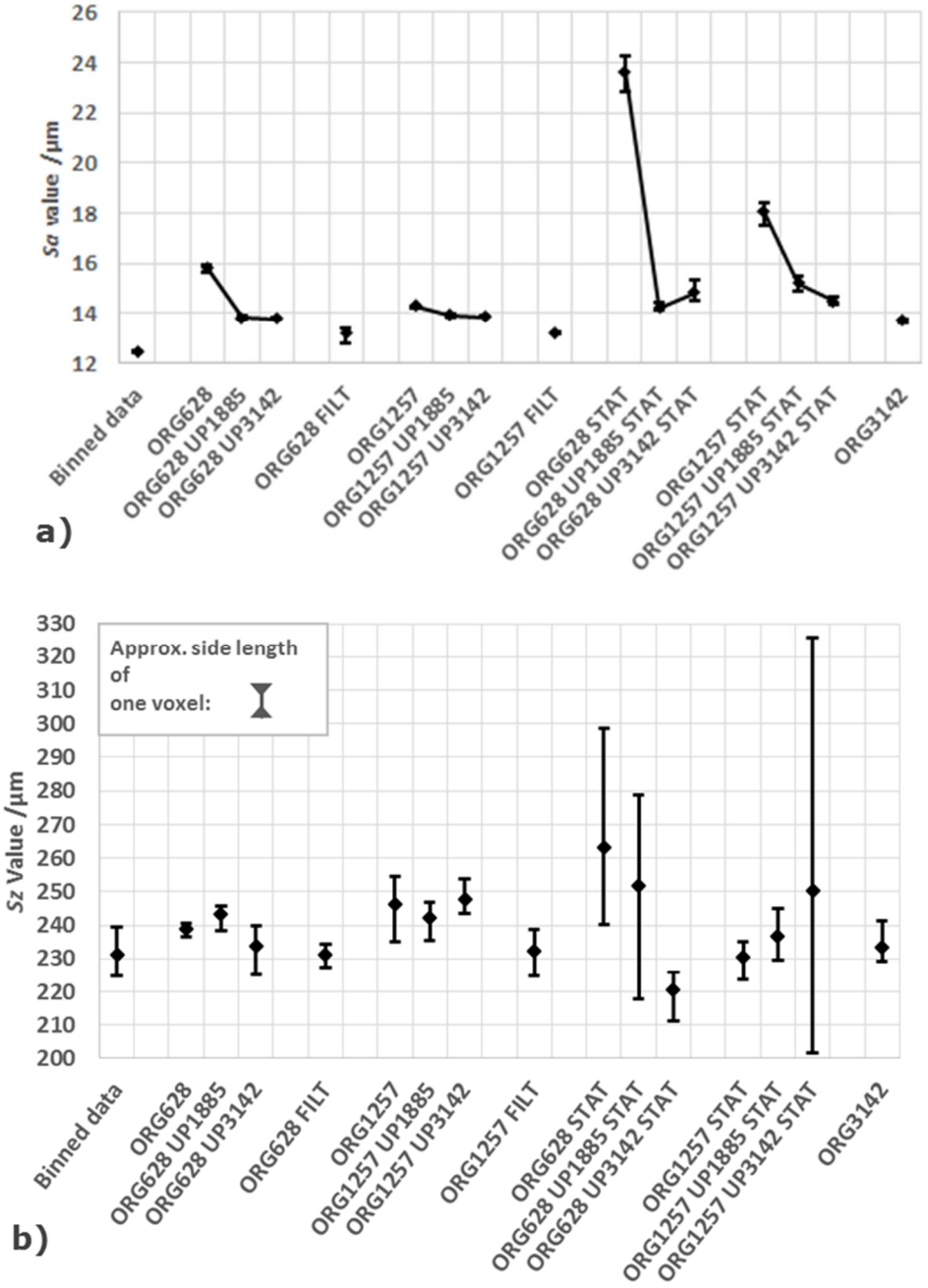

Figure 5-21 a) mean Sa value and its min-max range over three replicates; b) mean Sz value and its min-max range over three replicates. For a) and b) the error bars show the maximum range of the three repeats.

5.3.4 Discussion

XCT measurements can have large acquisition times. Reducing the number of projections reduces measurement times but may cause increased noise levels and artefacts in the volumetric reconstruction. Sinogram interpolation, pixel binning at the detector and median filtering of the reconstructed volume are methods which may be applied to reduce noise, but, together with reducing the number of projections, all such solutions have effects on the resolution, and on the quality of the surfaces extracted from reconstructed volumes. This work investigated the aforementioned effects by means of the computation of quantitative indicators of measurement quality, both in the reconstructed volumes (noise, resolution) and in the extracted surface topographies (discrepancy, local repeatability error).

Comparing the different acquisition modes, the binned setup had both larger mean width of the CIs as well as a larger discrepancy ratio than any sinogram interpolated case using more than 1885 real projections. The binned case outperformed the ORG1257 case (i.e. better precision, smaller CI widths), but not the sinogram interpolated version of ORG1257. However, while the binned setup showed the widest edge spread function compared to all other test conditions, it was much faster in the acquisition, as the exposure time could be reduced and the focal spot size could be increased. Overall, when comparing the acquisition time between the stationary and the continuous motion setups, the continuous motion showed a reduction of the acquisition time of around 5 min for 1257 projections and around 3 min for 628 projections. The acquisition times of the different continuous motion acquisitions were increasing linearly with respect to the number of projections as expected.

When investigating the effects of continuous motion on the quality of the obtained surface topography data, it is expected that continuous motion would reduce reconstruction quality, and consequently the quality of extracted surfaces (because of motion blurring affecting the original radiographs). However, the results showed that both the mean CI width (precision) and the discrepancy ratio with respect to the reference case (full number

of projections) were better for the continuous motion setup, compared to the stationary acquisition setup. This result is against expectations. Also unexpectedly, the mean width of the CIs of ORG1257 UP3142 STAT (stationary setup) was much larger than its continuous motion counterpart. This could be due to errors in the alignment process of the statistical topography modelling method, as the ORG1257 UP1885 STAT, shows similar levels of precision and discrepancy ratio with respect to its continuous motion counterparts. A possible explanation could be the effects of aliasing on the reconstructed data. The continuous motion is very likely to remove the higher spatial frequencies which will be present in the stationary acquisition. Thus the stationary acquisitions could be invested by aliasing artefacts in the reconstruction, which is supported by Figure 5-14. The question remains why the sinogram interpolation seems to remove the aliasing artefacts visually in Figure 5-14, but the mean width of the CIs are not correlating to this effect.

Sinogram interpolation can be used as a tool to suppress noise and artefacts when adopting a reduced number of projections for the purpose of saving acquisition time. Sinogram interpolation can yield improved results compared to median filtering and binning. However, it could be of interest to explore how sinogram interpolation compares against computationally more expensive methods, such as iterative reconstruction. However iterative reconstructions are computably expansive [137]. The computational burden is directly a function of the reconstructed volume size and the number of projections and the number of iterations [137]. Since in a single iteration, both forward and back projection is needed, the computation time of iterative techniques is by nature longer than with analytical techniques. Biguri et al. [137] showed in a comparison of a FDK reconstruction and an algebraic reconstruction technique-, the reconstruction time increased from 20 s to 46 min for using algebraic reconstruction techniques. This large time burden shifted the focus of further work in this thesis away from iterative techniques.

5.4 Chapter summary

This chapter mapped out the parameter space of sinogram interpolation and assessed it against median filtering and detector binning. One additively manufactured test sample was studied. The reconstructed volumes were analysed in terms of their noise behaviour and their resolution. The obtained surface topography data sets were compared using statistical surface topography models and in terms of selected surface parameters, namely Sa and Sz.

When looking at the noise levels alone, undersampling has been shown to worsen the noise behaviour. The effects of the undersampling also worsen the mean width of the confidence interval of the obtained statistical surface models, which indicates a reduction of precision of the undersampled test conditions. Sinogram interpolation showed a general trend to improve the precision of the undersampled test condition, except for the shortest acquisition. Here small amounts of sinogram upsampling improved the precision – but the mean confidence interval width increased with upsampling factors above three. Even small amounts of sinogram interpolation showed significant improvements for the agreement with the reference condition. The resolution is difficult to conclude upon, as the findings are believed to be confounded by the varying noise levels.

For large projection step angles (i.e. few projections acquisitions), the stationary acquisition did not improve the reconstructed volume nor improved the obtained surface models, counter to initial assumption. This has been attributed to the more prominent aliasing artefacts in the reconstructed volume data.

In terms of noise, median filtering outperformed sinogram interpolation. Comparing the sinogram interpolated data results against median filtering of the same initial data sets, the surface models render a conclusion that sinogram interpolation yields to better results, both in terms of precision and agreement with the reference scan. While binning the detector pixels showed to be with 12 min the investigated method with the shortest acquisition time, it performs worse than the shortest sinogram interpolation condition and showed a significantly worse resolution.

6 High aspect ratio tomography

From the literature review, one area was identified where the possibility exists to incorporate a priori information to optimise the number and placement of the projections in a circular acquisition trajectory, for high aspect ratio parts. The literature and industrial implementations show that for high aspect ratio parts, the acquisition can change from uniform spaced angular projections to a non-uniform spacing [148–151]. This concept so far has only been explored for stationary acquisition. This chapter assesses the feasibility of high aspect ratio tomography (HART) for continuous motion acquisitions. Some of the basis of this work was presented in a poster at a conference in 2019 [214].

6.1 HART

The fundamental reasoning behind approaches using analytical reconstruction techniques goes back to the central slice theorem, refer back to section 2.2. For a 2D tomogram, the 1D Fourier transform of the Radon function at an angle describes a radial line through the frequency domain of the reconstructed image at the same angle (compare back to Figure 2-8). Spectral richness is a term researchers have used to describe the magnitude distribution of the frequency domain of an imaged object [150]. It has been claimed that the magnitude of the 2D frequency domain of an imaged object with large aspect ratio

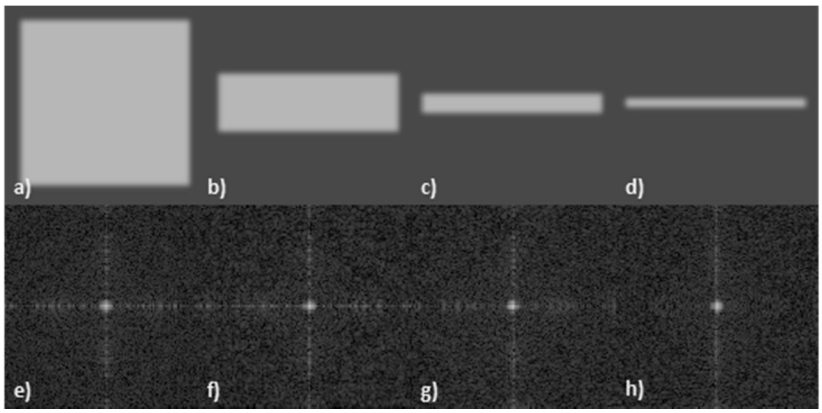

Figure 6-1 a) to d) show a tomogram of a rectangle increasing in its aspect ratio, e) to h) shows the Fourier domain of the a) to d) respectively. The magnitude of the horizontal components decreases from a) to d).

skews [151], also figuratively compare Figure 6-1 a) to h). Researchers proposed that knowledge of the spectral richness of tomogram can be used to vary the projection spacing along the circular trajectory. The skewed nature of the Fourier space of high aspect ratio parts is used in the justification of HART projection spacing [150,151,160]. While commercial adaptations exist [148,215], the literature detailing how to calculate the projection spacing and its effects is sparse [149,151].

Two concepts have been explored in this regard in the literature: adopted angular spacing of projections along a circular trajectory [148] and adaptive interpolation to upsample the sinogram data only along the direction needed [149]. In the medical literature, the variable angular spacing of the angular projections has been mentioned in respect to the patient's shoulder region, as the patient's shape is similar to an elongated ellipse [149]. Hsieh et al. [149] proposed a sinogram interpolation method which aims to only create virtual projections along with the elongated areas, where needed [149]. One industrial XCT manufacturer currently offers a software option of adopting the physical/acquired projection spacing and uses the term high aspect ratio tomography [148]. In 2019, a further manufacturer announced a similar capability [215]. However, detailed illustration of how to compute a suitable projection spacing for HART has not been presented in the literature.

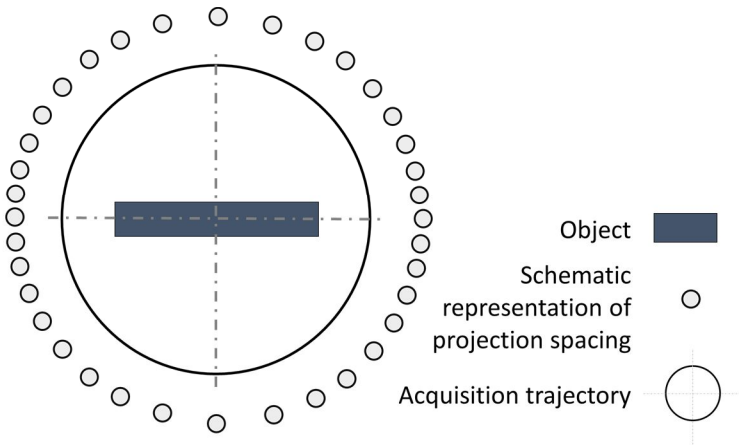

Figure 6-2 Schematic showing how the number of projections can vary across the *circular* trajectory. This diagram is artistic and not to scale.

6.2 Motion blurring, a projected limit

The diverging X-ray beam in an XCT system yields to different levels of magnification depending on the object detector distance (ODD) to the measured part. Motion blurring describes where the projection of a part moves during the integration time of the detector, yielding to an apparent blurring of the image (and thus a loss of the higher spatial frequencies) caused by the movement of the part. Looking at the magnification and at the rotation, the motion blurring will vary for each point of an object depending on its position. Assuming a point rotating around an axis, the effective magnification can be calculated simply by using trigonometry. Figure 6-3 shows a diagram of a simple fan-beam setup and highlights that magnification depends on the position in the imaging system.

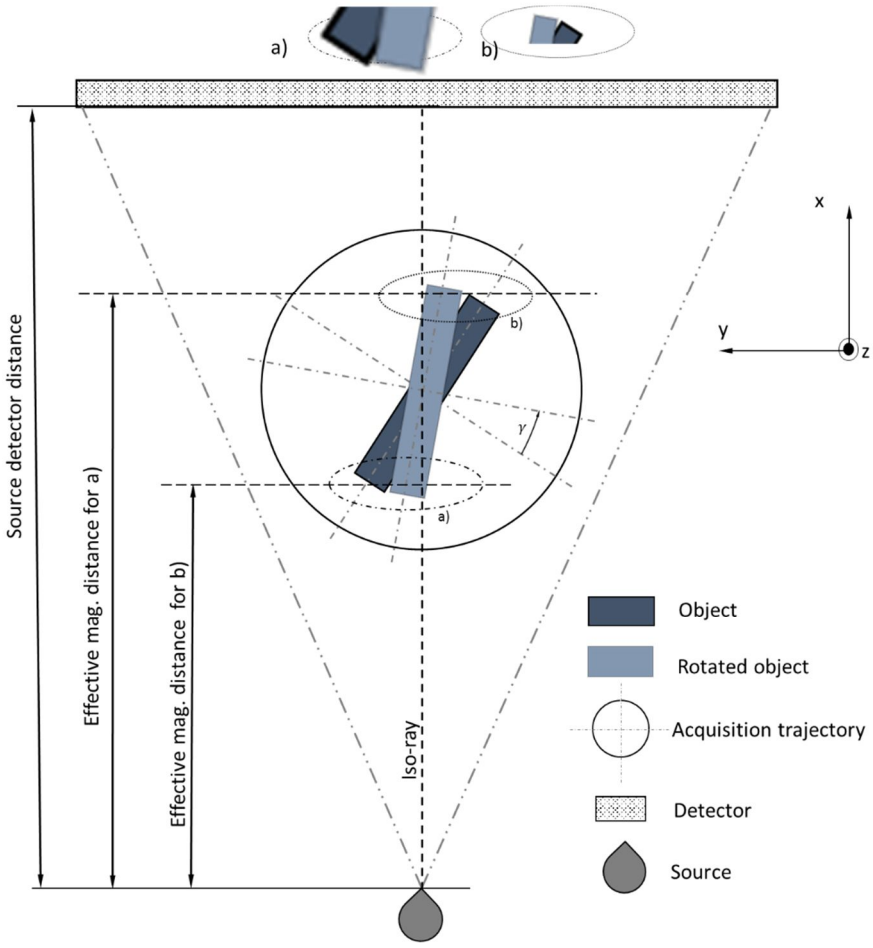

Figure 6-3 Schematic representation of the different magnification of part depending on the position along the fan beam.

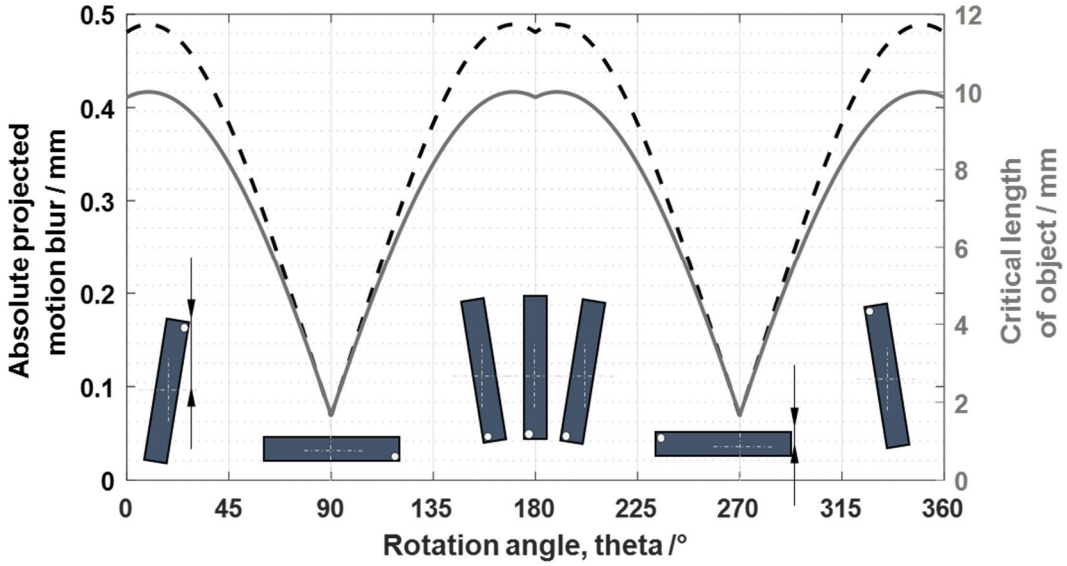

Figure 6-4 The motion blur (dashed black line) and the critical length, which dictates the number of projections (solid grey line). The object is schematically shown at key positions of the graph, and the critical length (the longest dimension in the direction along the iso-ray) is highlighted with arrows.

Assuming a rectangular object, or an object with a rectangular bounding box with an aspect ratio of twenty (ratio between the long and the short side of the object), Figure 6-4 shows the maximum motion blur of the part, assuming it rotates around the centroid. The graph in Figure 6-4 assumes that the object is rotated at constant speed. The graph also reports the 'critical length'. The critical length is the largest depth along the iso-ray direction. This length is assumed, in accordance with the spectral richness approach [150,151] and the central slice theorem, as the length which dictates the number of projections needed. What the graph shows is that where the least projections are needed for HART, the geometry of the high aspect ratio part also results in the least amount of projected motion blurring.

The coinciding relationship between projected blur and the object's orientation lends itself to a thought experiment of combining both motion blurred acquisition and HART. The literature discussion about HART has so far only included stationary acquisitions [150,151,160]. Thus the aim of this chapter is to explore the feasibility of running HART continuously to both reduce the number of projections and acquisition times. The

implementation of a potential motion control system is not included in the discussion here, and the investigation is limited to a simulation study to assess feasibility.

6.3 Projection density calculator

First, the number of projections and their location need to be estimated. An assumption made here is the reduction of a cone-beam problem to a fan-beam problem. This simplification can be applied, as the projected movement is dominated by geometry and trigonometry by the rotation angle, as opposed to the vertical position within the reconstruction volume. The calculation is based on the formulation by Schulz and Joseph [22] (see section 3.2). For the purpose of evaluating the maximum step angle for each projection, the reconstruction radius is evaluated as the current length away from the centre of rotation. From this number of projections, the step angle can be evaluated. The maximum frequency v_M (see section 3.2) is evaluated as half of the reciprocal of the pixel size. Figure 6-5 shows the revaluation of the step angle for a rectangular shape of aspect ratio twenty. The number of projections with HART spacing using the proposed method is computed as 828, compared to 1571 projections which would be recommended if using an equispaced approach [172].

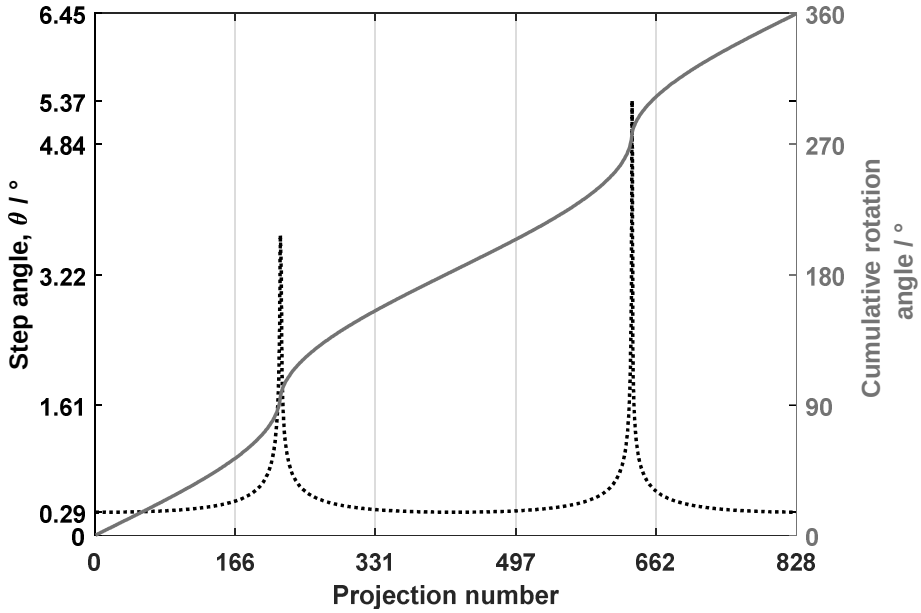

Figure 6-5 Shows the HART projection spacing for rectangle with an aspect ratio of twenty. The grey line shows the cumulative angle, whereas the dashed black line shows the step angle of each projection, the number of detector pixels is one thousand.

Simplified, the projection density for an object represented by a point cloud can be calculated following Pseudocode 1 in Appendix A, which is shown as a flow diagram in Figure 6-6.

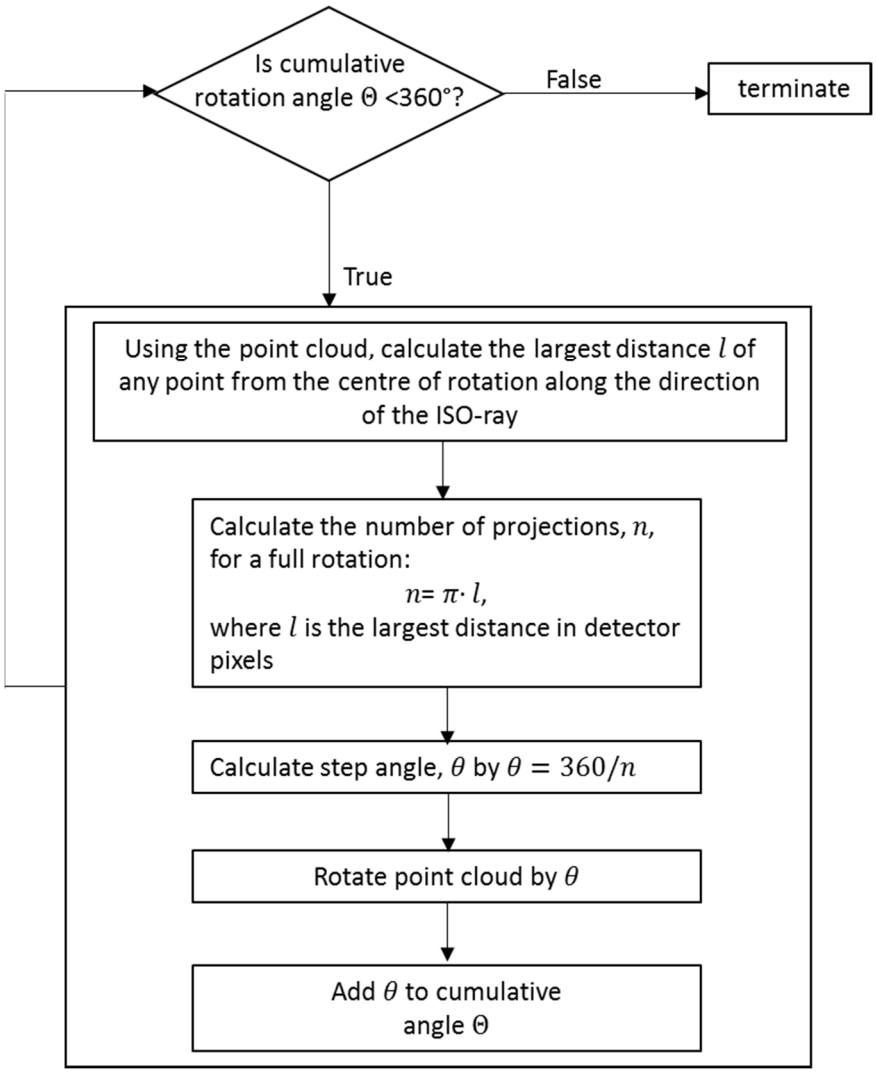

Figure 6-6 Flow diagram of calculating the projection density from a point cloud

What is shown in Pseudocode 1 in Appendix A, and depictured in a flow diagram in Figure 6-6 is an approach to evaluate the number of projections needed locally. However, when testing the code on high aspect ratio parts, the possibility of motion blurring can occur. Figure 6-7 shows the geometrically projected motion blurring in terms of detector pixels on the right-hand axis. The reported value is the largest geometric motion blurring of all points of the part's geometry.

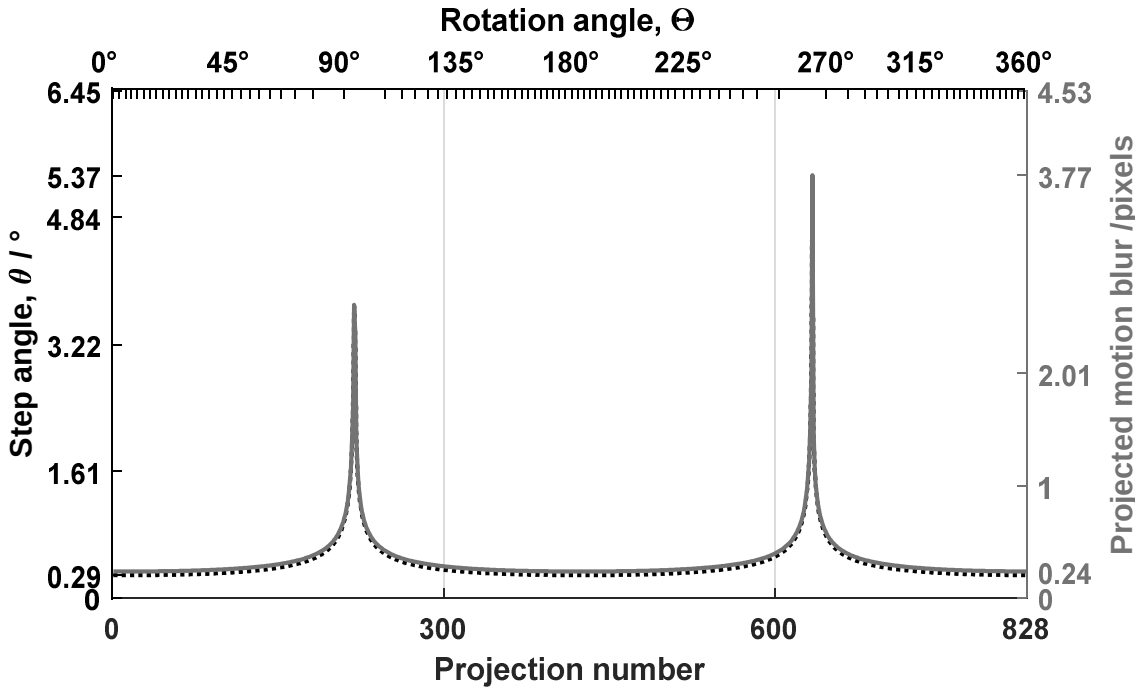

Figure 6-7 Shows the HART projection spacing for a rectangle with an aspect ratio of twenty. The dashed black line shows the step angle of each of the 828 projections. The grey line shows the geometric motion blurring which peaks at 3.77 detector pixels.

The blurring modelling used in these calculations is using the XCT geometry, combined with the pixel size and the CAD model, to calculate across how many pixels the projected image of the object is smeared. This geometric approach is the most common in computational modelling of motion blur in XCT and has been successfully been applied and demonstrated in [170].

As seen in Figure 6-7, some projections will lose their higher frequency content due to motion blurring. While only a few projections will experience blur, the blur-induced loss of information still translates into the reconstruction. Hence, the flow diagram of Figure 6-6 can be extended to limit the projected blurring, to:

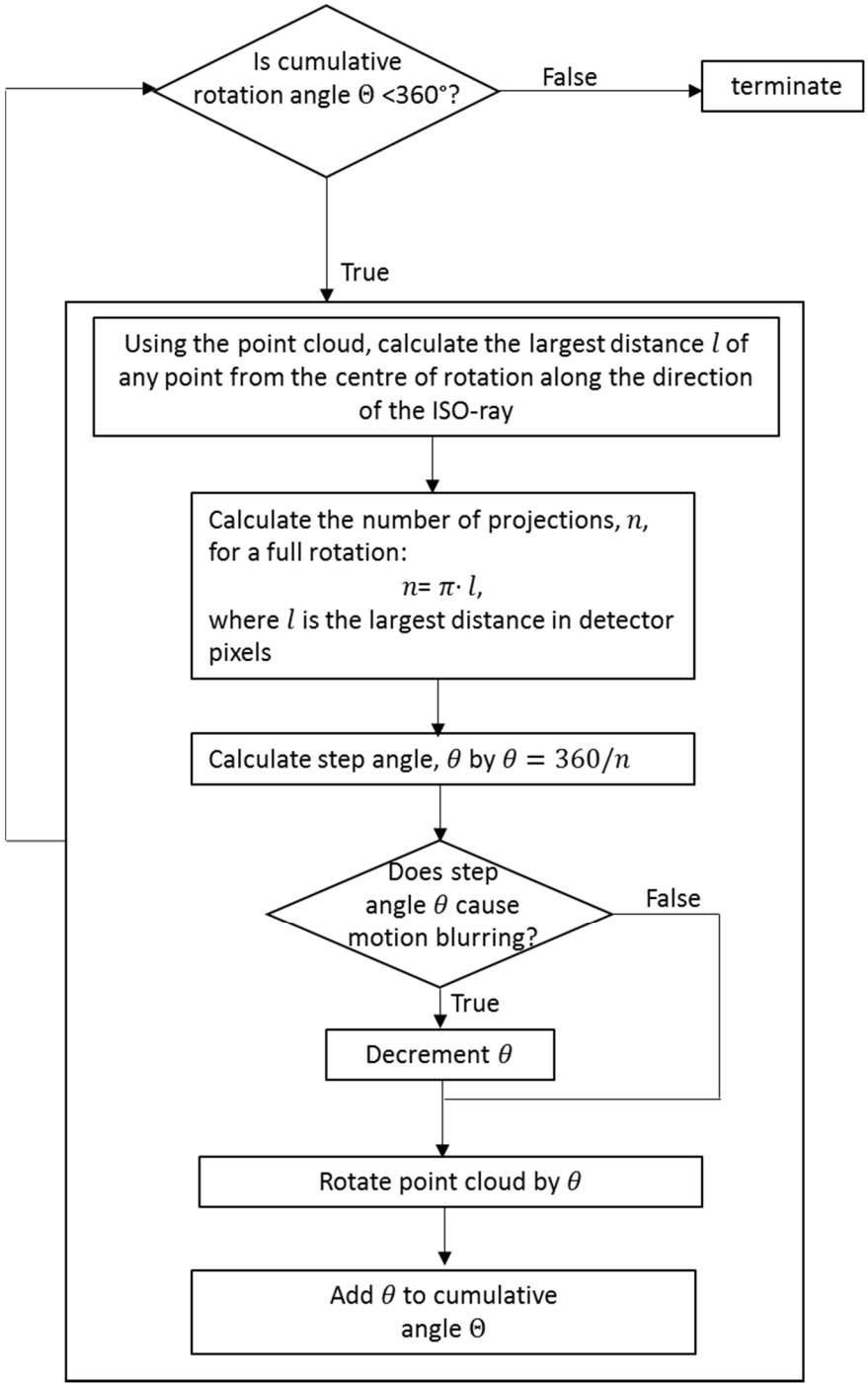

Figure 6-8 Extending Flow diagram in Figure 6-6 by a numerical decrementing approach to limit the step angle to avoid motion blurring

The extra while loop added in Figure 6-6 reduces the projection step angle where needed to numerically limit projected blurring above a given blur limit. Since the presented method is a numerical technique, the decrement subtracts a small but finite angle from the step angle. The same simulation conditions as Figure 6-7 are evaluated in Figure 6-9, but with the added blur limit, the number of projections required increases by ten to 838.

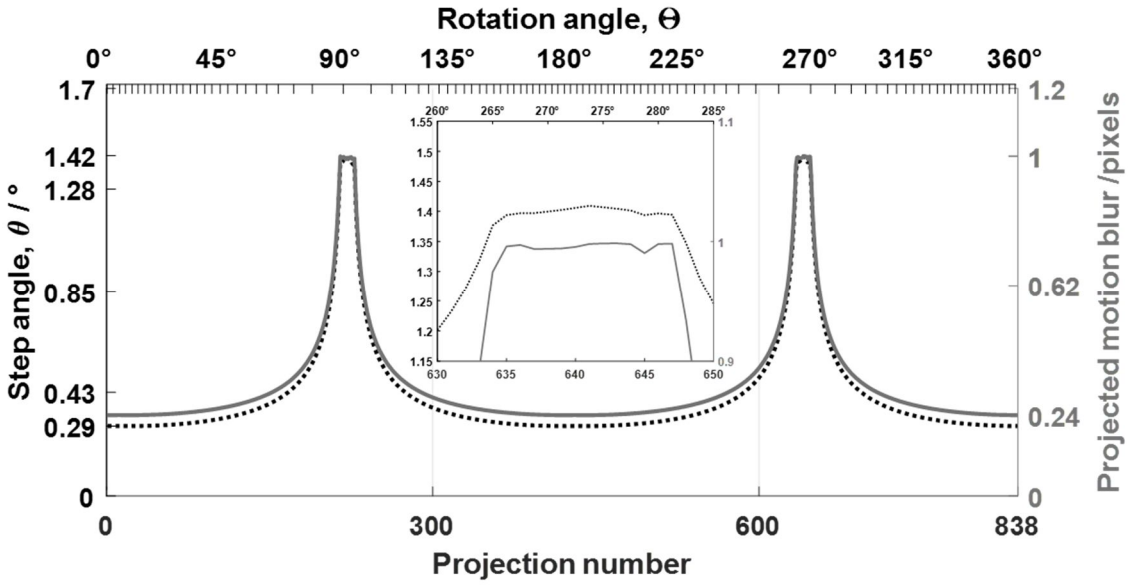

Figure 6-9 Shows the HART projection spacing for a rectangle with an aspect ratio of twenty. The dashed black line shows the step angle of each of the 838 projections. The grey line shows the geometric motion blurring which is limited to one.

The reduction of the number of projections achieved by the proposed method thus depends on blurring effects, and thus on the shape of the object. The graph shown in Figure 6-10

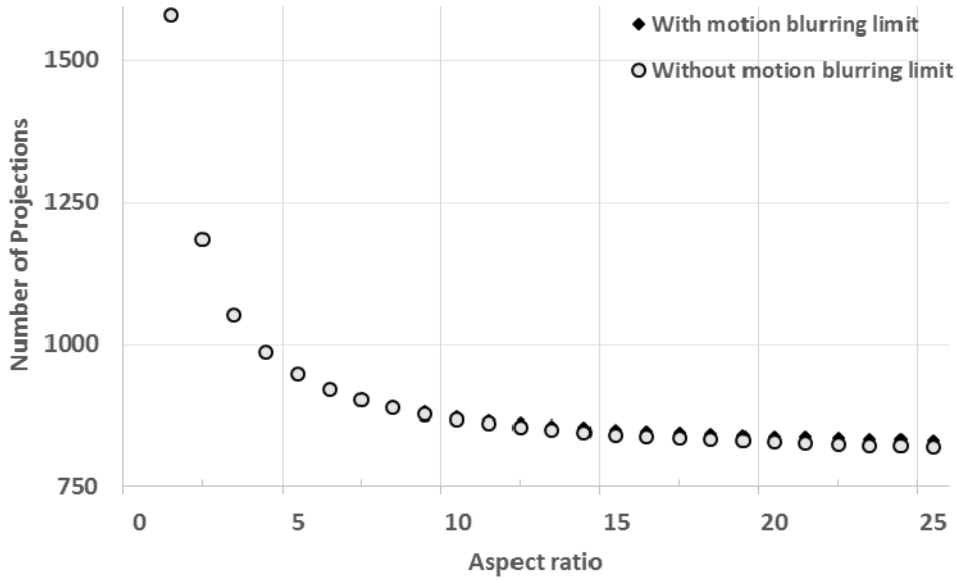

Figure 6-10 The proposed method mapped out for a cuboid of varying aspect ratio. Two conditions are shown, one limiting the motion to avoid motion blurring (black diamond), and one without limiting the step angle (grey circle). The difference is small for aspect ratios <15.

highlights this relationship for a cuboid, with varying aspect ratio, rotating around its centroid.

The collected projections with the variant spacing can be reconstructed using analytical reconstruction methods such as FDK. Three slices of reconstructions and details of a noise-free simulation are shown in Figure 6-11 and Figure 6-12.

A qualitative inspection of the noiseless reconstructions shown in Figure 6-11 and Figure 6-12 shows no significant artefacts arising from the HART spacing or from the non-equispaced sampling of the projection domain. The following section explores the effects of HART in more detail and with noisy simulated data on the basis of a case study.

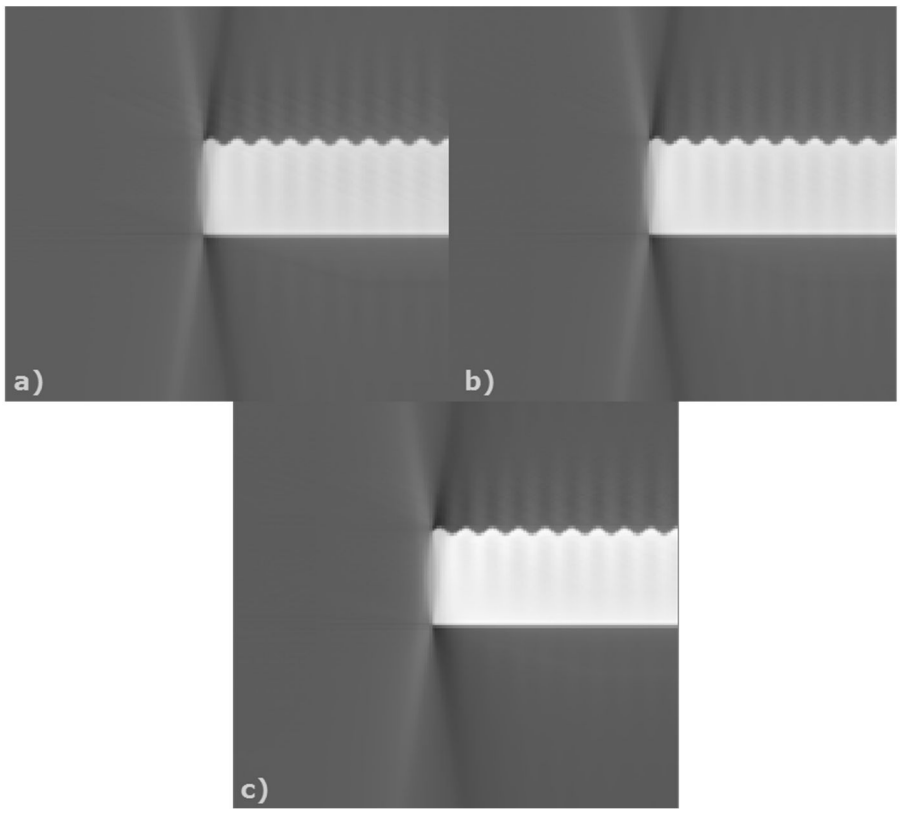

Figure 6-11 This figure shows details corresponding to the slices of the reconstructed volumes shown in Figure 6-12. a) used 838 equispaced projections b) used 1571 equispaced projections, whereas c) used 838 projections with the HART spacing. No significant change, aliasing or distortion are discernible.

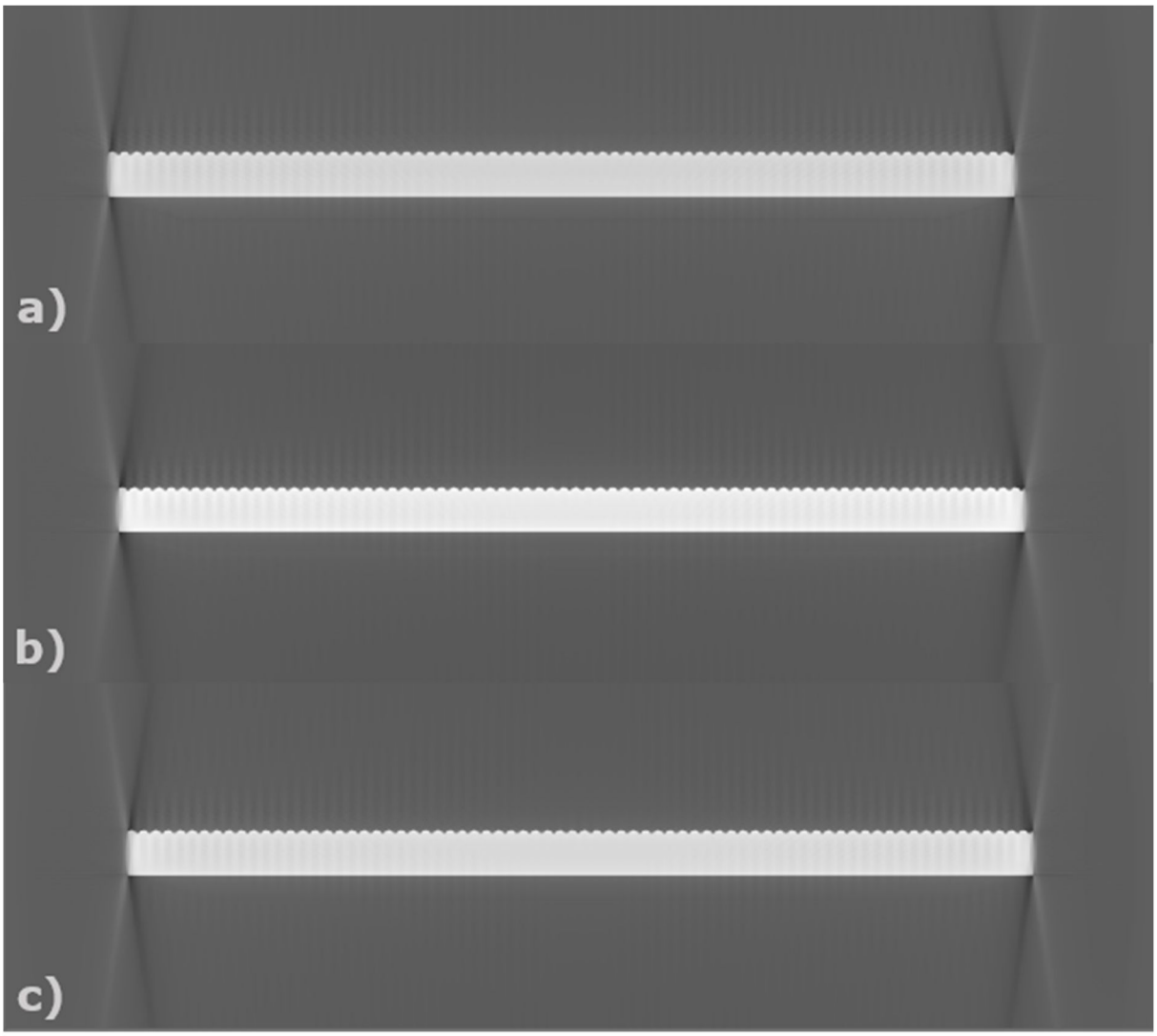

Figure 6-12 Three slices of noiseless reconstructions of a test part. a) used 838 equispaced projections b) used 1571 equispaced projections, whereas c) used 838 projections spaced as shown in Figure 6-9. No significant change, aliasing or distortion are discernible.

6.4 Simulation case study

The aim of this simulation case study is to explore the effect of continuous motion HART on the measurement of surface topographies using XCT. To reach this aim, the simulation study will have three cases which will be referred to as EQI838, HART838, and EQI1571 (also see Table 3). EQI1751 refers to a reference setup. The reference reconstruction uses 1571 equispaced (continuous motion) projections, as recommended in [172]. HART838 describes a reconstruction using 838 projections with variant projection spacing and continuous motion, as described in section 6.3 and shown in Figure 6-9. EQI838 describes a reconstruction using 838 equispaced projections and continuous motion. The simulation case study limits itself to the investigation of one cuboid high aspect ratio part.

Table 3 Table indicating the experimental conditions and the naming convention used in this chapter

Simulated continuous motion projections			
1571 projections	838 projections		
	HART838	HART	**Projection spacing**
EQI1571	EQI838	Equispaced	

The test part was created in MATLAB. The chosen design (STL geometry) is a cuboid with a 15.6 mm by 15.6 mm square base (on the *x*,*y* plane) and thickness of 0.77 mm, resulting in an aspect ratio of approximately twenty assuming the projections are taken along a circular trajectory whose axis lies on the *x*,*y* plane. A sinusoidal profile was superimposed on one of the surfaces to create artificial texture, whilst the opposite surface was left flat. The sinusoidal profile was given a wavelength of 0.21 mm, and an amplitude of 0.03 mm. The design was loosely based on a specimen of Rubert & Co Ltd [199]. Figure 6-13 shows a rendering of the test part, and Figure 6-14 indicates the orientation of the test part in the simulation setup with respect to the axis of rotation. The test part was designed such that a high aspect ratio is created.

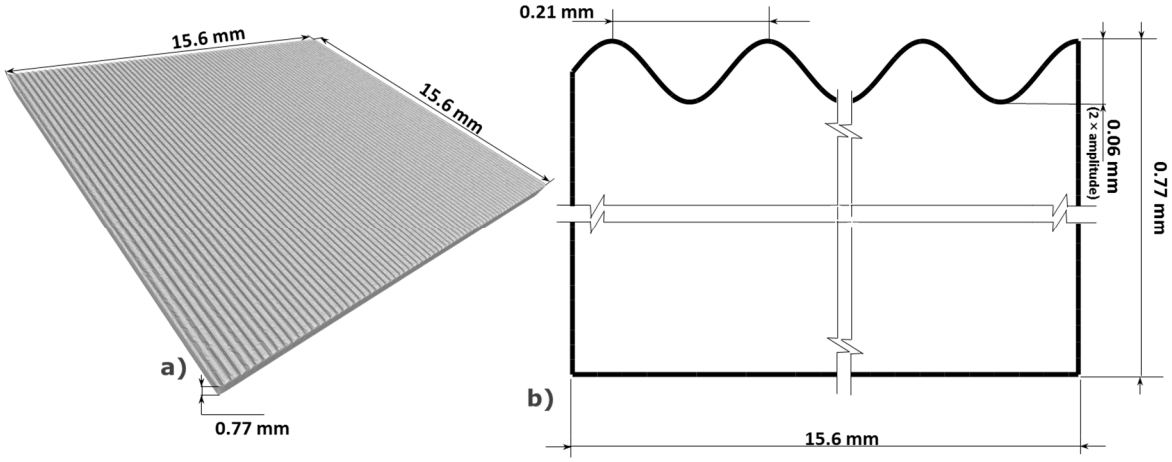

Figure 6-13 a) Rendering of the test part, and b) a schematic of the cuboid part used in this chapter's simulation study, b) The aspect ratio is approximately twenty.

6.4.1 Simulation setup data processing parameters

The software aRTist [197] was used for the simulation (see also section 4.3). A point source model of the focal spot was used; a tungsten spectrum was simulated with an acceleration voltage of 180 kV, a 21° target angle and an inherent filtration of 2 mm elementary aluminium. Photon noise was added post-simulation to the data following Freud et al.'s [216] approach using additive white Gaussian noise with a standard deviation of 0.05. A new seed of the random number generator was used for each simulation. The test part was set to elementary aluminium, and a filter of 1 mm copper was used. Scattering was not simulated, as the fraction of scattered photons is not high due to the material choice of aluminium and the low acceleration voltage. A square detector of 1000 x 1000 pixels was simulated with a pixel size of (0.4 x 0.4) mm. The source-detector distance was set to 1100 mm. The centre of rotation was assumed as the centroid of the test piece. This setup thus approaches the nominal parameters of the Nikon MCT225 system.

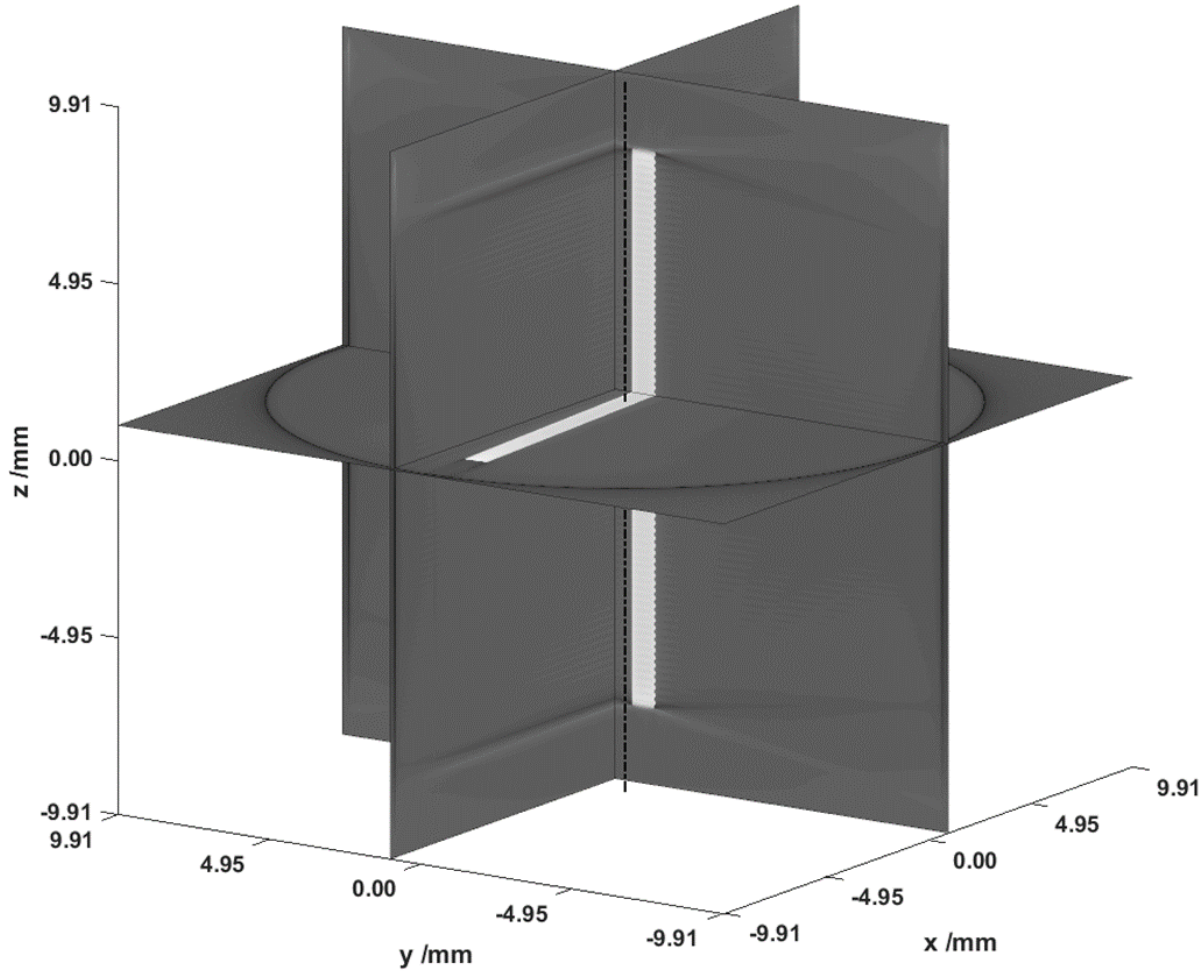

Figure 6-14 a rendering of three planes of a reconstructed volume of the test part. The dashed line highlights the axis of rotation.

The reconstruction of the simulated data was performed using the ASTRA toolbox [136]. The ASTRA toolbox is an open-source reconstruction software, which offers FDK reconstruction, as well as iterative reconstruction algorithms. As the data was simulated, no algorithmic centre of rotation determination was performed. The reconstructed voxel was approximately 19.8 µm. The back-projection angle is the mean angle of the motion-blurred projection. The projection data were filtered using a ramp filter. The reconstruction was performed using GPU acceleration [136]. The algorithm used was the ASTRA FDK implementation. The computation time was in the order of approximately one hour on a computer with 64 GB RAM, an Intel Xeon CPU E5-1620, and an NVS 310 graphics card with 48 CUDA cores and 1 GB of dedicated video memory and with a quoted CUDA compute

capability of 2.1. The driving reason behind the choice of reconstruction software is that the Nikon CT PRO software does not support overriding of angular position.

The reconstructed volumes were imported to VGStudio Max 3.0 and surface determination was performed using a search distance of 4 pixels for the 'advanced method' and the initial surface was the automated ISO-50 value. The export of surface topography in the form of STL files was performed using the VGStudio's default options, refer back to the methods section 4.

As outlined in section 4, the Shannon entropy was computed on the whole reconstructed volume. The 10% to 90% resolution estimate was performed on the flat side opposing the face with the sinusoidal wave (Figure 6-14).

The STLs of the extracted surfaces were aligned using EQI1571 as the reference, using the methods outlined in 4. The raster scan grid was set to 10 μm as it closely matches half of the reconstructed voxel size (19.8 μm). As highlighted in section 4, height maps from repeated simulations were used to compute statistical surface models. Texture parameters were calculated on an extracted area of (4 × 4) mm; levelled by a least-squares mean plane subtraction and an S-filter of nesting index 12 μm and an L-filter of nesting index 800 μm.

6.4.2 Motion projections from stationary simulations

In order to obtain the spatially varied projections, first 9999 equispaced stationary projections of the test part were simulated and were later composed into the motion-blurred projections. For consistency, three consecutive projections equispaced along the circular trajectory were averaged to obtain one simulated motion-blurred projection – independently of the range of the angular span. This is important as otherwise the noise level will improve to an unrealistic degree once many projections are averaged. The projection mean angle was calculated to floating-point precision, whereas the simulated projection data was rounded to the closest 0.036° (derived from 9999 projections). The mean angle was used for reconstruction.

6.4.3 Results

The aim of this section 6.4 is to assess the feasibility of reducing the number of projections needed for reconstruction by HART and continuous motion. Hence, three reconstructed surfaces are compared: a) from a reconstruction using 1571 projections, b) from a reconstruction using adjusted value but equally spaced, and c) a reconstruction using the adjusted number and adjusted location. Detail images and images of reconstructed slices are shown in Figure 6-15 and Figure 6-16 respectively. A different and grainier noise pattern of EQI838 is visually discernible in comparison to EQI2571 and HART838, in Figure 6-16 and more so in the detail images of Figure 6-15.

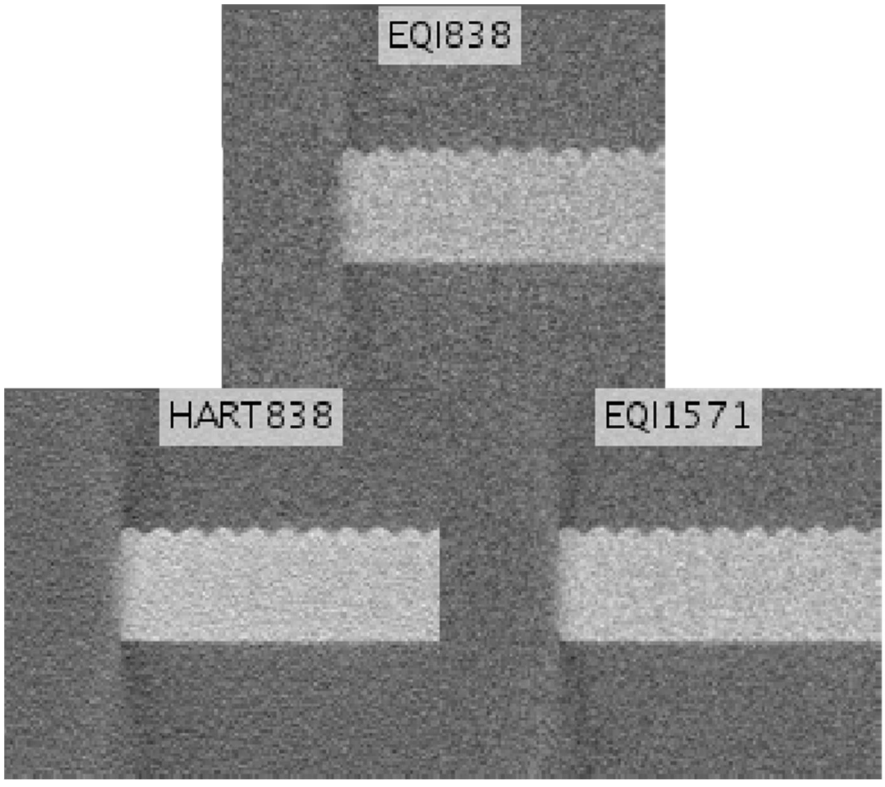

Figure 6-15 Three detail images of the reconstructed volumes. The details correspond to the slices shown in Figure 6-16. Minor variations of the noise texture can be observed in EQI838.

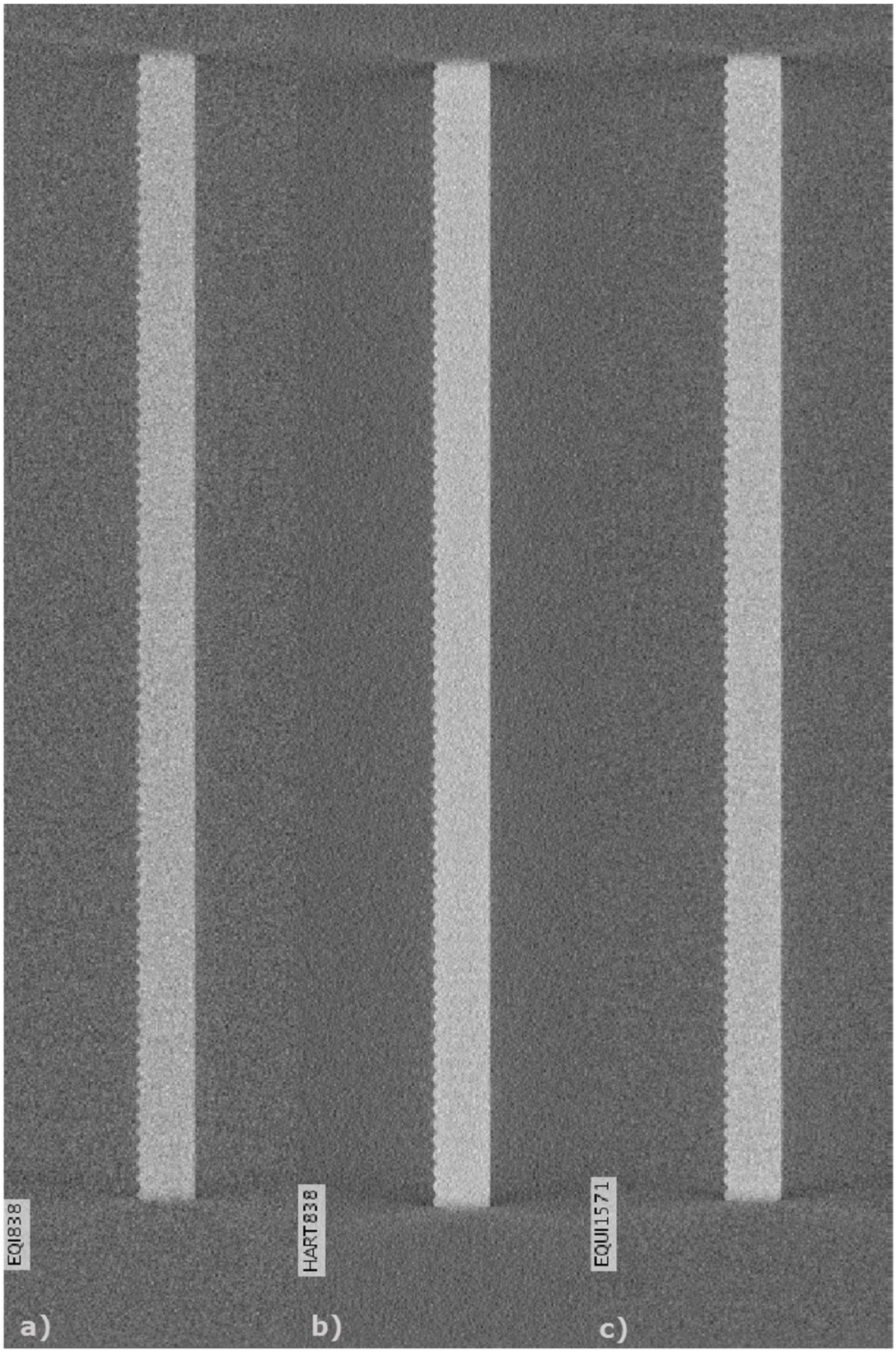

Figure 6-16 a) is a slice through the y-z plane (see Figure 6-14) of one of the EQI838 reconstructions. b) and c) show equivalent slices of HART838 and EQI1571 respectively. Minor variations of the noise texture can be observed in a) EQI838.

Statistical surface topography models

The statistical surface models were computed as described in Chapter 4 and the upper and lower bounds quoted at a 95% confidence interval. Both Figure 6-18 and Figure 6-17 show sections of varying enlargements of the computed surface models (Figure 6-18 a section of (2 × 2) mm and Figure 6-17 a section of (0.5 × 0.5) mm). The EQI838 case shows a grittier and rougher upper bound of the CI than HART838 and EQI1571 in Figure 6-18. A qualitative inspection of the mean line (magenta) in Figure 6-19 shows a poorer

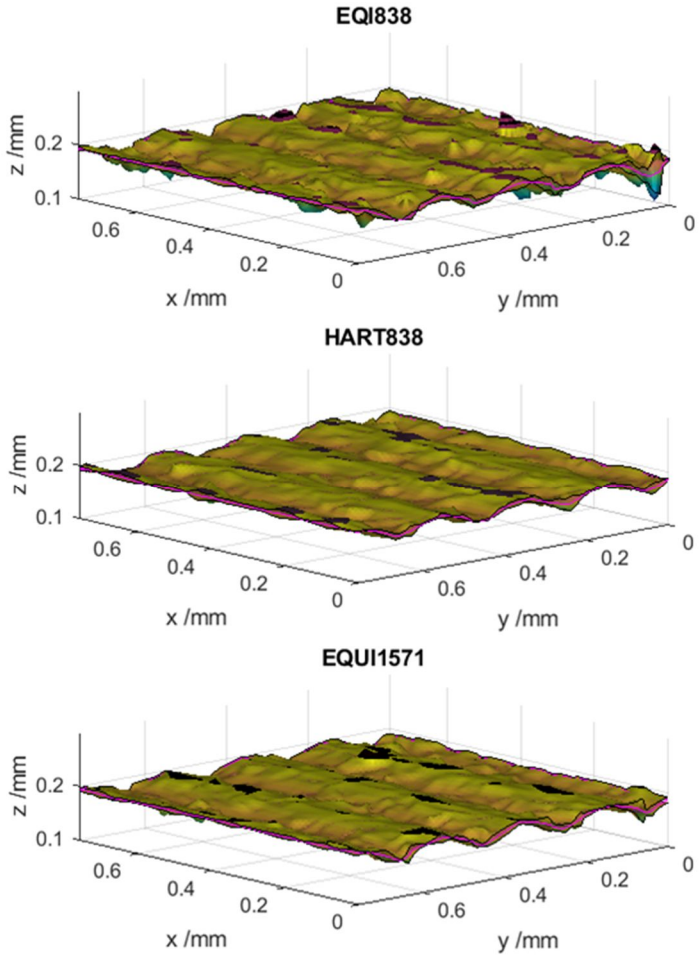

Figure 6-17 shows sections detailing (0.7 × 0.7) mm of the three computed statistical surface models. The magenta plane represents the mean line whereas the false colour surfaces represent the computed upper and lower bounds of the confidence intervals quoted at 95%.

representation of the shape a sinus wave as compared as HART838 and EQI1571. In the detail of Figure 6-19 the qualitative inspection indicates a slightly larger CI width of EQI838. Overall the qualitative inspection of the statistical surface models indicates an inferior performance of EQI838.

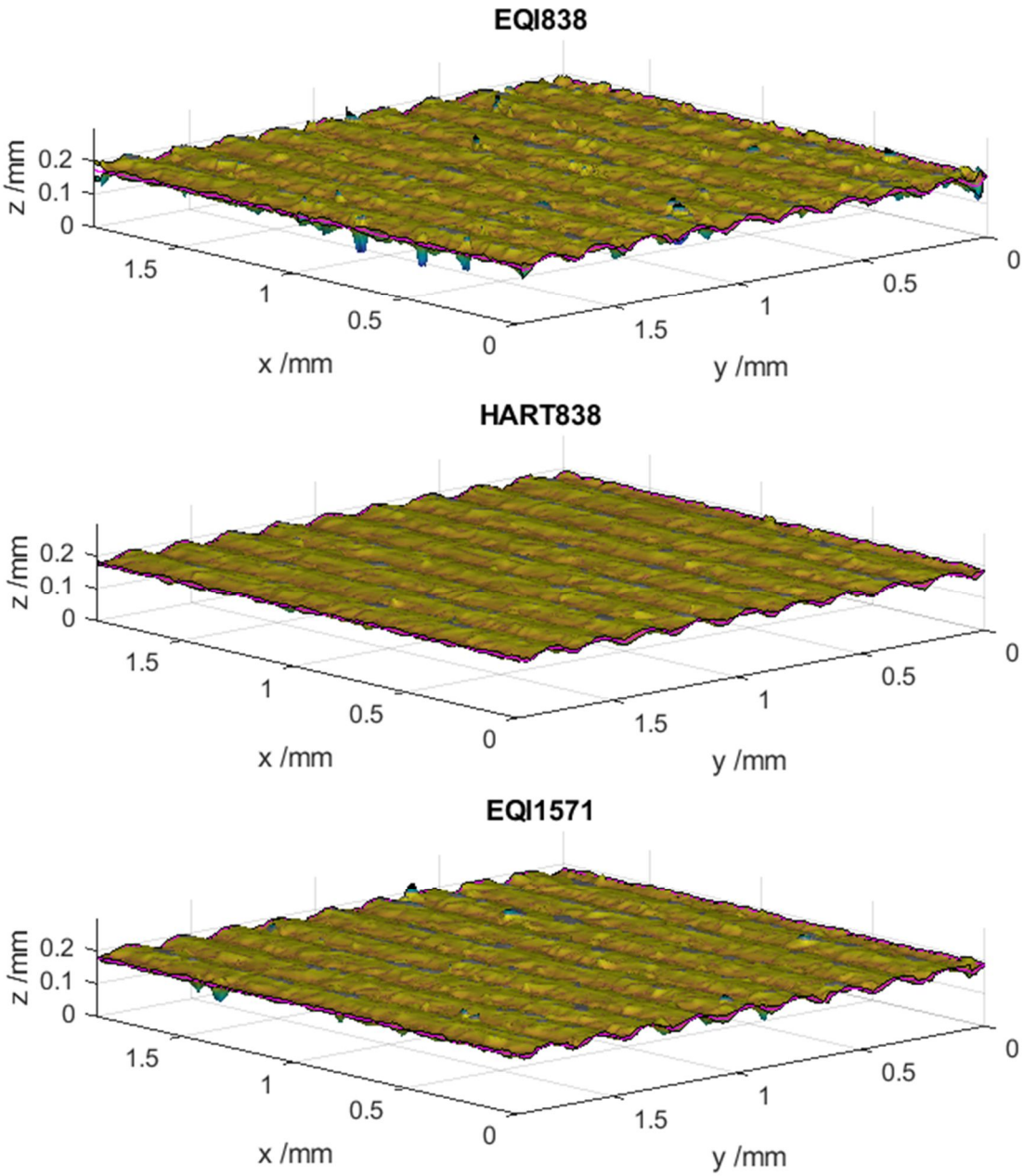

Figure 6-18 shows sections detailing (1.8 × 1.8) mm of the three computed statistical surface models. The magenta plane represents the mean line whereas the false colour surfaces represent the computed upper and lower bounds of the confidence intervals quoted at 95%.

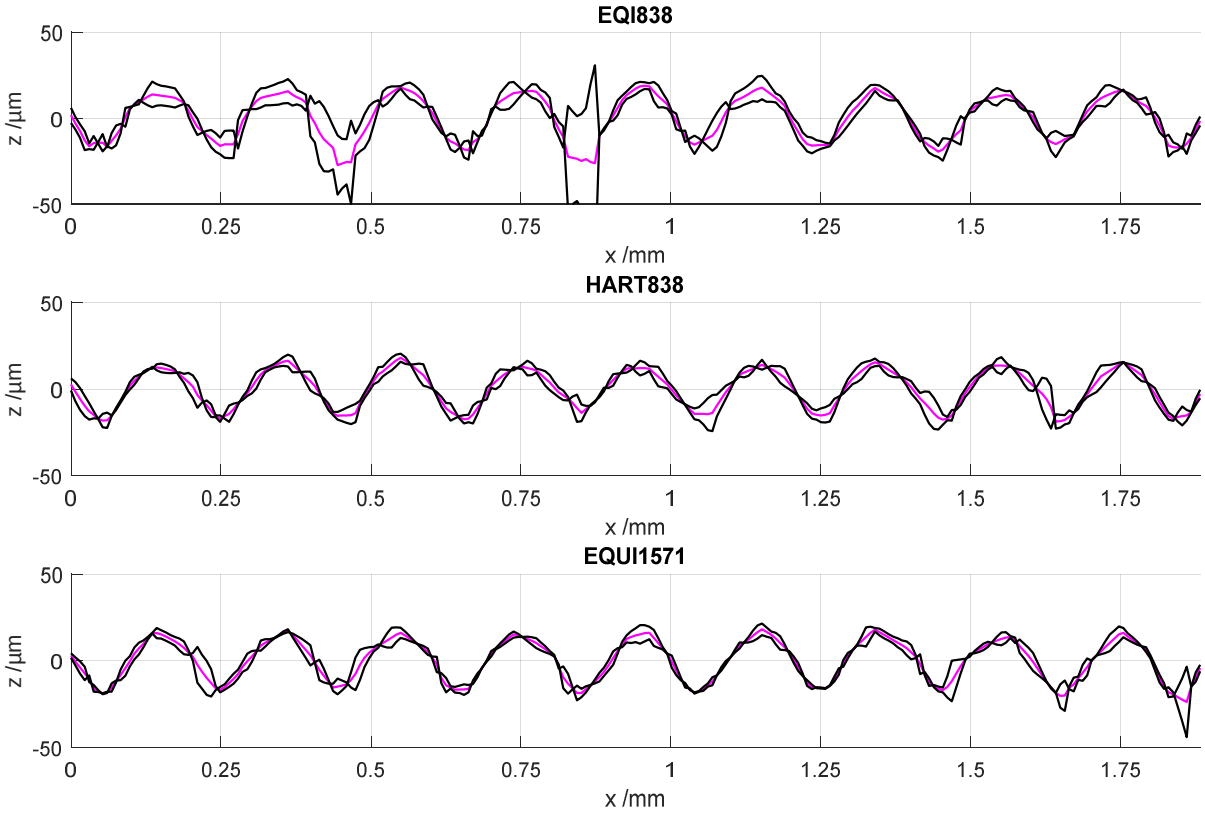

Figure 6-19 Details highlighting the sinusoidal profile of the investigated surface. The black lines represent the CI, and the magenta line the mean line. The presented data is located at approx. x=0.8 mm in the plots shown in Figure 6-18.

Noise in the reconstructed volume

The Shannon entropy was computed for the reconstructed volumes and the mean values are reported in Figure 6-20. EQI1571 shows the lowest noise levels in terms of Shannon entropy followed by HART838 and EQI838. The range over the three repeats is reported in Figure 6-20 as error bars. The low Shannon entropy value of EQI1571, and the lack of overlapping of the error bars, indicates the EQI1571 has improved noise levels, whereas EQI838 performs worst in terms of the noise behaviour. The qualitative inspection indicated an improved reconstruction of the volumes which relied on 838 HART projections as opposed to an equispaced 838 projections. This qualitative conclusion on image quality is also reflected in the quantitative evaluation of the reconstructed volumes. Here the HART acquisition showed a lower Shannon entropy than the equispaced acquisition with the same number of projections, though the Shannon entropy did not approach the value of the reference setup. This can be explained as an effect of the 'photon' noise, as more projections will generally be able to reduce these noise levels. However, while the EQI838 and HART838 had both the same number of projections, the improved noise levels in the reconstructed data set of HART838 suggest that the reconstruction using HART is more robust when dealing with noisy data. As such, this indicates that the continuous HART is a superior projection spacing for the investigated skewed aspect ratio part.

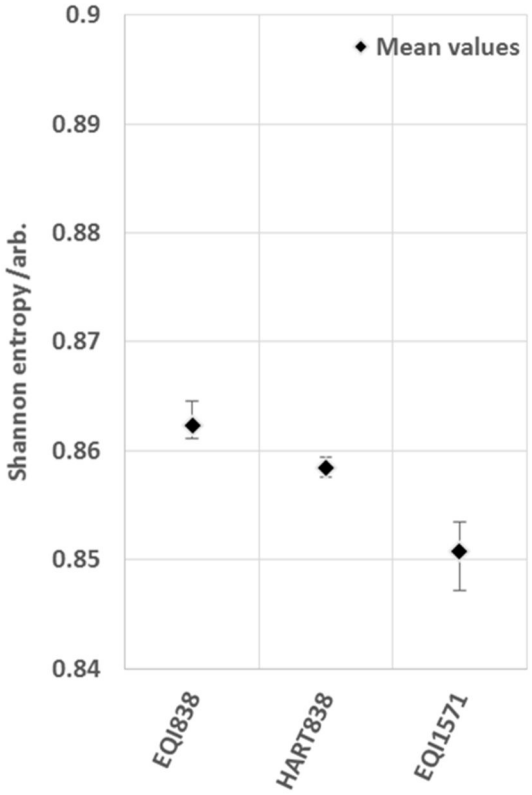

ect ratio tomography

Figure 6-20 shows the mean values of the computed Shannon entropy values for the investigated reconstructions. The error bars indicate the range of the computed Shannon entropy for the three repeats.

Resolution in the reconstructed volume

The mean values of the resolution are reported in Figure 6-21. The mean values of the three investigated cases, EQI838, HART838 and EQI1571, are within the minimum and maximum range of the computed resolution values of each investigated condition. In the qualitative inspection, no changes in the resolution were observed, nor were any image artefacts observed. The quantitative inspection showed also no significant changes for the resolution. Though the resolution data is hard to conclude upon as the range of the repeats, and thus the error bars, are large. However the mean values of the repeats agree well with one another, and the visual qualitative inspection resulted in no recognisable artefacts or loss in resolution.

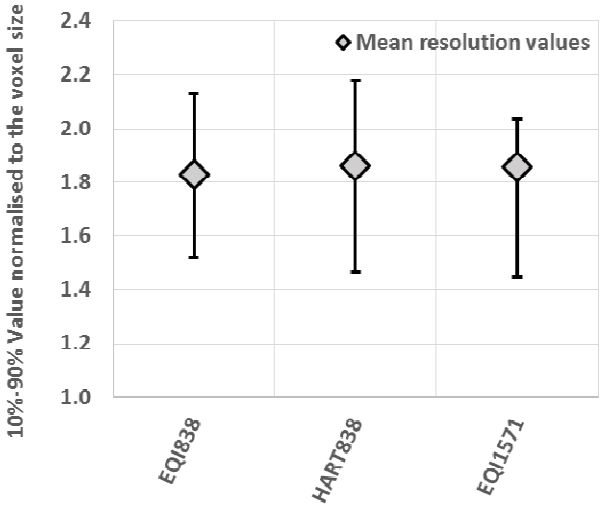

Figure 6-21 shows the mean values of the computed 10%-90% resolution values for the different reconstructions. The error bars indicate the range of the computed resolution value for the three repeats.

Discrepancy and repeatability error of the extracted surface topography

From the statistical surface models, the mean confidence width is computed for all the investigated cases and displayed in Figure 6-22. The mean width of the confidence interval is smallest for the EQI1571 case (0.013 mm, but is closely trailed by HART838 at 0.014 mm). The EQI838 performed worst in terms of mean width of the CI, which is computed as 0.023 mm. Figure 6-22 also reports the discrepancy ratio of HART838 and EQI838 paired against the reference condition which used 1571 simulated conditions. The level of disagreement of HART838 and EQI1571 was computed to be 0.012 and for the pairing of EQI838 and EQI1571 was found to be worse at 0.060. The results of the mean width of the CIs indicate a similar performance in terms of precision of both EQI1571 with the investigated HART projection spacing. The discrepancy ratios indicate that HART838 outpaces the equispaced acquisition of EQI838 and is a measurement with higher accuracy.

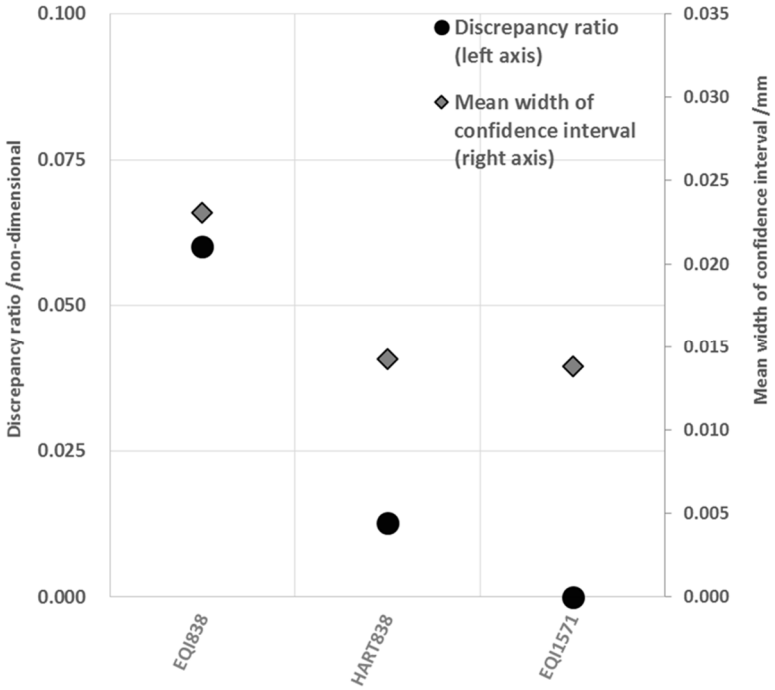

Figure 6-22, the grey diamond data points represent the mean width of the confidence interval of the statistical surface models, to be read off the right-hand axis. The black round data points (left-hand axis) are the discrepancy ratios with respect to the EQI1571 case.

The trend of HART to improve the image quality also translates to the exported surface topographies. The HART838 simulations showed a reduced width of the mean confidence interval, which indicates an improved precision of the extracted surface topography compared against the EQI838 case. The mean CI width of HART838 approaches the value of EQI1571, which suggests that continuous HART can decrease the acquisition times of surface topography measurements using XCT while maintaining good precision. The agreement between the surface models of HART838 and EQI838 to the EQI1571 surface model was quantified using the discrepancy ratio. The discrepancy ratio of HART838 is approx. only one-fifth of the EQI838 case, which indicates that HART considerably improved the extracted surface topography at a reduced number of projections.

Areal texture parameter comparison

Figure 6-23 reports both the calculated mean Sa values and the mean Sz values. The range of Sa and Sz of three repeated noisy simulations are represented as the error bars.

The Sa of HART838 and EQI1571 are 14.3 µm and 14.5 µm respectively while the EQI838 is 15.0 µm. The range of the three repeats is negligible for the Sa. The Sz value of HART838 shows good agreement with the Sz value of EQI1571. The mean value Sz of EQI838 is approximately 40 µm larger than that of EQI1571 and HART838, which is roughly twice the voxel size and roughly about the same magnitude as the calculate 10%-90% resolution value. This jump of 40 µm could indicate that the reconstruction of EQI838 introduced errors into the extracted topography, most likely facilitated by the higher noise levels in the volume data. Overall this indicates that noise components are still present in the data. The range of the Sz value of HART838 is larger than the EQI1571, which might indicate that volume data noise could have caused variations in the topography data, which in turn affected the repeatability of the Sz value. The performance of the Sz value is positive and supports the merit of using HART over an equispaced reduction of projections. For all the investigated cases, the computed mean Sa values are within 0.8 µm of another, and the range of the repeat noisy simulations within each case is negligible. The Sa value of

HART838 and EQI1571 are 14.3 µm and 14.5 µm respectively, this close agreement indicates and supports the hypothesis that the topography is not significantly confounding by using the proposed HART.

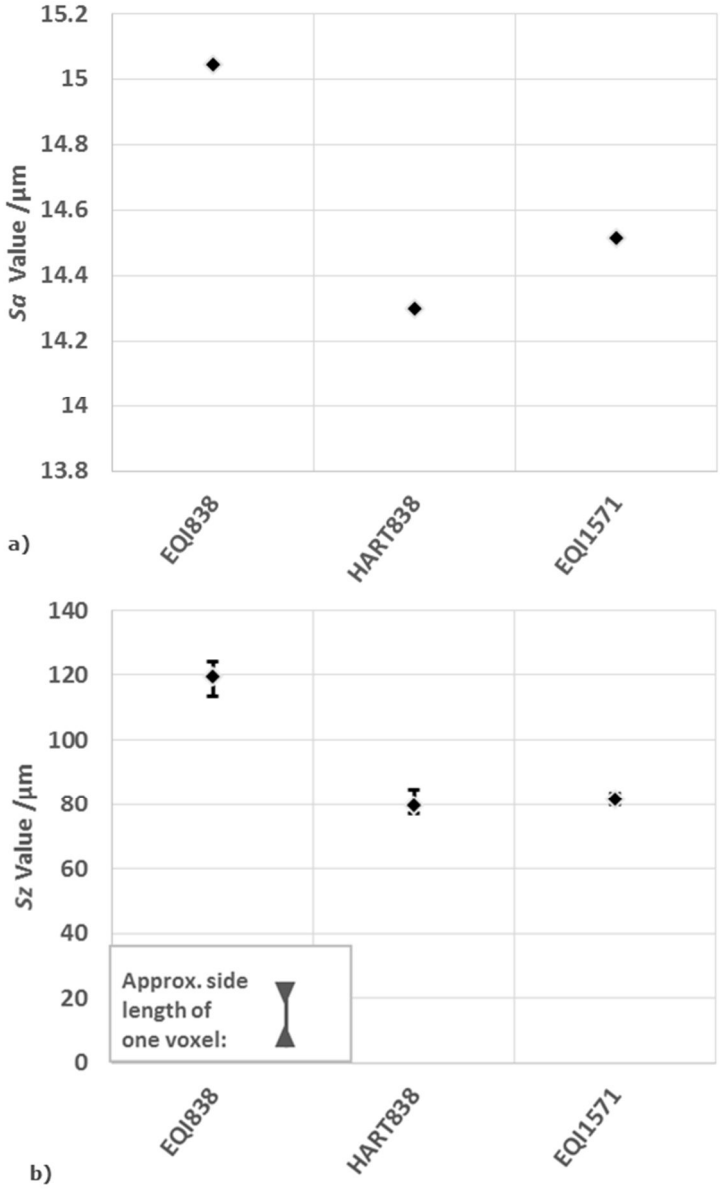

Figure 6-23 a) reports the mean Sa values of the three repeated noisy simulations. The range of the repeats is too small to be discernible as error bars. For all of the investigated cases, the range of the repeats fall within ±0.007 µm.
b) reports the mean Sz values. The error bars indicate the maximum range of the three repeat simulations.

6.5 Discussion

This chapter proposed a method to selectively locate projections around an object with a skewed aspect ratio. The proposed method is aimed at continuous motion acquisitions in XCT and as such it limits the motion blurring to be below one detector pixel for all the computed step angles. The work presented here is a simulated case study. The aim of the simulation is to explore the effect of continuous motion HART on the measurement of surface topographies using XCT. The HART projection spacing was calculated for the chosen test part. The projection spacing is reported in Figure 6-9, the total number of projections using the proposed HART method is 838. A conservative equispaced estimate for the number of continuous motion projections is 1571. Thus the proposed method allows a reduction of the acquisition times by approximately 47% for the investigated part. To reach the aim, two simulated cases were investigated, one which uses the HART projection spacing with 838 projections (HART838) and one equispaced case using 838 projections (EQI838). Both HART838 and EQI838 were compared against a reference case using 1571 projections (EQI1571). The degree of reduction is dependent on the part shape and a simplified relationship for cuboids was presented in Figure 6-10. Adding a constraint on the maximum allowed blur only added ten extra projections to the investigated test case.

The qualitative and quantitative image quality analysis both indicate that when reducing the number of projections using HART the image quality is superior compared to the equispaced reduction. Within the limitations of the utilised edge spread function, no discernible quantitative change in the locally analysed resolution was found, nor was any changes to the resolution discernible in the qualitative inspection of the reconstructed images. These positive findings indicating an advantage of using HART over a simple reduction is also reflected in the topography data. The CI width was improved by using HART over equispaced sinogram interpolation, and also improved the discrepancy ratio, which is reflected also in a smaller Sz value and a Sa, which agrees better with the slow acquisition.

There are some discussion points, which need to be highlighted. While the projection numerically evaluated reduction of projections was calculated for different aspect ratios, only one possible part with one aspect ratio was investigated. However, HART's foundation on the central slice theorem justifies a reasonable extrapolation to parts with other aspect ratios. Though the simulation used noisy data, it did not aim to simulate any other possible error sources such as motion stage errors, misalignments or any other random error components. So far only one arbitrarily chosen test part was investigated. However, a wider range of test parts could improve the generalisability of the continuous HART method. It would be interesting for future research to adopt the continuous motion projection spacing in a physical system. However, implementing continuous HART will require careful assessment in terms of object registration and the dynamics of the motion system.

Despite the limitations, overall the evidence suggests that HART spaced projections make the reconstruction more robust to noise when the number of projection is reduced, which ultimately translates into more precise surface topography data.

6.6 Chapter summary

It was demonstrated that the proposed HART projection spacing can lead to a reduction in the total number of projections, which is dependent on the object shape. Noisy simulation data was reconstructed and qualitatively inspected. The noise texture and behaviour of the HART reconstruction compares well against the reconstruction with more projections, which concludes that HART – at a reduced number of projections – is more robust to noisy projection data. This indicates that the proposed HART method is a promising technology to reduce the acquisition and even reconstruction times. The improvement of the reconstruction using HART is supported by the quantitative evaluation of the image quality. The quantitative noise estimate using Shannon entropy showed improved noise levels for the HART projection over the equispaced case when using a reduced number of projections. No significant changes in the resolution were observed. The advantage of the HART reconstruction also translates to the extracted surface topography data. The HART simulations showed a reduced width of the mean confidence interval, which indicates an improved precision of the extracted surface topography. The agreement to reference setup of the statistical surface models improved if using HART instead of equispaced projections when reducing the number of projections. While the findings are currently only limited to noisy simulated data, concluding, the presented evidence indicates that HART has the potential to reduce acquisition times while maintaining good quality reconstructed volumes and surface topographies for parts with skewed aspect ratios.

7 Discussion and conclusion

The presented work addresses the measurement time of surface topography measurement using X-ray computed tomography (XCT). XCT is a volumetric measurement technology and the volumetric nature is XCT's trump-card in comparison to traditional measurement technologies. The measurement time of XCT is a constraining factor in its industrial competitiveness. Particularly the acquisition time of the projection data is challenging as it can easily reach multiple hours for a high resolution but low noise acquisition. A recent report on the strategic positioning of XCT in the metrology market concluded that the measurement times needs to be decreased from hours to minutes [19]. With this industrial call for shorter measurement times in mind, the governing question behind the presented work arose as what methods exist to reduce the acquisition times and what characterises their effects on measurements of surface topography? The aim of this work is to identify and evaluate strategies, methods and approaches which reduce the required number of radiographs in XCT for the surface topography measurement.

The presented work firstly formulated a state-of-the-art review of the acquisition of radiographic projection data in XCT. The review focused on analytical reconstructions, due to their prominence in metrological applications of XCT. Topics covered were the synthesizing of virtual projections from experimentally acquired data, the variable spacing of the projection data along a circular trajectory, half scan data and region of interest approaches. Derived from the reviewed literature, two methods are examined in detail to assess their effects on the measurement of surface topography, namely sinogram interpolation (a method of synthesizing virtual projections) and high aspect ratio tomography (HART), a method to vary the projections spacing in analytical reconstructions.

A two-pillar methodology to assess both the reconstructed volume data and the measured surface topography is described in Chapter 4. Chapter 4 describes methods to quantify the image quality in terms of noise and resolution, as well as a statistical comparison approach

for assessing the precision and accuracy of surface topography measurement. Shannon entropy was used to measure the noise levels in the reconstructed volume data and an edge spread approach to quantify the resolution.

An approach to sinogram interpolation is explored in Chapter 5. Since it is not an analytical solution to handling data insufficiencies of the sinogram space, its parameter space is mapped out. The performance is evaluated against non-linear filtering operation and data-binning approaches. The precision and accuracy of the surface topography measurements are evaluated for a range of acquisition time improvements of 20% to 80%. At reduced acquisition times, sinogram interpolation under continuous motion is able to provide a reconstruction of reduced quality and the surface topography measurements at reduced levels of accuracy and precision.

The feasibility of HART and continuous motion is investigated in Chapter 6. HART uses a priori knowledge about the measurement object to reduce the number of projections. The reduced number of projections are unevenly spread across the circular trajectory. A case study is presented that analyses, using simulated noisy data, the effect of continuous motion HART. The case study showed that the variable spacing of projections improves the reconstructed volume and the precision and accuracy of the obtained surface topography, in comparison to reducing the number of projections but keeping them equispaced.

One of the objectives of this work was to devise a methodology to gauge the performance of different reconstruction methods. Overall, the utilised method (outlined in chapter 4) is sufficient to allow conclusions on the evaluated reconstruction approaches. Except for the resolution assessment, the utilised methods showed sufficient fidelity. The resolution assessment is confounded by noise. While noise is a fundamental issue, the utilised edge spread function attempted to overcome the limitations of noisy data by averaging of multiple edge spread functions. Nonetheless, the utilised edge spread function still showed – throughout chapters 5 and 6 – low precision. The obvious approach would be to attempt coherent averaging of multiple acquisitions, but this is not feasible for most investigations

and case studies, due to temporal limitations and instabilities. Further, the question arises if maybe one location of assessing the resolution might not be sufficient, given the nature of imaging artefacts (such as the aliasing artefacts in Figure 5-14). The approach of a single resolution value for an XCT system is in line with other approaches for measuring the resolution in XCT, such as [35,57,92] but is based on the limited assumptions of a homogenous resolution in reconstructed volumes. Further research is needed to carefully address the issue of assessing resolution, particular when significant a level of noise is present in the volume domain.

A further objective was to evaluate the performance of methods for reducing the measurement time in reference to surface topography measurements. Two methods were investigated in detail. The explored method of sinogram interpolation rendered itself as a powerful, yet a simple, computationally inexpensive operation. It improves the reconstruction quality once the projection sampling is grossly violated while it is capable of recovering some level of accuracy and precision of the measured surface topography. Hence, sinogram interpolation is a heuristic and 'lossy' method capable of reducing measurement time. Sinogram interpolation cannot recover the same reconstruction quality as an acquisition under perfect sampling. But, it was shown that useable data can still be extracted. This detailed mapping out of the parameter space is a useful contribution which expands the tool kit of the XCT application specialists. The second investigated method was HART in continuous motion. The HART reconstruction volumes and the obtained surface topographies presented higher levels of accuracy to the reference reconstruction than a projection reduction with equispaced projections spacing. While the measurement time saving is limited to the geometry of the object, time reductions were shown to be feasible. Experimental implementation is still needed, but the method was shown to be robust under noisy simulated conditions for the investigated part. The continuous motion HART method adds to the collective body of methods and approaches to reduce the measurement time in XCT. The simulation case study contributes to the XCT community by showcasing the effects of continuous motion HART.

The aim of this thesis was to identify and evaluate strategies, methods and approaches which reduce the required number of radiographs in XCT for the surface topography measurement. Both investigated methods (HART and sinogram interpolation) are shown to reduce the measurement time. As discussed in a more detailed level in sections 5.3.4, 5.2.5 and 6.5 there are limitations to the work.

Both chapter 5 and 6 of this work are limited to a single measured object each. As such these are case studies indicating the observed changes to the reconstruction quality and the obtained measurements. As such the findings can be used to assume parallels to other measurements only with limitations. The 'whole population of all XCT surface topography measurements' is not sampled enough in the case studies to draw generalisable conclusions. As such all findings can only be used as indicators of performance for the conscious XCT application specialist. This shortcoming is not limited to this work only, but it is a general and widespread issue in XCT, that currently there are no quantitative models that can predict the measurement uncertainty and the quality of the reconstructed images in XCT for any given object [1,40,85]. The exact nature of any XCT reconstruction depends on a large set of influencing factors, a lot of which are dependent on the geometry, material, orientation and placement of the part and system setup parameters such as acceleration voltage and power, exposure time [217], making the relationship between measurement uncertainty and object and system setup complex and hence limits analytical uncertainty estimation models [1,40,85]. In fact, the VDI/VDE 2630 1.2 [218] alone list over 50 influencing factors. Thus, the lack of generalised and quantitative prediction models and procedures on the tomographic process and of predicting the measurement uncertainty of any measurement in XCT translates directly into the limitations of this work, which in return, limits the achievement of the aim and affects the scope of the presented work. Furthering this issue, one has to recall that the collected projection/Radon data does not sample the part in the spatial domain. Following the central slice theorem, see section 2.2.1, the Radon data builds up the frequency sampling points of the imaged object. Hence, it is difficult to predict quantitatively and in detail how different objects will 'suffer' in the spatial domain when methods such as sinogram

interpolation and affect the frequency domain, which is even the case for unaltered filtered back projections. As such, there are no current benchmark objects or methods that are agreed by the research community that would allow one to draw a generalised but quantitative statement on the measurement uncertainty. Therefore case studies are used to highlight the effects of the different reconstructions. The use of case studies allows for the conscious XCT application scientist to judge if the investigated and presented methods in this thesis are of interest to his/her application, but realistically one cannot give a quantitative generalised prediction on how each any measurement will perform. This difficulty on precisely but quantitively relating different measurements of different objects also motivated the two pillar analysis technique, where both the extracted surface topography data are analysed and also the reconstructed image is analysed in terms of noise and resolution. This parallel approach allows for members of the research community who are interested in the technologies to understand the deterioration caused by the investigated XCT approaches.

The measurement chain used within this work is long and uses several different software tools. The tasks of the software tools range from reconstruction and surface determination to exporting the data into transferable data formats as well as the fitting algorithms. Especially the commercial software tools do not publish in detail the underlying principle and algorithms and hence a conclusion to what extent the data is manipulated can be difficult to draw. As such is challenging to comprehend and outline to what extent the measurement uncertainty and performance is determined by and affected by the different software tools. However, one should note that obtaining surface topography data from radiographic data is impossible without the use of reconstructions algorithms and other algorithmic procedures. This issue of using unknown software systems (or 'black boxes') further complicates any attempts of establishing generalised, quantitative and analytical measurement uncertainties estimation models. The exact implementation of the underpinning algorithms will directly affect the performance in terms of robustness and fidelity. As such it is questionable if the results obtained within this work can be replicated if other commercial and non-commercial surface determination, export and reconstruction

algorithms are used. While establishing traceability in XCT was not focus of this work, traceability alongside with uncertainty remains an open question for the XCT community. This work focused on comparatively assessing the measurement results using statistical tools and comparing them to slow reference measurements. The quantities of interest were not compared to a traceable measurement, as this work focused on describing and establishing the deterioration caused by reducing the measurement time, and not to focus on the difference of cross sensor comparison of measurement results.

There are several methods reviewed in the literature section, but only two were investigated in detail based on the reported performance in the literature. Both methods investigated in chapters 5 and 6 reduced the number of projections without adding a significant computational burden. This decision was made as the literature review indicated an improved reconstruction quality while reducing the measurement time. The chosen methods are of interest to the research and industry community since they – unlike iterative techniques [137] – do not significantly increase the computation. Therefore the chosen methods are of interest to potential industrial applications, as the measurement and the machine time are reduced without causing an excessive increase in the computational time. The additional However, the author believes that future work will likely continue to decrease the measurement times further by the heuristically exploring the capabilities of machine learning or even significant technological advances to the underpinning X-ray production and detecting principles, such as the currently under development laser driven hard X-ray sources [219]. Further, though, the overall reviewed methods in chapter 3 and the investigated methods in chapter 5 and 6 indicated that once one is deviating from good practice by reducing the number of projections, it is difficult to recover the image quality and thus maintain a low measurement uncertainty and one has to acknowledge that the reduction in the number of projections causes sacrifices with the current state of the art techniques. This work, however, highlighted one method that can be universally applied to all reconstructions, the sinogram interpolation and the HART method that can only be used on parts with high aspect ratios. While the presented work focused on the measurement time and the investigated methods addressed a reduction of

the measurement by reducing the collected projection data. The presented work used case studies to highlight the effect of sinogram interpolation and HART. Both methods successfully demonstrated in their case studies the effects on the measurement results when applying these methods. This work is one of the first studies looking into exploring computational and sampling schemes to reduce not just the measurement time but also by reducing the number of projections the methods also reduce the acquisition time on the system. However, the methods investigated are not capable to push the measurement times from 'hours to minutes' and do suffer symptoms in terms of precision of the measurement. Overall the methods address the interests of the XCT community and contributed to the collective body of knowledge.

7.1 Contributions

The presented work addresses some of the wider industrial aspects of the metrological XCT community. The work contributed by the review and dissemination of technical knowledge in the field of tomographic principles and methods which focus on the acquisition of radiographic projections.

The work utilised a novel analysis approach which benefits from carrying out the analysis in a two-pillar approach: with a method to understand and quantify the deterioration caused in the reconstructed volume, and with a method to quantify the effects on the measured surface topography.

The presented material addresses an important industrial facet of XCT in the modern manufacturing environment: the measurement time. By using case studies, the work demonstrates and showcases the ability of the investigated methods of sinogram interpolation and HART. The work presented is one of the earlier metrological works which focuses on decreasing the measurement time of XCT and analysing the effects on the measurement of surface topography data.

A further contribution is a detailed evaluation of sinogram interpolation. The evaluation of sinogram interpolation is performed in the context of surface metrology and is one of the

first published works on reducing the measurement time of XCT in the metrological setting. The work maps out the effects compensating a reduced number of projections by sinogram interpolation, and thus reduce measurement time, and highlights sinogram interpolation as a further tool to XCT community.

The presented work contributes to the collective body of knowledge with a case study into the feasibility of high aspect ratio tomography for surface topography measurement. The presented work contributed with a numeric approach to evaluate the HART projection spacing under continuous motion and a detailed evaluation of the effects on the reconstructed volume data and the effects on the measured surface topography.

7.2 Conclusion

This thesis focused on reducing the measurement time in X-ray computed tomography for measuring surface topographies. Originating from the medical diagnostic use, XCT is a 3D volumetric imaging technique. It relies on the penetrative power of X-ray radiation to reconstruct the internal and external shape of an object. Long measurement times in XCT are a hurdle for the large spread industrial acceptance of XCT. While the interaction of setup parameters, system identities and operator expertise are complex and all affect the measurement time, the focus of this work is on the use of radiographs in the analytical reconstruction process. The aim of this work is to identify and evaluate strategies, methods and approaches which reduce the required number of radiographs in XCT for the surface topography measurement.

A review was conducted with a focus on projection acquisition for analytical reconstruction techniques. The scope looks into the ways the projection data is acquired to improve the reconstruction quality or increase the speed of XCT. Based on the review, two methods are investigated in detail, namely sinogram interpolation and high aspect ratio tomography (HART). For analysing the effects of the two methods, a two-pillar analysis method was used. The analysis is based on both analysing the reconstructed volume to assist the understanding of the distorting effects on the reconstructed volume in more depth, but also to quantify the effects directly on the measured surface topography. While using the

Shannon entropy for the image noise analysis proved itself to be of sufficient precision and a helpful figure of merit, the resolution assessment of using an edge spread function on the volume data showed to be of limited precision for detecting subvoxel changes to the volume's resolution.

Reducing the number of projections is of interest to the research community and the industrial community, as using large flat panel X-ray detectors with many detector pixels requires large sets of projections in the reconstruction. Depending on the exact exposure time, the large number of projections required yields a large acquisition time, which challenges the economic desires of modern metrology environments. When the number of projections is reduced beyond the minimum number required, imaging artefacts, aliasing and noise start to distort the reconstructed volume and thus affect the precision and accuracy of the measurement. A computationally inexpensive method to suppress some of the negative effects of reducing the number of projections is sinogram interpolation. This method showed to be of good performance and can be used on any desired objects. This work showcased by means of a case study what interactions of noise and resolution will likely occur when sinogram interpolation is used to reduce the measurement time.

Another technique was investigated using a simulation case study. The case study was carried out to assess the feasibility of combing HART principles with continuous motion tomography. In analytical reconstructions, the principle behind HART creates a non-equispaced distribution of protections around an object with a high aspect ratio. The total number of projections needed in the reconstruction is reduced since for some views very large step angles are feasible, and thus a reduction in the measurement time can be realised. The HART method is however limited to objects with a high aspect ratio, the reconstructed surface topography showed minimal distortions in the case study. This indicates that the proposed continuous motion HART method is a promising technology to reduce the acquisition and even reconstruction times.

Concluding, the work contributed to the XCT research community by two detailed case studies. The case studies highlight the effects of the investigated methods, HART and

sinogram interpolation, and brought the methods and an example of their effects on the reconstructed volume and surface topography data to the consideration of the XCT research community.

7.3 Future work

Most importantly, the presented work here is certainly not the end but is just a single attempt to explore the infinite space of engineering possibilities of reconstructing surface topography data from radiographic images. The author strongly believes that many more evaluations of medical techniques will be published in the metrological context and novel approaches will follow. Iteratively techniques are not included in the evaluation of the presented work, due to their long reconstruction times. The feasibility of exploiting machine learning and artificial intelligence should be assessed, initial works in the medical field have already started [202]. Sinogram interpolation lends itself as an avenue for the potential exploitation of machine learning. A potential research ansatz is to replace the sinogram interpolation method by a machined learned interpolation technique. In fact, a combined approach to both suppress noise and interpolate the sinogram space could be an interesting research aim for a machine learning task. If of an adequate nature, such a combined approach would be of interest to the wider research community and potentially with significant impact.

While the literature highlights the computational burden, it would be still of interest to gauge the effects of some of the main iterative techniques with a reduced number of projections. One potential approach to tackle the computational burden of the iterations would be the use of simulated a priori data in the reconstruction process. A good initial simulated approximation of the object affects the solution convergence and thus the number of iterations in IRT. Exploring the effects and the feasibility would be an interesting starting point to reduce the reconstruction time and computational burden of convergence of the iterative reconstruction process.

Based on the reviewed literature, one area which allows for an increased resolution of the reconstructed volume data is the use of interlacing scan strategies and quarter offsets of

the imaging system. While details on this technique have been published before (e.g. [64,67,143,144]), simulation and experimental study on the noise and resolution of the interlacing scan strategies would assist the research community. By reducing the sampling distance, a change of the noise characteristics will be expected due to the fundamental stochastics of photon noise. Especially how the changed noise characteristics affect the measurement time would be an interesting discussion contributing to the industrial advancement of the XCT community.

The use of estimations of the full radiographic data is one approach to avoid truncation artefacts in region of interest scans, see section 3.4. Analytical, algorithmic or heuristic methods are needed but difficult to derive to estimate the full radiographic data of the imaged object in region of interest scans. It would be an interesting ansatz to assess the feasibility of using heuristic machine learning methods to synthesise the missing sinogram data from a region of interest sinogram. The synthesised data could then be used to suppress the truncation artefacts.

Looking beyond the focus of this work, one fundamental need of the XCT community is the development and distribution of useable, realistic and practical uncertainty estimation methods. Since the imaging process is complex, and thus limits traditional uncertainty budgeting models, the author believes uncertainty estimates which build on the local changes in the volume data (such as in [220,221]) and combine these with geometrical calibration data of XCT systems could lead to a feasible and yet practical approach to uncertainty estimation in XCT.

The presented work focused only on using the radiographs in the reconstruction process, rather than exploring the parameter space which dictates the imaging process, such as X-ray spectrum, exposure time, etc. While some work such as [101,102] started to propose optimisation tools for acquisition settings of radiographs, further tools are needed to help the community in planning and optimising XCT settings.

Appendix A

Pseudocode 1

While cumulative rotation angle <360

Calculate the largest distance from centre of rotation along iso-ray direction

Using this distance, calculate the number of projection for a full rotation:

$n = \pi \cdot l$ where l is the largest distance in detector pixels

Calculate step angle, θ by $\theta = 360/n$

Rotate point cloud by θ

Pseudocode 1 Method of calculating the projection density from a point cloud.

Pseudocode 2

While cumulative rotation angle <360

Calculate largest distance from centre of rotation along iso-ray direction

Using this distance, calculate the number of projection for a full rotation:

$n = \pi \cdot l$ where l is the largest distance in detector pixels

Calculate step angle, θ by $\theta = 360/n$

While projected blur caused by step angle > than blur limit

θ = decrease θ by decrement

Rotate point cloud by θ

Pseudocode 2 Extending Pseudocode 1 by a numerical decrementing approach to limit the step angle to avoid motion blurring

Publications and conference submissions

VAITHILINGHAM J, SALEH E, KÖRNER L, WILDMAN R D, HAGUE R, LEACH R K and TUCK C, 2017. Three-dimensional inkjet printing of macro structures from silver nanoparticles Materials & Design, Contribution: Performed the XCT analysis

THOMPSON A, KÖRNER L, SENIN N, LAWES S, MASKERY I and LEACH R K, 2017. Measurement of the internal surface texture of additively manufactured parts by X-ray computed tomography 7th Conf. Industrial Computed Tomography (Leuven, Belgium) Contribution: Contributed to the discussion

NASROLLAHI V, PENCHEV P, DIMOV S, KÖRNER L, LEACH R K and KYNGHAN K, 2017. Two-side processing method for producing high-aspect ratio micro holes ASME J. Micro Nano. Manufac. 5, 041006-14, Contribution: Performed the XCT analysis

THOMPSON A, SENIN N, MASKERY I, KÖRNER L, LAWES S and LEACH R K, 2018. Internal surface measurement of metal powder bed fusion parts Additive Manufacturing. 20, 126-133, Contribution: Contributed to the discussion

KÖRNER L, SU R, LAWES S, SENIN N and LEACH R, 2018 Development of an X-ray radiograph simulator: from STL file to grey scale image Conference: euspen 2018 In: Venice, Italy, Contribution: Main author, and developer of core of the presented work

KÖRNER L, LAWES S, NEWTON L, SENIN N and LEACH R 2018 Effects of sinogram interpolation for increasing throughput rate of surface topography measurements using X-

ray computed tomography Conference: Dimensional X-ray Computed Tomography In: Nottingham, UK, Contribution: Main author, created design of experiments and methods and developer of core of the work

KÖRNER L, LAWES S, NEWTON L, SENIN N, BATE D and LEACH R 2018 Sinogram interpolation to decrease acquisition time in X-ray computed tomography measurement of surface topography Conference: Proceedings of the 9th international conference on industrial computed tomography In: Padua, Italy, Contribution: Main author, created design of experiments and methods and developer of core of the work

VILLARRAGA-GÓMEZ H, KÖRNER L, LEACH R and SMITH S 2018 Representing the specification of industrial X-ray computed tomography with amplitude-wavelength space Conference: Proceedings of ASPE 32nd Annual Meeting In: Las Vegas, NV (USA). Contribution: contributed to the discussion and the proposed resolution and size limits of XCT, developed a polyspectral X-ray simulation tool

KÖRNER L, LAWES S, BATE D, NEWTON L, SENIN N and LEACH R 2019 Increasing throughput in X-ray computed tomography measurement of surface topography using sinogram interpolation Measurement Science and Technology Vol 30 125002, Contribution: Main author, created design of experiments and methods and developer of core of the work

References

[1] Kruth J P, Bartscher M, Carmignato S, Schmitt R, De Chiffre L and Weckenmann A 2011 Computed tomography for dimensional metrology CIRP Ann. - Manuf. Technol. 60 821–42

[2] Townsend A, Pagani L, Scott P and Blunt L 2017 Areal surface texture data extraction from X-ray computed tomography reconstructions of metal additively manufactured parts Precis. Eng. 48 254–64

[3] Carmignato S, Dewulf W and Leach R K 2018 *Industrial X-Ray Computed Tomography* (Cham, Switzerland: Springer International Publishing)

[4] Thompson A, Maskery I and Leach R K 2016 X-ray computed tomography for additive manufacturing: a review Meas. Sci. Technol. 27 1–17

[5] Leach R, Thompson A, Senin N and Maskery I 2017 A metrology horror story: The additive surface *ASPEN/ASPE Spring Topical Meeting on Manufacture and Metrology of Structured and Freeform Surfaces for Functional Applications* (Hong Kong)

[6] Townsend A, Senin N, Blunt L, Leach R K and Taylor J S 2016 Surface texture metrology for metal additive manufacturing: a review Precis. Eng. 46 34–47

[7] du Plessis A, Yadroitsev I, Yadroitsava I and Le Roux S G 2018 X-Ray Microcomputed Tomography in Additive Manufacturing: A Review of the Current Technology and Applications 3D Print. Addit. Manuf. 5

[8] Thompson A, Senin N, Maskery I, Körner L, Lawes S and Leach R K 2018 Internal surface measurement of metal powder bed fusion parts Addit. Manuf. 20 126–33

[9] Zanini F, Sbettega E and Carmignato S 2018 X-ray computed tomography for metal additive manufacturing: challenges and solutions for accuracy enhancement Procedia CIRP 75 114–8

[10] Zanini F, Pagani L, Scott P, Savio E and Carmignato S 2018 Measurement of

additively manufactured surfaces with re-entrant features by X-ray computed tomography *Proc. of ASPE and euspen Summer Topical Meeting - Advancing Precision in Additive Manufacturing* (Berkeley, California (USA))

[11] Zanini F and Carmignato S 2018 X-ray computed tomography for measurement of additively manufactured threaded parts *Proc. of ASPE and euspen Summer Topical Meeting - Advancing Precision in Additive Manufacturing* (Berkeley, California (USA))

[12] du Plessis A, Sperling P, Beerlink A, Kruger O, Tshabalala L, Hoosain S and Le Roux S 2018 Standard method for microCT-based additive manufacturing quality control 3: Surface roughness MethodsX 5 1111–6

[13] Ferrucci M, Leach R, Giusca C, Carmignato S and Dewulf W 2015 Towards geometrical calibration of x-ray computed tomography systems-a review Meas. Sci. Technol. 26

[14] Hiller J 2007 *Abschatzung von Unsicherheiten bem dimensionellen Messen mit CT (Dissertation)* (University of Freiburg)

[15] Flay N 2016 *An investigation of the factors associated with the x-ray tube and their influence on dimensional measurement in micro-focus cone-beam industrial x-ray computed tomography systems (Dissertation)* (Univeristy of Southampton)

[16] Lifton J J 2015 *The Influence of Scatter and Beam Hardening in X-ray Computed Tomography for Dimensional Metrology (Dissertation)* (University of Southampton)

[17] Hiller J, Genta G, Barbato G, De Chiffre L and Levi R 2014 Measurement uncertainty evaluation in dimensional X-ray computed tomography using the bootstrap method Int. J. Precis. Eng. Manuf. 15 617–22

[18] Dewulf W, Kiekens K, Tan Y, Welkenhuyzen F and Kruth J P 2013 Uncertainty determination and quantification for dimensional measurements with industrial computed tomography CIRP Ann. - Manuf. Technol. 62 535–8

[19] Frost and Sullivan 2015 *Strategic Analysis of Computed Tomography Technology in the Dimensional Metrology Market (Report)*

[20] Coordinator Neuschaefer-Rube PTB *AdvanCT project Annex I – JRP protocol Advanced Computed Tomography for dimensional and surface measurements in industry (Report)*

[21] A Joint Research Project within the European Metrology Research Programme EMPIR AdvanCT Advanced Computed Tomography for dimensional and surface measurements in industry https://www.ptb.de/empir2018/advanct/home/

[22] Joseph P M and Schulz R a 1980 View sampling requirements in fan beam computed tomography. Med. Phys. 7 692–702

[23] Anon 2012 JCGM 200 : 2012 International vocabulary of metrology – Basic and general concepts and associated terms (VIM) 3rd edition Vocabulaire international de métrologie – Concepts fondamentaux et généraux et termes associés (VIM) 3 e édition

[24] NPL 2019 *The measure of all things. An info brochure on the recent redefinitions of the SI base units* (Teddington, London: NPL)

[25] Leach R and Smith S T 2018 *Basics of Precision Engineering* (Boca Raton, Fl, USA: CRC Press)

[26] Senin N, Thompson A and Leach R K 20117 Characterisation of the topography of metal additive surface features with different measurement technologies Meas. Sci. Technol. 28

[27] digitalsurf Filtration Techniques for Surface Texture [Accessed on: August 6, 2019] https://guide.digitalsurf.com/en/guide-filtration-techniques.html

[28] Leach R *Good Practice Guide No. 37 The Measurement of Surface Texture using Stylus Instruments*

[29] Leach R 2013 *Characterisation of areal surface texture* (Berlin, Germany: Springer-Verlag)

[30] Pyka G, Kerckhofs G, Schrooten J and Wevers M 2013 The effect of spatial micro-CT image resolution and surface complexity on the morphological 3D analysis of

open porous structures Mater. Charact. 87 104–15

[31] Werth Messtechnik GmbH Werth Messtechnik GmbH [Accessed on: February 9, 2018] www.werth.de

[32] GOM GmbH GOM GmbH [Accessed on: February 9, 2018] https://www.gom.com

[33] WENZEL Group GmbH & Co. KG WENZEL Group GmbH & Co. KG [Accessed on: February 9, 2018] https://www.wenzel-group.com/en/

[34] Borges de Oliveira F, Stolfi A, Bartscher M, De Chiffre L and Neuschaefer-Rube U 2016 Experimental investigation of surface determination process on multi-material components for dimensional computed tomography Case Stud. Nondestruct. Test. Eval. 1 1–11

[35] Fleßner M, Vujaklija N, Helmecke E and Hausotte T 2014 Determination of metrological structural resolution of a CT system using the frequency response on surface structures *Proc. MacroScale* (Vienna, Austria)

[36] Lifton J J, Malcolm A A and McBride J W 2015 On the uncertainty of surface determination in x-ray computed tomography for dimensional metrology Meas. Sci. Technol. 26

[37] Bartscher M, Neukamm M, Hilpert U, Rube U N-, Härtig F, Kniel K, Ehrig K, Staude A and Goebbels J 2010 Achieving traceability of industrial computed tomography Key Eng. Mater. 437 79–83

[38] Jiménez R, Torralba M, Yagüe-Fabra J, Ontiveros S and Tosello G 2017 Experimental Approach for the Uncertainty Assessment of 3D Complex Geometry Dimensional Measurements Using Computed Tomography at the mm and Sub-mm Scales Sensors 17

[39] Muller P, Hiller J, Dai Y, Andreasen J L, Hansen H N, Chiffre L De and Mu P 2014 Estimation of measurement uncertainties in X-ray computed tomography metrology using the substitution method CIRP J. Manuf. Sci. Technol. 7 222–32

[40] Cuadra J A, Divin C and Panas R M 2017 Uncertainty Quantification of an X-ray

Computed Tomography System *Joint Special Interest Group meeting between euspen and ASPE Dimensional Accuracy and Surface Finish in Additive Manufacturing* (Leuven, Belgium)

[41] Weckenmann A and Krämer P 2009 Assessment of measurement uncertainty caused in the preparation of measurements using computed tomography *19th IMEKO World Congress 2009* vol 3(Lisbon, Portugal)pp 1787–91

[42] Hiller J and Reindl L M 2012 A computer simulation platform for the estimation of measurement uncertainties in dimensional X-ray computed tomography Meas. J. Int. Meas. Confed. 45 2166–82

[43] Kraemer P M 2012 *Simulationsgestützte Abschätzung der Genauigkeit von Messungen mit Röntgen-Computertomographie (Dissertation)* (Universität Erlangen-Nürnberg)

[44] Verein deutscher Ingenieure e.V. 2015 Computed tomography in dimensional measurement Determination of the uncertainty of measurement and the test process suitability of coordinate measurement systems with CT sensors VDI/VDE 2630-2.1

[45] Schmitt R and Niggemann C 2010 Uncertainty in measurement for x-ray-computed tomography using calibrated work pieces Meas. Sci. Technol. 21 54008

[46] ISO 2011 *ISO 14253-2:2011 Geometrical product specifications (GPS) — Inspection by measurement of workpieces and measuring equipment Part 2 : Guidance for the estimation of uncertainty in GPS measurement , in calibration of measuring equipment*

[47] 213 I 2011 ISO 15530-3:2011 Geometrical product specifications (GPS) -- Coordinate measuring machines (CMM): Technique for determining the uncertainty of measurement -- Part 3: Use of calibrated workpieces or measurement standards

[48] Committee of the ISO10360-11 *Unpublished status report and communication of the ISO 10360-11,* July 2017

[49] Verein deutscher Ingenieure e.V. 2009 Computed tomography in dimensional measurement Basics and definitions VDI/VDE 2630-1.1 1–35

[50] Bartscher M, Bremer H, Birth T, Staude A and Ehrig K 2012 The resolution of dimensional CT – an edge-based analysis *iCT2012: Conf. on Industrial Computed Tomography* (Wels, Austria) pp 191–201

[51] Carmignato S, Dreossi D, Mancini L, Marinello F, Tromba G and Savio E 2009 Testing of x-ray microtomography systems using a traceable geometrical standard Meas. Sci. Technol. 20 84021

[52] Lonardoni D W R, Deffner A and Kuhn C 2012 Geometric image distortion in flat-panel {X}-ray detectors and its influence on the accuracy of {CT}-based dimensional measurements *4th International Conference on Industrial Computed Tomography*

[53] Bircher B A, Meli F, Küng A and Thalmann R 2018 A geometry measurement system for a dimensional cone-beam CT iCT2018 8th confrence Ind. Comput. Tomogr. 1–7

[54] Lifton J J, Malcolm A A, Mcbride J W and Cross K J 2013 The Application of Voxel Size Correction in X-ray Computed Tomography for Dimensional Metrology *Singapore International NDT Conference & Exhibition* pp 19–20

[55] Welkenhuyzen F, Kiekens K, Pierlet M, Dewulf W, Bleys P and Voet A 2008 Industrial computer tomography for dimensional metrology : Overview of influence factors and improvement strategies *4th Int. Conf. on Optical Measurement Techniques* (Antwerp, Belgium) pp 1–9

[56] Carmignato S, Aloisi V, Medeossi F, Zanini F and Savio E 2017 Influence of Surface Roughness on Computed Tomography Dimensional Measurements CIRP Ann. - Manuf. Technol. 66 499–502

[57] Arenhart F A, Nardelli V C, Donatelli G D, Porath M C, Isenberg C and Schmitt R 2013 Design of a Multi-Wave Standard to Evaluate the Frequency Response of CT Measuring Systems *11th International Symposium on Measurement and Quality*

Control (Cracow-Kielce, Poland)

[58] Senin N 2018 xLib library, unpublished

[59] Digital Surf Mountains® France

[60] Pagani L, Qi Q, Jiang X and Scott P J 2017 Towards a new definition of areal surface texture parameters on freeform surface Measurement 109 281–91

[61] ASTM Standard Terminology for Additive Manufacturing Technologies F2792–12a

[62] Thompson A, Senin N, Giusca C and Leach R K 2017 Topography of selectively laser melted surfaces : A comparison of different measurement methods CIRP Ann. - Manuf. Technol. 66 543–6

[63] Zhang J 2019 Micro-blasting of 316L tubular lattice manufactured by laser powder bed fusion *European Society for Precision Engineering and Nanotechnology, Conference Proceedings - 19th International Conference and Exhibition, EUSPEN 2019* pp 254–5

[64] Hsieh J 2009 *Computed Tomography* (Bellingham, Washington: SPIE Press)

[65] Deans R S 1983 *The Radon Transform and Some of Its Applications* (New York: Wiley, 1983.)

[66] Barret H and Swindell W 1981 *Radiological Imaging The theory of Image formation, Detection, and Processing Volume 1* (New York, USA: Academic Press)

[67] Kalender W A 2000 *Computed Tomography: Fundamentals, System Technology, Image Quality, Applications* (Weinheim, Germany: Publicis)

[68] Beister M, Kolditz D and Kalender W A 2012 Iterative reconstruction methods in X-ray CT Phys. Medica 28 94–108

[69] Hsieh J, Nett B, Yu Z, Sauer K, Thibault J-B and Bouman C A 2013 Recent advances in CT image reconstruction Curr. Radiol. Rep. 1 39–51

[70] Barrett H, Swindell W, Barret H and Swindell W 1981 *Radiological Imaging The theory of Image formation, Detection, and Processing Volume 2* (New York, USA: Academic Press)

[71] Natterer F 1986 *The Mathematics of Computerized Tomography* (Chichester: John Wiley & Sons)

[72] Buzug T 2004 *Einfuehrung in die Computertomographie. Mathematisch-physikalische Grundlagen der Bildrekonstruktion.* (Berlin, Germany: Springer)

[73] McCullough E C 1977 Reconstruction Tomography in Diagnostic Radiology and Nuclear Medicine Radiology 125

[74] Zhao Z, Gang G J and Siewerdsen J H 2014 Noise, sampling, and the number of projections in cone-beam CT with a flat-panel detector. Med. Phys. 41

[75] Buratti A, Achour S Ben, Isenberg C and Schmitt R 2016 Frequency - based method to optimize the number of projections for industrial computed tomography *6th Conference on Industrial Computed Tomography* (Wels, Austria) pp 1–8

[76] Kalender W A 2011 *Computed Tomography: Fundamentals, System Technology, Image Quality, Applications* (Weinheim, Germany: Publicis)

[77] Hsieh J 2009 *Computed Tomography: Principles, Design, Artifacts, and Recent Advances* (Bellingham, Washington: SPIE)

[78] Brooks R A, Weiss G H and Talbert A J 1978 A New Approach to Interpolation in Computed Tomography. J. Comput. Assist. Tomogr. 2

[79] Schäfer D, Grass M and van de Haar P 2011 FBP and BPF reconstruction methods for circular X-ray tomography with off-center detector. Med. Phys. 38

[80] Bartscher M, Staude A, Ehrig K and Ramsey A 2012 The influence of data filtering on dimensional measurements with CT *18th World Conference on Nondestructive Testing* (Durban, South Africa) pp 1–13

[81] Feldkamp L A, Davis L C and Kress J W 1984 Practical cone-beam algorithm J. Opt. Soc. Am. 1 612

[82] Seeram E 2016 *Computed Tomography: Physical Principles, Clinical Applications, and Quality Control* (St. Louis, USA: Saunders Elsevier)

[83] Grimmer R, Oelhafen M, Elstrøm U and Kachelrieß M 2009 Cone-beam CT image

reconstruction with extended z range Med. Phys. 36 3363–70

[84] Tuy H K 1983 An inversion formulas for cone-beam reconstruction J. Appl. Math. 43 546–52

[85] Christoph R and Neumann H 2011 *X-ray Tomography in Industrial Metrology* (81677 Munich: Süddeutscher Verlag onpact GmbH)

[86] Grangeat P 1991 *Mathematical framework of cone-beam 3D reconstruction via the first derivative of the Radon transform* (Berlin, Germany: Springer)

[87] Defriese M and Clack R 1994 A cone beam reconstruction algorithm using shift-variant filtering and cone beam backprojection IEEE Trans. Med. Imaging 13 186–95

[88] Katsevich A 2012 Theoretically exact filtered backprojection-type inversion algorithm for spiral CT Soc. Ind. Appl. Math. 62 2012–26

[89] Leach R, Giusca C, Henning A, Sherlock B and Coupland J 2014 ISO definition of resolution for surface topography measuring instruments *Fringe 2013 - 7th International Workshop on Advanced Optical Imaging and Metrology* pp 405–10

[90] Sparrow C M 1916 On Spectroscopic Resolving Power Astrophys. J. 44 76

[91] Abbe E 1874 A contribution to the theory of the microscope and the nature of microscopic vision Proc. Bristol Nat. Soc. 1 1 200–61

[92] ICRU 2012 Report No.87: Radiation Dose and Image-Quality Assessment in Computed Tomography J. Int. Comm. Radiat. Units Meas. Publ. by Oxford Univ. Press 12

[93] Arenhart F A, Nardelli V C and Donatelli G D 2015 Characterization of the metrological structural resolution of CT systems using a multi-wave standard *XXI IMEKO World Congress "Measurement in Research and Industry"* (Prague, Czech Republic) pp 1–6

[94] Illemann J, Bartscher M, Jusko O, Härtig F, Neuschaefer-Rube U and Wendt K 2014 Procedure and reference standard to determine the structural resolution in

coordinate metrology Meas. Sci. Technol. 25

[95] Weiß D, Shi Q and Kuhn C 2012 Measuring the 3D resolution of a micro-focus X-ray CT setup Conf. Ind. Comput. Tomogr. 1–9

[96] European Committee for Standardization Non-destructive testing -- Radiation methods -- Computed tomography -- Part 2: Examination practices ISO 15708-2

[97] Verein deutscher Ingenieure e.V. Computed tomography in dimensional measurement Guideline for the application of DIN EN ISO 10360 for coordinate measuring machines with CT sensors VDI/VDE 2630-1.3

[98] Bartscher M, Neuschaefer-Rube U, Illemann J, Borges de Oliveira F, Stolfi A and Carmignato S 2018 Qualification and Testing of CT Systems *Industrial X-Ray Computed Tomography* ed S Carmignato, W Dewulf and R Leach (Cham, Switzerland: Springer)

[99] Carmignato S, Pierobon A, Rampazzo P, Parisatto M and Savio E 2012 CT for industrial metrology-accuracy and structural resolution of CT dimensional measurements *Conf. Industrial Computed Tomography (iCT)* (Wels, Austria)

[100] Hiller J, Fuchs T O J, Kasperl S and Reindl L M 2011 Einfluss der Bildqualität röntgentomographischer Abbildungen auf Koordinatenmessungen: Grundlagen, Messungen und simulationen Tech. Mess. 78 334–47

[101] Kraemer A, Kovacheva E and Lanza G Projection based evaluation of CT image quality in dimensional metrology *Digital Industrial Radiology and Computed Tomography (DIR 2015) 22-25 June 2015* pp 1–10

[102] Schabunow A 2018 *Einstellung von Aufnahmeparametern mittels projektionsbasierter Qualitätskenngrößen in der industriellen Röntgen-Computertomographie (Dissertation)* (Karlsruhe: Shaker Verlag)

[103] Handel H 2009 *Medizinsche Bildverarbeitung* (Wiesbaden, Germany: Vieweg+Teubner)

[104] Yu L and Pan X 2003 Half-scan fan-beam computed tomography with improved

noise and resolution properties Med. Phys. 30 2629–37

[105] Baek J and Pelc N J 2011 Effect of detector lag on CT noise power spectra Med. Phys. 38 2995–3005

[106] DeVries H 1943 The qunatum character of light and its bearing upon thrshold of vision, the differential sensitivity and visual acuity of the eye Physica(Utrecht) 10 553

[107] Rose A 1948 The sensitivity of the eye on an absolute scale J. Opt. Soc. Am 38 196

[108] Schielein R, Schröpfer S, Kiunke M, Zabler S and Kasperl S 2014 Quantitative evaluation of CT Images by means of Shannon Entropy *11th European Conference on Non-Destructive Testing* (Prague, Czech Republic) pp 2–4

[109] Als-Nielsen J and McMorrow D 2011 *Elements of Modern X-ray Physics* (Chichester, UK: John Wiley & Sons, Inc.)

[110] Pavlinsky G V 2008 *Fundamentals of x-ray physics* (Cambridge, UK: Cambridge International Science Publishing Ltd)

[111] Hernandez A M, Boone J M and Hernandez A M 2014 Tungsten anode spectral model using interpolating cubic splines : Unfiltered x-ray spectra from 20 kV to 640 kV Med. Phys. 42

[112] Comet Group Datasheet XRS-Modules Generators [Accessed on: October 25, 2016] http://www.comet-xray.com/resources/broschuren/datenblatt/xrs-modules---generators.pdf

[113] Nickoloff E L and Berman H L 1993 Factors Affecting X-ray Radiographics 13 1337–48

[114] Mehranian A, Ay M R, Alam N R and Zaidi H 2010 Quantifying the effect of anode surface roughness on diagnostic x-ray spectra using Monte Carlo simulation. Med. Phys. 37 742–52

[115] Tennet W 1970 *The Diagnostic X-Ray Tube* (Surrey: Mullard educational service)

[116] De Chiffre L, Carmignato S, Kruth J-P, Schmitt R and Weckenmann a. 2014

Industrial applications of computed tomography CIRP Ann. - Manuf. Technol. 63 655–77

[117] Hubbell J H 1982 X-Ray Mass Attenuation Coefficients Int. J. Appl. Radiat. Isot. 33 1269–90

[118] Radiation Physics Division PML NIST 2004 NIST: X-Ray Mass Attenuation Coefficients [Accessed on: November 8, 2016] www.nist.gov

[119] Beer 1852 Bestimmung der Absorption des rothen Lichts in farbigen Flüssigkeiten Ann. Phys. 162 78–88

[120] Barret H and Swindell W 1981 *Radiological Imaging The theory of Image formation, Detection, and Processing Volume 2* (New York, USA: Academic Press)

[121] Seibert J A and Boone J M 2005 X-ray imaging physics for nuclear medicine technologists. Part 2: X-ray interactions and image formation J. Nucl. Med. Technol. 33 3–18

[122] Radiopaedia.org https://radiopaedia.org [Accessed on: August 20, 2019] https://radiopaedia.org

[123] Podgorsak E B 2010 *Radiation Physics for Medical Physicists* (Heidelberg, Germany: Springer)

[124] Cherry S R, Sorenson J A and Phelps M E 2012 chapter 6 - Interaction of Radiation with Matter *Physics in Nuclear Medicine (Fourth Edition)* ed S R Cherry, J A Sorenson and M E Phelps (Philadelphia: W.B. Saunders) pp 63–85

[125] Verein deutscher Ingenieure e.V. 2014 Computed tomography in dimensional measurment Fundamentals and definitions VDI/VDE 2630-1.1 Draft

[126] Perkin and Elmer GmbH Perkin and Elmer Company presentation: High-resolution Digital Detector Arrays for Cone Beam Computed Tomography

[127] Hermanek P, Ferrucci M, Dewulf W and Carmignato S 2017 Optimized reference object for assessment of computed tomography instrument geometry iCT2017 7th confrence Ind. Comput. Tomogr. 7–8

[128] Warnett J M, Titarenko V, Kiraci E, Attridge A, Lionheart W R B, Withers P J and Williams M A 2015 Towards in-process x-ray CT for dimensional metrology Meas. Sci. Technol. 35401

[129] Aloisi V, Carmignato S, Schlecht J and Ferley E 2017 Investigation on the effects of X-ray CT system geometrical misalignments on dimensional measurement errors *iCT2017 7th confrence on industrial computed tomography* (Leuven, Belgium)

[130] Ferrucci M, Ametova E, Carmignato S and Dewulf W 2016 Evaluating the effects of detector angular misalignments on simulated computed tomography data Precis. Eng. 45 230–41

[131] Heismann B J, Leppert J and Stierstorfer K 2003 Density and atomic number measurements with spectral x-ray attenuation method J. Appl. Phys. 94 2073–9

[132] Crystals Saint-Gobain Datasheet: CsI(Tl), CsI(Na) Cesium Iodide Scintillation Material [Accessed on: August 1, 2019] https://www.crystals.saint-gobain.com/sites/imdf.crystals.com/files/documents/csitl-and-na-material-data-sheet_69771.pdf

[133] Wang G, Liu Y, Lin T H and Cheng P C 1994 Half-scan cone-beam x-ray microtomography formula. J. Scanning Microsc. 16 216–20

[134] Lee S W and Wang G 2003 A Grangeat-type half-scan algorithm for cone-beam CT Med. Phys. 30 689–700

[135] Varga L 2013 *Information Content of Projections and Reconstruction of Objects in Discrete Tomography (Dissertation)* (University of Szeged, Szeged, Hungary)

[136] van Aarle W, Palenstijn W J, Cant J, Janssens E, Bleichrodt F, Dabravolski A, De Beenhouwer J, Joost Batenburg K and Sijbers J 2016 Fast and flexible X-ray tomography using the ASTRA toolbox Opt. Express 24 25129

[137] Biguri A, Dosanjh M, Hancock S and Soleimani M 2016 TIGRE: A MATLAB-GPU toolbox for CBCT image reconstruction Biomed. Phys. Eng. Express 2

[138] Collaborative Computational Project in Tomographic Imaging Core Imaging Library

(CIL) [Accessed on: November 21, 2019] https://www.ccpi.ac.uk/cil

[139] Weiss G H, Talbert A J and Brooks R A 1982 The use of phantom views to reduce CT streaks due to insufficient angular sampling Phys. Med. Biol. 27 1151–62

[140] Epstein C L 2003 *Introduction to the mathematics of medical imaging* (New Jersey, USA: Pearson Education INC.)

[141] Parker D L 1982 Optimal short scan convolution reconstruction for fan beam CT Med. Phys. 9 254–7

[142] Schäfer D, Van De Haar P and Grass M 2017 Modified Parker weights for super short scan cone beam CT 14th Int. Meet. Fully Three-Dimensional Image Reconstr. Radiol. Nucl. Med. 49–52

[143] Landstorfer P and Hiller J 2017 Strategies to improve the spatial resolution in micro computed tomography imaging *iCT2017 7th Confrence on Industrial Computed Tomography* (Leuven, Belgium)

[144] Sun K, Kiess S and Simon S 2019 Spatial resolution enhancement based on detector displacement for computed tomography *Proceedings of the 9th Conference on Industrial Computed Tomography* (Padua, Italy)

[145] Desbat L, Roux S, Grangeat P and Koenig A 2004 Sampling conditions of 3D parallel and fan-beam x-ray CT with application to helical tomography. Phys. Med. Biol. 49 2377–90

[146] Thompson W and Huang Z 2016 Pub. No.: US2016/0252467 A1 X-ray CT microscopy system and method utilizing lattice sampling

[147] Placidi G, Alecci M and Sotgiu A 1995 Theory of Adaptive Acquisition Method for Image Reconstruction from Projections and Application to EPR Imaging J. Magn. Reson. Ser. B 108 50–7

[148] Carl ZEISS X-Ray Microscopy Inc 2013 User Manual Xradia 510Versa

[149] Hsieh J, Slack C L, Dutta S, Gordon III C L, Li J and Chao E 2001 Adaptive view synthesis for aliasing artifact reduction *Proc. SPIE 4320, Medical Imaging 2001:*

Physics of Medical Imaging vol 4320(San Diego, USA)pp 673–80

[150] Haque M A, Ahmad M O, Swamy M N S, Hasan M K and Lee S Y 2013 Adaptive projection selection for computed tomography IEEE Trans. Image Process. 22 5085–95

[151] Simo Y and Tayag T J 2012 Non-uniform projection angle processing in computed tomography Proc. SPIE - Int. Soc. Opt. Eng. 8494

[152] Manglos S H, Gagne G M, Krol A, Thomas F D and Narayanaswamy R 1995 Transmission Maximum-Likelihood Reconstruction with Ordered Subsets for Cone Beam CT Phys. Med. Biol. 40 1225–41

[153] Maltz J S, Bose S, Shukla H P and Bani-Hashemi A R 2007 CT Truncation artifact removal using water-equivalent thicknesses derived from truncated projection data Annu. Int. Conf. IEEE Eng. Med. Biol. - Proc. 2907–11

[154] Maaß C, Knaup M, Sawall S and Kachelrieß M 2010 ROI-Tomografie (Lokale Tomografie) *3rd Industrielle Computertomografie Tagung* (Wels, Austria) pp 251–60

[155] Ohnesorge B, Flohr T, Schwarz K, Heiken J P and Bae K T 2000 Efficient correction for CT image artifacts caused by objects extending outside the scan field of view Med. Phys. 27 39–46

[156] Kolditz D, Meyer M, Kyriakou Y and Kalender W A 2011 Comparison of extended field-of-view reconstructions in C-arm flat-detector CT using patient size, shape or attenuation information Phys. Med. Biol. 56 39–56

[157] Maaß C, Knaup M, Lapp R, Karolczak M, Kalender W A and Kachelrieß M 2008 A new weighting function to achieve high temporal resolution in circular cone-beam CT with shifted detectors Med. Phys. 35 5898–909

[158] Kyrieleis A, Titarenko V, Ibison M, Connolley T and Withers P J 2010 Region-of-interest tomography using filtered backprojection: Assessing the practical limits J. Microsc. 241 69–82

[159] Galigekere R, Wiesent K, Mertelmeier T and DW 2000 On intermediate view estimation in computed tomography Circuits, Syst. 19 279–99

[160] Hsieh J 2001 United States Patent US6529574 B1: Methods and apparatus for FOV-dependent aliasing artifact reduction

[161] Fischer A, Lasser T, Schrapp M, Stephan J and Noël P B 2016 Object Specific Trajectory Optimization for Industrial X-ray Computed Tomography Sci. Rep. 6

[162] Stayman J W and Siewerdsen J H 2013 Task-based trajectories in iterative reconstructed interventional cone-beam CT Int. Meet. Fully Three-Dimensional Image Reconstr. Radiol. Nucl. Med. 257–60

[163] Dabravolski A, Batenburg K J and Sijbers J 2014 Dynamic angle selection in X-ray computed tomography Nucl. Instruments Methods Phys. Res. Sect. B Beam Interact. with Mater. Atoms 324 17–24

[164] Varga L, Balazs P and Nagy A 2010 Projection selection algorithms for discrete tomography Lect. Notes Comput. Sci. (including Subser. Lect. Notes Artif. Intell. Lect. Notes Bioinformatics) 390–401

[165] Batenburg K J and Sijbers J 2011 DART: A practical reconstruction algorithm for discrete tomography IEEE Trans. Image Process. 20 2542–53

[166] Batenburg K J and Sijbers J 2006 Dart: A fast heuristic algebraic reconstruction algorithm for discrete tomography Proc. - Int. Conf. Image Process. ICIP 4 2–5

[167] Alves Pereira L F, Janssens E, Cavalcanti G D C, Tsang I R, Van Dael M, Verboven P, Nicolai B and Sijbers J 2017 Inline discrete tomography system: Application to agricultural product inspection Comput. Electron. Agric. 138 117–26

[168] Schrapp M J and Herman G T 2014 Data fusion in X-ray computed tomography using a superiorization approach Rev. Sci. Instrum. 85

[169] Cant J, Palenstijn W J, Behiels G and Sijbers J 2014 Tomographic image reconstruction from continuous projections third Int. Conf. image Form. X-ray Comput. Tomogr. 295–8

[170] Cant J, Palenstijn W J, Behiels G and Sijbers J 2015 Modeling blurring effects due to continuous gantry rotation: Application to region of interest tomography. Med. Phys. 42 2709–17

[171] Gondrom-Linke S 2016 Basics and physics of X-ray imaging & 3D computed tomography *Volume Graphics User Group Meeting* (Heidelberg, Germany)

[172] Nikon Metrology NV *Nikon 3DCT PRO Manual*

[173] Hiller J, Maisl M and Reindl L M 2012 Physical characterization and performance evaluation of an x-ray micro-computed tomography system for dimensional metrology applications Meas. Sci. Technol. 23

[174] Hiller J and Hornberger P 2016 Measurement accuracy in X-ray computed tomography metrology: Toward a systematic analysis of interference effects in tomographic imaging Precis. Eng. 45

[175] Maskery I, Aboulkhair N T, Corfield M R, Tuck C, Clare A T, Leach R K, Wildman R D, Ashcroft I A and Hague R J M 2016 Quantification and characterisation of porosity in selectively laser melted Al–Si10–Mg using X-ray computed tomography Mater. Charact. 111 193–204

[176] Matern D, Herold F and Wenzel T 2016 On the Influence of Ring Artifacts on Dimensional Measurement in Industrial Computed Tomography *6th Conference on Industrial Computed Tomography (2016)* (Wels, Austria)

[177] Heinzl C, Reiter M, Allerstorfer M, Kastner J and Gröller E 2010 Artefaktreduktion mittels Dual Viewing für Röntgencomputertomographie von Multimaterialbauteilen DGZfP-Jahrestagung 2010 1–8

[178] https://uk.mathworks.com/products/matlab.html MATLAB

[179] Radiology Key Image Reconstruction [Accessed on: November 19, 2019] https://radiologykey.com/image-reconstruction/

[180] Leng S, Zhuang T, Nett B E and Chen G-H 2005 Exact fan-beam image reconstruction algorithm for truncated projection data acquired from an asymmetric

half-size detector Phys. Med. Biol. 50 1805–20

[181] Reisinger S, Schmitt M and Voland V 2012 Geometric adjustment methods to improve reconstruction quality on rotational cone-beam systems Conf. Ind. Comput. Tomogr. 2012 Proc. 261–70

[182] Körner L, Lawes S, Newton L, Senin N, Bate D and Leach R 2019 Sinogram interpolation to decrease acquisition time in X-ray computed tomography measurement of surface topography *iCT2019 9th Confrence on Industrial Computed Tomography* (Padova, Italy)

[183] Körner L, Lawes S, Bate D, Newton L, Senin N and Leach R K 2019 Increasing throughput in X-ray computed tomography measurement of surface topography using sinogram interpolation Meas. Sci. Technol. 30

[184] Thompson A, Senin N, Maskery I and Leach R K 2017 A sensitivity analysis for the measurement of internal additively manufactured surfaces by X-ray computed tomography *A contribution at NPL's Second Dimensional X-ray Computed Tomography Conference* (Coventry, UK)

[185] Volume Graphics GmbH VG Studio 2.0 [Accessed on: June 2, 2018] www.volumegraphics.com

[186] Besl P J and McKay N D 1992 A Method for Registration of 3-D Shapes IEEE Trans. Pattern Anal. Mach. Intell. 14 239–56

[187] National Physical Laboratory Data File Format. [Accessed on: November 18, 2019] http://resource.npl.co.uk/softgauges/help.htm

[188] Surface and Nanostructure Metrology Group Semiconductor and Dimensional Metrology Division Physical Measurement Laboratory Acceptable Data Format [Accessed on: November 18, 2019] https://physics.nist.gov/vsc/jsp/dataformat.jsp#a

[189] Boslaugh S 2012 *Statistics in a nutshell* (Sebastopol, USA: O'Reilly Media)

[190] ISO ISO 25178-2:2012 Geometrical product specifications (GPS) -- Surface

texture: Areal -- Part 2: Terms, definitions and surface texture parameters

[191] British Standards Institution ISO 12233:2017 Photography — Electronic still picture imaging — Resolution and spatial frequency responses

[192] Otsu N 1979 A Threshold Selection Method from Gray-Level Histograms IEEE Trans. Syst. Man. Cybern. 9 62–6

[193] Nikon Metrology NV nikonmetrology.co.uk [Accessed on: October 24, 2016] nikonmetrology.co.uk

[194] Kiekens K, Welkenhuyzen F, Tan Y, Bleys P, Voet A, Kruth J-P and Dewulf W 2011 A test object will parallel grooves for calibration and accuracy assessment of industrial computed tomography CT metrology Meas. Sci. Technol. 22

[195] Kasperl S, Hiller J and Krumm M 2009 Computed tomography metrology in industrial research and development Mater. Test. 51 405–11

[196] Hiller J, Kasperl S, Hilpert U and Bartscher M 2007 Coordinate measuring with industrial X-ray computed tomography Tech. Mess. 74

[197] Bundesanstalt für Materialforschung und -prüfung (BAM) artist Simulation software [Accessed on: February 5, 2017] http://www.artist.bam.de/

[198] Thompson A, Senin N, Maskery I and Leach R 2018 Effects of magnification and sampling resolution in X-ray computed tomography for the measurement of additively manufactured metal surfaces Precis. Eng. 0–1

[199] Rubert & Co Ltd 2018 Precision Reference Specimens [Accessed on: May 2, 2019] http://www.rubert.co.uk/reference-specimens/

[200] Veldkamp W J H, Joemai R M S, Van Der Molen A J and Geleijns J 2010 Development and validation of segmentation and interpolation techniques in sinograms for metal artifact suppression in CT Med. Phys. 37 620–8

[201] Zhang H and Sonke J J 2013 Directional sinogram interpolation for sparse angular acquisition in cone-beam computed tomography J. Xray. Sci. Technol. 21 481–96

[202] Lee H, Lee J, Kim H, Cho B and Cho S 2018 Deep-Neural-Network-Based Sinogram

Synthesis for Sparse-View CT Image Reconstruction IEEE Trans. Radiat. Plasma Med. Sci. 3 109–19

[203] European Committee for Standardization Non-destructive testing - Characteristics of focal spots in industrial X-ray systems for use in non-destructive testing - Part 5 : Measurement of the effective focal spot size of mini and micro focus EN 12543-5-1999

[204] Bavendiek K, Ewert U, Riedo A, Heike U and Zscherpel U 2012 New Measurement Methods of Focal Spot Size and Shape of X-ray Tubes in Digital Radiological Applications in Comparison to Current Standards *18th World Conference on Non-Destructive Testing*

[205] British Standards Institution Determing the characteristics of focal spots in diagnostic X-ray tube assemblies for medical use BS 65301994

[206] Oliveira A D, Fartaria M J, Cardoso J, Santos L M, Oliveira C, Pereira M F and Alves J G 2015 The determination of the focal spot size of an X-ray tube from the radiation beam profile Radiat. Meas. 82 138–45

[207] Jain A, Panse a, Bednarek D R and Rudin S 2014 Focal spot measurements using a digital flat panel detector. Proc. SPIE--the Int. Soc. Opt. Eng. 9033 4–7

[208] Carmignato S 2012 Accuracy of industrial computed tomography measurements: Experimental results from an international comparison CIRP Ann. - Manuf. Technol. 61 491–4

[209] Thalmann R, Spiller J, Küng A and Jusko O 2012 Calibration of Flick standards Meas. Sci. Technol. 23 1–7

[210] Committee of the ISO 25178 2012 ISO 25178 Geometrical product specifications (GPS) — Surface texture : Areal Part 3 : Specification operators

[211] Leach R K 2014 *Fundamental Principles of Engineering Nanometrology* (Oxford: William Andrew)

[212] Illemann J, Neuschaefer-rube U, Bartscher M and Bate D 2018 Determining

spectrum-dependent source and detector positions in cone-beam CT 8th Conf. Ind. Comput. Tomogr. 3–10

[213] Arenhart F A, Nardelli V C and Donatelli G D 2016 Comparison of surface-based and image-based quality metrics for the analysis of dimensional computed tomography data Case Stud. Nondestruct. Test. Eval. 6 111–21

[214] Körner L, Lawes S, Senin N and Leach R K 2019 Simulation of continuous high aspect ratio tomography for surface topography measurements *dXCT2019* (Huddersfield, UK)

[215] Warwick T High Aspect Ratio Tomography (Bruker HART PLUS) [Accessed on: July 12, 2019] http://www.blue-scientific.com/high-aspect-ratio-micro-tomography/

[216] Freud N, Duvauchelle P and Babot D 2000 Simulation of X-Ray {NDT} Imaging Techniques *15th World Conference on Non-Destructive Testing, Roma, 15-21 October 2000*

[217] Welkenhuyzen F 2016 *Investigation of the accuracy of an X-ray CT scanner for dimensional metrology with the aid of simulations and calibrated artifacts* (KU Leuven)

[218] Verein deutscher Ingenieure e.V. 2010 Computed tomography in dimensional measurement Influencing variables on measurement results and recommendations for computed-tomography dimensional measurements VDI/VDE 2630-1.2

[219] Thornton C, Armstrong C, Brenner C, Bourgeois N, Gregory C and Katzir Y 2019 Laser driven sources for a new generation of high resolution hard x-ray CT machines *iCT2019 9th Confrence on Industrial Computed Tomography* (Padua, Italy)

[220] Fleßner M, Müller A, Helmecke E and Hausotte T 2014 Evaluating and visualizing the quality of surface points determined from computed tomography volume data *Proc. MacroScale* (Vienna, Austria)

[221] Amirkhanov A, Heinzl C, Kuhn C, Kastner J and Gröller M E 2013 Fuzzy CT Metrology *Spring Conference on Computer Graphics - SCCG '13* (Smolenice, Slovak Republic)

pp 81–90